Ultrawideband and Multi-state Reconfigurable Antennas with Sum and Difference Radiation Patterns

by

Seyedali Malakooti

B. S. (Electrical and Electronic Engineering),
Razi University, Kermanshah, Iran, 2010
M. S. (Electrical and Electronic Engineering),
Razi University, Kermanshah, Iran, 2013

Thesis submitted for the degree of

Doctor of Philosophy

in

School of Electrical & Electronic Engineering
Faculty of Engineering, Computer & Mathematical Sciences
The University of Adelaide

2019

Supervisors:

Prof. Christophe Fumeaux, School of Electrical & Electronic Engineering

Assoc. Prof. Damith Chinthana Ranasinghe, School of Computer Science

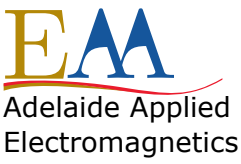

THE UNIVERSITY of ADELAIDE

To my better half, Sophie
and to my parents with all my love.

Contents

Abstract

PATTERN diversity is a term used to describe the operation of several antenna elements working together to produce multiple different radiation patterns with the aim of improving the quality and reliability of a communications system. One useful implementation of pattern diversity considers sum and difference radiation patterns which can be exploited to extend high-gain space coverage and tackle multipath fading. The conventional forms of such pattern diversity antennas are generally working at a single or multiple narrowband frequencies and are designed for specific applications. Hence, generating sum and difference pattern diversity in wide range of frequencies requires the development of new pattern diversity antenna designs. Ultrawideband and frequency reconfigurable designs of pattern diversity antennas are desirable to help reduce the cost and increase the flexibility in applications of pattern diversity antennas. These two types of performances constitute the principal parts of this thesis.

The first part of this thesis deals with the challenges of designing ultrawideband Vivaldi antennas with sum and difference radiation patterns. When two Vivaldi antennas are placed next to each other, two mutually exclusive phenomena of grating lobe generation at the highest end of frequency and mutual coupling at the lowest end of frequency will define the bandwidth. Hence, to enhance the bandwidth, the separation between the antenna elements is reduced, which delays the grating lobes generation, and the coupling at lower frequencies is mitigated by introducing an asymmetry in the design of each Vivaldi antenna element. It is shown that this method can be extended to multi-element Vivaldi antennas for higher gain. Next, the bandwidth is further enhanced by adding two vertical metal slabs between the antenna elements improving the isolation at lower frequencies. The proposed antennas use commercially available couplers as feeding networks. As a potential replacement for couplers, an out-of-phase power divider with unequal power division is also proposed.

In the second part of this thesis, the pattern diversity function is combined with multi-state frequency-reconfigurable filtering functions in a series of novel designs. In the first proposed design, two quasi-Yagi-Uda antennas are used for pattern diversity,

while two switchable and reconfigurable bandpass-to-bandstop filters are used to excite the antenna elements. The whole system is excited by an external commercially available rat-race coupler. In a next step, this design is modified to attain wideband, tunable bandpass, and tunable bandstop operations while obviating the need for an external coupler by using three antenna elements excited by a switchable power divider. In another implementation, the filtering functions is extended to dual-band independently tunable bandpass and bandstop to excite wideband antennas. While all the former designs featured E-plane pattern diversity, in another design aiming at increasing space coverage, a switchable patch antennas with sum and difference radiation patterns in both E- and H-plane of the antenna is designed.

Originality Declaration

I certify that this work contains no material which has been accepted for the award of any other degree or diploma in my name, in any university or other tertiary institution and, to the best of my knowledge and belief, contains no material previously published or written by another person, except where due reference has been made in the text. In addition, I certify that no part of this work will, in the future, be used in a submission in my name, for any other degree or diploma in any university or other tertiary institution without the prior approval of the University of Adelaide and where applicable, any partner institution responsible for the joint-award of this degree.

I acknowledge that copyright of published works contained within this thesis resides with the copyright holder(s) of those works.

I also give permission for the digital version of my thesis to be made available on the web, via the Universitys digital research repository, the Library Search and also through web search engines, unless permission has been granted by the University to restrict access for a period of time.

	10/12/2019
Signed	Date

Acknowledgments

I would like to express my deep gratitude to my supervisors Prof. Christophe Fumeaux and Assoc. Prof. Damith Chinthana Ranasinghe who gave me a great chance to apply for Ph.D degree at the University of Adelaide and successfully win a competitive Adelaide Scholarship International (ASI) scholarship in late August 2016. Since then, they helped me understand the basic concepts of antennas and propagation and helped me gain confidence in my research pathway. Prof. Fumeaux is a model of a supportive and kind supervisor who selflessly supports his students and encourages them to work diligently for their goals. His deep knowledge and experience in electromagnetics and antennas has always inspired me. Caring about the high quality of research and encouraging students to think critically about their research achievements are his iconic images. Dear ***Prof. Christophe Fumeaux***, before coming to Australia and starting my research with you, I had no idea that I would secretly be guided to work with a person that I had always wanted to work with and learn from. I would like to, from the bottom of my heart, express my deepest appreciation to all your selfless support to me and my family. Assoc. Prof. Ranasinghe has very comprehensive knowledge about antennas and their diverse applications in computer science. My respectful supervisory panel has always patiently and critically corrected my manuscripts and provided critical feedbacks and suggestions without which I would not be able to publish my research papers. They have made my Ph.D journey marvelous and invaluable experience that I will carry on for the rest of my life. I highly appreciate all their time, ideas, generous experience sharing, high standard requirements and contributions.

I am so grateful for the support and advices from my friends and colleagues in our Applied Electromagnetics Group at the University of Adelaide, Dr. Withawat Withayachumnankul, Dr. Shengjian Jammy Chen, Dr. Nghia-Nguyen Trong, Dr. Wendy Suk Ling Lee, Dr. Siti Nailah Mastura Zainarry, Dr. Morteza Shahpari, Mr. Weijie Gao, Mr. Xiaolong You, Mr. Ken Paramayudha, Mr. Xiaojing (Alex) Lv and Mr. Xiaoyang Yin. I enjoyed very much the time of our group meetings and discussions. In particular, I am indebted to Dr. Withawat Withayachumnankul who always welcomed scientific discussions and was ready to give critical feedback. I also would like to acknowledge the kindness and assistance from my colleagues and friends in the University of Adelaide:

Mr. Alban O'Brien, Mr. Ian Linke, Mr. Brandon Pullen, Mr. David Bowler, Mr. Danny Di Giacomo, Ms. Jodie Schluter, Ms. Laura Hall, and Ms. Laura McNamara.

I gratefully acknowledge the generous financial support from the University of Adelaide due to the provision of Adelaide Scholarship International (ASI) to support my expenses during my Ph.D. Additionally, I would like to express my gratitude to the School of Electrical & Electronic Engineering for the annual travel grants (2017-2019), and to the University of Adelaide and University of Stuttgart in Germany for providing me with travel grants (2019) so that I could attend several international conferences to explore new ideas and knowledge.

My deepest gratefulness and love go to my wife Somayeh (Sophie) who has always supported and stood by me during the vicissitudes of a new life in a new country and studying Ph.D. I love you so much! I also wish to express my sincerest appreciation to my parents and siblings who provided me with a great chance to follow my dreams.

Seyedali Malakooti
December 2019
Adelaide, Australia

Thesis Conventions

The following conventions have been adopted in this Thesis:

Typesetting

This document was compiled using LaTeX2e. TeXstudio is used as text editor interfaced to LaTeX2e. Inkscape was used to produce schematic diagrams and other drawings.

Referencing

The referencing and citation style adopted in this thesis are based on the Institute of Electrical and Electronics Engineers (IEEE) Transaction style.

System of units

The units comply with the international system of units recommended in an Australian Standard: AS ISO 1000–1998 (Standards Australia Committee ME/71, Quantities, Units and Conversions 1998).

Spelling

American English spelling is adopted in this thesis.

Awards and Scholarships

2019

- Best Student Paper Award (Platinum), IEEE 8th Asia-Pacific Conference on Antennas and Propagation (APCAP 2019)
- Travel Scholarship, German Microwave Conference (GeMiC 2019)
- Research Travel Scholarship, The University of Adelaide

2018

- Applied Electromagnetics Supplementary Industrial Scholarship
- Student Paper Award (Second Prize), IEEE 7th Asia-Pacific Conference on Antennas and Propagation (APCAP 2018)

2016

- Adelaide Scholarship International (ASI), The University of Adelaide

Publications

Journal Articles

S.-A. Malakooti, M. Moosazadeh, D. C. Ranasinghe, and C. Fumeaux, "Antipodal Vivaldi antenna for sum and difference radiation patterns with reduced grating lobes," *IEEE Antennas Wirel. Propag. Lett.*, vol. 16, pp. 3139 - 3142, Oct. 2017.

S.-A. Malakooti, S. M. H. Mousavi, and C. Fumeaux, "Tunable bandpass-to-bandstop quasi-Yagi-Uda antenna with sum and difference radiation patterns," *IEEE Trans. Antennas Propag.*, vol. 67, no. 4, pp. 2260 - 2271, Apr. 2019.

S.-A. Malakooti and C. Fumeaux, "Comments on "Wideband radiation reconfigurable microstrip patch antenna loaded with two inverted U-slots"," *IEEE Trans. Antennas Propag.*, in print, 2020.

S.-A. Malakooti and C. Fumeaux, "Pattern-reconfigurable antenna with switchable wideband to frequency-agile bandpass/bandstop filtering operation," *IEEE Access*, vol. 7, pp. 167065 - 167075, Nov. 2019.

Conference Articles

S.-A. Malakooti and C. Fumeaux, "Multi-element Vivaldi antenna with sum and difference radiation patterns," *IEEE Asia-Pacific Conference on Antennas and Propagation (APCAP)*, Auckland, New Zealand, Aug. 2018, pp. 34 - 35. **[Student Paper Award (Second Prize) of APCAP 2018]**

S.-A. Malakooti and C. Fumeaux, "Bandwidth enhancement of a double-element Vivaldi antenna with sum and difference radiation patterns," *Asia-Pacific Microwave Conference (APMC)*, Nov. 2018, Kyoto, Japan, pp. 1166 - 1168.

S.-A. Malakooti and C. Fumeaux, "Wideband out-of-phase power divider with large power division ratios," *12th German Microwave Conference*, Mar. 2019, Stuttgart, Germany, pp. 174 - 177.

S.-A. Malakooti and C. Fumeaux, "Dual-band bandpass filtering monopole antenna with independently tunable frequencies," *IEEE Asia-Pacific Conference on Antennas and*

Propagation (APCAP), Aug. 2019, Incheon, Korea, pp. 1 - 2. **[Best Student Paper Award of APCAP 2019]**

S.-A. Malakooti and C. Fumeaux, "A pattern diversity microstrip antenna with switchable sum and difference beams in E- and H-plane," *International Conference on Electromagnetics in Advanced Applications*, Sep. 2019, Granada, Spain, pp. 623 - 625.

S.-A. Malakooti and C. Fumeaux, "Independently tunable dual-band bandstop filtering antenna," in *IEEE Radio and Antenna Days of the Indian Ocean*, Sep. 2019, Reunion Island, France, pp. 1 - 2.

List of Figures

List of Tables

Chapter 1

Introduction

THIS introductory chapter describes the concept of antenna diversity along with its applications, realization methods, and challenges. Following those considerations, an overview of the thesis objectives is given in conjunction with the statement of original contributions. This section ends with the thesis outline including a short summary of each chapter.

1.1 Introduction

Antenna diversity is a method used to increase the robustness and link reliability between wireless systems by utilizing two or more antenna elements as transmitters or receivers. Antenna diversity can find applications in mitigating multipath fading [1], increasing channel capacity [2–4], allowing transmitted and received signals to be isolated in base station antennas [5], and enlarging the angular range of high-gain signal coverage [6, 7]. Pattern diversity antennas belong to a type of antennas which have been conventionally realized by different mode perturbation of double- or multiple-input antennas. There are different methods to excite the antenna inputs to diversify the patterns. One salient method of excitation is using in-phase and anti-phase signals for double-input antennas to generate different radiation patterns. Utilizing this method, designs in [2, 3, 8, 9] provided broadside directive and conical radiation patterns employing different input excitations. Also, using the same methods, sum and difference radiation patterns were generated with the planar designs presented in [10, 11]. This method has also been applied in multiple-input antennas as in [12, 13] to enhance the gain and spatial coverage. Another widespread method is to feed two or more antennas with different radiation characteristics and adequate isolation separately, thereby generating diverse patterns [4, 6, 14–17]. Another approach to design pattern diversity antennas is using electronic switches in the radiating section of an antenna. This method has received tremendous attention over the last decade owing to the flexible and low cost solutions it offers. With all different designs presented in the open literature, there are however some unresolved challenges towards designing pattern diversity antennas meeting the current demands of higher data rate and coping with microwave frequency spectrum congestion.

Increasing the bandwidth of pattern diversity antennas can enhance the channel capacity and provide higher data rate for communications. However, enhancing the bandwidth in diversity antennas is quite challenging due to two mutually exclusive phenomena. First, densely packed antennas exhibit strong mutual coupling which is detrimental to the overall throughput of the system [18]. Second, if the distance between the antenna elements is enlarged to alleviate the coupling problem, the overall system will become more voluminous and grating lobes will appear at higher frequencies as a result of large distance between the antennas compared to the wavelength. Addressing these mutually exclusive problems can bring about higher bandwidth for pattern diversity antennas.

Spectrum scarcity due to the exhaustive utilization of available frequency bands by licensed users requires antennas that can sense a wideband frequency spectrum, identify idle frequencies, and allocate the unused frequencies to waiting users. These are the requirements for cognitive radio systems. To ensure wide angular space coverage and reliable links in cognitive radio systems, pattern diversity function is needed to be incorporated into cognitive radio systems. For these purposes, advanced pattern diversity antennas are required with specific frequency responses. In the sensing state of cognitive radio systems, a wideband antenna is required to sense the frequency spectrum and identify the idle bands. A reconfigurable antenna is required for allocating the idle narrow frequency bands to the waiting users. Also, a reconfigurable notch-band antenna is required to avoid interference with already occupied narrow frequency bands. The simultaneous realization of these functionalities with different antennas may result in a voluminous front-end network. An important challenge is then to combine pattern diversity with the aforementioned multistate frequency responses in a single compact system, with the aim of reducing the cost and complexity of the hardware. In the context of these stated challenges, this dissertation investigates the design and fabrication of ultrawideband and multi-state reconfigurable antennas with pattern diversity function.

1.2 Objectives of the thesis

The objective of this thesis is to address the mentioned challenges and the research work can be divided according to the following two main objectives.

1. **Planar ultra-wideband antennas with sum and difference radiation patterns**

   As mentioned earlier, an increase in the bandwidth and the number of channels for pattern diversity antennas would further contribute to higher data rate by allowing several systems to co-exist. To this end much attention has been paid to bandwidth enhancement for pattern diversity antennas over the last decade. The 3D design proposed in [2] provided broadside to conical radiation patterns with 45% overlapping bandwidth. This wide bandwidth was achieved by improving the isolation between two independently functioning wideband antenna elements. To enhance the bandwidth with planar antenna structure, planar UWB monopole antennas with various isolation improvement techniques have been reported in the open literature. In [19], active elements were used to reduce the

coupling between two adjacent monopole antennas, whereas [20] used carbon black film to reduce the coupling between two monopole antennas. Manipulating the ground plane structure of the antenna was another salient method applied for mutual coupling reduction of adjacent monopole antennas [21–23]. Orthogonal arrangement of tightly packed antenna elements for pattern diversity was also proven as a useful method to reduce the mutual coupling [24–26]. All the above mentioned planar structures featured monopolar pattern diversity apart from [26]. Although [26] presented a design with 4 directive patterns in 4 different directions, its realized gain was limited. Besides, it required a 3D structure for the generation of its 4 different radiation patterns. Importantly, it was demonstrated that obtaining ultra-wide bandwidth for pattern diversity antennas with planar structures requires an antenna element with intrinsically wide bandwidth.

Although planar monopole antennas have these features, they cannot be used for sum and difference radiation pattern generation due to their inabilities to produce unidirectional patterns. Hence, planar unidirectional antennas can be good candidates for this goal. The most renowned types of planar directive and wideband antennas include Vivaldi [27–29], Log-periodic [30–32], and quasi Yagi-Uda antennas [33–37]. Generating sum and difference radiation patterns with these types of antennas is feasible by arranging two elements side by side and exciting the inputs by in-phase and anti-phase signals. To enhance the overall design bandwidth, an improved isolation between two elements at lower frequencies is a must. The simple method to achieve isolation is to increase the distance between the two antenna elements. However, this will bring up another issue which is the appearance of grating lobes at frequencies where the distance between the input ports is larger than λ. These grating lobes will set a limit to the highest operating frequency. Therefore, the objective of this thesis is to resolve the mutually exclusive problems of reducing the mutual coupling between two antennas in close proximity and mitigating the grating lobe appearances at higher frequencies. This will lead to further performance improvement in terms of gain and bandwidth.

2. **Planar reconfigurable antennas with multi-state filtering functions**

   Although ultrawideband antennas are utilized in many different communications applications, they offer some disadvantages limiting their applicability in

modern communications era. First, ultrawideband antennas are subject to interference from the bands which are not in use, thus yielding a low signal-to-noise ratio. Also, today's congested frequency spectrum requires a more efficient method of utilizing the available frequency bands. To this end, antennas with frequency reconfigurability can overcome the shortcomings of ultrawideband antennas. They work in a narrowband frequency range that can be tuned discretely or continuously over a wide frequency band [38–43]. This feature can enhance the level of signal-to-noise ratio while providing a broad instantaneously available frequency coverage. Recently, much attention has been paid to antennas offering the flexibility of different states of reconfigurability realized on one single radiating structure. The desirable combined reconfigurability features include: frequency- and pattern-reconfigurable antennas [42, 43], frequency- and polarization-reconfigurable antennas [40, 41], and pattern- and polarization-reconfigurable antennas [44–46]. Although these types of compound reconfigurabilities are useful for design agility and reducing cost and complexity of antennas, there are still some applications with unmet demands. For example, cognitive radio systems as efficient means of reducing spectrum congestion in modern communications require two stages of operation. For the first stage, they need antenna front-ends with the ability of scanning a wide frequency spectrum to detect unused bands and allocate those unused bands to secondary users. In the second stage, they need a wideband antenna in their front-end with the ability to dynamically tune a notch frequency to avoid interference with the already occupied band [47]. Developing a hardware for cognitive radio system that uses a single antenna is a big challenge for antenna designers. Hence, in this thesis the next goal is to realize a system fulfilling the requirements of cognitive radio systems. This goal will be enhanced by providing pattern diversity and multiband operation to the system.

1.3 Original contributions summary

In this dissertation, the original contributions are classified into two major sections. The first section presents variations of pattern-diversity and ultrawideband Vivaldi antennas with reduced grating lobes and enhanced isolation. The presented work focuses on novel methods to improve the gain and bandwidth beyond conventional designs. The second section proposes concepts of planar antenna systems which suit cognitive

radio applications while offering pattern diversity and multiband performances. The detailed statement of original contributions is as follows.

1.3.1 Pattern-diversity and ultrawideband Vivaldi antennas

In this section, the original contributions on Vivaldi antennas with radiation pattern diversity, namely sum and difference patterns are listed as presented in Chapter 3 and Chapter 4 of this thesis.

- A design of an E-plane double-element Vivaldi antenna with sum and difference radiation patterns is proposed in Chapter 3. The antenna operates in the frequency range of 2.3 GHz to 15 GHz (ratio of 6.5:1) with the highest grating lobe level of -10 dB at 15 GHz and competitive gain performance from 6.8 dBi at 2.3 GHz up to 14.7 dBi at 15 GHz. The grating lobes are reduced effectively by decreasing the distance between the two input ports to one wavelength at the highest operating frequency. The active S-parameters of the antenna are improved using modifications of the geometry, including a new method consisting of an increased length of the internal flares, as well as combinations of known methods such as elliptical corrugations on the outer edges and optimal shaping of inner edges of the antenna. The gain is also improved by the addition of a dielectric lens, which also provides extra space for lengthening the internal flares. The proposed double-element antenna satisfactorily provides the sum and difference radiation patterns when fed by a wide-band rat-race coupler. To warrant a near ideal beam symmetry, the antenna is designed so that the directive radiation pattern occurs when the antenna elements are fed by out-of-phase signals, i.e. when the difference (Δ) port of the coupler is excited. This design has been published in *IEEE Antennas and Wireless Propagation Letters* under the title of "Antipodal Vivaldi Antenna for Sum and Difference Radiation Patterns with Reduced Grating Lobes" [48].

- Chapter 3 extends the idea of bandwidth enhancement by applying it to multi-element Vivaldi antennas. Ultrawideband Multi-element Vivaldi antennas can compensate the low gain at lower frequencies and the loss generated by the feeding coupler. This multi-element design can cover the band of 3.9 GHz to 18 GHz, with a gain increasing from 10 dBi at 3.9 GHz up to 16.5 dBi at 18 GHz. The grating lobes at higher frequencies are mitigated through an increased proximity of

the antenna elements in conjunction with reduced mutual coupling. The realized gain enhancement is obtained through the adoption of four tapered slot elements and a semicircular dielectric substrate lens, which also provides extra space for elongating the internal flares. The proposed antenna also generates two different radiation patterns based on the excitation phase of the input ports, namely sum and difference radiation patterns. This work has been published in *Asia-Pacific Conference on Antennas and Propagation (APCAP 2018)* under the title of "Multi-element Vivaldi Antenna with Sum and Difference Radiation Patterns" [49]. This paper was awarded the second prize in the in the student paper contest of APCAP 2018 in Auckland, New Zealand.

- The next design presented in Chapter 3 further enhances the bandwidth of the antenna presented in the first part of this chapter to the range from 2.6 GHz to 18 GHz with a gain increasing from 7.3 dBi at 2.6 GHz up to 15.1 dBi at 18 GHz. The bandwidth extension is obtained in the base double-element Vivaldi antenna by reducing the distance between the two elements and elongating the inner flares, thus delaying the emergence of grating lobes as described above. The mutual coupling level between the ports is further decreased by introducing two vertical metal slabs between the antenna elements. Some well-known methods are also adopted to improve the scattering parameters and enhance the radiation performance including etching elliptical corrugations on the outermost edges of the antenna, abruptly bending the inner edges, and incorporating a semicircle dielectric substrate lens into the antenna boresight. In order to realize the pattern diversity function, an ultrawideband 180° hybrid coupler is utilized to excite the antenna elements with in-phase and out-of-phase signals. This design has been published in *Asia-Pacific Microwave Conference 2018 (APMC 2018)* under the title of "Bandwidth Enhancement of a Double-Element Vivaldi Antenna with Sum and Difference Radiation Patterns" [50].

- In our former designs we proved that the mirror arrangement of antennas on the E-plane will bring about more beam symmetry at the expense of feeding antennas with out-of-phase inputs to generate a directive radiation pattern. Moreover, an antenna feeding network with unequal power division at its output will help reduce the sidelobe levels when feeding several antenna elements with nonuniform power distribution. Hence, an out-of-phase power divider with large power division ratios and broadband response is realized in the next design (Chapter 4))

based on the double-sided parallel-strip lines with an inserted conductor as a virtual ground. The wideband performance is achieved through sacrificing the perfect isolation and return loss at the main frequency by modifying the impedance of only two transmission lines. Using a third-order approximation based on the least squares fitting method, the need for optimization of the two targeted transmission lines producing wideband response is bypassed. To substantiate the design method and equations, a circuit with 25:1 power division ratio in conjunction with 80% operational bandwidth referring to 15 dB return loss and isolation is developed. The measured results show the maximum 0.8 dB amplitude deviation from the specified power division ratio with a phase difference between the output ports of $180\pm5^{\circ}$. This work has been published in *German Microwave Conference (GeMiC 2019)* under the title of "Wideband Out-of-Phase Power Divider with Large Power Division Ratios" [51].

- A misconception about dual-input antennas and their performance is pointed out and explained in the Appendix A. It is demonstrated how using S_{11} as opposed to active S_{11} will result in incorrect interpretation of some performance metrics for a multi-port antenna. This work has been accepted and published as an Early Access article in *IEEE Transactions on Antennas and Propagation* under the title of "Comments on "Wideband Radiation Reconfigurable Microstrip Patch Antenna Loaded with Two Inverted U-Slots"" [52].

1.3.2 Planar multi-state reconfigurable antennas with filtering function

The original contributions for planar and multi-state reconfigurable antenna systems by integration of the separate designs of filters and antennas are presented in Chapters 5 to 7 as listed below:

- A design of a double-element E-plane quasi Yagi-Uda antenna is proposed in Chapter 5 offering two different radiation patterns and reconfigurable bandpass-to-bandstop frequency tunable responses. The double-element antenna covers a wideband frequency range that is exploited for the realization of tunable bandpass-to-bandstop responses. This is achieved by the integration of a pair of bandpass-to-bandstop filters, each of which can be reconfigured using two varactor diodes and one PIN diode. The PIN diode serves the function of switching between

bandpass and bandstop states. The varactors provide the continuous frequency tuning function with the tuning range reaching 50% for the bandpass state and 50.4% for the bandstop state. Importantly, the reconfigurable filtering functionality of the two-element antenna is preserved when fed by a wideband hybrid coupler to produce both the sum- and difference radiation patterns. To obtain a high beam symmetry, the antenna elements are fed by the difference (Δ) signal to produce the directive radiation pattern and they are fed by the sum (Σ) port to produce the null in the main radiation direction. Experimental results validate this concept. This work has been published in *IEEE Transactions on Antennas and Propagation* under the title of "Tunable Bandpass-to-Bandstop Quasi Yagi-Uda Antenna with Sum and Difference Radiation Patterns" [53].

- While the antenna presented in Chapter 5 offered some attractive features for cognitive radio systems, the state of wideband in its performance was missing. Moreover, the use of coupler as a feeding network will introduce extra loss and cost to the design. Hence, a three-element antenna system with the ability to operate in a unique set of switchable and frequency-tunable configurations is presented in Chapter 6, where a significant enhancement is its ability to operate without the coupler feeding. Firstly, this antenna system can switch between sum and difference radiation patterns using a mirrored arrangement of antenna feeding lines that bypasses the need for an additional phase inverter. Secondly, the frequency response of this antenna can be switched between three states of operation, namely wideband, tunable bandpass, and tunable bandstop characteristics. Importantly, the pattern reconfigurability function can be generated in all three states of the frequency-agile response. To realize this extended set of selectable functionalities, a three-state filter and a switchable power divider are used to feed a triple-element quasi-Yagi-Uda antenna array. The proposed system is experimentally validated, demonstrating sum and difference patterns over a measured 79.8% fractional bandwidth for the wideband state of operation, and a tunability of 51.3% for the bandpass state and 50.3% for the bandstop state. This design has been published in *IEEE Access* under the title of "Pattern-Reconfigurable Antenna With Switchable Wideband to Frequency-Agile Bandpass/Bandstop Filtering Operation" [54].

- In all the pattern diversity designs that have been presented in the previous chapters, the pattern diversity feature was along the E-plane of the antenna. In other

words, two different radiation patterns namely sum and difference patterns were mostly different along the E-plane of the antenna. However, for broader space coverage and effectively tackling multipath fading in communications systems, it is required to have sum and difference beams along E- and H-plane of the antenna. Hence, a design of a planar microstrip patch antenna with pattern diversity along both E- and H-plane is presented in Chapter 6. At first, a microstrip design with switchable E-plane sum and difference patterns is presented with its operation based on selective excitation of two fundamental modes. On this basis, the design is extended to a double-element configuration along the H-plane. This arrangement enables pattern diversity along both E- and H-plane. For the single element antenna, a configuration of ten PIN diodes and a decoupling shorting via are utilized to switch between the TM01 and TM02 modes without relying on a feeding network. For the double-element antenna, a coupler acts as a feeding network and allows to generate the sum and difference patterns along the H-plane. This design has been accepted and presented in the *International Conference on Electromagnetics in Advanced Applications (ICEAA 2019)* under the title of "A Pattern Diversity Microstrip Antenna with Switchable Sum and Difference Beams in E- and H-plane" [55].

- The bandpass filter presented in Chapter 5 is extended to a dual-band independently frequency-tunable design which is then integrated with a planar monopole antenna to provide a dual-band tunable antenna with independent frequency tuning in Chapter 7. The wideband frequency range of the planar monopole antenna is exploited to cover the dual-band tunable filtering response. The two operating frequencies are continuously and independently tuned by four varactor diodes biased by two different biasing voltages. The omnidirectional response of the antenna remains intact under the filtering response due to the use of an external tunable feeding network with an unobtrusive biasing. The experimental results substantiate the simulated monopolar performance of the antenna under independently tunable dual-band operation. This work has been accepted and presented at the *Asia-Pacific Conference on Antennas and Propagation (APCAP 2019)* under the title of "Dual-Band Bandpass Filtering Monopole Antenna with Independently Tunable Frequencies" [56]. This paper was awarded the top (platinum) best student paper award in the student paper contest of APCAP 2019 in Incheon, South Korea.

- The bandstop filtering functionality of the design in Chapter 5 is modified to generate a dual-band independently tunable bandstop filter in the next design presented in Chapter 7. In this design, two varactor-tuned single-band bandstop filters are cascaded to develop a dual-band independently tunable bandstop filter. This filter can also be utilized as a second order single-band tunable bandstop filter. The filter is then integrated with an ultrawideband quasi-Yagi-Uda antenna. The wideband frequency range of the this antenna is exploited to cover the tunable filtering functionality. The directive radiation pattern of the antenna remains intact under the filtering response due to the use of an external tunable feeding network with an unobtrusive biasing. The experimental results substantiate the simulated performance of the antenna under independently tunable dual-band operation. This design has been accepted and presented at the *IEEE Radio and Antenna Days of the Indian Ocean (RADIO 2019)* under the title of "Independently Tunable Dual-Band Bandstop Filtering Antenna" [57].

1.4 Thesis structure

The thesis outline represented in Fig. 1.1 comprises eight different chapters. The first two chapters include the introductory backgrounds and necessary information for the rest of this thesis. The next five chapters delineate the original contributions of this thesis, before the conclusion and future works described in Chapter 8. The detailed description of each section is presented as follows.

- **Background (Chapters 1 & 2)**

  This part includes the current chapter and background information required for the rest of the thesis which is presented in Chapter 2. This background information includes the fundamental of multi-element Vivaldi antennas, sum and difference radiation patterns generation and feeding networks for multi-element antennas. This chapter also provides the introduction and literature review about reconfigurable filters, reconfigurable power dividers and their applications as antenna feeding networks.

- **Multi-element Vivaldi antennas (Chapters 3 & 4)**

  In this section, a design challenge for a double-element Vivaldi antenna with sum and difference radiation patterns is explained and several solutions are provided.

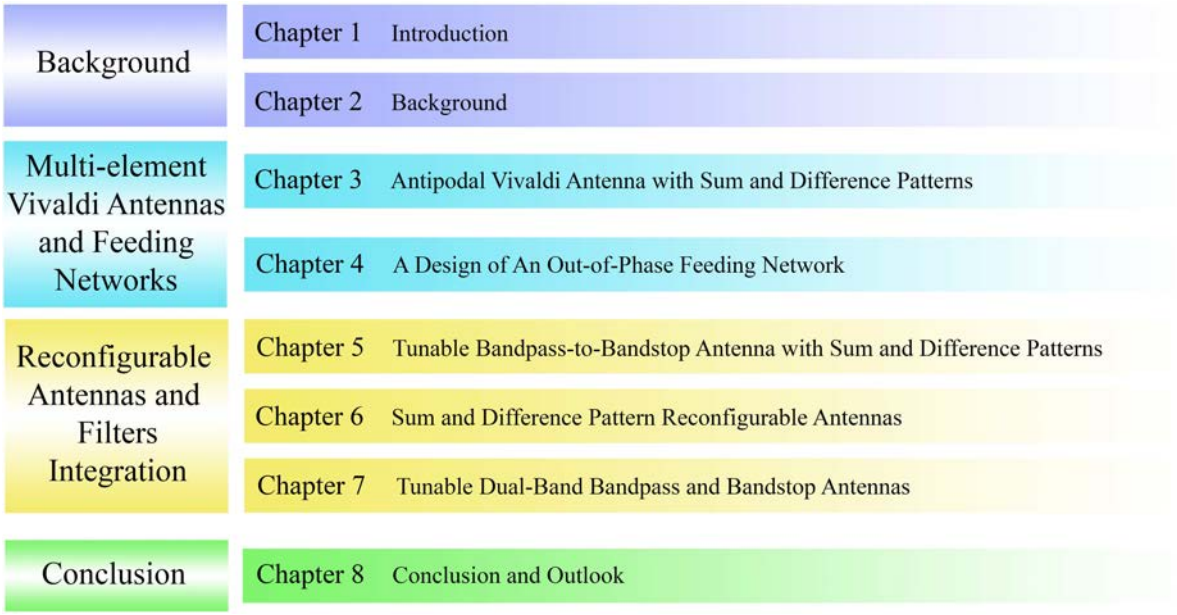

Figure 1.1. Thesis outline. This thesis consists of 8 chapters with the original contributions divided into two major parts as: multi-element Vivaldi antennas and reconfigurable antenna filter integration.

Chapter 3 provides a solution to tackle the mutual coupling enhancement occurring at lower frequencies and grating lobe appearance at higher frequencies for Vivaldi antennas. Chapter 3 also investigates further improvement of gain and bandwidth of pattern diversity Vivaldi antennas. In Chapter 4, a design of an out-of-phase power divider with wideband response, which is potentially applicable as a feeding network of multi-element wideband antennas is investigated and experimentally validated.

- **Reconfigurable antenna filter integration (Chapter 5 & 6 & 7)**

  In this part, filters and Antenna filter integration with multi-state tunability are presented. Moreover, sum and difference pattern diversity based on input feedings and switches are investigated. Chapter 5 proposes an antenna system with tunable bandpass-to-bandstop filtering functions while generating sum and difference radiation patterns in end-fire direction. This method has been extended in Chapter 6 to provide beam switching between the sum and difference radiation patterns using three antenna elements while providing a triple-state filtering function of allpass to tunable bandpass and tunable bandstop. Moreover, in this chapter the pattern diversity function has been extended to two orthogonal planes of a dual-input patch antenna using switches in the antenna structure and

a feeding network.. Chapter 7 proposes two dual-band filter schemes with independently tunable frequencies. These filters are integrated with planar monopole and end-fire quasi Yagi-Uda antennas with wideband response to generate tunable filtering antenna functions.

- **Conclusion (Chapter 8)**

  The last chapter provides a conclusive summary of all the projects included in this thesis, as well as a prospective view about the future work.

Chapter 2

Background

PATTERN diversity antennas featuring ultrawideband frequency responses and different states of reconfigurability are desirable components for modern wireless communications systems in the congested microwave frequency spectrum. They can reduce the cost and enhance the reliability of communications systems by adding flexibility to the frequency response and radiation patterns of the antenna front-ends. However, there are many technical challenges towards developing such antennas. This chapter presents a literature review of some fundamental constituents of pattern diversity antennas and highlights selected notable efforts that have been put forth to enhance the bandwidth of pattern diversity antennas.

2.1 Introduction

One of the most important components for every wireless communications system is the antenna. Modern communications systems require low-cost antennas which offer flexibility and reliability in their performances. To this end, antennas generating diverse radiation patterns have emerged, recently, with the aim of mitigating the unwanted phenomenon called multipath fading while keeping the cost of the communications system low. Multipath fading occurs when transmission-reception link is adversely affected by extra paths to a receiver and destructive interference between those paths, bringing about a faded or very weak signal at the receiver. Pattern diversity antennas can be realized by adopting two or more antenna elements working together in a close proximity to generate different radiation patterns, while their cross talks have been suppressed. The realization of ultrawideband pattern diversity antennas has remained a big challenge for researchers. One challenge for ultrawideband realization is to keep a high isolation between antenna elements working together in close proximity, while preventing the generation of unwanted lobes called grating lobes at frequencies where the distance between antenna elements is more than half a wavelength. Hence, developing strategies to overcome these mutually exclusive requirements can lead to bandwidth enhancement of pattern diversity antennas.

In parallel, the rapid development of communications systems causes frequency congestion due to inefficient spectrum utilization. Alleviating this problem has been facilitated by introduction of cognitive radio systems which sense the electromagnetic environment and adapt their operation to the conditions for best performance. Cognitive radio systems sense a wide spectrum using a wideband antenna to detect unused bands and based on the gained information they can dynamically tune their operating frequencies to adapt to the imposed condition. Therefore, enhancing the tunability states of an antenna structure is necessary for cognitive radio applications. Pattern diversity antenna can be applied to cognitive radio systems by combining their radiation agility with multi-state tunability function in their frequency responses.

This chapter is organized as follows. A literature review on ultrawideband antennas as the building blocks of ultrawideband pattern diversity antennas is presented in Section 2.2. Different methods of developing pattern diversity antennas are reviewed in Section 2.3 with the main focus placed on the challenges linked to increasing the operation bandwidth. In the end, frequency reconfigurability techniques based on antennas and filter integration for cognitive radio systems are reviewed in Section 2.4.

2.2 Ultrawideband antenna structures

The fundamental building block of a pattern diversity antenna with ultrawideband performance is an antenna element which has ultrawideband response. Ultrawideband antennas can have different types of radiation patterns such as directional, bidirectional, omnidirectional, and conical. The history of antennas used for wireless transmission-reception link dates back to 1898 when biconical, spherical, and bow-tie dipole and monopole antennas were used. The growing interest in the middle of 20th century sparked the reinvention of biconical, conical monopole antennas, and spherical dipoles for ultrawideband wireless communications [58]. Also, with the advent of television, much wider bandwidth for video streaming was required which led to the development of an ultrawideband horn antenna by Lindenblad in 1941 [58]. Examples of the above-mentioned antennas are illustrated in Fig. 2.1. As seen, all these designs have voluminous 3D structures. They are inconvenient for integration with monolithic microwave integrated circuits (MMIC). To reduce the antenna size and enable integratability, some planar ultrawideband antennas have been developed and studied recently. Spiral antennas [59], slot bowtie dipole antennas [60], printed monopole antennas [61], Log-periodic [62–65], electric bowtie [66], Vivaldi [27, 29, 67, 68], and quasi Yagi-Uda antennas [69–74] are some examples of UWB antennas with planar structures. These antennas are illustrated in Fig. 2.2. As the Vivaldi and quasi Yagi-Uda antennas are frequently used in this thesis, more attention will be paid to them in this chapter.

2.2.1 Vivaldi antennas

This type of antenna was first proposed by Gibson as a class of traveling wave antenna with a directive radiation pattern towards the end-fire direction of the antenna [27]. Due to the tapering structure of this antenna and smooth transition of line impedance, it can cover ultrawide frequency range. Vivaldi antennas appear in two major different planar types, namely coplanar or antipodal structure. The coplanar structure shown in Fig. 2.3a has the tapered geometry etched on the bottom side of the substrate with a microstrip to slotline transition as the top side. The microstrip to slot line transition acts as a balanced-to-unbalanced (Balun) transmission line limiting the maximum attainable bandwidth for the coplanar Vivaldi structure. Despite the drawback of bandwidth limitation, coplanar Vivaldi antennas are attractive for some applications since

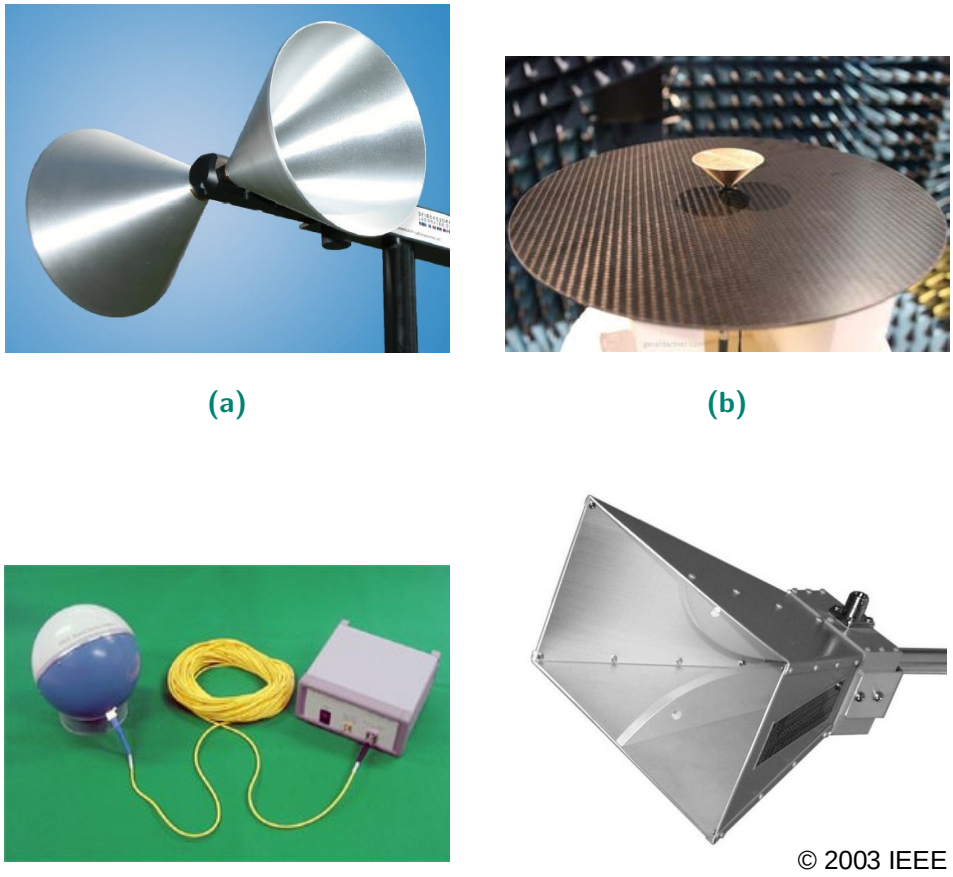

Figure 2.1. Examples of different types of 3D ultrawideband antennas presented in [58]. (a) Biconical antenna. (b) Conical monopole antenna. (c) Spherical antennas. (d) Horn antennas.

they have high polarization purity due to the very small amount of vertical electric field being radiated inside the substrate. The other type of Vivaldi antenna shown in Fig. 2.3b is called antipodal Vivaldi antenna where the two tapered structures are on different sides of the substrate with a transition from coaxial cable to microstrip line as the feeding. This geometry removes the barrier of bandwidth limitation imposed by the balun in coplanar structure at the expense of increasing the cross-polarization level due to some vertical electric field components being generated inside the substrate. Miniaturization and performance improvement of Vivaldi antennas have been widely researched over the past few years. One salient design method which helps miniaturize the Vivaldi antenna structure and improve the gain and sidelobe level was identified as etching corrugation on the outer edges of Vivaldi antennas [48,76,77]. Different types of corrugation etching were shown to be helpful in shifting the lowest operating frequency to lower values, thereby miniaturizing the structure in terms of wavelength.

© 1979 IEEE

(a)

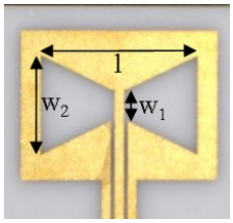

© 1999 IET

(b)

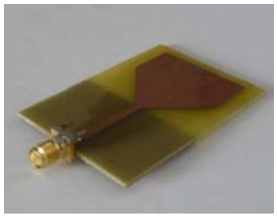

© 1998 IEEE

(c)

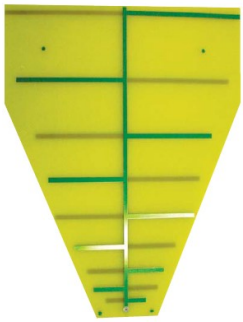

© 1977 IEEE

(d)

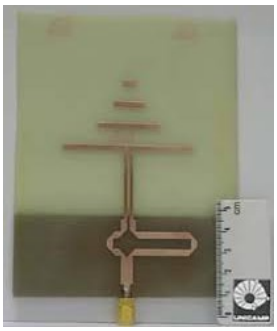

© 1998 IET

(e)

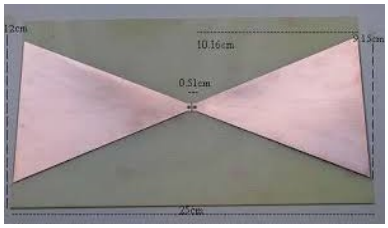

© 1996 IET

(f)

© 2011 IEEE

(g)

Figure 2.2. Different types of planar ultrawideband antennas. (a) Spiral antennas [59]. (b) Slot bow-tie antenna [60]. (c) Planar monopole antenna [61]. (d) Log-periodic antenna [62]. (e) Quasi-Yagi-Uda antenna [69]. (f) Electric bow-tie antenna [66]. (g) Vivaldi antenna [27].

Bottom Layer Top Layer

© 2013 IEEE

(a)

© 2011 IEEE

(b)

Figure 2.3. Two different models of Vivaldi antennas. (a) Top and Bottom layers of a Coplanar Vivaldi antenna [75]. (b) Antipodal Vivaldi antenna [67].

For example, the structure in [77] uses elliptical corrugations as indicated in Fig. 2.4 to improve the frequency response and the radiation characteristics of the antenna. It was demonstrated that for the design with elliptical corrugation the lowest operating frequency starts at 2.4 GHz, whereas for the conventional structure of antipodal Vivaldi antenna with the same dimensions, this value is 3.3 GHz. Another method to

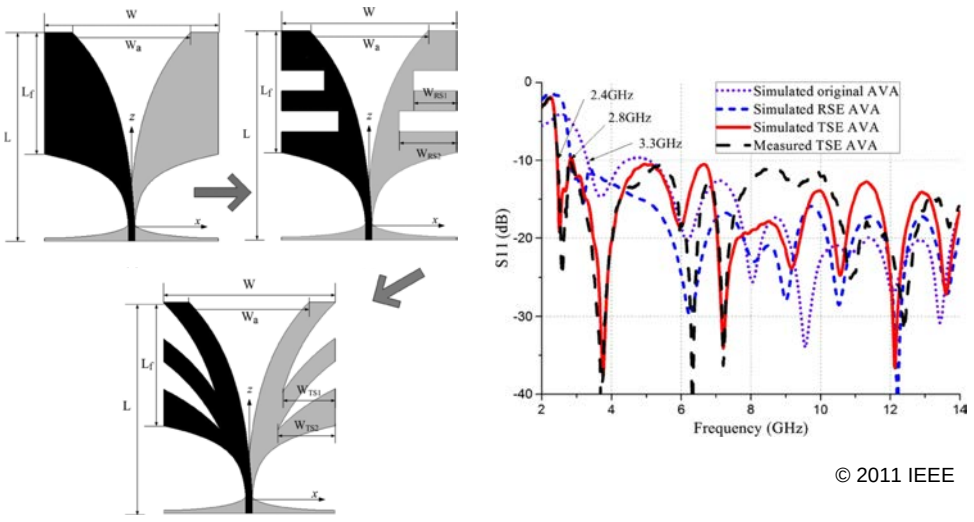

(a) (b)

Figure 2.4. Two types of the Vivaldi antenna corrugations and the corresponding scattering parameters from [77]. (a) Rectangular and elliptical corrugation development. (b) Reflection coefficients comparison for the conventional Vivaldi antenna, Vivaldi antenna with rectangular corrugations, and Vivaldi antenna with elliptical corrugations.

improve the reflection coefficient and to further miniaturize of a Vivaldi was proposed in [78]. In this case, the tapering rate of the antenna flares was increased resulting in sharp bending of the inner edges of each flare. The substrate length can be reduced to half while the scattering response is improved as shown in Fig. 2.5. This is however at the expense of a nominal gain loss at lower frequencies. The next prominent method for the Vivaldi antenna improvement has been the addition of a dielectric lens to the boresight of the antenna structure, thus concentrating the electric field in this region and consequently increasing the gain at higher frequencies. This phenomenon is illustrated in Fig. 2.6 which was presented in [79] with a dielectric lens taking the form of a trapezoidal elongation of the substrate. The dielectric lens increases the gain of the antenna at higher operating frequencies. The maximum gain improvement can be obtained when the length of this dielectric lens is properly adjusted. As this type of

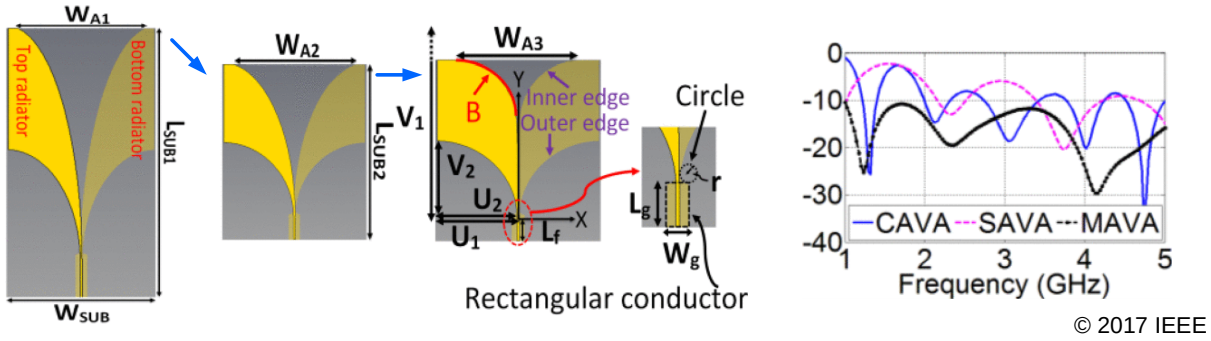

Figure 2.5. Antipodal Vivaldi antenna with sharper bending of the inner edges [78]. (a) Design evolution from the conventional structure (CAVA) to shorter structure (SAVA) and the modified antipodal Vivaldi antenna (MAVA). (b) Frequency response for each evolution step.

antenna generates ultrawideband response and directive radiation pattern, it is potentially applicable in pattern diversity antenna systems with ultrawideband responses.

2.2.2 Planar quasi-Yagi-Uda antenna

The Yagi-Uda antenna was first introduced in 1926 and named after its inventors. It comprises three different parts contributing to the end-fire radiation of this antenna. The main part is a dipole antenna which is excited by an input port. The secondary parts are a reflector which blocks the backward radiation, and several coupled parasitic elements to drive the radiation pattern towards the end-fire direction of the antenna. The modified printed version of this antenna, which was also called quasi-Yagi-Uda antenna, was first introduced in [80]. This antenna consisted of an excited patch antenna with a reflector and several parasitic patches to drive the radiation into the end-fire direction. This antenna had a slightly tilted beam towards the broadside of the patch while having limited operating bandwidth. Several efforts have been invested in the last two decades to enhance the radiation characteristics as well as the bandwidth of such antenna. The first effort to enhance the bandwidth was published in [81] with a microstrip dipole driven by balun and a parasitic transmission lines. Based on these results shown in Fig. 2.7, the obtained bandwidth was increased to around 48% with a directive end-fire radiation pattern showing no beam tilting.

However, as in the case of the coplanar Vivaldi antenna, the structure of the input balun may adversely affect the bandwidth. Hence, increasing the operational bandwidth of

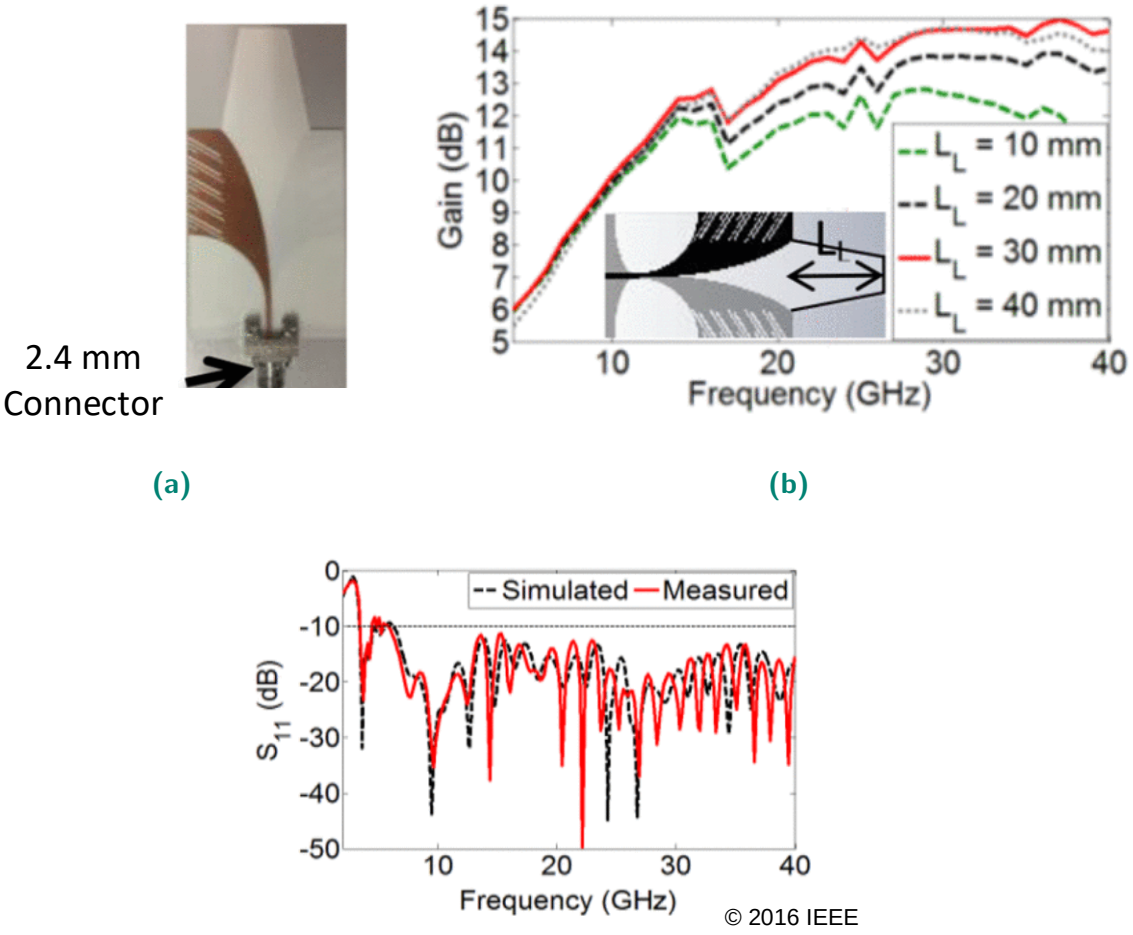

Figure 2.6. The effect of adding dielectric lens on Vivaldi antenna gain [79]. (a) Antenna structure with trapezoidal dielectric lens. (b) Gain versus frequency for different lengths of the lens. (c) The simulated and measured reflection coefficients.

the feeding balun will lead to an increased bandwidth of the overall antenna design. This method has led to the a design of a wideband quasi-Yagi-Uda antenna with a different feeding method, which was presented in [82]. It is shown in Fig. 2.8 that it can cover the wide frequency bandwidth of 70%.

An investigation aiming at enhancing the bandwidth while reducing the antenna size was reported in [34], leading to an obtained frequency bandwidth of more than 100%. The antenna structure and its results are shown in Fig. 2.9. The compact structure was attained based on decreasing the width of the reflector which was facilitated by a pair of stubs connected to the sides of antenna reflector.

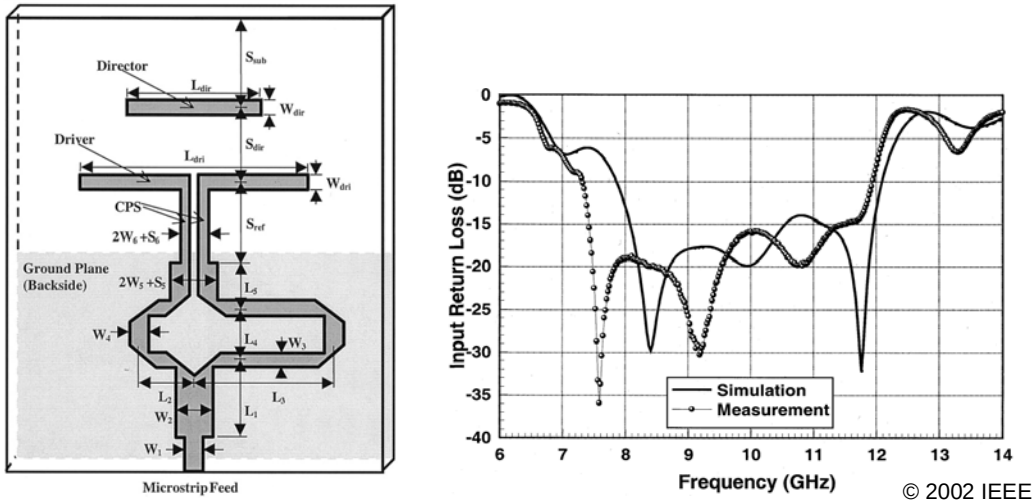

Figure 2.7. Wideband quasi-Yagi-Uda antenna using a planar balun presented in [81]. (a) Antenna structure. (b) Input reflection coefficients.

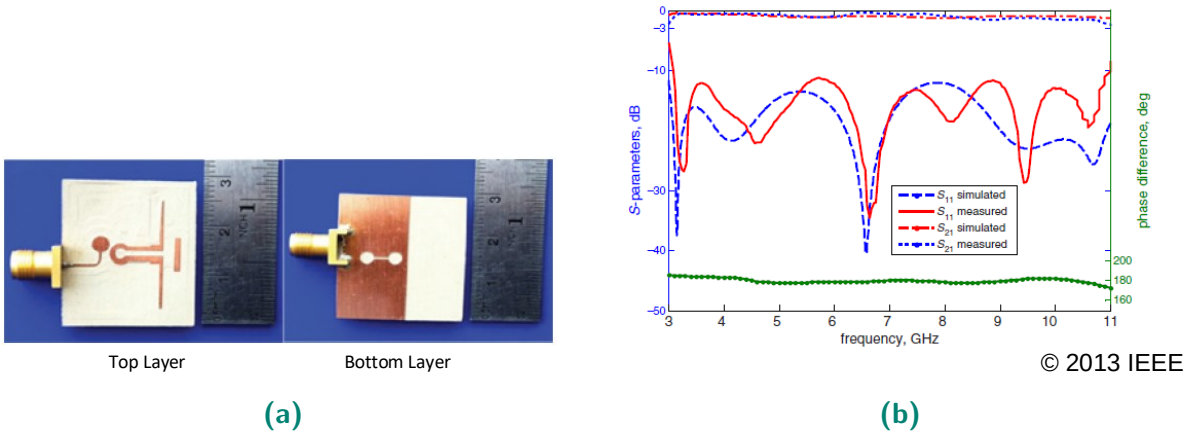

Figure 2.8. Wideband quasi-Yagi-Uda antenna using a microstrip to coplanar line transition presented in [82]. (a) Antenna structure. (b) Input reflection coefficients.

Even though the bandwidth of this antenna is still limited compared to some of its counterparts such as Vivaldi antennas, its compact topology will make it an appealing candidate for future investigation in this thesis.

2.3 Pattern diversity antenna design methods

As mentioned earlier, antennas that can generate diverse radiation patterns can enhance the flexibility and reliability of modern communications systems. These types

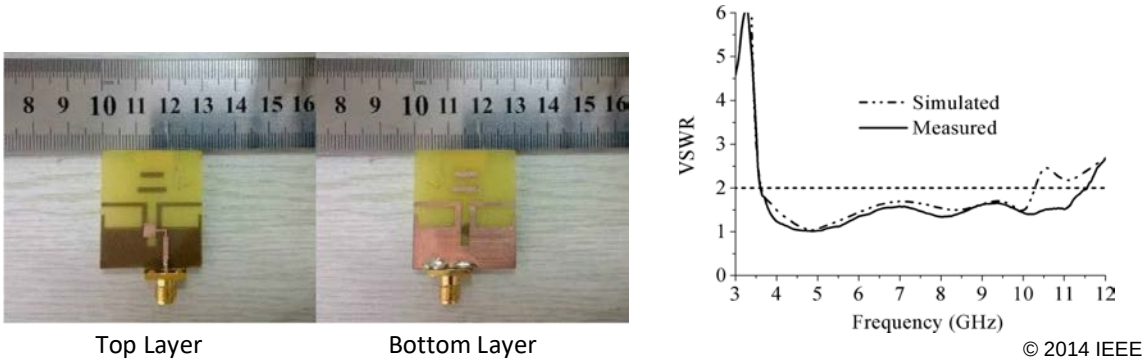

Figure 2.9. Ultra-wideband quasi-Yagi-Uda antenna with compact structure from [34]. (a) Antenna structure. (b) Input VSWR.

of antennas can adapt their radiation performance depending on the requirements imposed by their environment. There are two salient methods to develop antenna structures with pattern diversity functions, which are explained in more detail in this section.

2.3.1 Coupler-fed designs

One of the most prominent and conventional methods for pattern diversity is exciting double- or multi-port antennas with a single or multiple 180° hybrid couplers. Hybrid couplers which will be explained in more detail later are one type of prominent feeding networks used to split the input power to the two output ports with 0 degrees or 180 degrees phase difference between the output signals. This phase difference enables to generate different radiation patterns for multi-element antennas.

The structure in Fig. 2.10 is an example of a pattern diversity antenna which utilizes a coupler in its feeding network. The working principle is that different modes of the patch antenna are excited by different excitations of the coupler ports resulting in the generation of directive and conical radiation patterns [8]. The design presented in [83] provides another example of such pattern diversity systems which generates broadside sum and difference patterns. The antenna structure and its radiation performance are shown in Fig. 2.11. There are two closely spaced but isolated antennas which are fed by a coupler operating at 5.2 GHz.

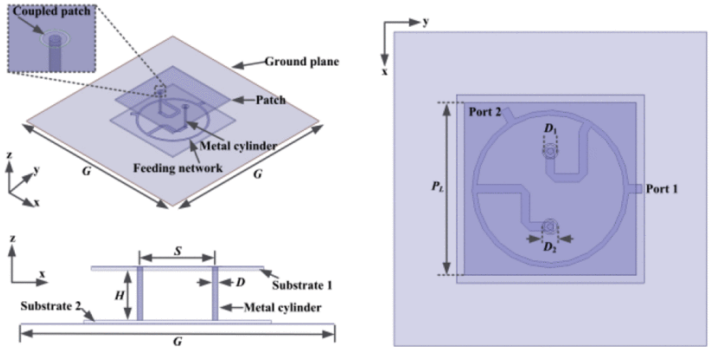

(a)

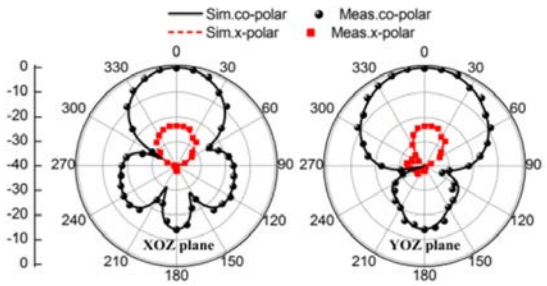

(b)

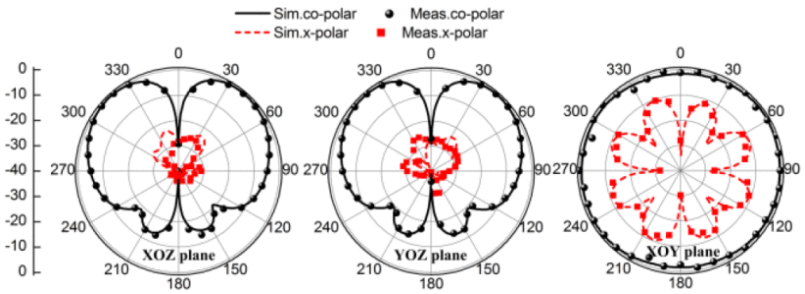

(c)

Figure 2.10. Directive to conical pattern diversity antenna fed by a hybrid coupler from [8]. (a) Antenna structure. (b) Directive radiation pattern. (c) Conical radiation pattern.

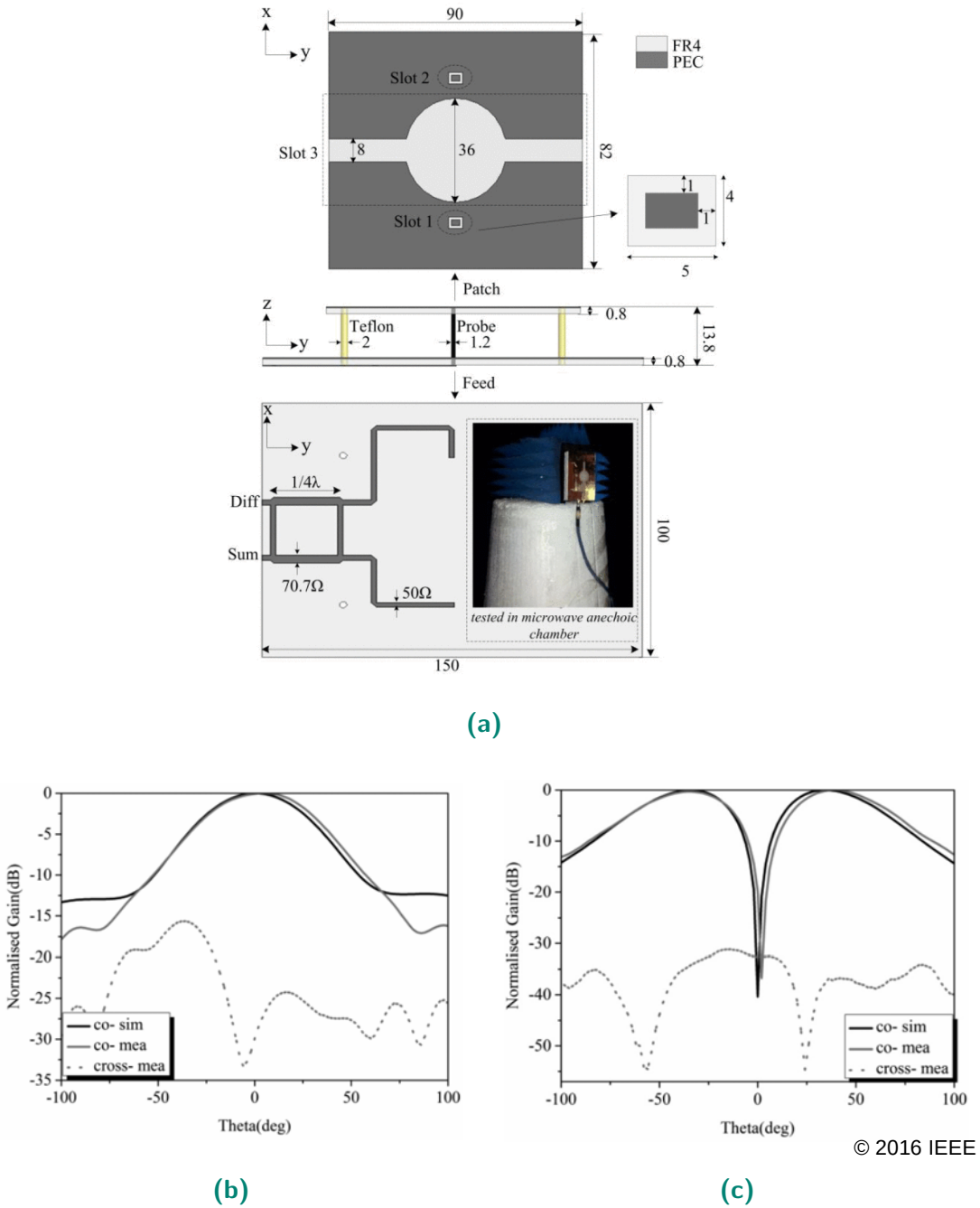

Figure 2.11. Broadside sum and difference pattern diversity antenna fed by a hybrid coupler presented in [83]. (a) Antenna structure. (b) Sum radiation pattern. (c) Difference radiation pattern.

The pattern diversity antennas mentioned above are examples of narrowband systems. Several efforts to enhance the bandwidth of pattern diversity antennas have been proposed in the literature thus far. For instance, in [10], a technique to reduce the mutual coupling and grating lobes for a double-element Vivaldi antenna was proposed and experimentally verified. This antenna covered the frequency band of 3.1 GHz to 10.6 GHz with sum and difference radiation pattern generation. The antenna structure with a wideband rat-race coupler as a feeding network is shown in Fig. 2.12a. Sum and difference radiation patterns at different operating frequencies are illustrated in Fig. 2.12b.

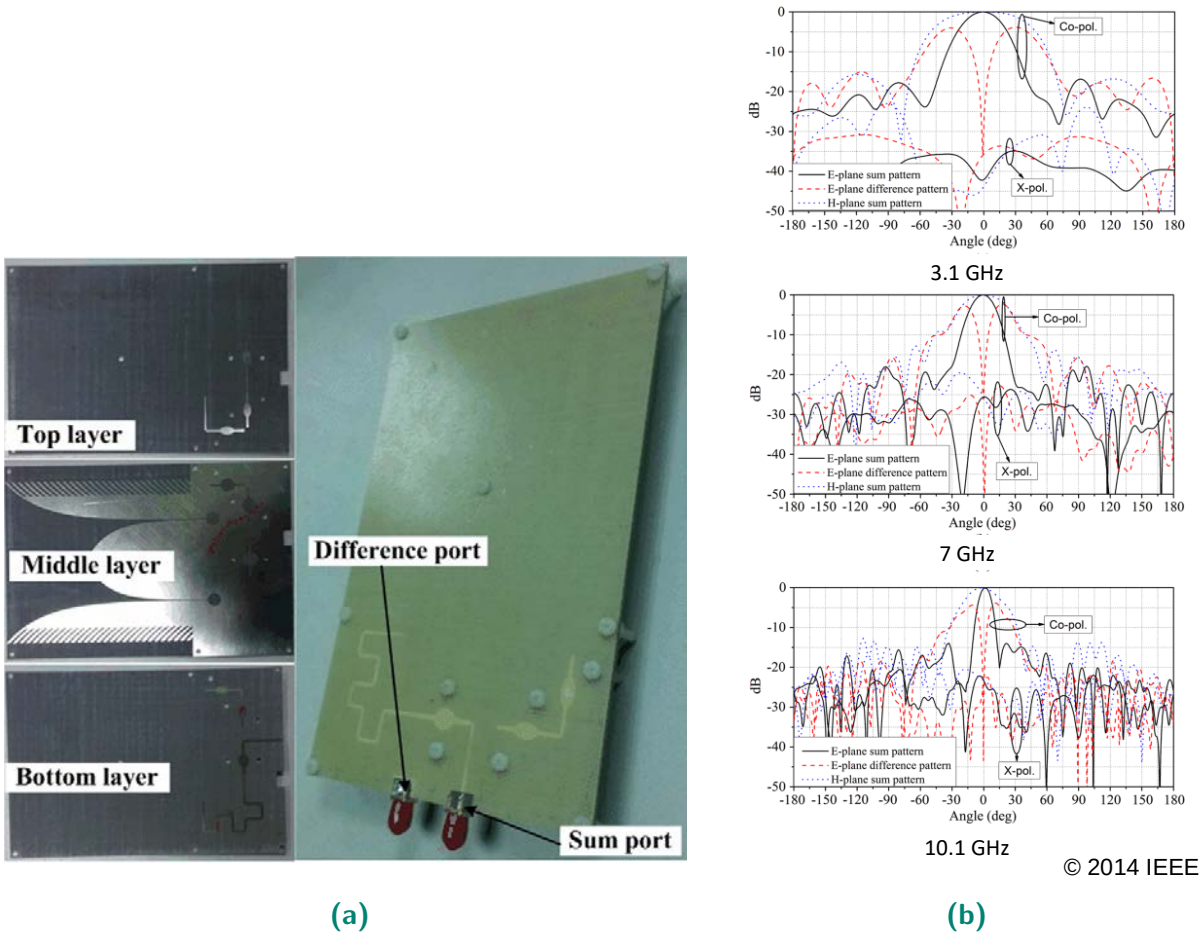

Figure 2.12. Vivaldi antenna design with sum and difference radiation patterns from [10]. (a) Antenna structure. (b) Sum and difference radiation patterns at different operating frequencies and on E- and H-plane.

Another example of wideband sum and difference pattern diversity antenna was presented in [11] using double-element Vivaldi antennas which are externally excited by

couplers. This design claims that it can cover the bands of 0.7 GHz to 2.7 GHz. The structure of this design along with its radiation patterns at different operating frequencies are shown in Fig. 2.13. In this design, the single-element Vivaldi antenna is tilted and evolved to a dual-element design.

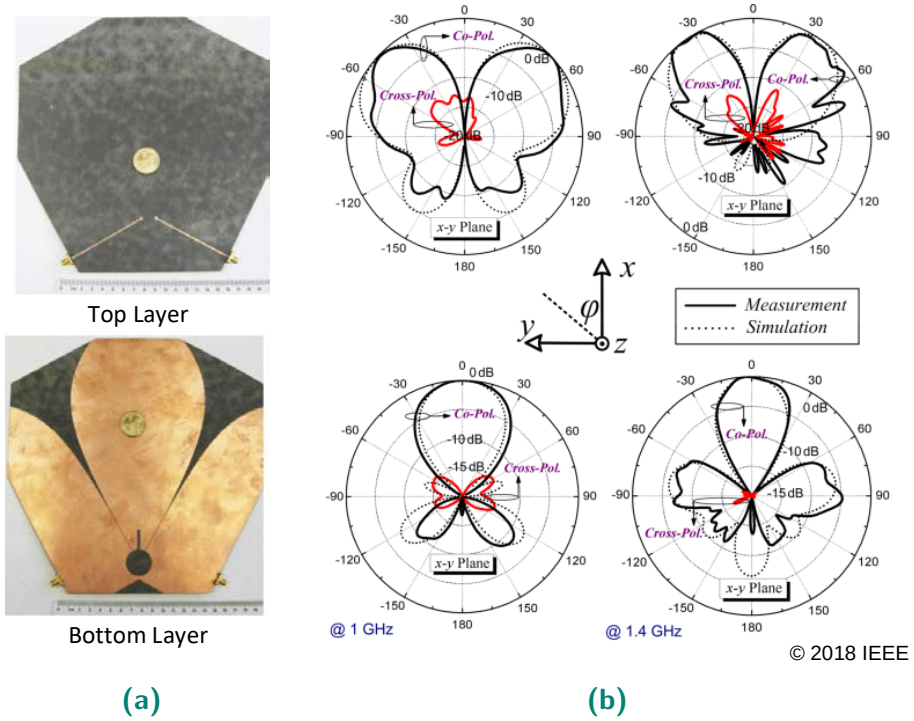

Figure 2.13. Vivaldi antenna design with sum and difference radiation patterns presented in [11]. (a) Antenna structure. (b) Sum and difference radiation patterns at different operating frequencies and on E- and H-plane.

180° hybrid coupler

Hybrid couplers, also known as ring or rat-race couplers are an integral part of dual-input pattern diversity antennas with sum and difference radiation patterns. They are four-port networks with the block diagram shown in Fig. 2.14a. On the one hand, Port 1 must be excited to split the input signals to the output Ports (Ports 2 and 3) equally in both magnitude and phase. On the other hand, Port 4 must be excited to divide the input signal to two equal output signals with 180° phase difference between them. Ports 1 and 4 are called sum and difference input ports, respectively. The schematic and fabricated prototype of a printed hybrid ring coupler are shown in Figs. 2.14b and 2.14c, respectively. Each transmission line characteristic impedance is equal to 70.7 Ω. Three

transmission lines have quarter wavelength electrical lengths and one transmission line has three-quarter wavelength electrical length. These values have been obtained analytically based on even- and odd-mode half-circuit analyses explained in [84]. The simulated scattering parameters of the conventional ring hybrid working at 1 GHz are shown in Fig. 2.14d.

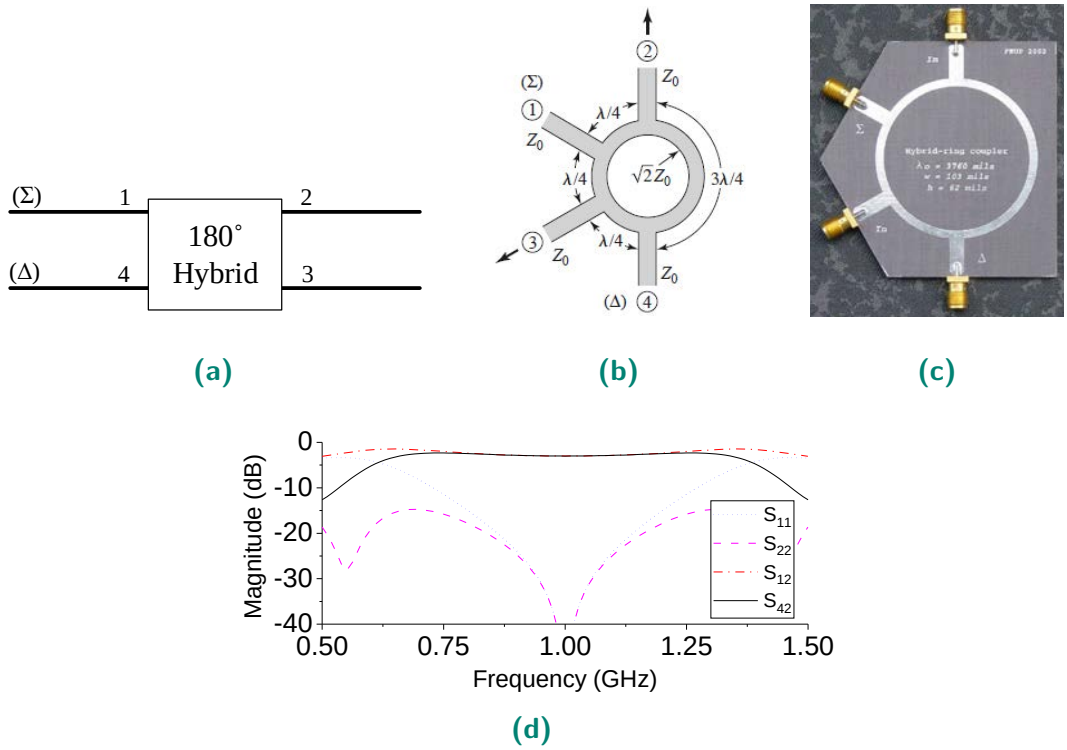

Figure 2.14. Conventional rat-race coupler [84]. (a) Rat-race coupler block diagram. (b) Schematic of the conventional rat-race coupler. (c) Fabricated prototype of the conventional rat-race coupler. (d) Frequency response of the conventional rat-race coupler.

2.3.2 Pattern switchable antenna designs

In the past few years, several designs of single-input pattern diversity antennas, i.e. antennas which do not use couplers as a feeding network were proposed. They utilized electrically reconfigurable elements to switch between multiple radiation patterns from a single radiating structure based on perturbations of different modes. These types of antennas can be classified in two different groups. The first group uses reconfigurable elements in the feeding network of the antenna to generate different radiation patterns. The second group utilizes embedded reconfigurable elements in the resonant structure

of the antenna to generate different radiation patterns. These two different groups of pattern switchable antennas are studied in detail in this subsection.

Pattern-reconfigurable antennas with switchable feeding networks

An example of a pattern switchable antenna with broadside and conical radiation patterns using reconfigurable input feeding network was presented in [85]. The antenna structure is shown in Fig. 2.15a comprising of a patch antenna excited by two ports which are connected to a feeding network with switchable in-phase and out-of-phase output signals perturbing two different modes of the antenna resonant cavity. The schematic diagram of the feeding network is illustrated in Fig. 2.15b. This feeding network is composed of a wideband switchable phase shifter at one of the output ports. The embedded PIN diodes in the feeding network structure enable switching the output phase difference between 0° and 180°. The radiation patterns of this antenna are shown in Fig. 2.16.

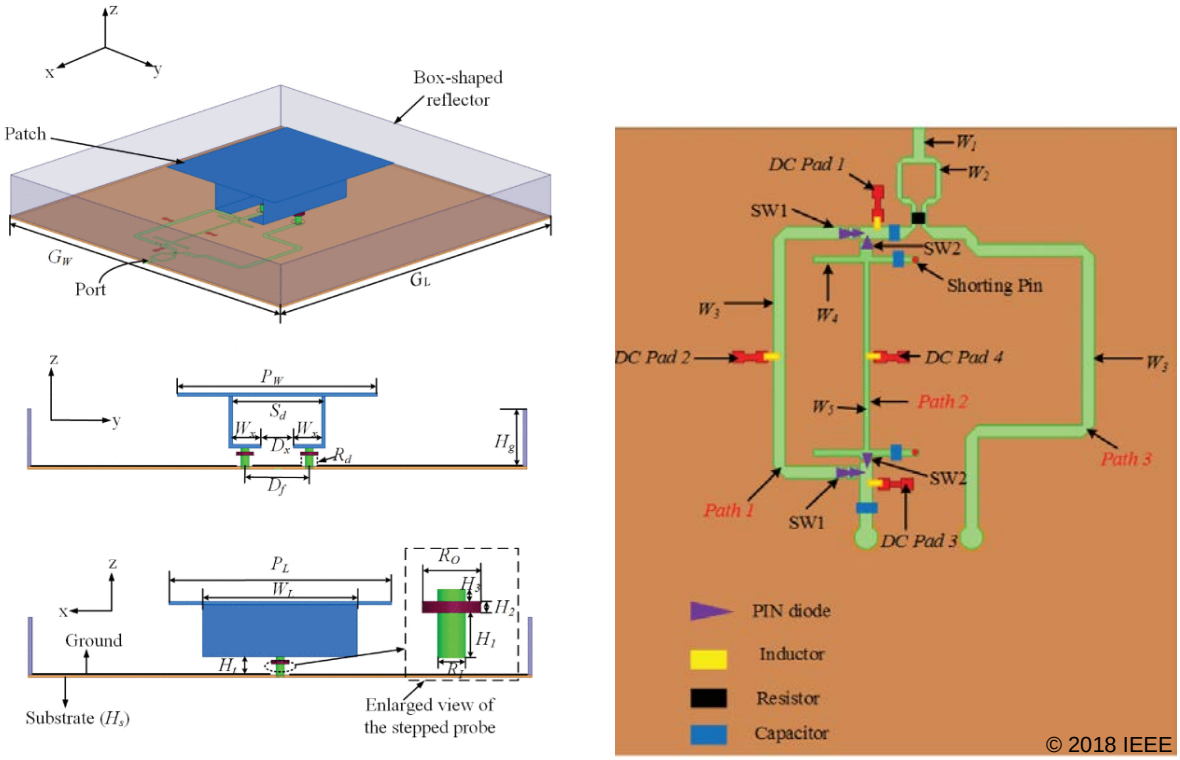

(a) (b)

Figure 2.15. Pattern-reconfigurable antenna with switchable feeding network in [85]. (a) Antenna structure. (b) Feeding network structure with switchable phase shifter.

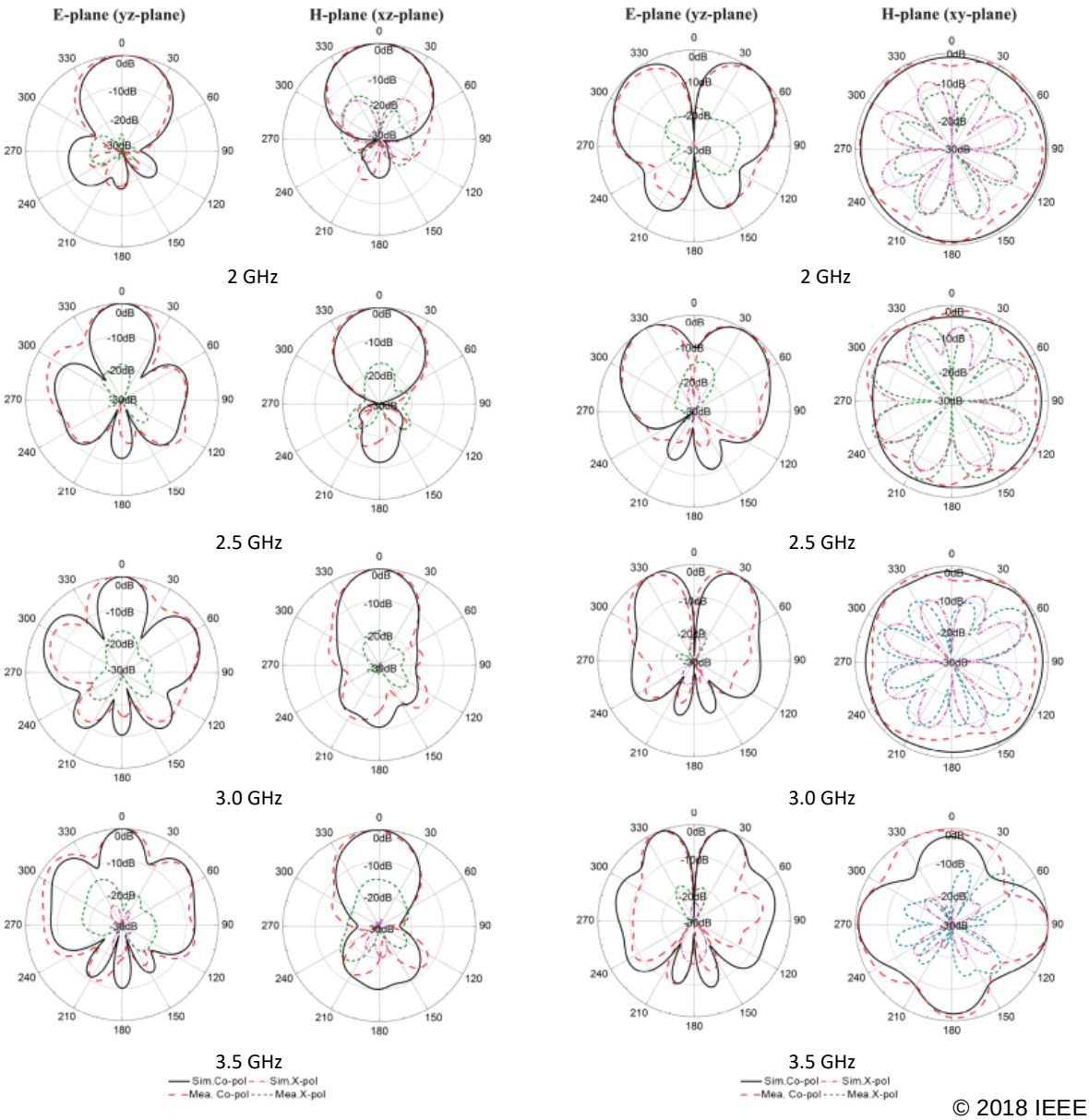

Figure 2.16. Radiation patterns of the pattern switchable antenna at different operating frequencies of the design in [85]. (a) Directive broadside radiation patterns. (b) Conical radiation patterns.

Another example of a pattern-reconfigurable antenna with broadside to conical radiation patterns using a switchable feeding input line was presented in [7]. The antenna structure is shown in Fig. 2.17a and it is composed of two different types of closely spaced antennas with different radiation patterns. The PIN switches at the bottom side of the antenna separate the excitation for these antennas. Therefore, at a time, only one antenna radiates and the other one is switched OFF. The small circular patch antenna in the middle generates the broadside radiation pattern and the bigger circular patch with several shorting posts generates conical radiation patterns. The surface current distribution under these two switching conditions are illustrated in Fig. 2.17b. This antenna has an overlapping frequency bandwidth of 23.5%. The radiation patterns at different frequencies are shown in Fig. 2.17c.

Pattern-reconfigurable antennas with embedded switching elements in the resonant structure

The other type of pattern-reconfigurable antenna embeds the reconfigurable elements inside the resonant structure of the antenna. By switching or tuning such elements, the radiation pattern can be changed to various states of radiation pattern. One salient example of this type of antenna was presented in [86], based on varactor diodes. This design is shown in Fig. 2.18 consisting of a center-shorted patch antenna with six stub-loaded varactor diodes. The center-shorted patch antenna creates two resonance frequencies with the lower frequency of operation generating a conical radiation pattern and the higher one generating a directive broadside radiation pattern. These frequencies are simultaneously tunable when applying a variable voltage to the varactor diodes. An overlapping bandwidth of 2.68 to 3.51 GHz is achieved in which the antenna can work on either one of the radiating modes. The measured and simulated scattering parameters as well as the radiation patterns at different frequencies are represented in Fig. 2.19.

Some implementations of pattern-reconfigurable antennas have been demonstrated to generate more than two radiation patterns. A sample of such designs was presented in [87] where a directive radiation pattern can be switched along the azimuth plane of the antenna. The antenna structure consisting of four PIN switchable dipoles is shown in Fig. 2.20. The working principle is that each dipole antenna with ON input transmission line will be radiating and the radiation pattern will be directed towards the boresight of that particular dipole. Hence four directive radiation patterns towards 0°, 90°, 180°, and 270° can be generated. The overlapping bandwidth of this antenna

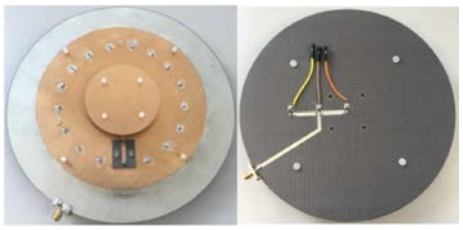

(a)

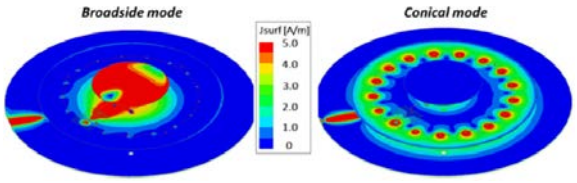

(b)

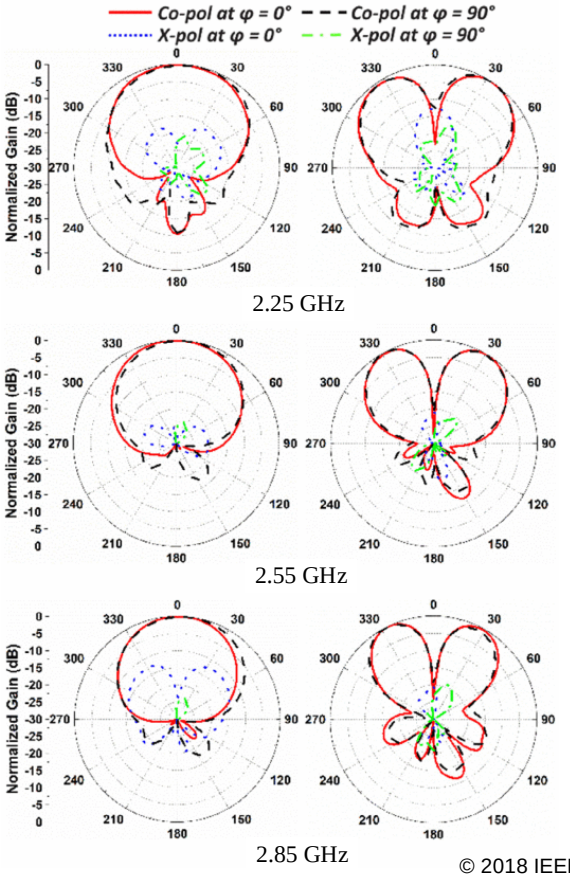

(c)

Figure 2.17. Pattern-reconfigurable antenna with switchable feeding line presented in [7]. (a) Antenna structure. (b) Surface current distribution. (c) Radiation patterns.

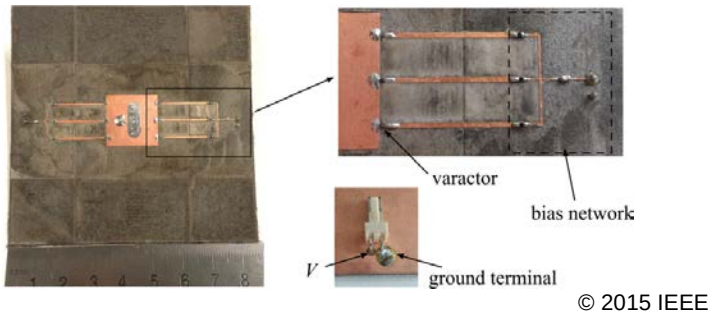

Figure 2.18. Center-shorted pattern- and frequency-reconfigurable patch antenna [86].

for four different radiation patterns is 33.6%. The simulated and measured radiation patterns of this antenna are shown in Fig. 2.21.

2.4 Reconfigurable antennas based on filter design integration

In this section, filters are studied as one of the most fundamental components in communications systems and their importance towards reconfigurable antenna designs with multi-state reconfigurability is illustrated. Filters are two-port networks which are generally classified into four types, namely lowpass, highpass, bandpass, and bandstop. The ideal frequency responses of different types of filters are illustrated in Fig. 2.22. As ideal filters are non-causal systems, such ideal responses cannot be implemented in practice. However, obtaining near ideal transfer functions is feasible by taking into account proper design considerations. Filters are made of one or several building blocks called resonators which create operating frequencies, transition bands, and stopbands in their frequency responses.

Reconfigurable filters have been subjects of some recent studies as they offer flexibility in their filtering performance. Generally, these filters use electrically tunable or switchable lumped components to tune the operating frequencies or change their states of operation. In the following section, we will study some of these reconfigurable filter configurations which are relevant to this thesis, and their integration with antenna designs will be described.

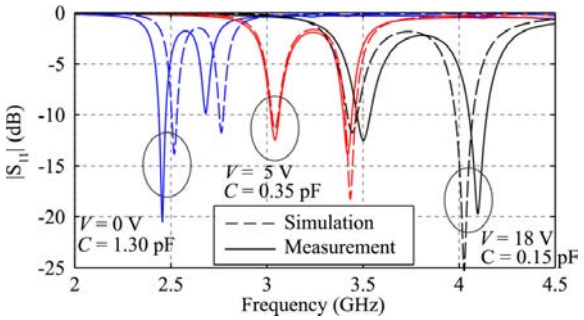

(a)

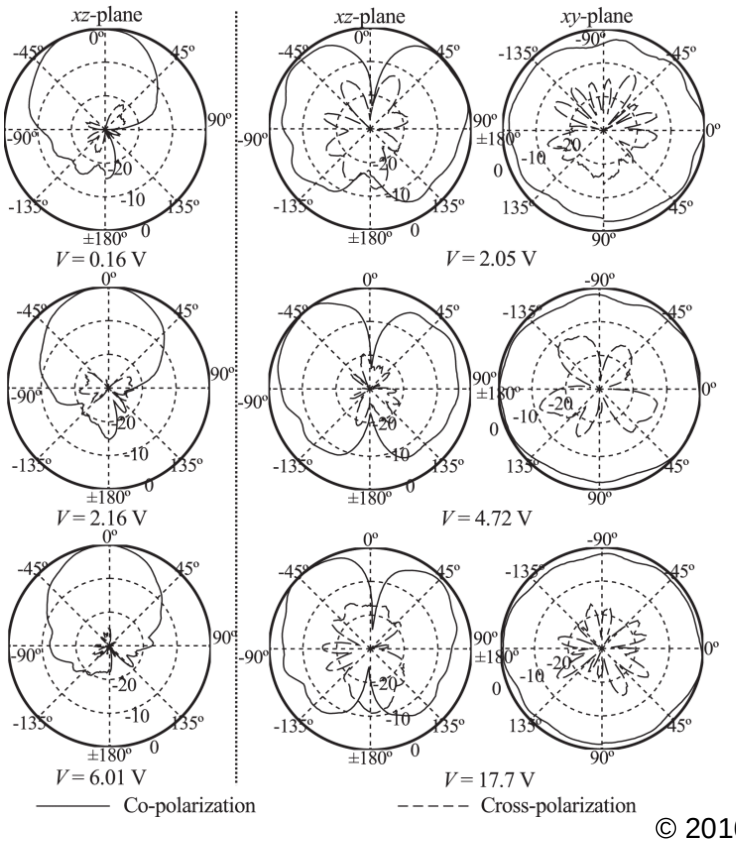

(b)

Figure 2.19. Center-shorted patch antenna frequency response and radiation patterns from [86]. (a) Reflection coefficients. (b) radiation patterns.

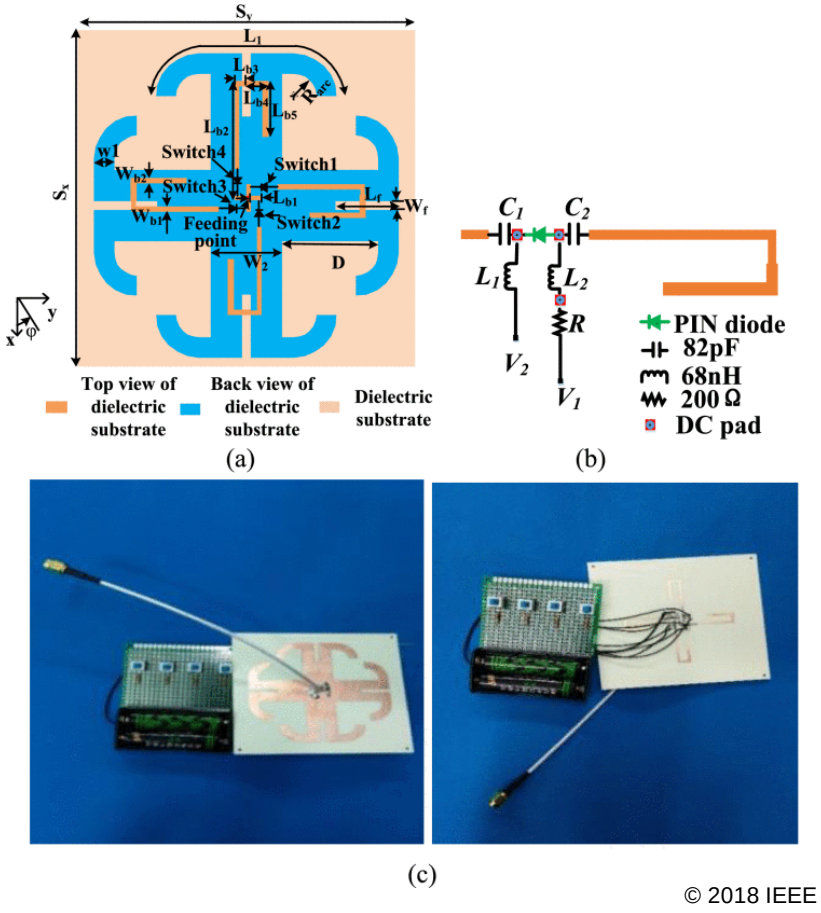

Figure 2.20. Pattern-reconfigurable dipole antennas presented in [87]. (a) Antenna structure. (b) Feeding line structure. (c) Fabricated design.

2.4.1 Reconfigurable bandpass filters

A design of a frequency-tunable bandpass filter using varactor diodes was presented in [88]. It was designed using two coupled resonators and four varactors which were tuned by two bias voltages. The operating frequency was controlled by proper adjustment of two voltages. The design structure along with its simulated and measured results are illustrated in Fig. 2.23. Based on these results, it is seen that this filter is able to cover a relatively wide tuning range of 0.6 GHz to 1 GHz (or 50% fractional tuning range).

The above-mentioned bandpass filter was working only at a single tunable operating frequency. A design approach to implement a dual-band bandpass filter with independently tunable frequencies was reported in [89]. The filter schematic is shown in Fig. 2.24a. It comprises two resonators with eight embedded varactors which are coupled to a transmission line with a gap in the middle. There are two independent bias

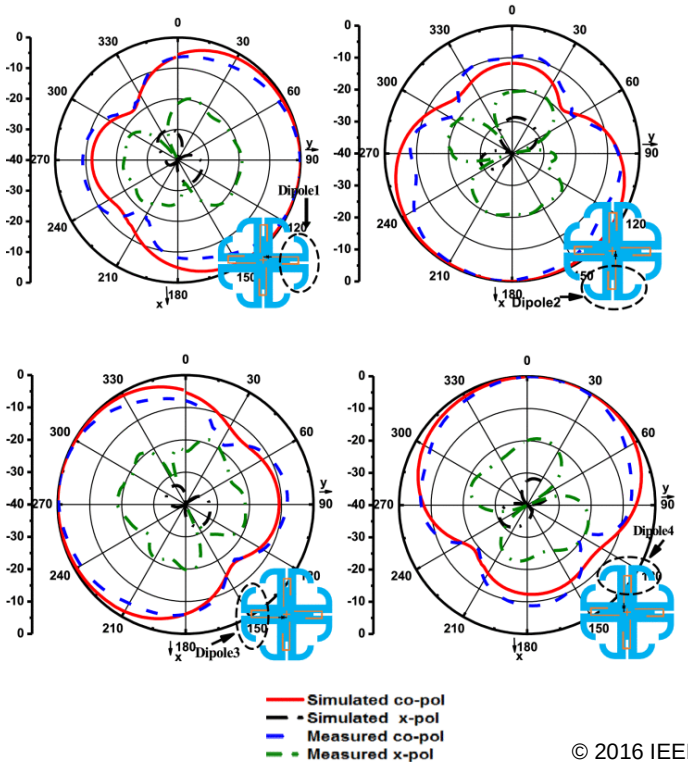

Figure 2.21. Radiation patterns of pattern-reconfigurable dipoles at 2.45 GHz from [87].

voltages which are used to control each frequency band independently. The frequency responses of this dual-band filter are shown in Fig. 2.24b and 2.24c. As seen, due to high isolation between the two coupled resonators, tuning one frequency does not affect the other. This is a favorable feature for some applications such as carrier aggregation systems.

2.4.2 Reconfigurable bandstop filters

Like bandpass filters, frequency-reconfigurable bandstop filters have been subjects of intensive research thrust over the last few years. They are useful building blocks for dynamic interference rejection. One example of recently published papers about a bandstop filter with tunable frequencies was presented in [90]. Its schematic diagram and fabricated prototype are shown in Figs. 2.25a and 2.25b, respectively. The design consists of two cascaded resonators, four diodes and two biasing voltages. Tuning the biasing voltages leads to tuning the notch frequency of this filter. The frequency response of this filter with different varactor voltages is illustrated in Fig. 2.25c. In this

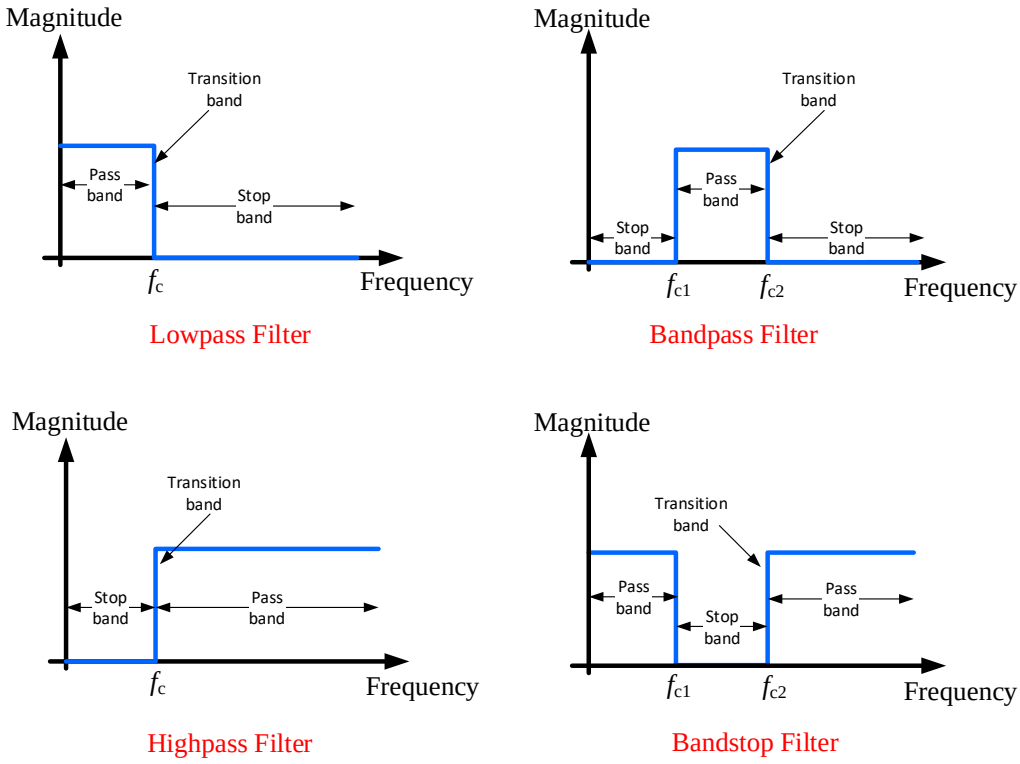

Figure 2.22. Ideal frequency responses of different types of filters.

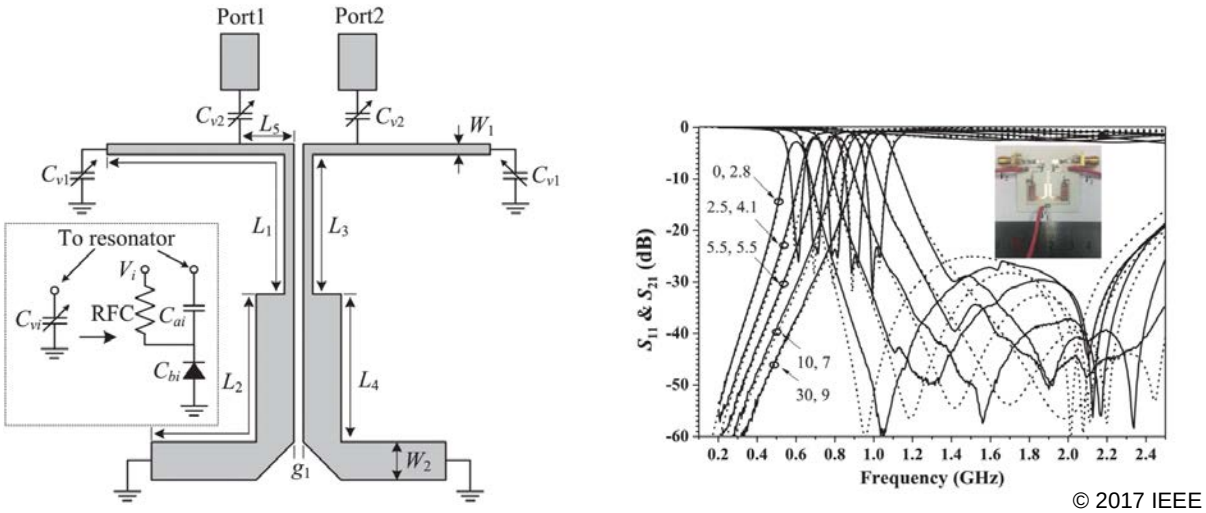

(a) **(b)**

Figure 2.23. Single-band tunable bandpass filter [88]. (a) Schematic diagram. (b) Reflection coefficient.

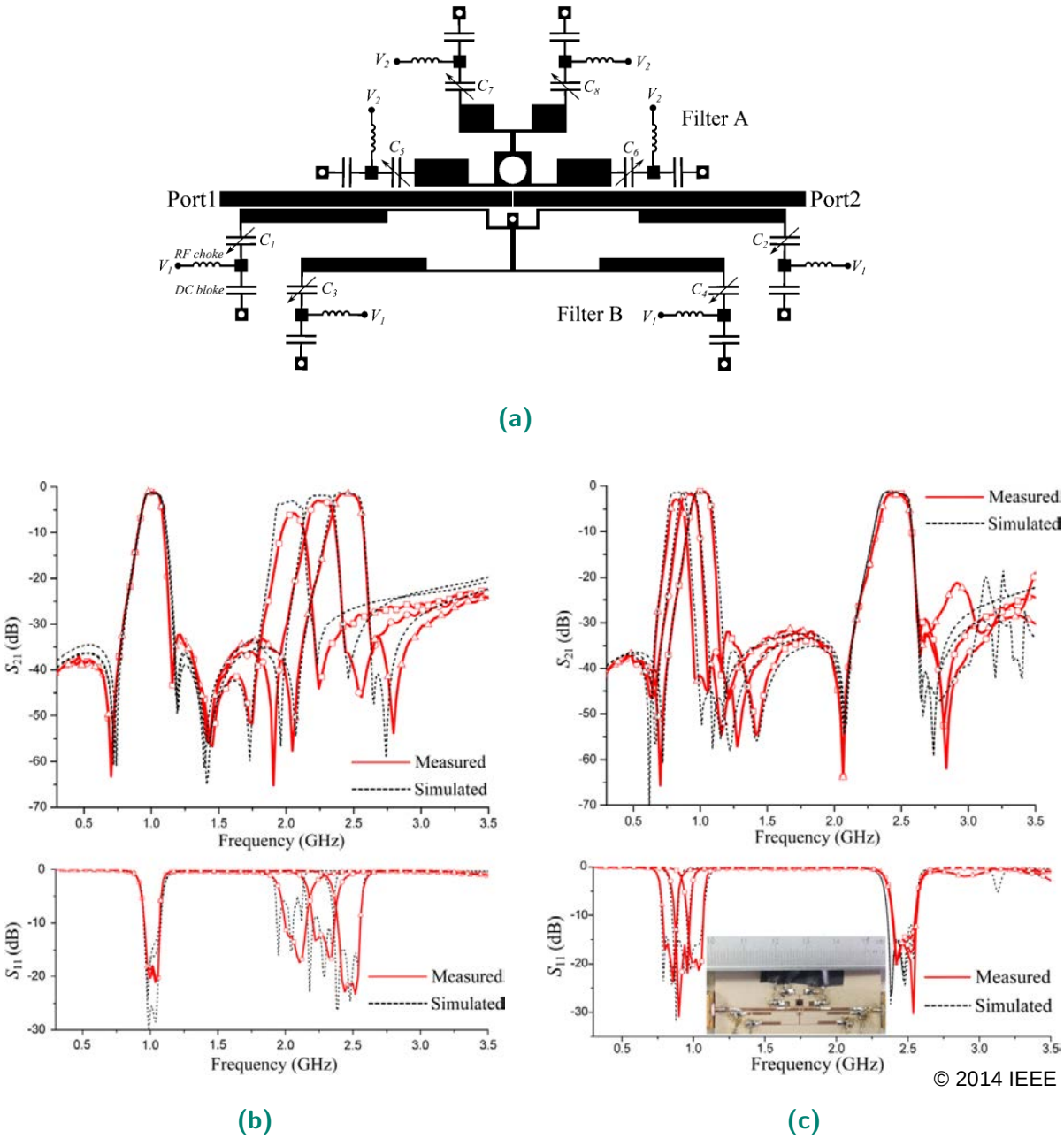

(a)

(b)

(c)

Figure 2.24. Dual-band tunable bandpass filter from [89]. (a) Schematic diagram. (b) Reflection coefficient for tunable first band and fixed second band. (c) Reflection coefficient for fixed first band and tunable second band.

response which is called second-order response, there are two adjacent transmission poles at the stopband due to the presence of two resonators in the structure.

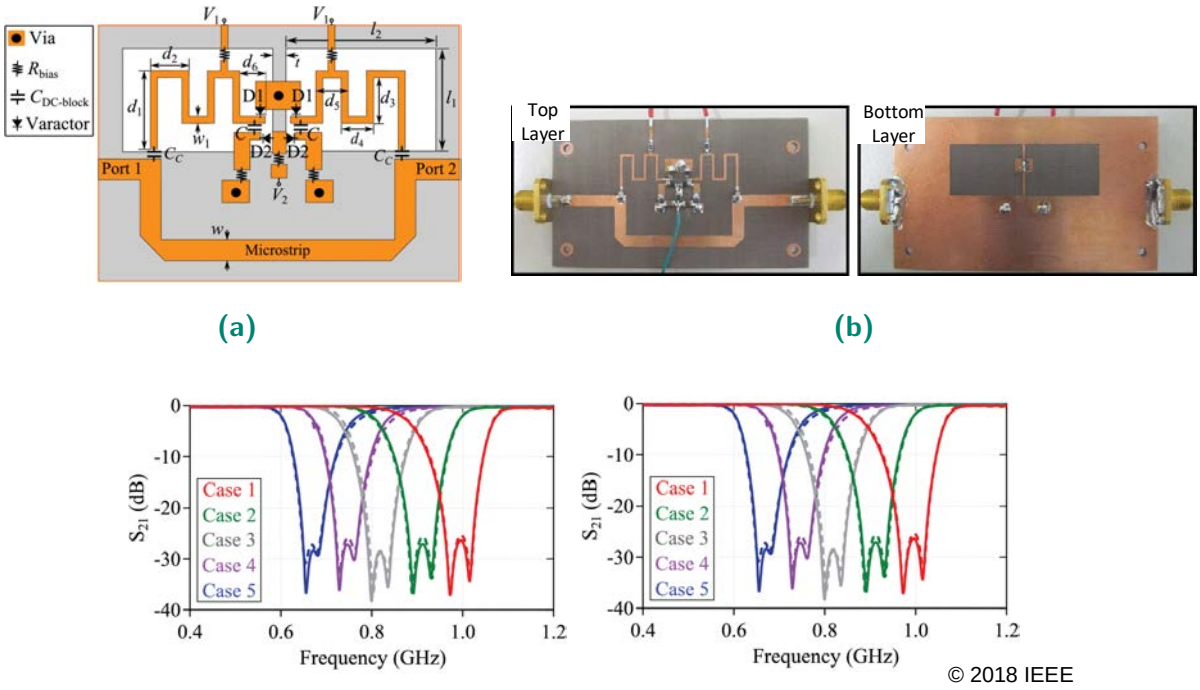

Figure 2.25. Single-band tunable bandstop filter [90]. (a) Schematic diagram. (b) Fabricated filter structure. (c) S_{11} and S_{21} of the tunable bandstop filter.

In another design which was presented in [91], two microstrip bandstop filters are cascaded to create a second-order bandstop filter with a frequency-tunable response. There are two varactor diodes in each section of the bandstop filter, i.e. four varactors in total which are all biased by the same voltage. The single resonator and the whole filter structure are illustrated in Figs. 2.26a and 2.26b. The frequency response of this filter is shown in Fig. 2.26c with the tuning range of 2.06 GHz to 2.81 GHz (30% tuning range).

2.4.3 Multi-state reconfigurable filters

Despite the stated advantages of the designs formerly presented in this chapter further extensions of the functionality are desirable. More specifically, for cases where selectable multi-state filtering functions are needed, several tunable filter structures need to be developed, which inadvertently increase the cost, size, and complexity of the system. Hence, filters with multi-state frequency agility are of high interest. Multi-state

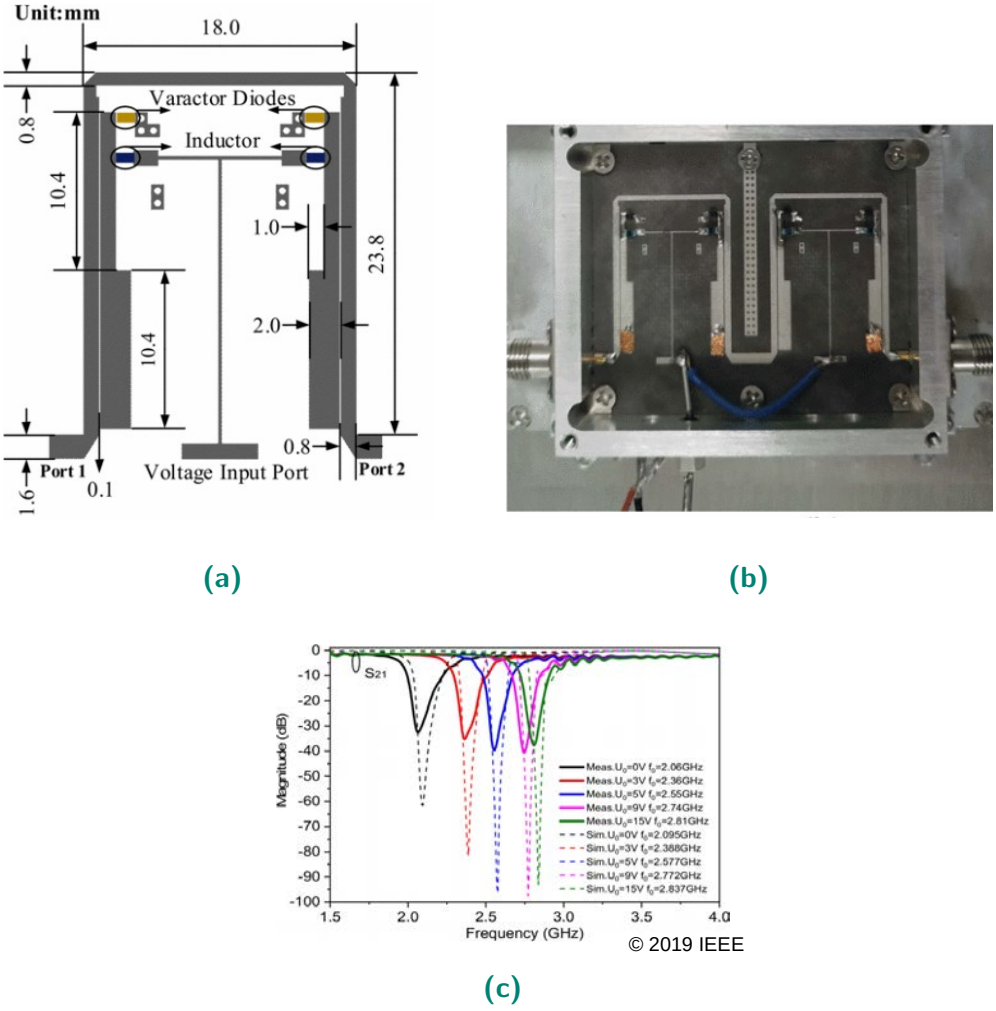

Figure 2.26. Cascaded tunable bandstop filter presented in [91]. (a) Structure of the fundamental resonator. (b) Fabricated filter prototype. (c) S_{21} of the tunable bandstop filter.

functions can include wideband-to-bandpass or bandpass-to-bandstop filtering with frequency agility. The resulting filters are potentially applicable in software-defined radio or cognitive radio systems operating in harsh electromagnetic environments. Such selective functionalities have been studied more intensely in the past few years due to growing demands.

An example of a bandpass-to-bandstop filter with tunable frequencies was presented in [92]. This filter structure, which is illustrated in Fig. 2.27a, uses a switch between its resonators and ten varactor diodes which are biased by four different tuning voltages. The switch can change the state of operation. The bandpass state of operation takes place when the switch is OFF and there is no direct path from the input to the output. In this case, the coupled resonators play a key role in creating a narrow resonance

frequency, which can be tuned by altering the varactors bias voltages. The bandstop state of operation happens when the switch is ON and there is a direct path between the input and output port. The bandstop resonator play a key role in rejecting a specific band from a wideband frequency range which is created by the direct patch from the input to the output. This band can be tuned by altering the bias voltages of the varactors. The measured frequency responses of this filter are shown in Fig. 2.27c to Fig. 2.27f. The bandpass tuning range is from 0.78 GHz to 1.1 GHz (34% tuning range) and the bandstop tuning range is from 0.77 GHz to 1.1 GHz (35% tuning range).

2.4.4 Multi-state reconfigurable filter antenna integration

Selective multi-state tunability filters have been applied to filter-antenna integrated systems in recent studies, owing to their importance in some applications such as software-defined radio or cognitive radio systems.

A successful implementation of such antenna was recently reported in [93] with a filter as a feeding network which is reconfigurable between wideband and tunable bandpass states. The structure of this antenna is shown in Fig. 2.28a. A printed circular monopole antenna with ultrawideband response was used as the antenna module. The states of operation of this monopole antenna is changed by changing the state of PIN diode switch. When the PIN diode is ON, the antenna is working in its wideband state and when the PIN diode is OFF, the coupled resonator with embedded varactors plays a key role in tuning the operating frequency of the monopole antenna. The reflection coefficients of the antenna under different operating states are illustrated in Fig. 2.28b and the radiation patterns of this antenna under different operating states are shown in Fig. 2.28c. The monopolar radiation pattern of the printed circular monopole antenna remained intact after the introduction of the multi-state filter. Another example of antennas which are fed by a filter with multi-state reconfigurability was presented in [94] with a bandpass-to-bandstop filter as a feeding network. The structure of this antenna is shown in Fig. 2.29a. The filter is feeding a wideband printed monopole antenna. The wide spectrum of the monopole antenna enables bandpass and bandstop tunable responses for the whole systems with the wide frequency tuning range. In this design, only the tunable bandstop performance was experimentally verified with a notch tuning range of 3.1 to 3.7 GHz, as shown in Fig. 2.29b. The radiation patterns for the passband of this bandstop antenna are shown in Fig. 2.29c which verifies the unobtrusive behavior of the feeding network to the monopole antenna.

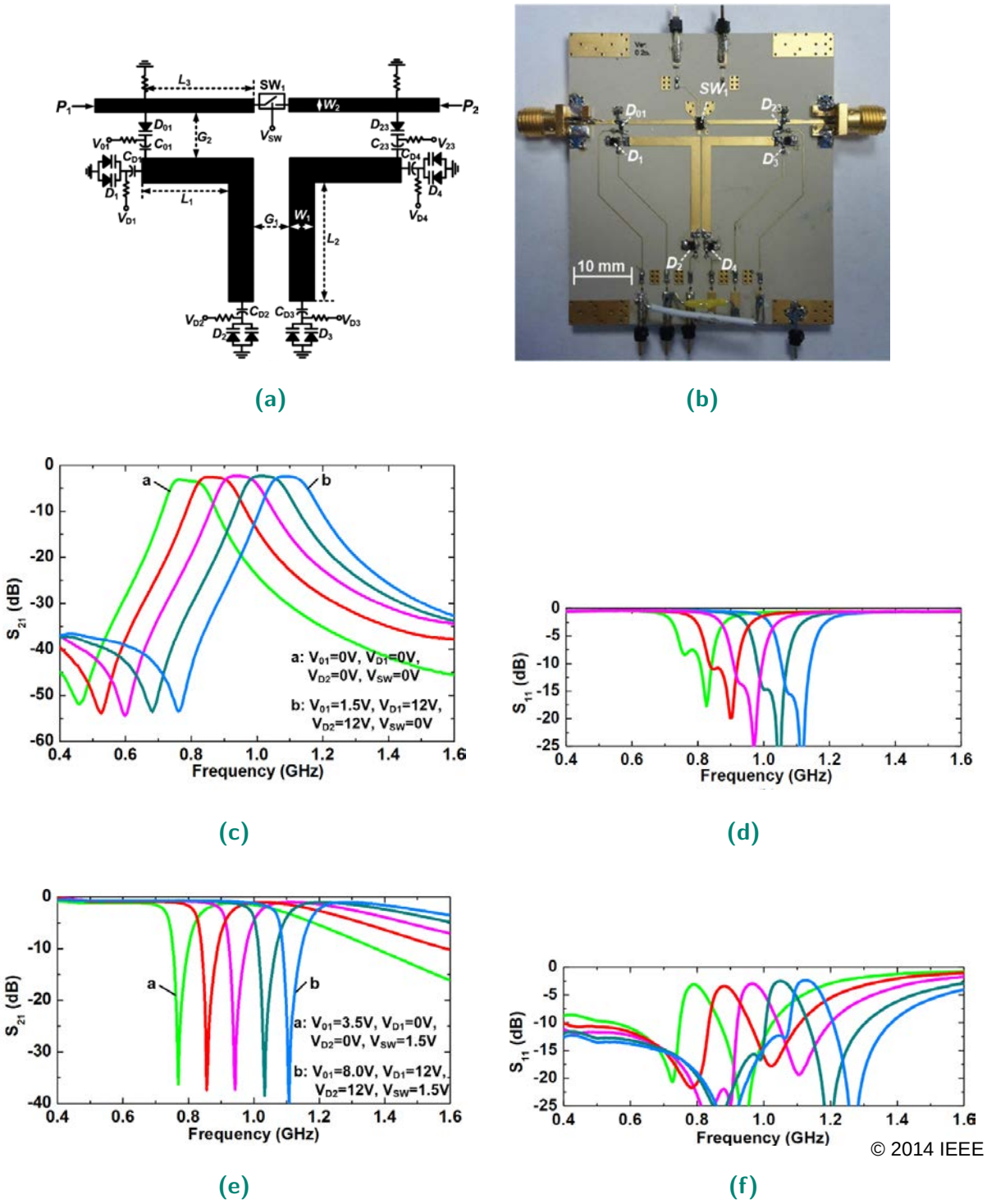

Figure 2.27. Tunable bandpass-to-bandstop filter from [92]. (a) Filter structure. (b) Fabricated filter prototype. (c) S_{21} of the tunable bandpass state filter. (d) S_{11} of the tunable bandpass state filter. (e) S_{21} of the tunable bandstop state filter. (f) S_{11} of the tunable bandstop state filter.

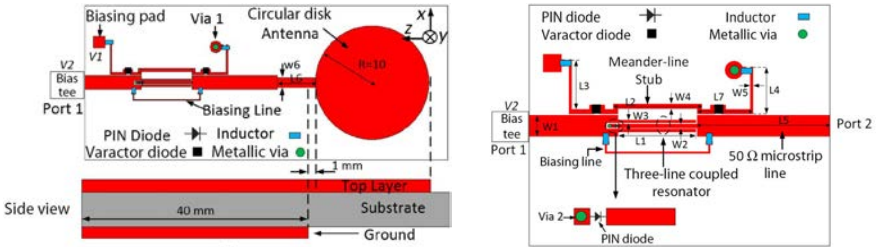

Antenna Structure | Input Filter Structure

(a)

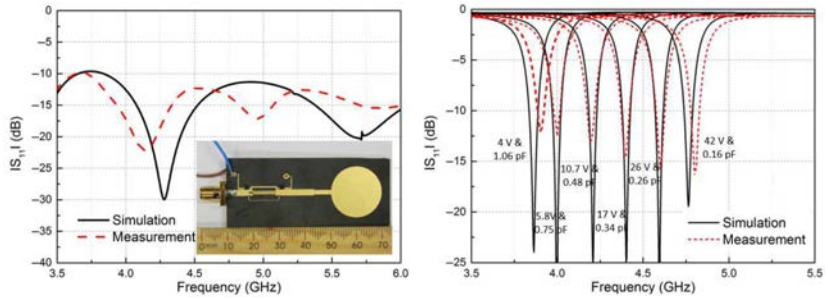

Wideband State Reflection Coefficient | Tunable State Reflection Coefficient

(b)

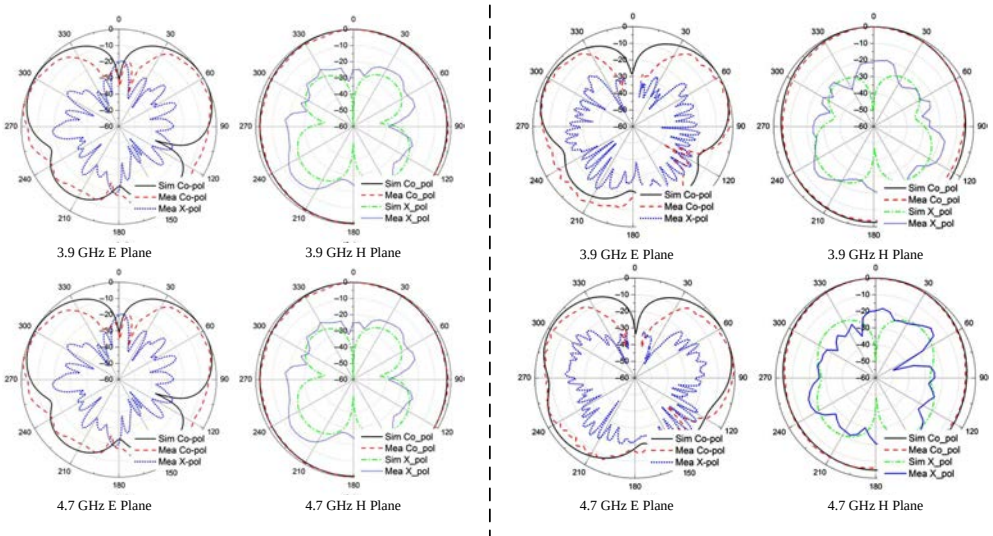

Wideband State Radiation Patterns | Tunable Bandpass State Radiation Patterns

(c)

Figure 2.28. Wideband to tunable bandpass monopole antenna [93]. (a) Antenna structure with magnified filter section. (b) Reflection coefficients for the wideband and tunable bandpass states. (c) Radiation patterns for the wideband and tunable bandpass states.

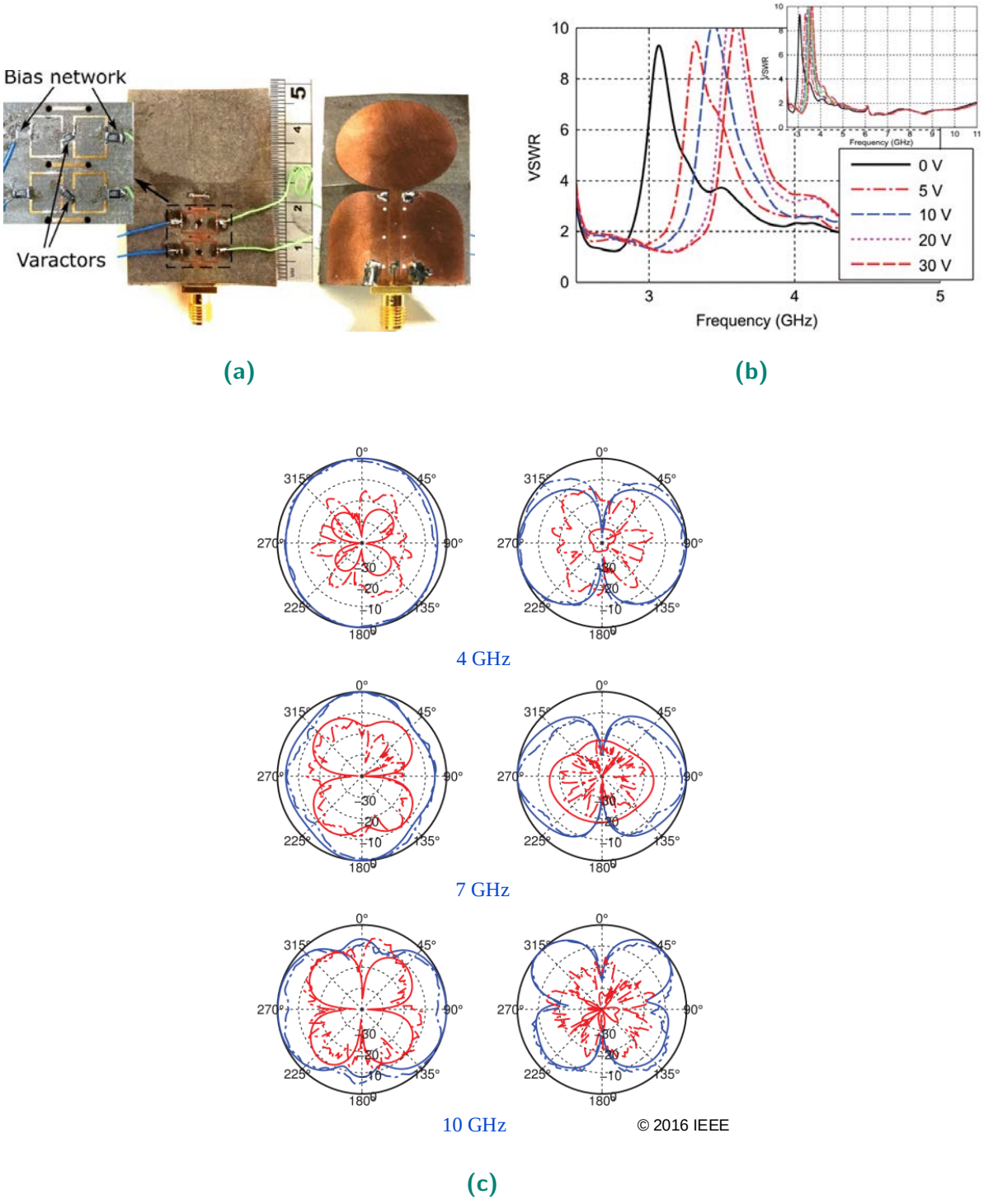

(a) (b) (c)

Figure 2.29. Tunable bandstop antenna based on a bandpass-to-bandstop filter as a feeding network [94]. (a) Antenna structure. (b) VSWR versus frequency. (c) Radiation patterns for the passband.

2.5 Summary

This chapter has presented a descriptive literature review about pattern diversity antenna systems and their constituents. Moreover, this chapter has delved into the structures and designs of the necessary modules for pattern diversity antennas with different modalities, and has outlined the challenges towards developing them. Hence, the information in this chapter can be used as preliminary knowledge for the rest of this thesis.

Chapter 3

Antipodal Vivaldi Antennas with Sum and Difference Patterns

CO–EXISTENCE of ultrawideband frequency response and pattern diversity functions for antennas offers enhanced reliability of communications systems while lowering the manufacturing cost. The ultrawideband response allows several channels to coexist, thereby reducing the cost and complexity of the antenna front end. Sum and difference pattern diversity enables extended angular coverage with higher gain compared to omnidirectional antennas. Using multiple ultrawideband antennas and feeding them with in-phase and out-of-phase excitations is a conventionally salient method to generate sum and difference radiation patterns. However, the lower and higher end of the inherent bandwidth of the fundamental antenna element will be limited by two factors, namely mutual coupling and grating lobes, respectively.

This chapter in its first section proposes a new method to extend the bandwidth of a double-element pattern diversity antenna. For this goal, antipodal Vivaldi antennas are chosen as the fundamental elements owing to their planar geometry with exceptional radiation and frequency responses. In the next section, this method is proved to be effective in multi-element Vivaldi antennas with ultrawideband response and higher realized gain. In the last part of this chapter, a method is introduced which adds to the former techniques to further enhance the isolation and bandwidth of a pattern diversity Vivaldi antenna.

3.1 Introduction

The Vivaldi antenna initially introduced by Gibson in 1979 [27] is a type of traveling wave antenna with a directive end-fire radiation pattern. Owing to the exceptional characteristics of this type of antenna, such as ultrawideband performance, unidirectionality, and stable radiation patterns over a wide frequency range, it has been used in many different applications, such as microwave imaging [76, 95] or satellite communications [96]. During the last decade several studies have focused on improving radiation characteristics while reducing the size and sidelobe levels of the antenna. The most prominent methods are identified as introducing corrugation to the outer antenna edges [77, 97] and adding a dielectric lens to the structure [79, 98]. An alternative way of enhancing the gain and directivity is combining several Vivaldi antenna elements. Recently published designs based on the combination of two elements of Vivaldi antennas demonstrated that this approach can improve the directivity within an ultrawide frequency band [99–101]. Another design based on antipodal structure was presented in [102] with the aim of extending the bandwidth to higher frequencies. All the aforementioned structures have directive radiation patterns, whereas in [10], a dual-port structure was shown to be capable of operating between sum and difference radiation patterns, the later having a deep null in the main direction of radiation. This was achieved by using an in-phase and out-of-phase dual-port feeding mechanism. It was also shown that the grating lobes can be reduced by decreasing the length of the internal flares, with an example where up to 1.77 wavelength spacing between the elements at 10.6 GHz did not result in the appearance of strong grating lobes. This has led to the increase of the upper limit of the operating bandwidth. As for the lower limit of the bandwidth, reducing the mutual coupling level plays a key role in further bandwidth enhancement. Different techniques have been adopted to decrease the mutual coupling level between closely spaced antenna elements. Defected ground structure and slot lines have been adopted in [103] for a multi-element antenna. Near-field horizontal resonators were used to enhance the isolation in [104]. Complementary split ring resonators were shown to change the surface wave propagation in [105], thereby reducing the mutual coupling between two slot antennas. Vertically placed metamaterial cells were also demonstrated to be effective in the reduction of mutual coupling in [106].

In the first part of this chapter, a development of double-element Vivaldi antenna with sum and difference pattern diversity towards wider frequency bandwidth is presented.

Both the sum and difference radiation patterns are demonstrated with high beam symmetry in a wide operating frequency range. The wider operating bandwidth is attained through reduction of the grating lobes at higher frequencies and mitigation of mutual coupling at lower frequencies. The main steps to reach this goal are based on novel geometry features enhanced with a new combination of known techniques. The novel design features consist of reducing the distance between the input ports while increasing the length of internal flares. This delays the occurrence of grating lobes while maintaining the active return loss below -10 dB within the operational band. The new combination of four known methods further enhance the performance and include bending of the inner edges [107], adding a semicircle dielectric lens [77], adding corrugations at the external flares [97], and feeding the sum pattern with out-of-phase signal and the difference pattern with in-phase signal to maintain a high beam symmetry and lower cross polarization for the directive pattern [108]. In the second part of this chapter, the same method is extended to quad-element Vivaldi antenna for higher gain achievement. In the last part of this chapter, a double antipodal Vivaldi antenna with enhanced bandwidth is realized by introducing a method to further reduce the mutual coupling. This further reduction enables bringing the antenna elements even closer to one another which leads to further delaying the appearance of grating lobes, thereby improving the bandwidth.

3.2 Double-Element Design Configuration

The configuration of a conventional Vivaldi antenna is used as a starting point as shown in Fig. 3.1a and the steps taken to improve the design are illustrated in Fig. 3.1b to Fig. 3.1f as described in the following. By convention, the xy-plane is the E-plane and yz-plane is the H-plane. The substrate used for all the designs is Rogers RO4003C^{TM} with relative permitivity of 3.38 and loss tangent of 0.0027. The substrate thickness is chosen as 0.2032 mm. Because a slant near-z-component of the E-field appears between the two metal edges of the antipodal Vivaldi antenna, inside the substrate, this choice of a thin substrate will bring about a lower level of cross-polarization. According to the conventional antipodal Vivaldi antenna design structure, the aperture width should be equal to half wavelength at the desired lowest frequency of operation. A semicircle dielectric lens is also added to the boresight of the antenna to enhance the gain at higher frequencies [77]. As shown in Fig. 3.1b, the inner edges of the flares of the conventional antenna are sharply curved as discussed in [107] for more compactness and improved

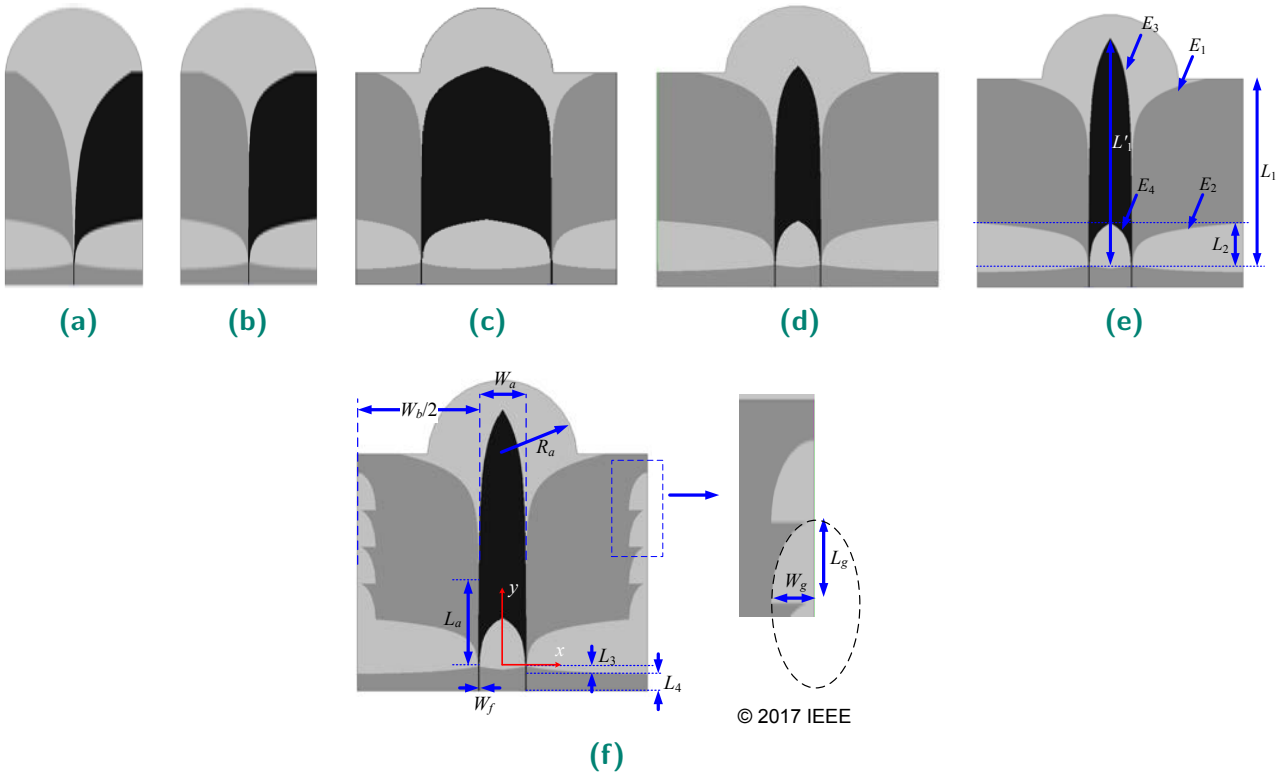

Figure 3.1. Design evolution of the proposed antipodal Vivaldi antenna with the black part as the top metal layer, the dark gray part as the bottom metal layer, and the light gray part as the substrate. (a) Conventional Vivaldi antenna with dielectric lens. (b) Inner edge bending based on the method proposed in [107]. (c) Double-element evolution of the design in (b) (d) Double-element design based on the reduced space between the elements. (e) Double-element design with increased length of internal flares. (f) Final design with outer edge elliptical corrugation.

scattering parameters compared to the conventional antenna. On that basis, the design is extended to a dual-port double-element antenna (Fig. 3.1c) where the directional radiation pattern is fed by out-of-phase input signals at the two input ports. It has been demonstrated [108] that this layer arrangement will result in perfectly symmetrical beam in the full operation bandwidth. The main limitation of this antenna is that according to the classical array factor equation and the pattern multiplication theorem, grating lobes will appear for frequencies where the spacing between the two elements (d) is more than around one wavelength for directive elements.

To further enhance the bandwidth and mitigate the grating lobes, the input ports need to be brought as close as possible to each other as shown in Fig. 3.1d. Unfortunately, this proximity will result in a high level of mutual coupling at the lower end of the frequency range, which will limit the frequency range of satisfactory operation. As

a remedy, it is proposed to elongate the internal flares, as illustrated in Fig. 3.1e to reduce the mutual coupling at the lower end of the frequency band, thereby enhancing the active scattering parameters and increasing the gain. However, increasing the length of the internal flares generally increases the sidelobe level. Therefore, as shown in Fig. 3.1f, elliptical corrugations are added to the edge of the external flares to enhance the radiation characteristics over the ultra wideband frequency range. Based on these design steps, the geometry has been optimized using Ansys HFSS, and the finally obtained dimensions are tabulated in Table 3.1 where the equations for each edge E_1–E_4 referring to Fig. 3.1e are as follows

$$E_1 : x(y) = W_f/2(exp(P_2L_2) - exp(P_1y)) \\ (L_a \leq y \leq L_a + P_2L_2/P_1) \tag{3.1}$$

$$E_2 : x(y) = W_f/2(exp(P_2L_2) - exp(P_2y)) \\ (0 \leq y \leq L_2) \tag{3.2}$$

$$E_3 : x(y) = W_f/2(exp(P_2L_2) + exp(P_3y)) \\ (L_b \leq y \leq L_b + P_4L_2/P_3) \tag{3.3}$$

$$E_4 : x(y) = W_f/2(exp(P_2L_2) + exp(P_4y)) \\ (0 \leq y \leq L_2) \tag{3.4}$$

The E-field distributions at the frequency of 2.4 GHz, i.e. close to the lowest frequency of operation, for the three last configurations (corresponding to Fig. 3.1d to Fig. 3.1f) are shown in Fig. 3.2 when only the right-hand side input port is excited. As observed by comparing Fig. 3.2a and Fig. 3.2b, by increasing the length of the internal flares, the mutual coupling at the lower end of frequency range can be reduced. Moreover, adding the corrugations can enhance the gain and slightly reduce the mutual coupling at lower frequencies (Fig. 3.2c). The elliptical corrugations introduced in this design are capable of mitigating the sidelobes at higher frequencies, whereas at lower frequencies they slightly increase the back-lobes. Figure 3.3 illustrates the value of active S-parameters and mutual coupling between the elements. The detailed information about active S-parameters and a common misconception about them are clarified in Appendix A as a side result of this thesis. For the lower frequency range (below 6.2 GHz), it is seen that the active S_{11} in case of sum (Σ) port excitation (Fig. 3.3a) is improved down to the value of 2.3 GHz when using the combination of added corrugations and increased internal flare length. This is due to the decreased level of mutual coupling (Fig. 3.3c) at lower frequencies. The active S_{11} for the case of difference port excitation (Fig. 3.3b)

does not show significant change since the small mutual coupling value subtracts from the return loss value. The simulated radiation patterns are shown in Fig. 3.4 for different frequencies when in-phase and out-of-phase input signals are used as the excitations. The cross polarization levels are not visible in Fig. 3.4 for lower frequencies in the E-planes, but they increase as the frequency increases. The cross polarization level is also not visible in H-plane for the whole frequency band. Figure 3.5 illustrates the value of realized gain and sidelobe level versus frequency for different configurations shown in Fig. 3.1b to Fig. 3.1f. The final design configuration has the lowest sidelobe level across the frequency range and highest gain in the frequency range of more than 10 GHz.

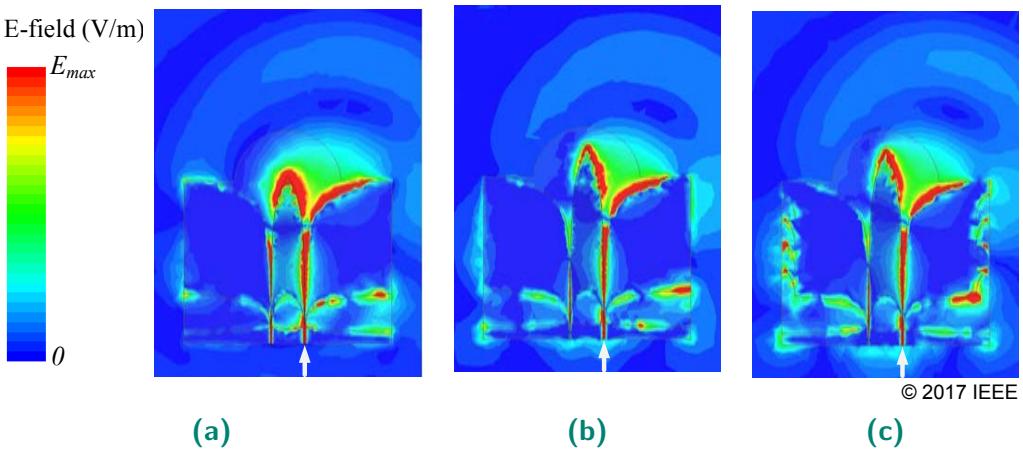

Figure 3.2. Mutual coupling between the elements at 2.4 GHz. (a) Short middle flares. (b) Long middle flares. (c) Final design with outer edge corrugation.

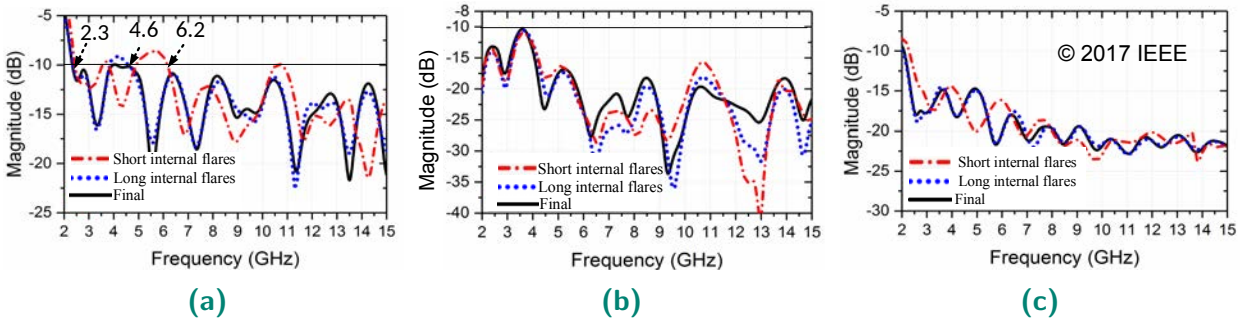

Figure 3.3. Scattering parameters versus frequency. (a) Active S_{11} when out-of-phase feeding is applied. (b) Active S_{11} when in-phase feeding is applied. (c) S_{21}.

3.2.1 Fabrication Results

As shown in Fig. 3.6, the proposed fabricated double-element antenna is connected to an ultra-wideband rat-race coupler with 2-18 GHz bandwidth [109] to realize the sum

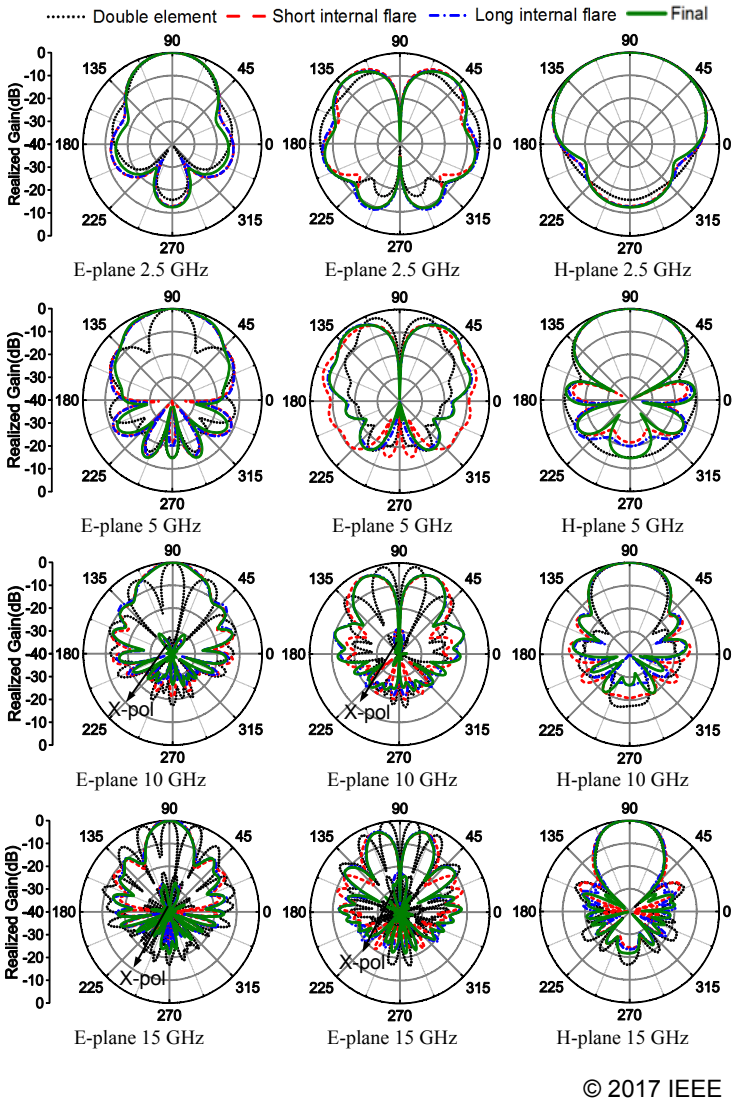

Figure 3.4. Comparison of the radiation patterns for different types of antipodal Vivaldi antennas. Left column: E-plane when out-of-phase feeding is applied. Middle column: E-plane when in-phase feeding is applied. Right column: H-plane when out-of-phase feeding is applied.

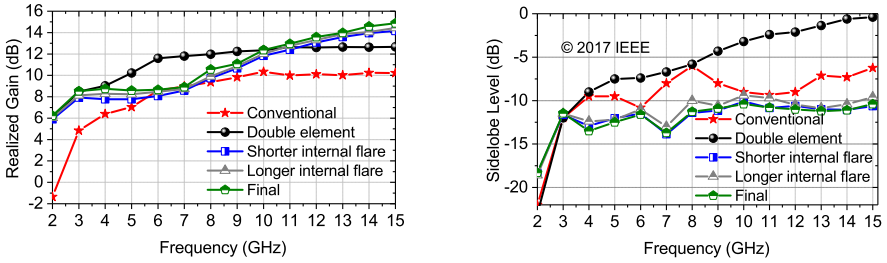

(a) **(b)**

Figure 3.5. Performance comparison of the different types of antennas shown in Fig. 3.1. (a) Realized gain versus frequency. (b) Sidelobe level versus frequency.

Table 3.1. Parameters of the double-element Vivaldi antenna

params.	value (mm)	params.	value (mm)	params.	value
L_1	90	L_g	15.2	P_1	$P_2L_2/(L_1-L_a)$
L_1'	105	R_a	31	P_2	$\ln(W_a/W_f)/L_2$
L_2	20	W_a	20	P_3	$P_4L_2/(L_1'-L_a)$
L_3	3	W_b	62	P_4	$\ln(W_b/W_f)/L_2$
L_4	7	W_f	0.46		
L_a	37	W_g	8		

and difference radiation pattern over the wideband frequency range. The measured reflection coefficients at the input ports of the coupler are shown in Fig. 3.7. As predicted in the simulation, referring to 10 dB return loss, the lowest end of the frequency band within specifications is determined by the case when the sum (Σ) port of the coupler is excited. Furthermore, the highest end of frequency range is determined by the value of sidelobe level, becoming higher than -10 dB, even though the return loss is better than 10 dB for frequencies over 15 GHz. Therefore, the measured range of frequencies within satisfactory specifications extends from 2.3 GHz to 15 GHz. The discrepancies between the simulated and measured results, especially at higher frequencies can be attributed to the difference between the ideal coupler used in simulation and the lossy practical coupler used in experiments. The measured radiation patterns for sum and difference excitations are illustrated in Fig. 3.8 with reasonable agreement with the simulated results. For comparison, the simulated and measured gain and sidelobe level are illustrated in Fig. 3.9. The discrepancies for the measurements with coupler are more pronounced at higher frequencies and can be attributed to the lossy nature of the coupler. As the frequency increases, so does the coupler insertion loss, with the maximum value of around 1.8 dB. To make a better comparison with the simulation results, Fig. 3.9a shows another gain plot, where the extra insertion loss from the coupler is removed.

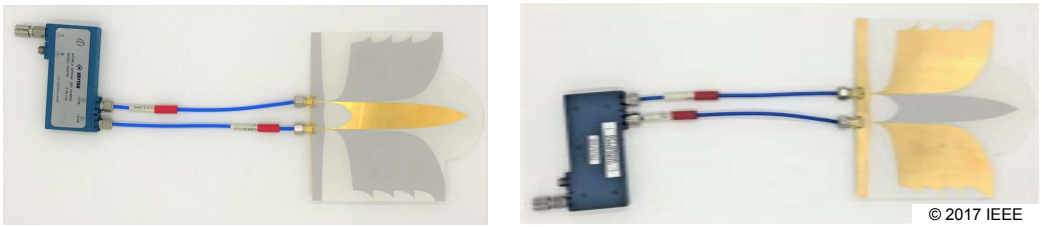

(a) (b)

Figure 3.6. Fabricated antenna with the coupler. (a) Top layer. (b) Bottom layer.

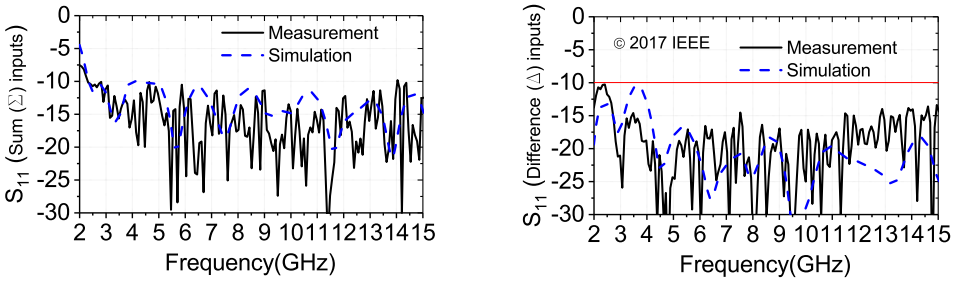

(a) (b)

Figure 3.7. Measured reflection coefficients with the connected coupler versus simulated one with the ideal coupler for (a) in-phase input ports, and (b) out-of-phase input ports.

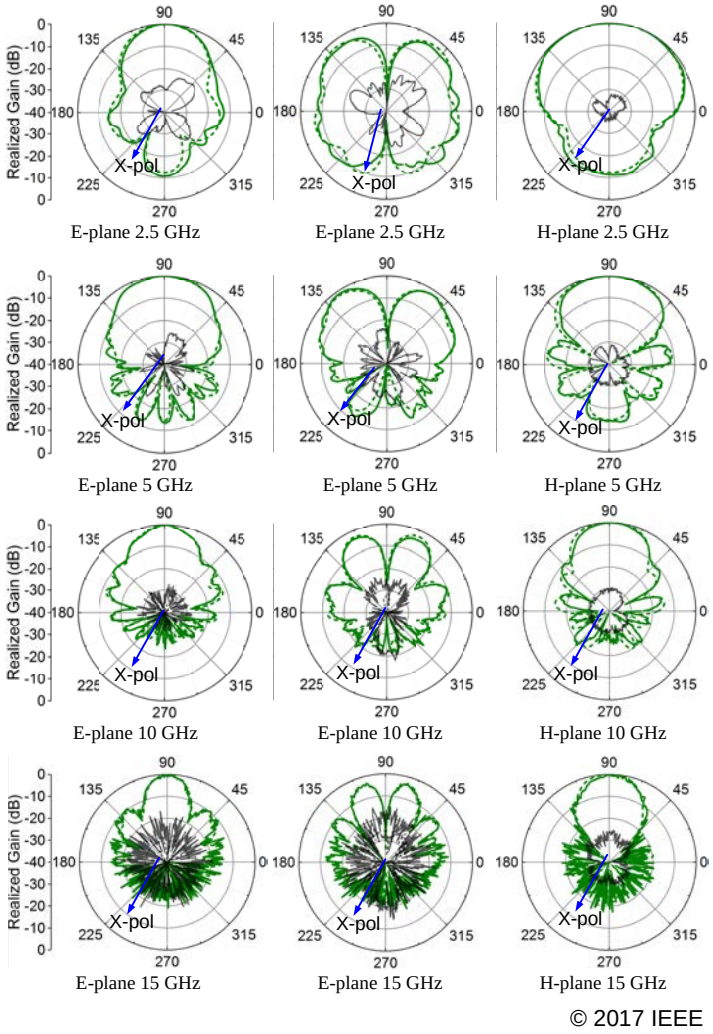

Figure 3.8. Solid line: measured radiation pattern. Dash line: simulated radiation pattern. Left column: E-plane when difference (Δ) port of the coupler is excited. Middle column: E-plane when sum (Σ) port of the coupler is excited. Right column: H-plane when difference (Δ) port of the coupler is excited

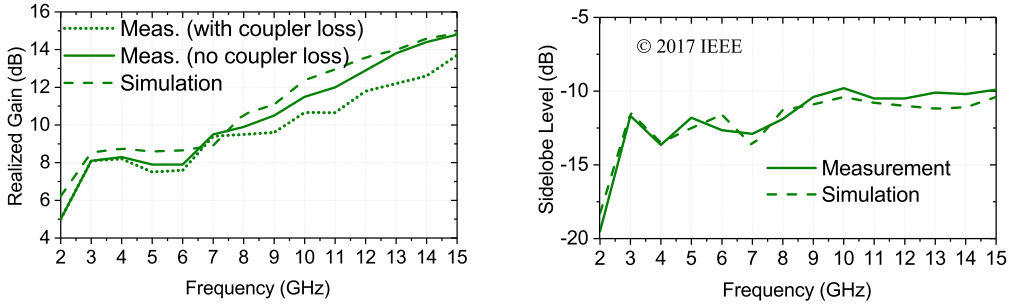

(a) (b)

Figure 3.9. Measured and simulated performance comparison of the proposed antenna. (a) Realized gain versus frequency. (b) Sidelobe level versus frequency.

Table 3.2. Comparison of the proposed double-element design with recently published designs

Refs.	Size (λ_0^2)	BW (GHz)	Gain (dBi)	SLL (dB)	Sum Diff
[99]	0.67 × 1.25	2.5-15	7-15	−7 dB	no
[100]	0.67 × 1.25	2.5-15	7-15	N.S	no
[101]	0.67 × 1.25	2.5-28	9-15	N.S	no
[102]	1.16 × 2.75	4.7-20	10.3-14.8	−10 dB	no
[110]	0.53 × 1.00	2-18	6-15	−7 dB	no
[108]	0.79 × 0.47	2.8-15	∼5-15	−10 dB	no
[10]	1.0 × 1.5	3.1-10.6	10.1-15.0	−13 dB	yes
This Work	0.95 × 0.98	2.3-15	6.8-14.7	−10 dB	yes

3.2.2 Performance Comparison

Table 3.2 summarizes the recently published best performing double-element antipodal Vivaldi antennas and compares them with the proposed design. It is evident that except for [10], the rest of the designs are not capable of generating sum and difference radiation patterns. Although the bandwidths of [101] and [110] are wider than the proposed design, the sidelobe levels are higher in those references and the capability of producing sum and difference radiation patterns is lacking. Although [10] exhibits a higher gain and lower sidelobe level, the proposed design has approximately 35% smaller area and its bandwidth is roughly 50% wider.

3.3 Multi-Element Design Configuration

To compensate the low gain at lower frequencies and the input loss of the coupler, the method presented in Section 3.2 is extended to quadruple-element Vivaldi antenna

with ultrawideband response. The antipodal Vivaldi antenna structure is illustrated in Fig. 3.10a with the xy plane as the E-plane and the yz plane as the H-plane. The utilized substrate is Rogers RO4003C^{TM} with relative permitivity $\varepsilon_r = 3.38$, loss tangent of 0.0027 and thickness of 0.2023 mm. The top and bottom layers of the fabricated structure fed by a wideband rat race coupler [109] are shown in Fig. 3.10b and Fig. 3.10c, respectively. The design comprises four tapered slot antenna elements with two T-junction power dividers to yield an overall two-port antenna structure. The quadruple-element antenna has a mirror symmetry along its y axis which leads to a perfect symmetry in its radiation pattern. For gain enhancement at higher frequencies, a semicircular dielectric lens is formed from the substrate at the antenna boresight and for more compactness and better scattering parameters response, the inner edges of the antennas are sharply bent [107]. According to the conventional design theory,

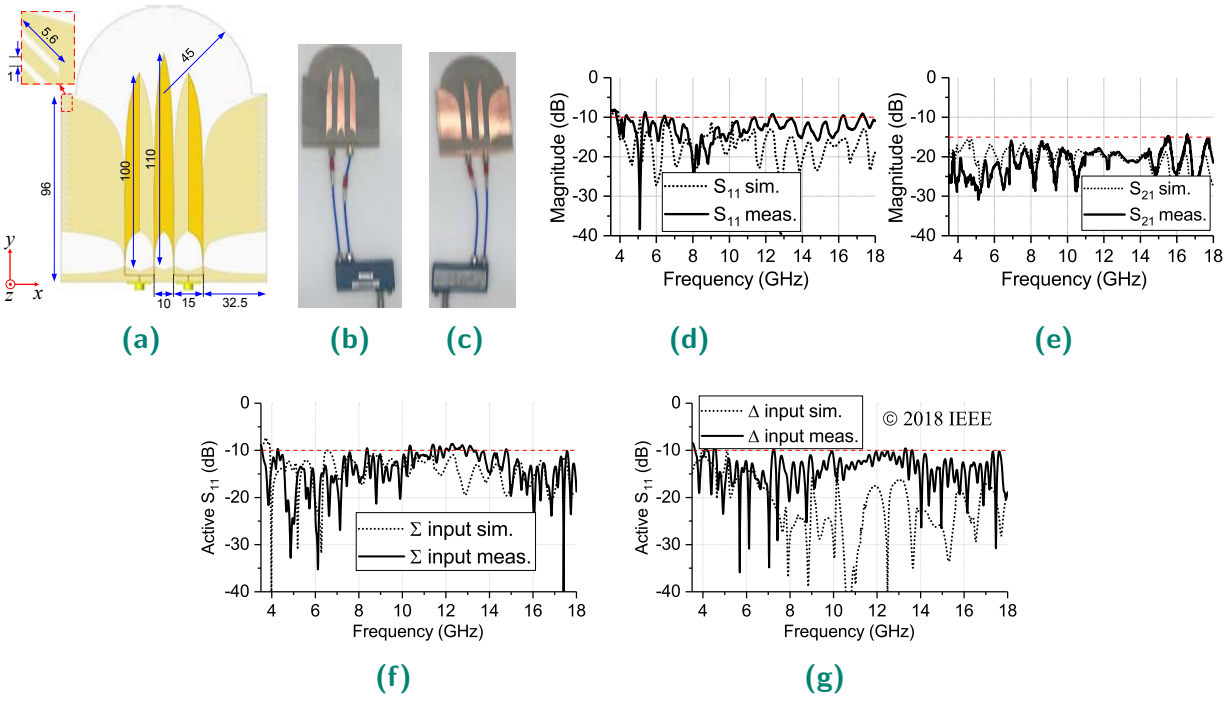

Figure 3.10. Design configuration, fabricated antenna, and S-parameters. (a) Four-element antenna design with dark yellow layer as the top layer and light yellow layer as the bottom layer (dimensions are in mm). (b) Top layer of the fabricated antenna fed by a rat race coupler. (c) Bottom layer of the fabricated antenna fed by a rat race coupler. (d) Simulated and measured reflection coefficient of the antenna itself. (e) Simulated and measured mutual coupling between the antenna input ports. (f) Active S-parameters for sum (Σ) port excitation. (g) Active S-parameters for difference (Δ) port excitation.

the antenna elements should be of equal dimensions and the aperture size of each of them should be equal to half wavelength at the lowest operating frequency. However,

utilizing antenna elements with the same size can limit the frequency range of the antenna due to the appearance of grating lobes at higher frequencies as a result of the increased relative distance between the input ports in terms of wavelength. To alleviate this problem, the antenna elements are modified so that the adjacent elements are kept in close proximity. Nonetheless, a small distance between the antenna elements will bring about high levels of mutual coupling between the feeding ports. To mitigate the mutual coupling the inner antenna flares are markedly elongated to extend into the antenna lens. Following this design methodology, the antenna structure has been parametrically optimized using Ansys HFSS and the reflection coefficient and mutual coupling results based on the simulation and the measurement are illustrated in Fig. 3.10d and Fig. 3.10e, respectively. According to [10], the active S-parameters, which are the combination of coupling and reflection coefficients can better illustrate the performance of the antenna in presence of an external feeding network. In Fig. 3.10f and Fig. 3.10g, these parameters are shown for sum (Σ) and difference (Δ) excitation, respectively. The comparison between the simulated active S_{11} and measured active S_{11} shows an impedance bandwidth (defined for an active S_{11} below -10 dB) extending from 3.9 GHz to 18 GHz, with minor breaches in the measured results. The difference between the simulated and measured results for active S_{11} is due to the use of ideal coupler in the simulation while for the measurement the coupler loss is affecting the performance. It is noteworthy that the active S_{11} is still below -10 dB for frequency ranges beyond 18 GHz, but the level of the grating lobes progressively become comparable to the main lobes, defining a limit for the highest working frequency. In this case, the measured results at 18 GHz show -9.8 dB sidelobe level. Three samples of measured radiation patterns for sum and difference excitation are illustrated in Fig. 3.11, with a reasonable correlation with the simulated results over the whole frequency band. For comparison, the measured and simulated maximum realized gains and highest sidelobes are illustrated in Fig. 3.12. Based on the coupler datasheet, the insertion loss increases as the function of frequency and it is equal to 1.8 dB at the highest frequency end. To make a better comparison with the simulation results, Fig. 3.12a also shows the gain plot excluding the insertion loss from the coupler. In this case the measured antenna gain excluding the extra insertion loss of the coupler ranges from 10 dBi at 3.9 GHz to 16.5 dBi at 18 GHz. Comparison between the performance of the double-element and quad-element Vivaldi antennas is summarized in Table 3.3.

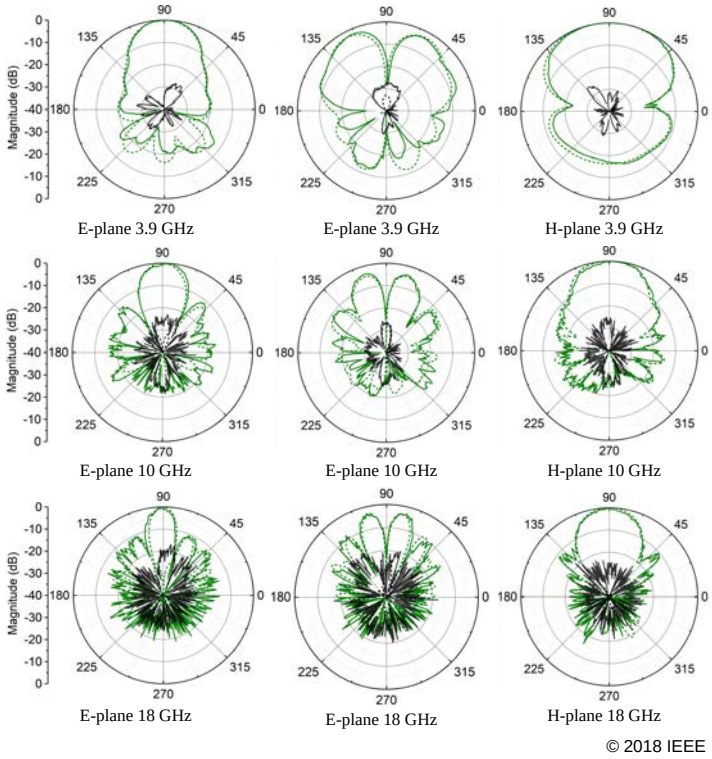

Figure 3.11. Measured (solid lines) versus simulated (dashed lines) radiation patterns. Left column: E-plane directional pattern when the difference (Δ) port of the coupler is excited. Middle column: E-plane differential pattern when the sum (Σ) port of the coupler is excited. Right column: H-plane when the difference (Δ) port of the coupler is excited

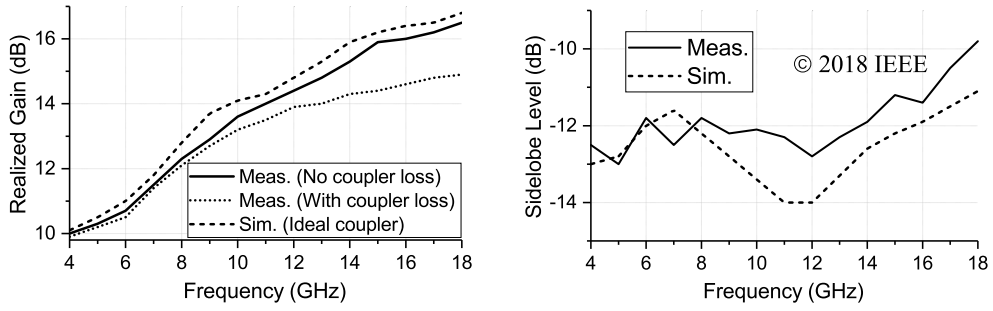

Figure 3.12. Measured versus simulated realized gain and sidelobe levels as the function of frequency. (a) Maximum realized gain. (b) Maximum sidelobe.

Table 3.3. Comparison of the proposed quad-element design with the double-element counterpart

Refs.	**Size** (λ_0^2)	**BW** (GHz)	**Gain** (dBi)	**SLL** (dB)	**Sum Diff**
Double-element	0.95 × 0.98	2.3-15	6.8-14.7	−10 dB	yes
Quad-element	1.33 × 1.41	3.9-18	10.0-16.5	−10 dB	yes

3.4 Pattern diversity Vivaldi antenna design with higher isolation

The double-element structure given in the first section of this chapter had a high frequency limitation defined by the grating lobes appearance at its highest end and a low frequency limitation defined by the combination of mutual coupling and the degradation of reflection coefficient. Hence, one way of improving the overall bandwidth can be the simultaneous reduction of mutual coupling and delay of the appearance of grating lobes at higher frequencies. In this work, the antenna elements are brought even closer to each other compared to the first design presented in this chapter by setting the distance between the two adjacent elements equal to one wavelength at 18 GHz. This value corresponds to 16.7 mm meaning that the first grating lobe will not appear up to 18 GHz. However, as the distance between the elements is reduced, the mutual coupling is increased which is an undesired effect. To cope with this problem, two metal slabs are placed vertically on the top and bottom layers between the antenna elements. The proposed double-element Vivaldi antenna is shown in Fig. 3.13. It is implemented on a dielectric substrate Rogers RO4003C with relative permitivity of 3.38, loss tangent of 0.0027, and thickness of 0.2032 mm. The E-plane is defined as the xy-plane and the H-plane is the yz-plane.

3.4.1 Simulation results

To illustrate the effectiveness of adding these metal slabs between the ports, the scattering parameters simulated with Ansys HFSS for the antenna designs with and without metal slabs are shown in Fig. 3.14. It is observed in Fig. 3.14a and Fig. 3.14b that the reflection coefficient and mutual coupling are improved significantly with the introduction of the slabs in the middle of the antenna. However, the critical parameters showing the performance of the antenna in the presence of a feeding network are the active S-parameters, which are obtained by combining the mutual coupling levels and reflection coefficients. The active S-parameters for the two cases of in-phase and out-of-phase feeding are shown in Fig. 3.14c and Fig. 3.14d demonstrating the improvement brought by the introduction of the metal slabs in the middle of the antenna. The E-field distribution in the configurations of the antenna with the metal slabs and without the metal slabs is shown in Fig. 3.15 at 18 GHz. In this case only the right-hand input port

is excited and the interaction between the elements is observed. It can be clearly observed that, the interaction between the E-field of the two antenna elements is reduced by the introduction of the metal slab.

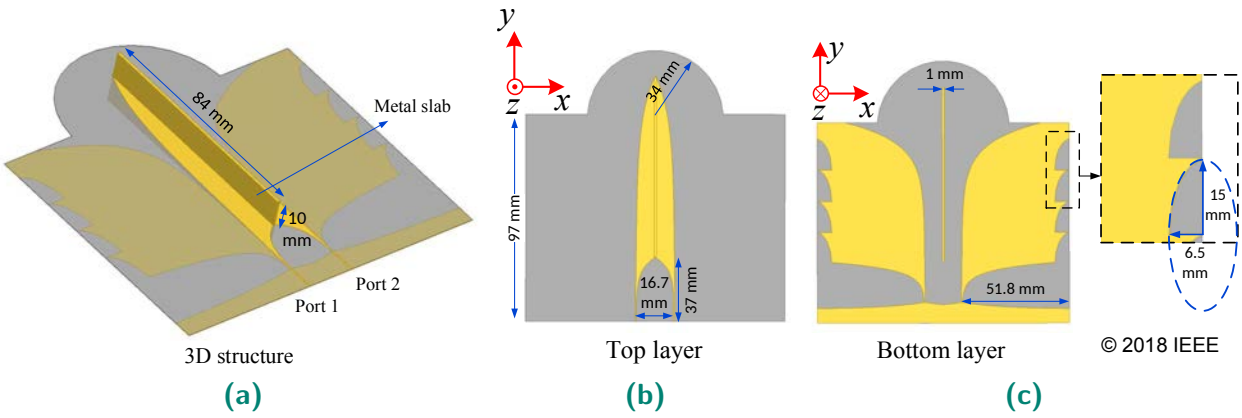

Figure 3.13. Antenna structure. (a) 3 dimensional view with metal slabs between the antenna elements. (b) Top view of the antenna. (c) bottom view of the antenna.

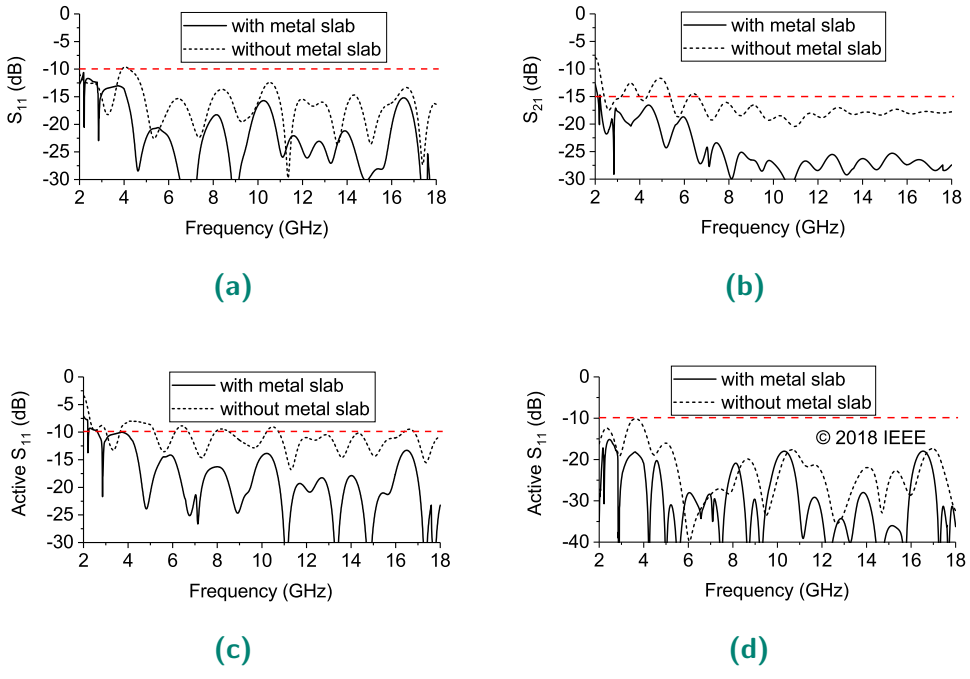

Figure 3.14. Comparison of the simulated scattering parameters for the antenna with metal slab and without metal slab. (a) Reflection coefficient. (b) Mutual coupling. (c) Active reflection coefficient for in-phase feeding. (d) Active reflection coefficient for out-of-phase feeding.

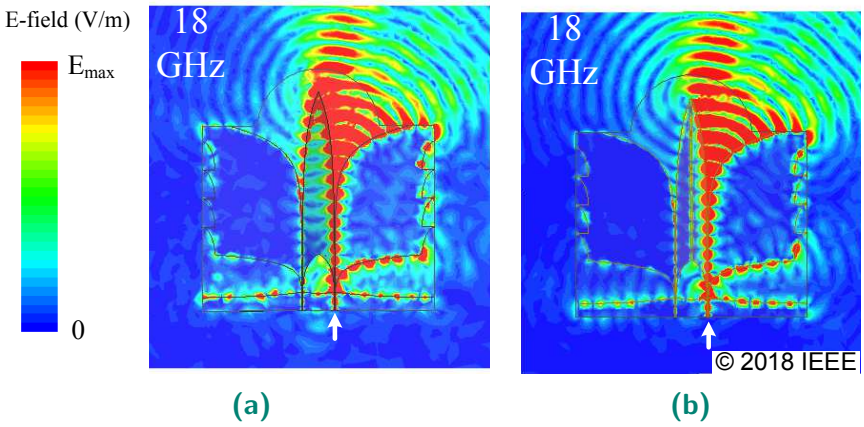

Figure 3.15. Electric field intensity between the antenna elements when only one port is excited. (a) The antenna without a metal slab between the elements. (b) The antenna with a metal slab between the elements.

3.4.2 Experimental results

Based on the simulation results, the antenna has been fabricated and its photograph is shown in Fig. 3.16. A commercial 2-18 GHz ultrawideband rat-race coupler [109] is used as the feeding network. The measured versus the simulated scattering parameters for the antenna itself and the whole system including the coupler are illustrated in Fig. 3.17, showing a reasonable correlation. The discrepancies between the simulated and measured active S_{11} are ascribed to the utilization of an ideal coupler scheme in the simulation. Figure 3.18 represents the comparison between the simulated and measured radiation patterns when the sum and difference ports of the coupler are excited at a time. Based on the measured and simulated results for the case of directive radiation pattern, Fig. 3.19 plots the maximum realized gain and highest sidelobe levels versus the operating frequency. The coupler datasheet states that the insertion loss at higher frequencies increases up to 2 dB. Thus, the extra insertion loss introduced by the coupler is removed from the gain plot in one of the curves for better comparison between the simulation and measurements. In Table 3.4, the proposed design is compared to some of the most recent antenna structures with related specifications. The proposed design exhibits the lowest level of mutual coupling among the featured references. Even though the antenna structure in [110] has a slightly wider bandwidth, it only has a directive radiation pattern, with high sidelobe levels for its highest frequency end.

(a) (b) (c)

Figure 3.16. Photograph of the fabricated antenna. (a) 3D view. (b) Top view with the attached coupler. (c) Bottom view with the attached coupler

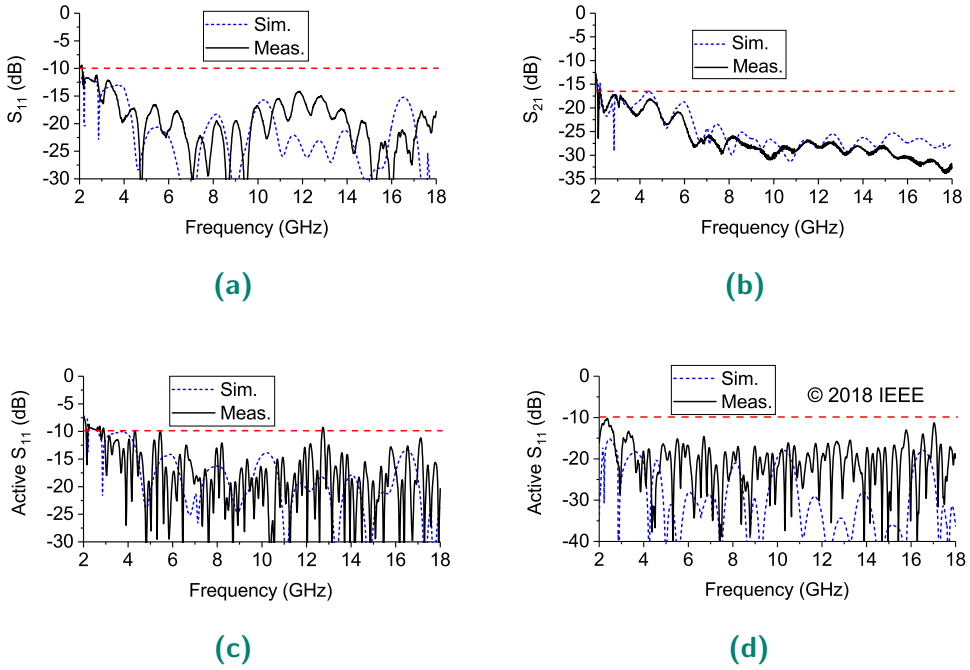

(a) (b) (c) (d)

Figure 3.17. Measured versus simulated scattering parameters. (a) Reflection coefficient. (b) Mutual coupling. (c) Active reflection coefficient for in-phase feeding. (d) Active reflection coefficient for out-of-phase feeding.

Table 3.4. Comparison of the bandwidth enhanced Vivaldi antenna with similar designs

Refs.	Size (λ_0^2)	BW (GHz)	Gain (dBi)	$\lvert S_{21}\rvert$ (dB)	SLL (dB)	Sum Diff
[10]	1.0×1.5	3.1−10.6	10.1−15.0	< -15	−13	yes
[11]	0.60×0.59	0.7−2.7	3.8−8.2	< -10	−10	yes
[110]	0.53×1.00	2−18	6−15	NS	−7	no
Double-Element Antenna	0.95×1.00	2.3−15	6.8−14.7	< -15	−10	yes
This work	**1.04×1.05**	**2.6−18**	**7.3−15.1**	< -17	**−9.2**	**yes**

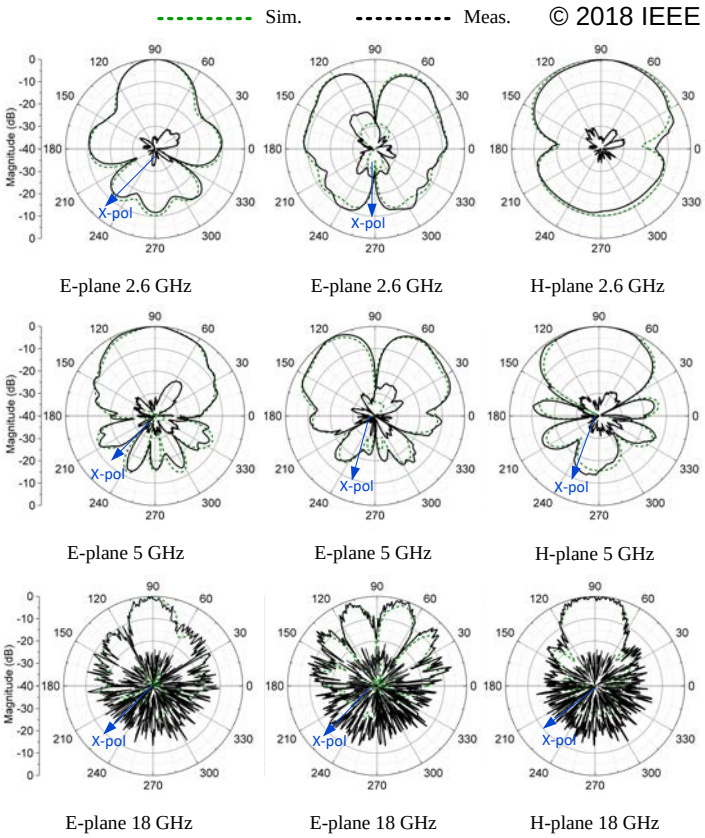

Figure 3.18. Measured and simulated normalized radiation patterns. Left column: E-plane when the difference port of the coupler is excited. Middle column: E-plane when the sum port of the coupler is excited. Right column: H-plane when the difference port of the coupler is excited.

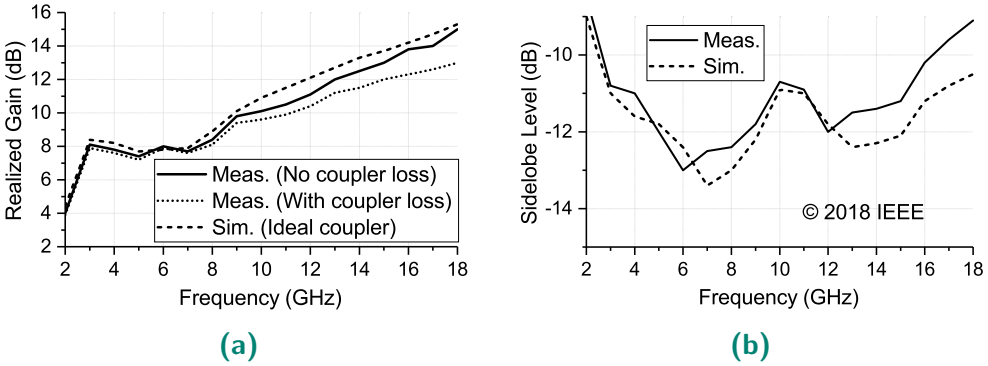

Figure 3.19. (a) Measured and simulated realized gain versus frequency. (b) Measured and simulated sidelobe levels versus frequency

3.5 Conclusion

A new design of a double-element E-plane antipodal Vivaldi antenna for sum and difference radiation patterns has been presented and experimentally validated in the first part of this chapter. This design has been successfully extended to multi-element structure for higher gain in the next part of this chapter. In the final part of this chapter, the bandwidth of the double-element antenna has been extended with further isolation improvement. The presented designs feature several combined improvements over existing designs, summarized as follows: 1) enhanced bandwidth obtained by suppressing the grating lobes at the higher end of the frequency range and reduction of the mutual coupling at the lower end of frequency range; 2) generation of sum and difference radiation patterns over the entire band by a standard rat-race coupler feeding; 3) symmetrical radiation patterns where out-of-phase feeding is applied for producing the directional beam and in-phase feeding is applied for producing the on-axis null of the radiation beam.

Chapter 4

A Design of An Out-of-Phase Feeding Network

IN the pattern diversity Vivaldi antennas that we have hitherto proposed in Chapter 3, it has been demonstrated that the mirror arrangement of antennas on the E-plane brings about more beam symmetry. This is at the expense of feeding antennas with ultrawideband out-of-phase inputs to generate a directive radiation pattern. Since the commercial coupler utilized for proof-of-concept experimental validation is prohibitive for most practical applications, a new design of a bespoke feeding network can help reduce the cost of the overall system.

Therefore, this chapter focuses on the design of an out-of-phase power divider with arbitrary power division ratios featuring improved bandwidth as the power division ratio increases. Arbitrary power division ratios can provide more flexibility in the antenna performance when nonuniform power distribution is required for sidelobe reduction in multi-antenna systems.

4.1 Introduction

As double-input antennas need a feeding network for their excitations, design of a compact and cost effective feeding network is necessary. Power dividers and combiners are playing a key role as feeding networks for antenna arrays. Two important challenges for power divider designs are compatibility with the design of balanced circuits and generation of unequal power at the output ports without adding sophistication to the design. These requirements motivate the design of out-of-phase power dividers with unequal power division. Using double-sided parallel strip lines (DSPSLs), with possibly a conducting plane inserted in between the strips, is particularly well adapted to fulfill the requirement of out-of-phase and unequal power division. One of the most significant advantages of inserting a conductor as virtual ground in between the conductors of DSPSLs is the ability to isolate the top and bottom layers of non-identical circuits, thereby occupying a smaller area and reducing the overall fabrication cost [111]. Applications of DSPSLs for frequency-independent out-of-phase outputs have been extensively investigated [112–118]. Although a planar structure in [119] yielded an out-of-phase result with wideband performance, the level of phase imbalance was relatively high across the bandwidth. Furthermore, unequal out-of-phase power dividers with arbitrary port resistances have yet to be fully investigated. The sole structure for an unequal power divider with out-of-phase response was reported in [116], with appreciable performance, albeit with a limited power split ratios.

In this chapter, a new out-of-phase power divider with arbitrary power division ratios and port impedances is proposed. The circuit is designed analytically based on the principle of reciprocity and perfect matching at all ports. It is demonstrated that optimizations of only two transmission line impedances brings about the optimum design bandwidth.

4.2 Out-of-phase power divider with arbitrary power division design

In this section, an analytical design of a new feeding network with arbitrary power division is explained. All the impedances in the analytical derivations are normalized to 50 Ω for simplicity. The schematic diagram of the ideal design is illustrated in Fig. 4.1. The input port is the balanced Port 1 connecting to top and bottom layers and splitting

the power unequally between the out-of-phase Port 2 and Port 3. The dashed line in the middle of the circuit design indicates the location of the conductor between the top and bottom layers. The design comprises six transmission lines, all of which have identical electrical lengths (θ = 90°) at the fundamental frequency and one isolation resistor R. The design structure enables us to assign an arbitrary value to the isolation resistor, such that a value of commercially available resistor can yield a precise power division ratio in practice. The two transmission lines denoted by Z_m and Z_n can play the role of a phase inverter as in a planar Gysel power divider [120]. Likewise, they can control the bandwidth if $Z_m = Z_n$. The lower the value of their impedances, the higher the bandwidth. Since this structure is not symmetrical, a modified even- and odd-mode analysis [121] is applied to obtain the unknown parameters.

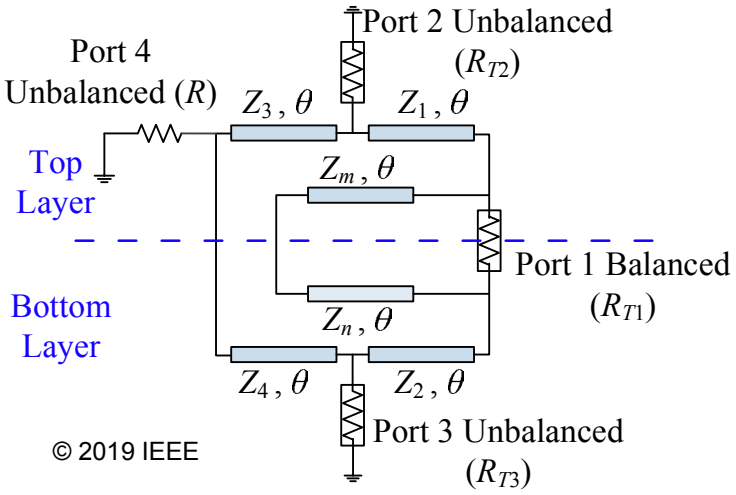

Figure 4.1. The schematic diagram of the proposed circuit

4.2.1 Odd-mode Analysis of the Power divider

In this case, the input port (Port 1) is excited and the two output ports (Port 2 and Port 3) have opposite phases. There is no power dissipation allowed in the isolation resistor and it can be short circuited. Hence, the equivalent circuit can be simplified as in Fig. 4.2a. Writing ABCD matrices and applying some basic circuit principles, we can obtain the following equations

$$V_1' = -\frac{Z_m}{Z_n} V_1, \tag{4.1}$$

$$V_1' = I_{1a} R_{T1} + V_1, \tag{4.2}$$

$$I_{1b} = -I_{1c} \frac{Z_n}{Z_m}. \tag{4.3}$$

By equating (A.1) and (A.2), the value of I_{1a} is attained as follows

$$I_{1a} = -\frac{V_1(Z_m + Z_n)}{R_{T1}Z_n}. \tag{4.4}$$

The power division ratio is defined as K^2 and since most of the power is delivered to Port 2 in the unequal case, the following equation is derived

$$\frac{P_2^o}{P_3^o} = \frac{|V_2^o|^2}{R_{T2}} / \frac{|V_3^o|^2}{R_{T3}} = K^2. \tag{4.5}$$

Therefore, the value of V_2^o in terms of V_3^o and port resistances can be determined as

$$V_2^o = \frac{K\sqrt{R_{T2}}V_3^o}{\sqrt{R_{T3}}}. \tag{4.6}$$

Writing the ABCD matrix for the branch containing Z_1 and equating the obtained voltage to V_1', the value of V_3^o can be obtained as

$$V_3^o = -\frac{j\sqrt{R_{T2}R_{T3}}V_1Z_m}{KZ_1Z_n}. \tag{4.7}$$

Likewise, writing the ABCD matrix of branch containing Z_2 and equating the obtained voltage to V_1 can result in the value of Z_2 in terms of Z_1 as

$$Z_2 = \frac{K\sqrt{R_{T3}}Z_1Z_n}{\sqrt{R_{T2}}Z_m}. \tag{4.8}$$

Using Kirchoff's Current Law (KCL) at node V_1' yields I_{1c} as follows

$$I_{1c} = \frac{V_1Z_m(R_{T1}R_{T2}Z_m - Z_1^2(Z_m + Z_n))}{R_{T1}Z_1^2Z_n^2}. \tag{4.9}$$

Similarly, KCL at node V_1 can result in Z_1 as

$$Z_1 = \frac{Z_m\sqrt{(1+K^2)}R_{T1}R_{T2}}{K(Z_m + Z_n)}. \tag{4.10}$$

Two unknown parameters, Z_1 and Z_2, have been derived from the odd-mode analysis and two other unknowns can be obtained from the even-mode.

4.2.2 Even-mode Analysis of The Power Divider

In the state of even-mode, the input port is open circuited inasmuch as no current flows through it. The same reasoning is available for the phase inverter structure (Z_m and Z_n), where the middle dashed line of the circuit can be regarded as an open circuit.

Consequently, the equivalent structure is simplified as Fig. 4.2b. Evidently, in the unequal case, most of the reflected power is transmitted to Port 3 due to the reciprocity of the design. Hence, the following equation is valid.

$$\frac{P_3^e}{P_2^e} = \frac{|V_3^e|^2}{R_{T3}} / \frac{|V_2^e|^2}{R_{T2}} = K^2. \tag{4.11}$$

V_3^e in terms of V_2^e and termination resistances can be obtained as

$$V_3^e = \frac{K\sqrt{R_{T3}}V_2^e}{\sqrt{R_{T2}}}. \tag{4.12}$$

Writing the ABCD matrices of upper and lower branches and equating the obtained voltages at node V_4, the value of Z_3 is simplified as follows

$$Z_3 = \frac{K\sqrt{R_{T2}}Z_4}{\sqrt{R_{T3}}}. \tag{4.13}$$

Ultimately, using $Z_{in3} \,||\, Z_{in4} = R$ can yield the value of Z_4 as

$$Z_4 = \frac{\sqrt{(1+K^2)}RR_{T3}}{K}. \tag{4.14}$$

The impedance values attained from (4.8), (4.10), (4.13), and (4.14) have some degrees

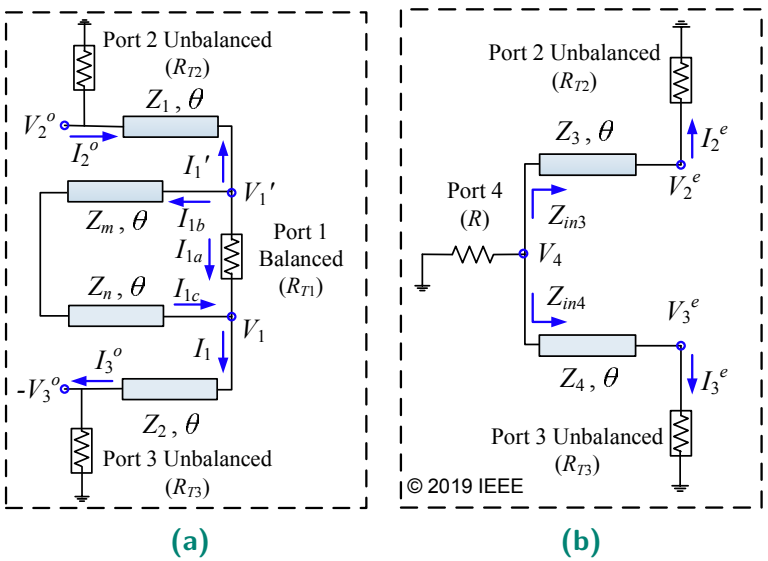

Figure 4.2. (a) Odd-mode and (b) even-mode half-circuit of the proposed design

of freedom including the port resistances (R_{T1}, R_{T2}, R_{T3}), the isolation resistor (R), $q = Z_m/Z_n$, and K. Therefore, there is an infinite number of solutions for the four impedance values. For specific purposes, a fixed value of K will be set by external specifications and the value of R_{T1} can be set equal to 1. To inspect the behavior of a

circuit without port transformers ($R_{T2} = R_{T3} = 1$), Fig. 4.3a shows the variation of Z_1 and Z_2 versus power division ratios, as calculated for three fixed values of q. Note that, these two impedances are independent from the isolation resistor value. In the same way, Fig. 4.3b shows the variation of Z_3 and Z_4 versus power division ratios with the fixed value of R. Notice that these two impedances are independent from the value of q. It is observed that when there is no need for impedance transformer ($R_{T2} = R_{T3} = 1$), the maximum achievable power dividing ratio, considering the practical limitations of line impedances (0.4 to 2.7), is 35:1 when $R = 0.2$. On the other hand, the flexibility offered by the proposed circuit can be exploited to enhance the bandwidth performance, while maintaining the large power division ratio, as described in the next section.

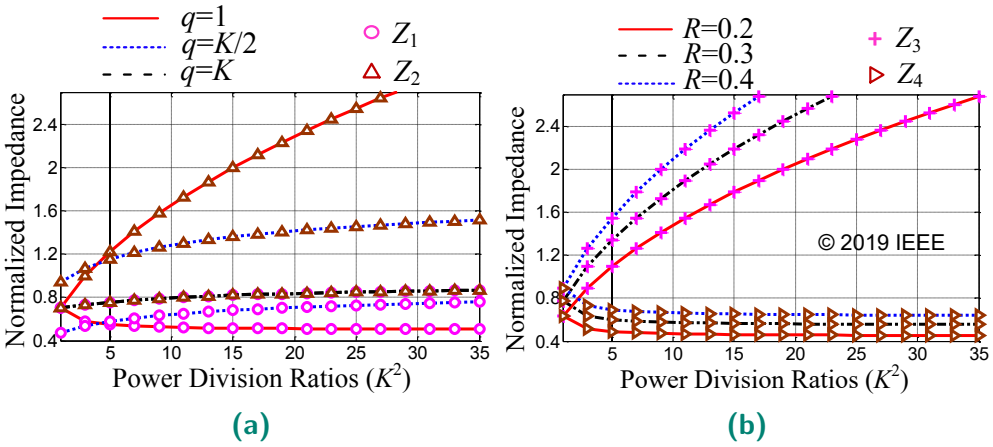

Figure 4.3. Transmission line impedance variations versus power division ratios. (a) Z_1 and Z_2 with fixed q. (b) Z_3 and Z_4 with fixed R

4.2.3 Wideband Design

Modifying the free variables in the design will yield different bandwidth. Thus, calculating and optimizing the schematic performance of the design using ideal components can lead to a significant bandwidth improvement. It is observed that when $q = K$, $Z_n = 0.4$, $R_{T2} = R_{T3} = 0.54$, $R = 0.48$, and two transformers at the output ports are used, the maximum bandwidth is achieved referring to 15 dB isolation and return loss for perfect match and output isolation. The derived impedance values for this case are $Z_1 = Z_2 = 0.6245$, $Z_3 = 2.596$, $Z_4 = 0.519$, $Z_m = 2$ and the bandwidth is approximately reaching 44%. Furthermore, within this operation band, the phase difference between output ports is $180 \pm 20°$. Further enhancement of the phase difference tolerance (from $180 \pm 20°$ to $180 \pm 5°$) and widening of the bandwidth (from 44% up to 80%) can be attained through modifying only Z_2 and Z_3, while retaining the other initial values. This

is however achieved at the expense of degrading the perfect matching and isolation at the fundamental frequency. The schematic of the wideband circuit is depicted in Fig. 4.4 showing the two transformers at the output ports and the two pink transmission lines which are the targeted transmission lines for modification. Note that the *wb* subscripts of Z_2 and Z_3 in this figure denote the finalized values of impedances for the wideband circuit. Optimizations based on the following criteria are carried out to obtain 80% fractional bandwidth with less than $180\pm5^\circ$ phase difference and less than 0.8 dB amplitude deviation with respect to 25:1 power division ratios. The return loss and port isolations ($|S_{11}|$, $|S_{22}|$, $|S_{33}|$, $|S_{32}|$) are set to be lower than 15 dB. The transmission coefficient values are set to $|S_{21}| = -0.1703$ dB and $|S_{31}| = -14.15$ dB (corresponding to 25:1 power division) across the whole bandwidth and the ensuing performance improvement is illustrated in Fig. 4.5. The ultimate values of optimized impedances are: $Z_2 = 1.859$ and $Z_3 = 1.920$.

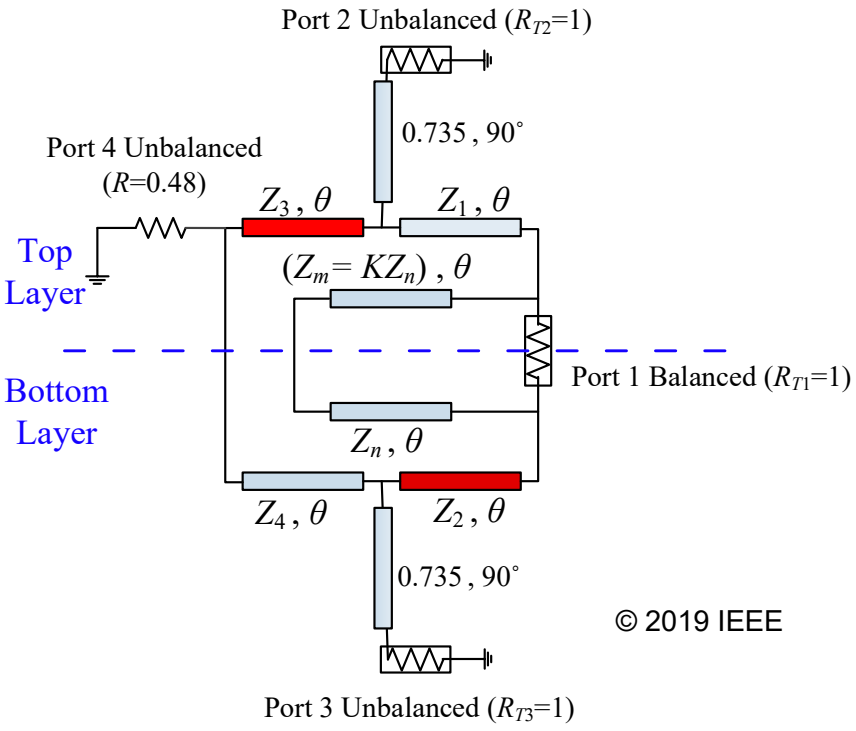

Figure 4.4. The equivalent schematic diagram of wideband circuit.

Using the same approach, we can obtain two sets of data for the modified impedance values of Z_2 and Z_3 versus power division ratios. In order to rule out the need for optimizations for any arbitrary values of power division, we can find an approximated equation for these sets of data through using least squares curve fitting method as follows.

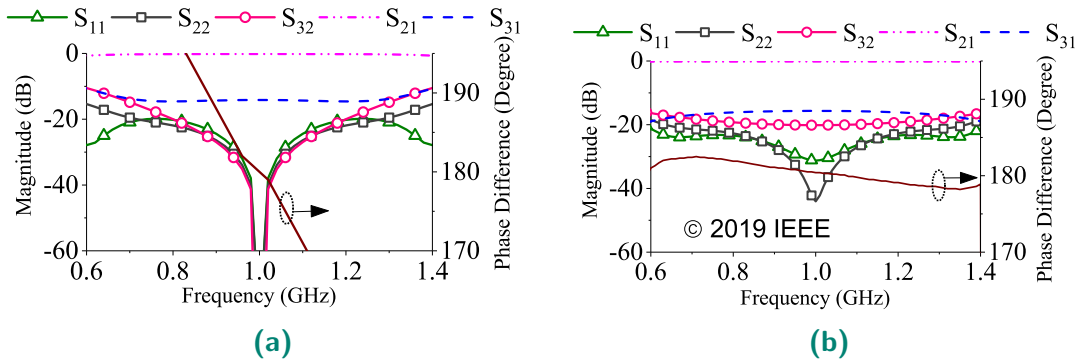

Figure 4.5. Simulation results of the proposed design with 25:1 power division ratio. (a) Results of the proposed design with perfect match at the frequency of 1 GHz and perfect isolation between the output ports. (b) Optimized results of the proposed design for wideband performance.

$$Z_{2wb} = Z_2.\alpha,\ Z_{3wb} = Z_3/\beta, \tag{4.15}$$

Where $u = K^2$ and

$$\alpha = 0.82 + 0.1446u - 0.0031u^2 + 0.0000344u^3, \tag{4.16}$$

$$\beta = 1.04312 + 0.04212u - 0.001573u^2 + 0.0000166u^3. \tag{4.17}$$

The relationships between the maximum attainable bandwidth and power division ratios obtained through the proposed technique as well as the comparison with conventional circuit are illustrated in Fig. 4.6. Contrary to the conventional circuit, which exhibits a deteriorating bandwidth with increasing power division, the presented wideband design shows an increasing bandwidth as the power division ratio increases.

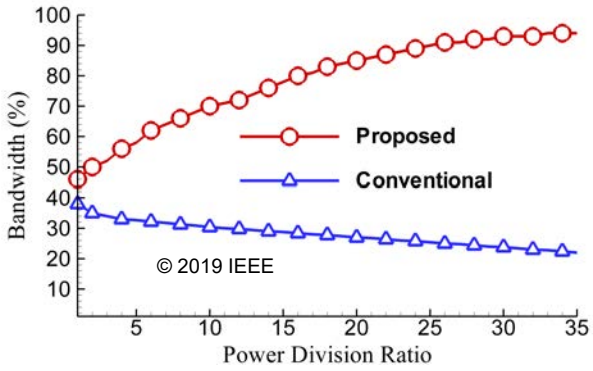

Figure 4.6. Bandwidth comparison of the proposed and conventional power dividers versus power division ratios.

4.2.4 Simulation and Measurement Results

Converting the specified values of impedances and electrical lengths to widths and lengths of transmission lines, electromagnetic (EM) simulations are carried out with HFSS. The power divider is designed on a Rogers (RO4003C) substrates with relative permitivity ε_r = 3.38 and thickness of 2×0.508 mm. The 3D and 2D views of the layout for the proposed wideband power divider are illustrated in Fig. 4.7. The three transmission lines and port transformers located on the top layer are connected to the bottom layer through two via holes. Note that, for compactness, some transmission lines are folded and also microstrip to parallel strip line transition for Port 1 is not needed due to the adoption of a very short input transmission line. A photograph of the fabricated power divider is shown in Fig. 4.8 where the two substrates are riveted together. The EM simulation and measurement results are illustrated in Fig. 4.9. The measurement results were obtained using an Agilent E8361C vector network analyzer. Based on the measured results, the isolation value is found to be better than 15 dB in the range of 0.6 to 1.4 GHz (80% FBW), where all return loss values are better than 15 dB. Moreover, within this range, the output phase difference is 180±5° and the amplitude deviation is less than 0.8 dB with respect to 25:1 power division ratio. To demonstrate competitive performance of the realized device, Table 4.1 compares some recently published out-of-phase power dividers and our proposed design. It is seen that the proposed circuit can reach a power division ratio of up to 35:1. The achievable bandwidth (defined for values of return loss and isolation better than 15 dB) will vary from 45% for equal power division to 90% when operating at the maximum power division ratio.

4.2.5 Summary of the proposed power divider

A new design of extremely unequal out-of-phase power divider based on the DSPSLs has been proposed. The initial design parameters have been based on the perfect matching and isolation at the fundamental frequency using odd- and even-mode analysis method. The ultimate broadband responses have been obtained from a simple modification of only two transmission line impedances. Intriguingly, when the isolation resistor is replaced by a 50 Ω SMA port, this circuit structure can be regarded as a rat-race coupler based on DSPSLs. This circuit is applicable in antenna arrays feeding networks for nonuniform amplitude distributions.

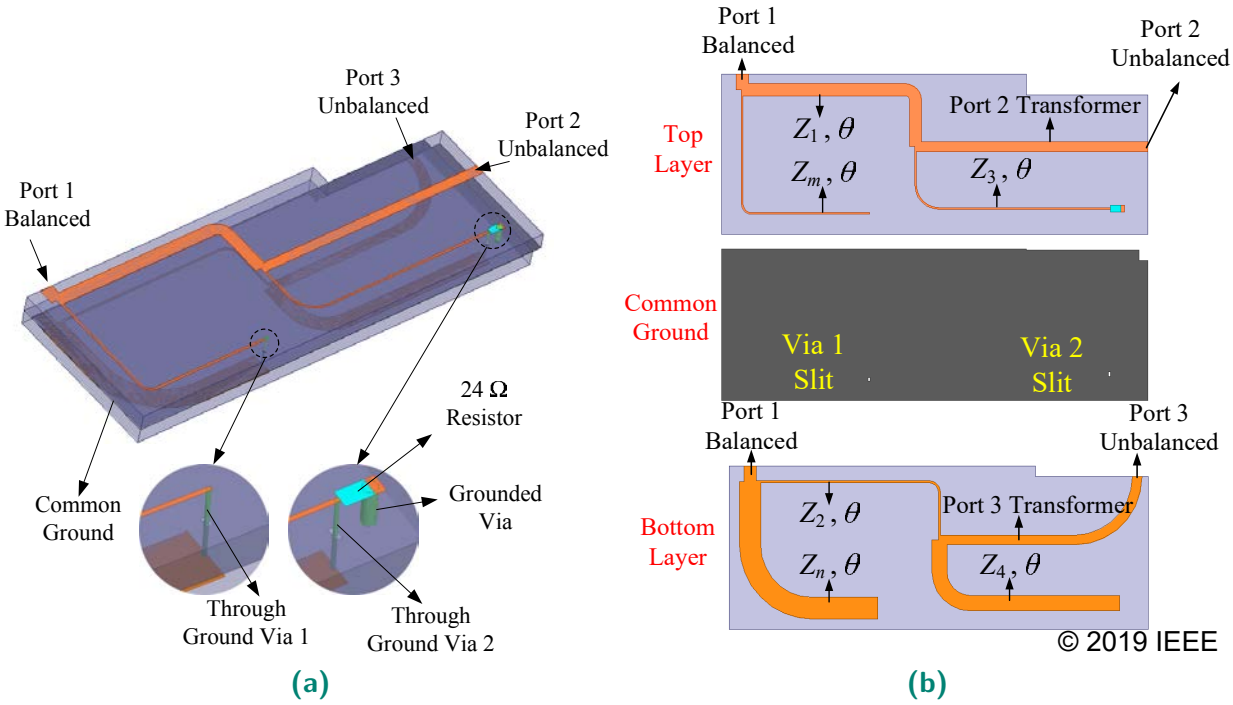

Figure 4.7. Layout of the proposed design. (a) 3D view. (b) 2D view of top, middle, and bottom layers.

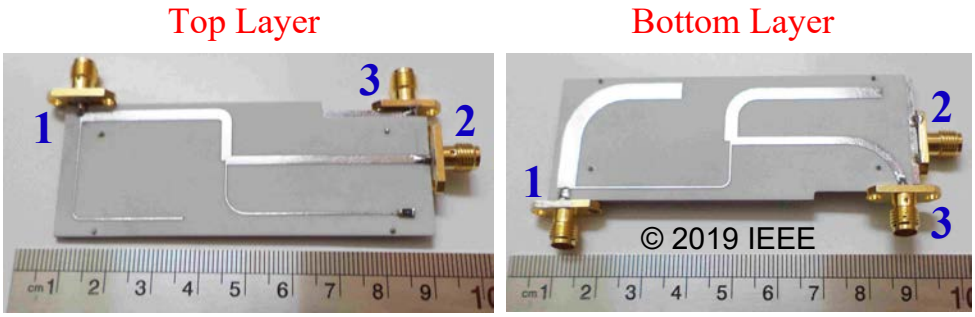

Figure 4.8. Photograph of the fabricated power divider

Table 4.1. Comparison of Proposed Power Divider With Some Similar Published Designs

Refs.	Power Division	Return Loss (dB)	Isolation (dB)	BW %	Resistor Value (Ω)
[116]	Equal	>15	>15	44.3	Variable
[117]	Equal to 4:1	>10	>15	59.6	Variable
[118]	Equal	>12	>16	84	100
[119]	Equal	>10	>16	66	50
This work	**Equal to 35:1**	**>15**	**>15**	**45 to 90**	**24**

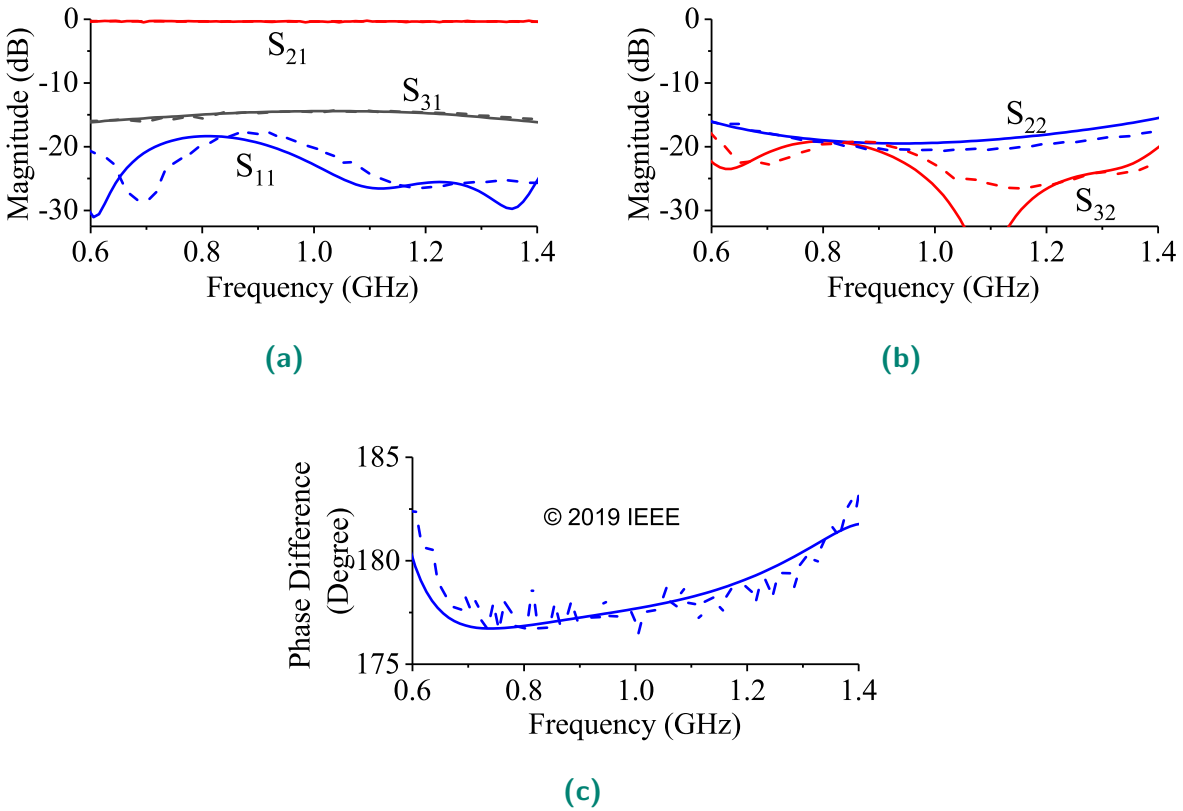

Figure 4.9. EM simulation versus measurement results of the proposed design with 25:1 power division ratio (solid lines are EM simulation and dashed lines are measured results.) (a) $|S_{11}|$, $|S_{21}|$, and $|S_{31}|$. (b) $|S_{22}|$ and $|S_{32}|$. (c) Output phase difference.

4.3 Conclusion

An analytical design of a new out-of-phase power divider with arbitrary power division ratios and port impedances has been proposed. This design has utilized optimizations for only two of its transmission line impedances to obtain optimum design bandwidth. The results have demonstrated that as the power division ratio increases, so does the operating bandwidth which is unlike the conventional power divider scheme. this design can obtain the maximum achievable power division ratio of 35:1 with the widest fractional bandwidth of 90%. The power

Chapter 5

Tunable Bandpass/Bandstop Antenna with Sum and Difference Patterns

RECONFIGURABLE antennas are essential components for modern communications systems. In contrast to the conventional antennas working at a single or multiple fixed frequencies, reconfigurable antennas can dynamically change their states of operation without a requirement for a new design fabrication. Hence, they can substantially reduce the cost and complexity of the antenna front-end. Moreover, the increasing congestion of the available frequency spectrum has led to the emergence of cognitive radio systems which use reconfigurable antennas to effectively utilize the available spectrum. Cost effective antenna front-end for cognitive radio systems requires reconfigurable antennas with multi-state frequency reconfigurability.

This chapter focuses on designing a reconfigurable and tunable antenna system with tunable bandpass-to-bandstop filtering responses, while generating sum and difference pattern diversity functions. To this end, a dual-element quasi-Yagi-Uda antenna with wideband response and acceptable isolation between the elements is proposed. Each antenna element is excited by a tunable bandpass-to-bandstop filter which is integrated with the structure. The overall design is then excited by an external commercially available rat race coupler to generate sum and difference radiation patterns.

5.1 Introduction

The rapid development of communication systems has led to the congestion of the available frequency spectrum due to its inefficient utilization. Cognitive radio systems can play a crucial role in alleviating this problem by adapting their operation to the electromagnetic environment, e.g. by switching from broadband to bandpass modes or from bandpass to bandstop modes [47]. Over the last few years, increasing attention has been paid to the implementation of reconfigurable antennas with switchable wideband/narrowband states, with the frequency tunability arising from the combination of a wideband antenna and an added filtering function [93, 122–128]. More specifically, in [93, 122–124], the tunability and the change of the operation states have been attained based on the replacement of the input feed line of the wideband antenna with a reconfigurable filter, whereas in [125–128], the filtering structure is embedded in the design of the antenna. In the latter case, there is a requirement for voltage-biased switches integrated in the radiating element design, which can adversely affect the radiation pattern [129]. Besides wideband-to-bandpass antennas, bandpass-to-bandstop antennas are also highly desirable components in cognitive radio systems. They can allocate a specific narrowband frequency spectrum to primary users, while they can provide a wideband signal to other secondary users without any interference with the already occupied spectrum. One such design is presented in [94] with the integration of a bandpass/bandstop filter with a standard ultra-wideband (UWB) monopole antenna yielding good bandstop response over a wide tuning range but poor bandpass performance. While the aforementioned studies use single-element antennas with fixed radiation patterns, there is a need for antennas with multiple radiation patterns to enhance diversity for different communication applications [10, 11, 48, 130, 131]. A frequency-tunable antenna with pattern diversity was presented in [132] operating in a single tunable bandpass mode. Another design, presented in [133] can produce sum and difference radiation patterns in different planes by using switches with the operation limited to a single fixed narrowband frequency.

In order to generate sum and difference radiation patterns with tunable bandpass-to-bandstop performances, there are three main requirements including a dual-port wideband antenna, a wideband hybrid coupler and tunable filters, as illustrated in Fig. 5.1. The first requirement for producing sum and difference radiation patterns is to have at least two antenna elements, with a directive radiation pattern and broadband performance. Their operation bandwidth must cover the frequencies specified

for bandpass and bandstop tuning. Although 3D antennas such as horns [134, 135] or resonant cavity antennas [136,137] can provide very high gain and stable radiation patterns over an ultrawideband frequency, they are voluminous, expensive, and difficult to integrate with planar microwave devices. Hence, planar directive and wideband antennas are preferred. The most renowned types of planar directive and wideband antennas include Vivaldi [29, 67, 68], Log-periodic [63–65], and quasi Yagi-Uda antennas [70–74]. As a prominent example, a single element of modified quasi Yagi-Uda was proposed in [34] and it demonstrated more compactness and wider bandwidth than classical designs. The second requirement, as shown in Fig. 5.1 is the feeding network to excite the antenna. The feeding network has to comprise a wideband hybrid coupler, responsible for the production of sum (Σ) signal and difference (Δ) signals. Finally, the third requirement concerns the production of a tunable bandpass-to-bandstop filtering functionality. For this case, a tunable filter, able to switch between bandpass and bandstop states with sharp selectivity and good in-band and out-of-band responses is required, with the emphasis on avoiding detrimental effects on the antenna matching and radiation performance. Tunable bandpass-to-bandstop filters have been investigated in notable recent studies based on substrate integrated cavity resonators [138–140] with complex structure and using coupled resonators [92,141] and multiple varactors. While those studies show attractive performances, there is nevertheless an ongoing need for simple and efficient solutions. In this chapter, an antenna

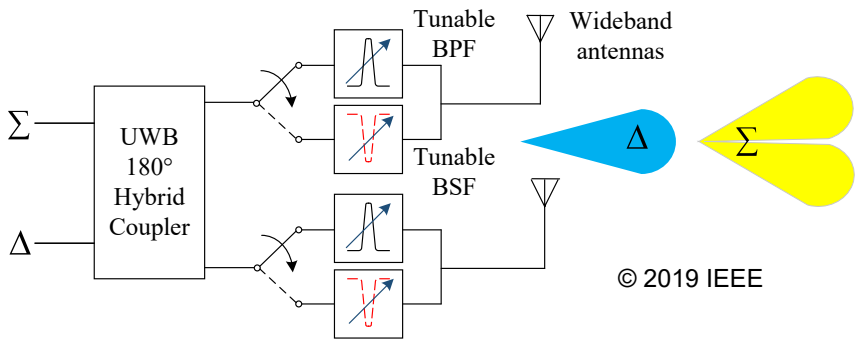

Figure 5.1. Reconfigurable bandpass-to-bandstop RF front-end with sum and difference radiation patterns. (BPF: banpass filter, BSF: bandstop filter)

system geometry meeting all the aforementioned requirements is proposed. First, a compact double-element quasi Yagi-Uda antenna working from 3 GHz to 7.5 GHz is introduced with high E-plane beam symmetry. The symmetry is achieved by a mirror image configuration of the two antenna element feeds. Through this modification, a π-phase is introduced between the two antennas if fed by the same inputs. Therefore,

out-of-phase signals will generate the directive radiation pattern and in-phase signals will produce a null in the main direction of the radiation. This technique can maintain a high beam symmetry in the E-plane and can lower the value of cross polarization for the directive radiation pattern [48, 110]. To add the filtering function, two tunable bandpass-to-bandstop filters with high selectivities are integrated to the design. Each filter consists of a main transmission line with a gap in which a PIN diode is inserted, as well as a narrow center-shorted coupled line equipped with two varactors. The PIN diode switches the circuit performance between the bandpass and bandstop states and the varactors can continuously tune the narrowband frequency for the bandpass state and the notch frequency for the bandstop state. The novelty aspects of this design can be identified as a combination of all the following features in a single reconfigurable system:

1. Ability to produce sum and difference radiation patterns for bandpass and bandstop states of operation with high level of beam symmetry.

2. Experimentally implementable and integratable tunable bandpass-to-bandstop filter structure with simple geometry and unobtrusive biasing network, resulting in minimal interaction with the radiating structure.

3. Two transmission zeros tuned by the agility of the pass-band yielding high selectivity (minimum roll-off rate = 57 dB/GHz) and out-of-band transmission coefficient (<-12 dB) in the bandpass state of the filter.

4. Strong in-band zeros (<-13 dB) and out-of-band poles (>-1 dB) in the bandstop state of the filter.

5. Experimentally validated dual-pattern bandpass-to-bandstop antenna with measured values of 50.0% tuning range for the bandpass state and 50.4% tuning range for the bandstop state.

The organization of this chapter is as follows. Section 5.2 explains the antenna structure and its characteristics. Section 5.3 clarifies the filter design and its performance. In section 5.4 the integration of the filter with the antenna is investigated. Section 5.5 provides the experimental validation of the whole system and compares the obtained results to the simulation. Finally, the conclusion is drawn in section 5.6.

5.2 Antenna design

In this work, a quasi Yagi-Uda is selected as an ideal option. There is a clear rationale for preferring the quasi Yagi-Uda to other planar antennas with wider bands, such as the Vivaldi antenna. The main reason for our choice is that the quasi Yagi-Uda antenna has a typical bandwidth of around 90%, which is commensurate with the achievable tunability band of the bandpass-to-bandstop frequency-reconfigurable filter. This is in contrast to the achievable ultrawide bandwidth of the Vivaldi antenna, which cannot be fully exploited in conjunction with tunable filters and comes at the cost of a significantly larger planar footprint and longer length compared to the relatively compact quasi Yagi-Uda antenna.

The 3D structure of the double-element quasi Yagi-Uda antenna is illustrated in Fig. 5.2. It is implemented on Rogers RO4003C with relative permittivity of 3.38, loss tangent of 0.0027, and thickness of 0.8128 mm. The single element is obtained from [34] and it is modified to work in the range of 3 GHz to 7.5 GHz. In order to generate symmetrical radiation patterns, the double-element antenna geometry should have symmetrical structure. The symmetrical geometry about XY-plane can be produced through using mirror symmetry of the antenna including its feed, as shown in Fig. 5.2. In this case, when the antenna elements are fed by out-of-phase signals, they generate the directive radiation pattern and when they are fed by in-phase signals, they generate the radiation pattern with a null in their mirroring plane. The high level of beam symmetry in this configuration contributes to the generation of a deep null in the main direction of the radiation. The detailed geometries of the top and bottom layers are illustrated in Fig. 5.3 and the related dimensions are summarized in Table 5.1. The antenna elements have a distance D_5 between them for sufficient isolation while avoiding any grating lobes at the highest operating frequencies. The design has been simulated and parametrically optimized to these dimensions using Ansys HFSS, with the final results summarized in Fig. 5.4. The reflection coefficient $|S_{11}|$ shown in Fig. 5.4a is below -12 dB in the frequency range of 3 GHz to 7.5 GHz, with the mutual coupling $|S_{21}|$ remaining below -16 dB in this band. Another important performance measure that will guarantee proper functionality in the presence of microwave filters in the feeding network is provided by the active scattering parameters, which are based on the combination of reflection coefficient and mutual coupling between the elements [10, 48]. These parameters lie below -10 dB from 3 GHz to 7.5 GHz for both the cases of in-phase and out-of-phase feeding as shown in Fig. 5.4b. From the simulation results,

Table 5.1. Parameters of the double-element quasi Yagi-Uda antenna

param.	value (mm)	param.	value (mm)	param.	value (mm)
W_0	75	D_0	70	D_9	1.2
W_1	1.8	D_1	16.6	D_{10}	5.2
W_2	1.8	D_2	4	D_{11}	0.8
W_3	1.8	D_3	13	D_{12}	2.4
W_{d1}	2	D_4	3.6	D_{13}	30
W_{d2}	2	D_5	5	G_1	1.4
W_4	1.8	D_6	3	G_2	1.9
W_5	1.4	D_7	44	R	2.4
W_6	0.9	D_8	3.2		

the maximum realized gain for the directive radiation pattern is expected to vary from 5.8 dBi to 11 dBi in the range of 3 GHz to 7.5 GHz as illustrated in Fig. 5.4c. The normalized simulated radiation patterns are shown in Fig. 5.5. The beamwidth is narrower in the E-plane than in the H-plane due to the larger aperture size in the E-plane. The cross polarization values for the H-plane are not visible in the dynamic range used in these figures.

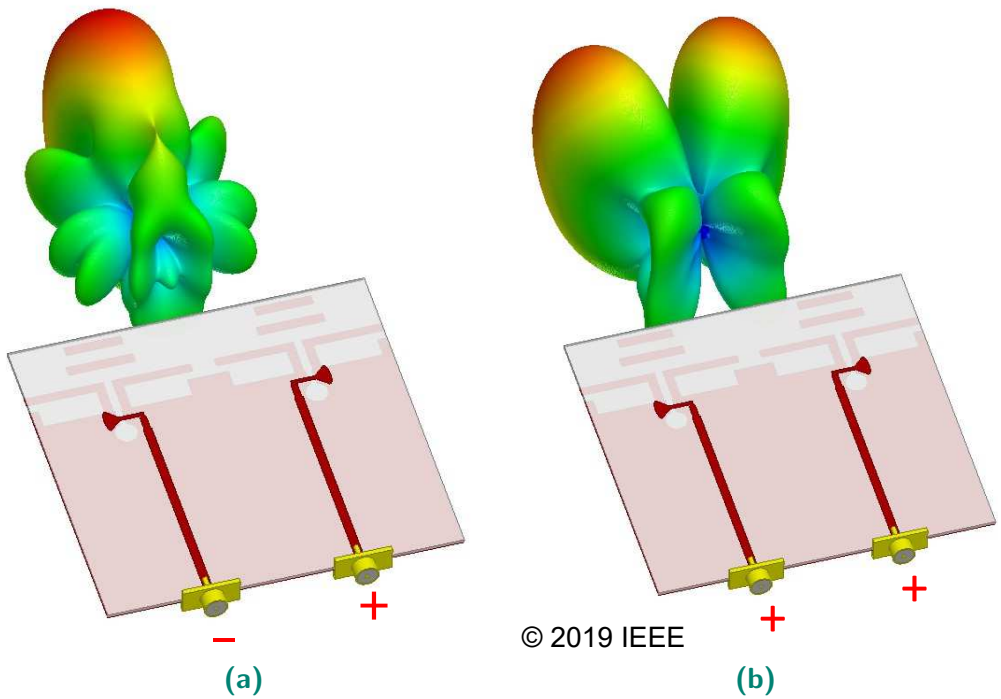

Figure 5.2. 3D structure of a double-element quasi Yagi-Uda antenna with sum and difference radiation pattern. (a) Sum pattern excited by the out-of-phase signals. (b) Difference pattern excited by the in-phase signals.

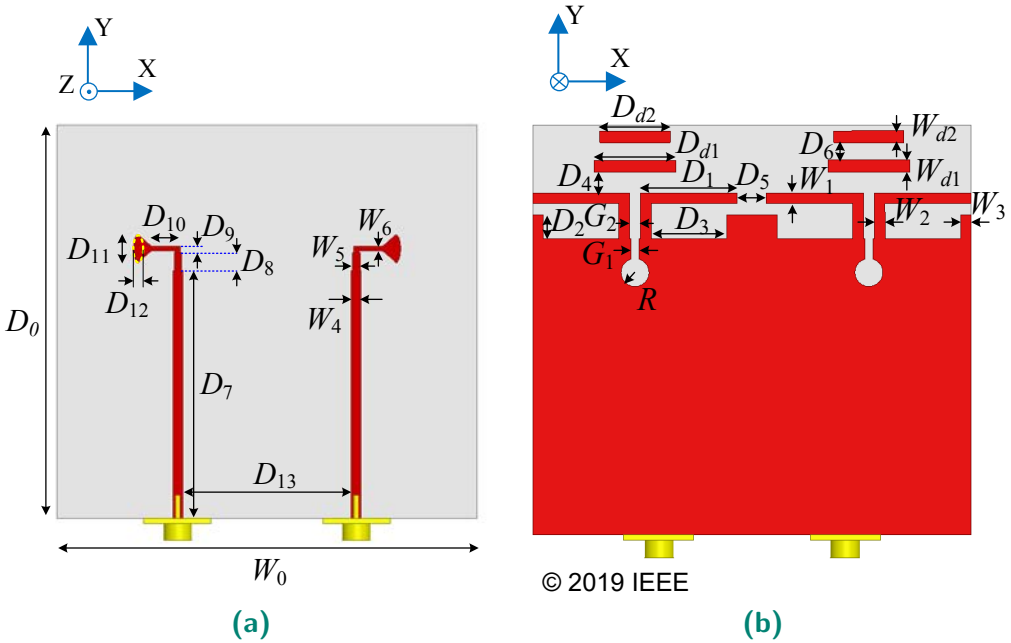

Figure 5.3. 2D Structure of the antenna with its dimensions. (a) Top layer. (b) Bottom layer.

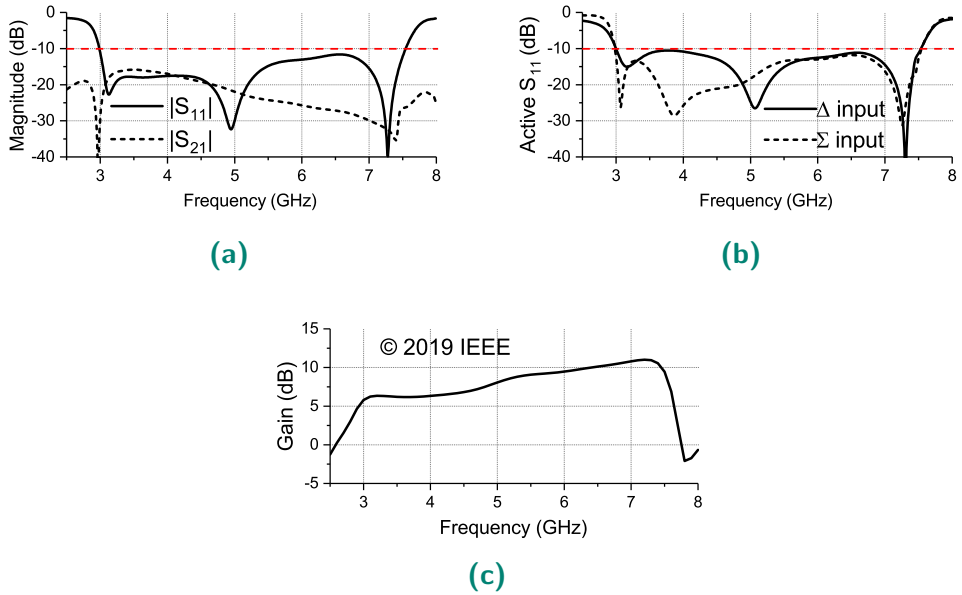

Figure 5.4. Scattering parameters and realized gain versus frequency. (a) Reflection coefficient and mutual coupling. (b) Active scattering parameters when Σ and Δ ports of the input coupler are excited. (c) Realized gain for the sum radiation pattern.

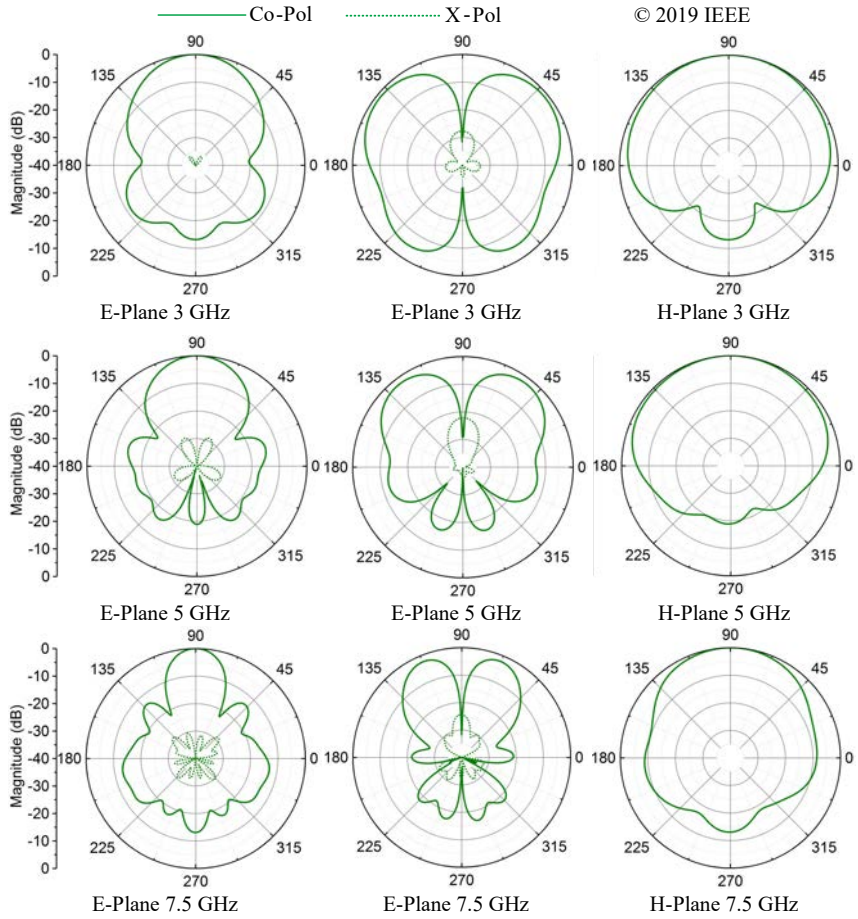

Figure 5.5. Radiation patterns for the isolated double-element quasi Yagi-Uda antenna at different frequencies. Left column: E-plane when out-of-phase excitation is applied. Middle column: E-plane when in-phase excitation is applied. Right column: H-plane when out-of-phase excitation is applied.

5.3 Tunable bandpass-to-bandstop filter design

Now that an antenna satisfying the requirements of pattern diversity and wideband performance has been obtained, the next step is to design a switchable and tunable filter with wide tuning range and sharp selectivity within the specified bandwidth of the antenna.

5.3.1 Tunable bandpass-to-bandstop filter layout and simulation

The tunable bandpass-to-bandstop filter design evolution is inspired by [142] and it is shown in Fig. 5.6. The conventional structure presented in [142] was exclusively operating in tunable bandpass state. A switchable and tunable bandstop state of operation is added to this design based on a new modification. The substrate used for

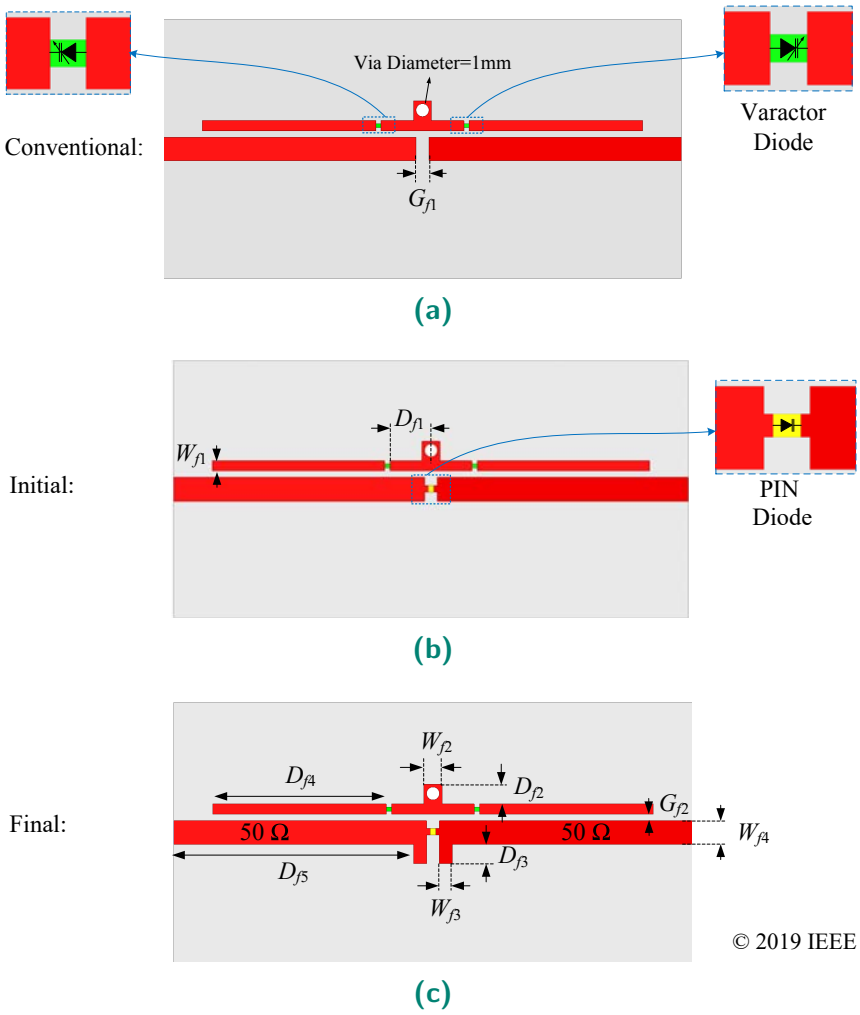

Figure 5.6. Evolution of bandpass-to-bandstop filter. (a) Modification of the bandpass filter presented in [142]. (b) Initial design of bandpass-to-bandstop filter. (c) Final design of bandpass-to-bandstop filter with improved performance.

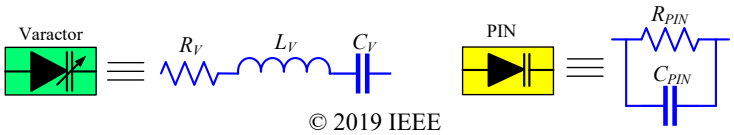

Figure 5.7. Varactor and PIN diodes equivalent circuits.

the filter is the same as the substrate used for the antenna. The dimensions of the filter are tabulated in Table 5.2. Based on Fig. 5.6a, the conventional bandpass filter is composed of a simple transmission line with 50 Ω characteristic impedance where a narrow gap is added in the center to block the direct path from input to output. To add the tunable filtering function, a narrow transmission line with two varactors and

Table 5.2. Parameters of the final design of tunable bandpass-to-bandstop filter

param.	value (mm)	param.	value (mm)	param.	value (mm)
W_{f1}	0.8	D_{f1}	3.2	D_{f5}	18.5
W_{f2}	1.4	D_{f2}	1.5	G_{f1}	1
W_{f3}	1	D_{f3}	1.5	G_{f2}	0.5
W_{f4}	1.8	D_{f4}	13.4		

a shorting via in its middle is tightly coupled to the 50 Ω transmission line. This coupled line with embedded varactors can provide a path for the input signal to reach the output at a selected frequency. This frequency can then be tuned based on the modification of varactor capacitance values. The filter shown in Fig. 5.6a is only capable of tuning frequencies in the bandpass state [142]. However, by taking advantage of the gap in the middle of the 50 Ω transmission line, the filter mode of operation can be reversed from bandpass to bandstop. As depicted in Fig. 5.6b, the PIN diode placed in the gap acts as a switch bridging the gap, thereby making a new direct path from the input to the output when it is switched ON and blocking the path as it is switched OFF. When the PIN diode is switched ON, the feed line provides an ultrawideband response; however the coupled line and the embedded varactors block the signals path from the input to the output at a certain frequency. This frequency can be tuned by varying the varactor diode capacitance, yielding a bandstop filter with tunable notch frequency. The bandstop filter response in this case has a strong pole at lower frequencies and a weak pole at higher frequencies, whereas two strong poles would be desirable for high selectivity and better functionality of the overall system when the antenna is fed by the filters. To resolve this problem and to further enhance the performance of the filter in its bandstop state, stronger poles are introduced at higher frequencies, using two shunt stubs attached to the connection point of the PIN diode as illustrated in Fig. 5.6c. Through this method the strong pole adjacent to the stopband at the lower frequencies is moderated and a stronger pole is introduced at higher frequencies providing a balance between the lower and higher out-of-band frequency responses. For simulations based on Ansys HFSS, the varactors and PIN diodes are modeled by their equivalent circuits, depicted in Fig. 5.7. The varactor diode has an internal series resistance R_V, capacitance C_V (which is equal to the combination of parasitic capacitance and junction capacitance of the diode), and a parasitic inductance L_V. The PIN diode can be modeled as a resistor R_{PIN} and a parallel capacitor named C_{PIN}.

The varactor diode used for this design is M/A-COM MA46H120 with R_V = 1.6 Ω, 0.15 pF < C_V < 1.3 pF, and L_V = 0.05 nH. The PIN diode is M/A-COM MA4FCP300 with equivalent R_{PIN} = 20 KΩ and C_{PIN} = 0.04 pF when the PIN diode is switched OFF and R_{PIN} = 4 Ω and C_{PIN} = 0 pF when the PIN diode is switched ON. Based on the equivalent circuit for varactor and PIN diodes, the different stages of the filter design have been simulated and the scattering parameters are illustrated in Fig. 5.8 for an arbitrarily chosen (representative) varactor capacitance value of C_V = 0.3 pF. From Fig. 5.8a, it is observed that while the parallel capacitance of the PIN diode can improve the filter selectivity, it degrades the out-of-band suppression level. However, the $|S_{21}|$ level is still below −12 dB at higher frequencies. Moreover, the bandpass performance remains the same by introducing the two shunt stubs. Similarly, the bandstop filter performance for initial and final designs is demonstrated in Fig. 5.8b. For the initial design, the value of $|S_{11}|$ above the stop frequency is unsatisfactory and would lead to the performance degradation when the filters feed the double-element antenna. This problem is alleviated in the final design with the addition of the two shunt stubs on either side of the the PIN diode. The scattering parameters of the final design of the bandpass-to-bandstop filter under different values of varactor capacitance is illustrated in Fig. 5.9. As seen in Fig. 5.9a, by changing the value of C_V from 1.3 pF to 0.15 pF the bandpass filter covers the frequency range of 3.37 GHz to 5.61 GHz, which corresponds to 49.9% relative range. The highest insertion loss of 2.7 dB appears at the lowest tuning frequency and it is mainly attributed to the series resistance of the varactor diodes. The return loss values are all higher than 15 dB with two adjacent transmission poles and a nearly fixed bandwidth of 180 MHz over the whole tuning range. The filter selectivity at all frequencies is high since the adjacent transmission zeros are also tuned when the varactor capacitance values are changing. This is contrary to the designs presented in [93] and [124], where the transmission zeros were fixed, thus deteriorating the selectivity of the design in bandpass state. The bandstop filter scattering parameters with C_V changing from 1.3 pF to 0.15 pF are shown in Fig. 5.9b. The corresponding tuning frequency range is from 3.31 GHz to 5.53 GHz, which corresponds to a relative range of 50.2%. The minimum return loss and stopband insertion loss are respectively 3 dB and 13 dB at the lowest frequency. However, these values improve with the increase in the operating frequency. This phenomenon is attributed to the PIN diode resistance in ON state and the varactors series resistances having stronger effects at lower frequencies. It is seen that the bandstop frequencies

for a given varactor capacitance are almost the same as the bandpass frequencies with roughly 70 MHz offset towards lower frequencies.

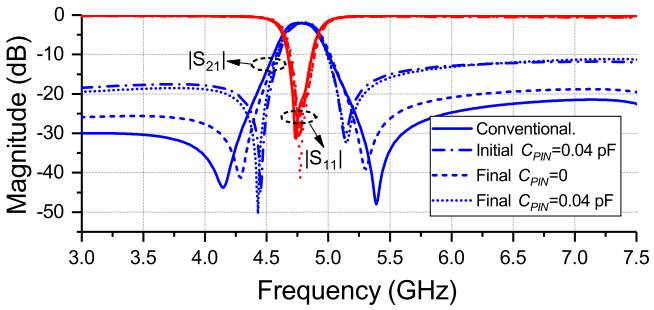

(a)

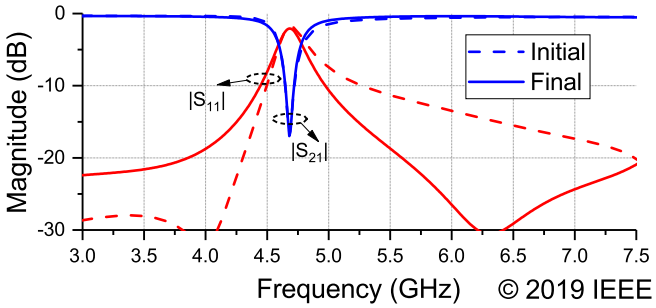

(b)

Figure 5.8. Filter response for $C_V = 0.3$ pF. (a) Bandpass response for three different cases of circuit evolution. (b) Bandstop response for two last cases of circuit evolution.

5.3.2 Equivalent LC model for the tunable bandpass-to-bandstop filter

In order to analyze the proposed bandpass-to-bandstop filter, its LC equivalent circuit is provided in Fig. 5.10a with varactor and PIN diodes equivalent models in blue, coupling capacitors in red, and transmission line models in black. Advanced Design System (ADS) is used to simulate the behavior of the proposed LC model. In the equivalent circuit, a model of asymmetric coupled line in ADS is used for the long coupled transmission line connected to the input and output ports with the length of D_{f4}. The reason behind this choice is that the coupled-line section would need to be broken down into LC equivalent circuit with a prohibitively high number of cascaded

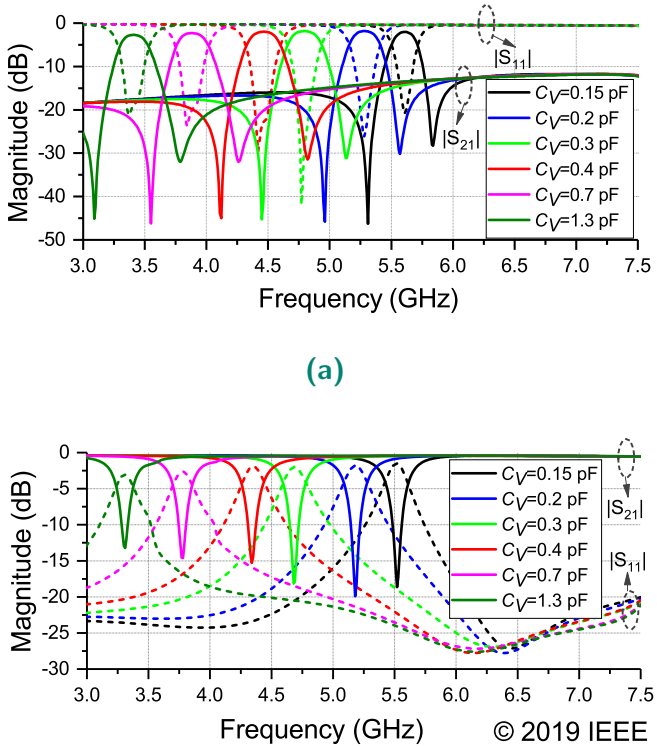

Figure 5.9. Frequency response of the final design of the bandpass-to-bandstop filter under different varactor capacitance values. (a) Bandpass response when the PIN diode is OFF and the varactor capacitance values are changing from 0.15 pF to 1.3 pF. (b) Bandstop response when the PIN diode is ON and the varactor capacitance values are changing from 0.15 pF to 1.3 pF.

infinitesimal elements for sufficient accuracy. This model is however readily available in the library of ADS, which adds simplicity to the structure and analysis of the equivalent circuit. The capacitance C_{g1} denotes the coupling capacitance for the gaps in which the varactor diodes are placed. The coupled line segment with the length of $D_{f1} - W_{f3} - G_{f1}/2$ is modeled by L_1, L_2, and the two coupling capacitances C_{g2} on either side of L_1 and L_2. The inductance L_3 is the equivalent model for a small section of the high-impedance transmission line with the width of W_{f1} that is capacitively coupled to the bend connecting the open-ended stub to the 50 Ω transmission line. This bend is described in the equivalent circuit by the T model of the L_{bend} inductances and the C_{bend} capacitance. The capacitance of C_{g2} on the right side of L_{bend} and L_3 accounts for the aforementioned coupling between the high-impedance transmission line and the bend. The open-ended stubs with the width of W_{f3} are modeled by the equivalent capacitances of C_{oc} and the small coupling between these open-ended stubs is modeled

by C_{g3}. The T-section in the middle of the high-impedance transmission line is modeled by L_T, whereas the short-ended stub with the length of D_{f2} is modeled together with the shorting vias by L_{sc}. The values of the lumped elements for the filter are calculated based on the method provided in [143] and [144] as follows (C: pF, L: nH, R: Ω): $L_1 = 0.75$, $L_2 = 0.45$, $L_3 = 0.45$, $L_{bend} = 0.14$, $L_T = 0.4$, $L_{sc} = 0.25$, $L_V = 0.05$, $C_{g1} = 0.015$, $C_{g2} = 0.02$, $C_{g3} = 0.01$, $C_{bend} = 0.1$, $C_{oc} = 0.11$, and $R_V = 1.6$. For the bandpass state of operation $C_{PIN} = 0.04$ pF and $R_{PIN} = 20{,}000$ Ω. Based on these values, the scattering parameters are shown for three different varactor capacitances and they are compared with the full-wave electromagnetic (EM) simulation results in Fig. 5.10b and Fig. 5.10c. The passband frequency can be tuned by altering the varactor capacitance of C_V from 1.3 pF to 0.15 pF. The corresponding center frequency of the LC model of this filter in the bandpass state varies from 3.4 GHz to 5.67 GHz. For the bandstop state of operation, the PIN diode is switched on which means that $R_{PIN} = 4$ Ω and $C_{PIN} = 0$ pF. The EM and LC circuit simulation results are shown in Fig. 5.10d and Fig. 5.10e with the EM simulation scattering parameters analogous to the LC counterpart. By changing C_V from 1.3 pF to 0.15 pF, the location of the transmission zero produced by LC model of the bandstop filter can be tuned continuously from 3.3 GHz to 5.60 GHz. An acceptable similarity between the LC circuit model and EM simulation demonstrates the accuracy of the calculations and the appropriateness of the equivalent circuit model for the bandpass and bandstop states.

5.4 Design of frequency tunable system with sum and difference radiation patterns

The frequency tunable antenna system with sum and difference radiation patterns can be attained by integrating the bandpass-to-bandstop filter to the double-element antenna and exciting the whole structure using a commercially available wideband 180° hybrid coupler. The final geometry of the tunable system with biasing circuit for the filters is illustrated in Fig. 5.11. As seen, there are four bias lines for controlling the varactor diodes with the single voltage denoted as V_{var}. The via in the middle of the narrow coupled lines can serve as the path to the DC ground which is the bottom metal plane. The PIN diodes are also biased by a single voltage denoted as V_{PIN}. The 50 Ω lines connected to the input ports are connected to the bottom plane through metallic vias and choke inductors, and thus they can serve as the DC grounds for the PIN

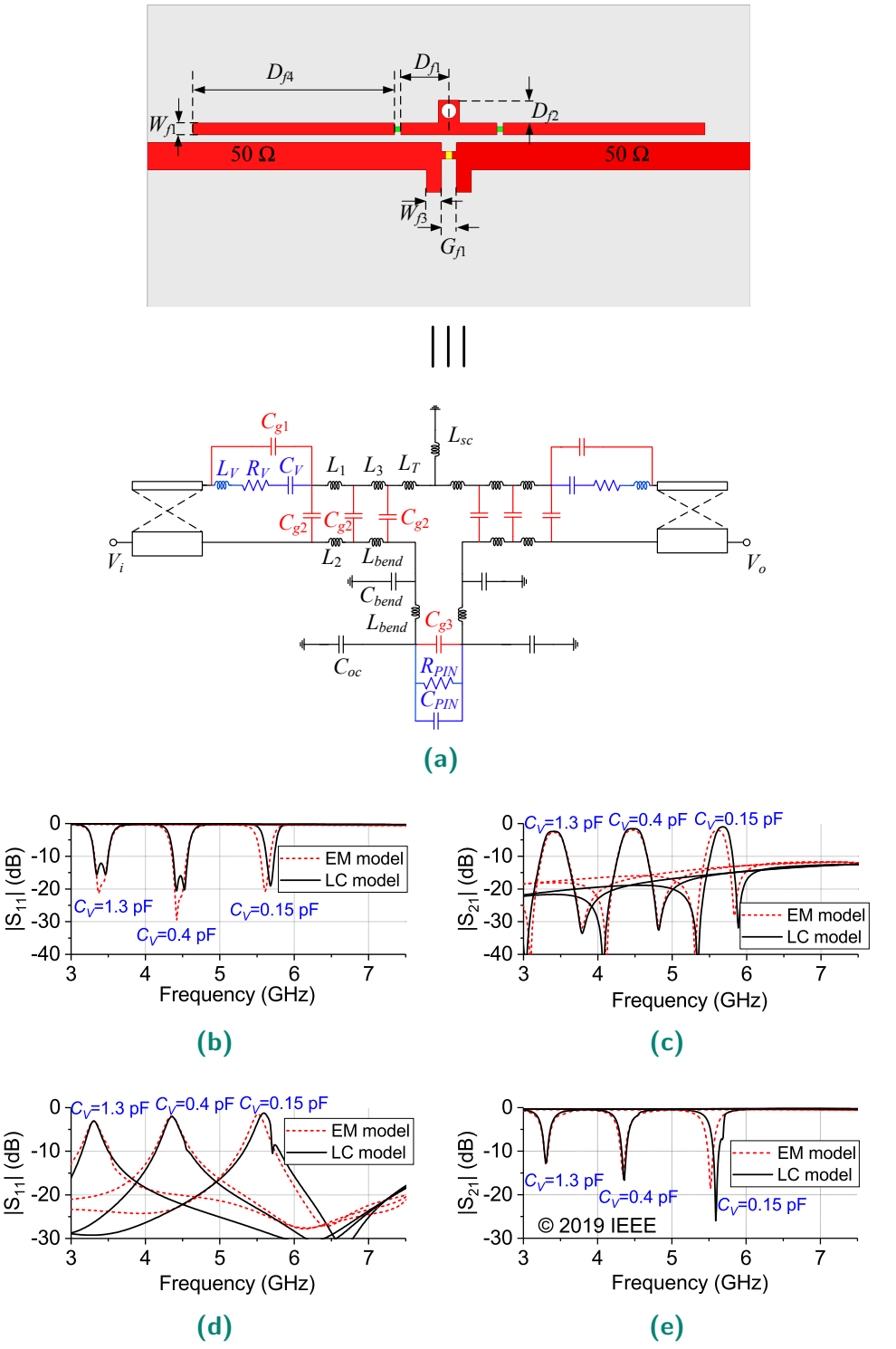

Figure 5.10. (a) LC equivalent circuit of the proposed filter. (b) Bandpass state: comparison of the input reflection coefficient for EM and LC circuit models. (c) Bandpass state: comparison of the transmission coefficient for EM and LC circuit models. (d) Bandstop state: comparison of the input reflection coefficient for EM and LC circuit models. (e) Bandstop state: comparison of the transmission coefficient for EM and LC circuit models.

diodes. There is no need for DC block capacitor in this design due to two reasons. First, the varactor diodes are placed on the narrow coupled line with no DC path to combine with RF signal. Second, the part of the 50 Ω transmission line connected to the input port serves as the DC ground, thereby again preventing any combination of DC and RF signal. In order to choke the RF signal, surface mount inductors with inductance of 24 nH and self-resonance frequency of 3.5 GHz along with high impedance transmission lines are used.

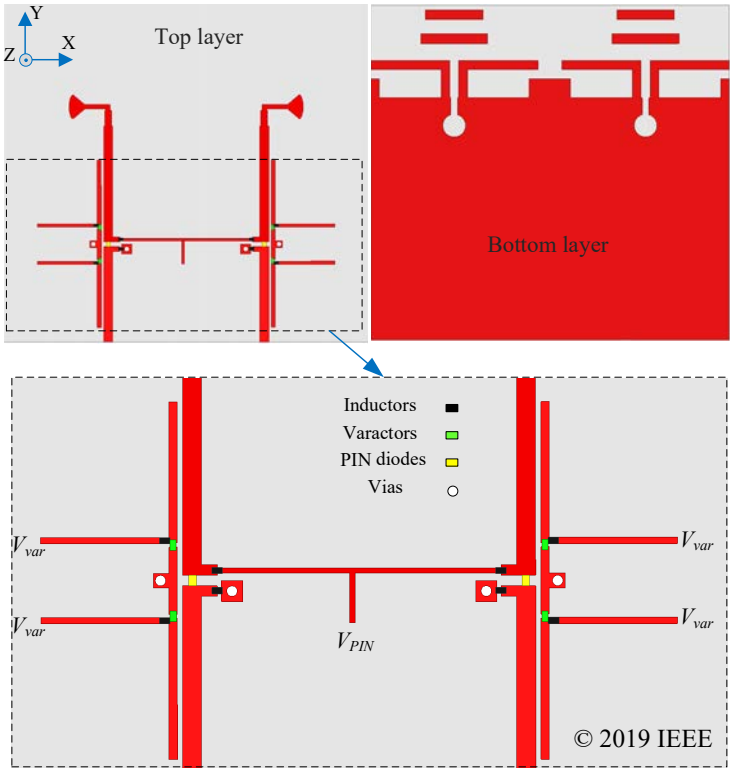

Figure 5.11. Configuration of the proposed antenna system with the biasing network.

5.5 Experimental results

In this section, the simulation and measurement results of the bandpass-to-bandstop system are expounded. A prototype of the two-element antenna with integrated reconfigurable filters has been fabricated and is shown with a connected wideband coupler [109] in Fig. 5.12. The overall system dimensions excluding the wideband coupler are $W \times L \times H = 75 \times 70 \times 0.8128$ mm^3. Accordingly, the planar electrical length in terms of wavelength at the lowest working frequency of the antenna is $0.75\lambda_0 \times 0.7\lambda_0$.

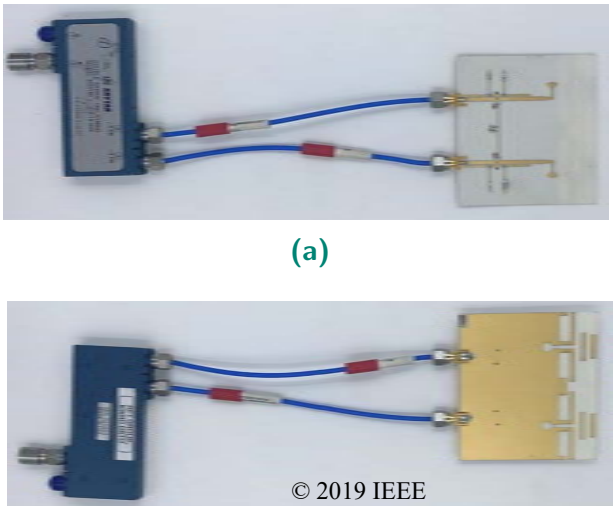

(a)

(b)

Figure 5.12. Photograph of the fabricated design connected to the wideband hybrid coupler (a) Top layer. (b) Bottom layer.

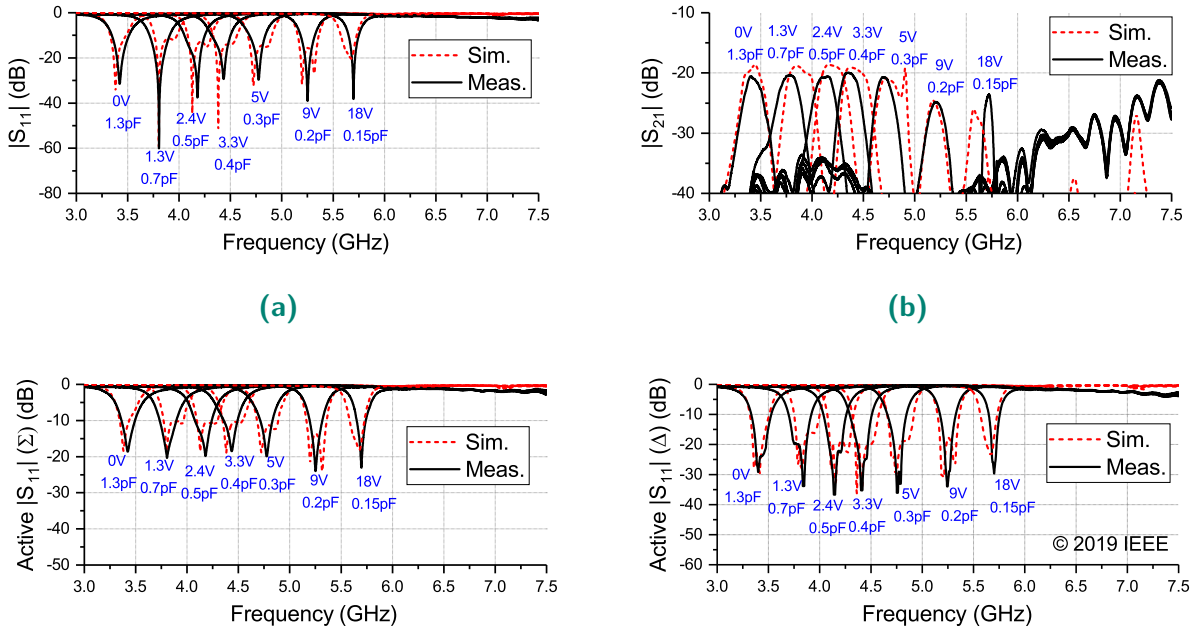

(a)

(b)

(c)

(d)

Figure 5.13. Measured versus simulated scattering parameters of the bandpass antenna system with different values for varactor capacitances and voltages. (a) $|S_{11}|$. (b) $|S_{21}|$. (c) Active $|S_{11}|$ for the case when the Σ port of the coupler is excited. (d) Active $|S_{11}|$ for the case when the Δ port of the coupler is excited.

The measured and simulated scattering parameters at the input ports of the antenna as well as at the input ports of the coupler for the bandpass mode of operation are illustrated in Fig. 5.13. In this case, the PIN diodes are OFF with no voltage applied to them and the varactor capacitances (bias voltages) are varying from 0.15 pF (18 V) to 1.3 pF (0 V). It is observed that the whole system takes on the characteristics of the bandpass filter, with the simulated (measured) return loss higher than 10 dB for the tuning range of 3.38 GHz to 5.67 GHz (3.42 GHz to 5.70 GHz), corresponding to the fractional bandwidth of 50.6% (50.0%). The simulated (measured) coupling between the elements is below -18 dB (-20 dB) for the whole range. The active $|S_{11}|$ is the combination of S_{11} and S_{21} in the simulation results and corresponds to the experimental results at the input ports of the coupler. As seen, the bandpass filtering response is maintained in the presence of the coupler in both simulation and measurement results. To activate the bandstop mode of operation, the PIN diodes are switched ON by applying 1.0 V across them and thereafter the notch frequency is tuned by altering the varactors bias voltages. The measured and simulated scattering parameters at the input ports of the antenna are illustrated in Fig. 5.14 where the VSWR plot is shown to emphasize the bandstop performance over the whole tuning range. It is noted that the filter has no adverse effect on the antenna frequency response for out-of-band results and the whole system takes on the characteristics of the bandstop filter. The simulated (measured) notch frequency VSWR varies from 5.6 to 9.4 (4.7 to 7.1) over the tuning range of 3.31 GHz to 5.51 GHz (3.34 GHz to 5.59 GHz) corresponding to a fractional bandwidth of 49.9% (50.4%). The simulated (measured) mutual coupling between the two input ports is similar to the double-element antenna mutual coupling shown in Fig. 5.4a, except that it decreases to lower than -40 dB (-32 dB) at the notch frequencies.

The active VSWR is the combination of S_{11} and S_{21} converted to VSWR in the simulation results, which corresponds to the experimental results at the input ports of the coupler. The simulation and measurement results indicate the bandstop functionality in the presence of the coupler.

The antenna total efficiencies for the two states of operation are illustrated in Fig. 5.15. The in-band total efficiency of the antenna in bandpass state is varying from 60% at the lowest frequency to 78% at the highest frequency, whereas the out-of-band total efficiency is lower than 12%. The in-band total efficiency of the antenna in bandstop state is lower than 15% across the tuning range, whereas the out-of-band total efficiency is

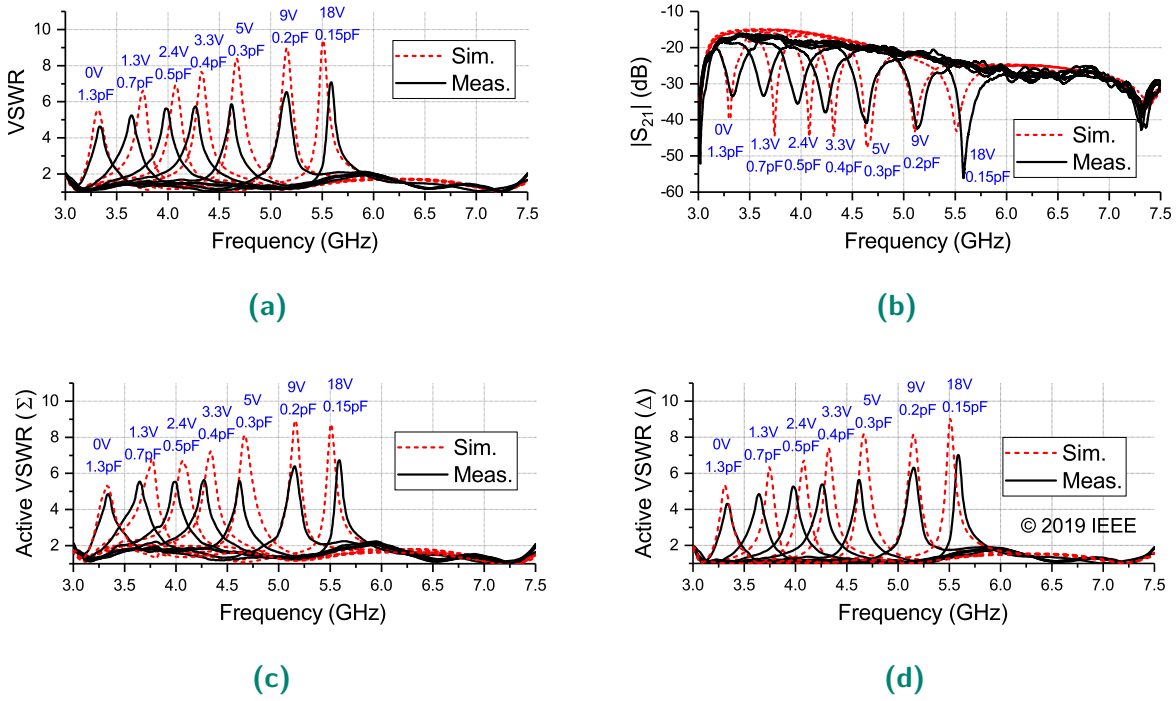

Figure 5.14. Measured versus simulated scattering parameters of the bandstop antenna system with different values for varactor capacitances and voltages. (a) VSWR (for better visibility of the band notch). (b) $|S_{21}|$ (c) Active VSWR for the case when the Σ port of the coupler is excited. (d) Active VSWR for the case when the Δ port of the coupler is excited.

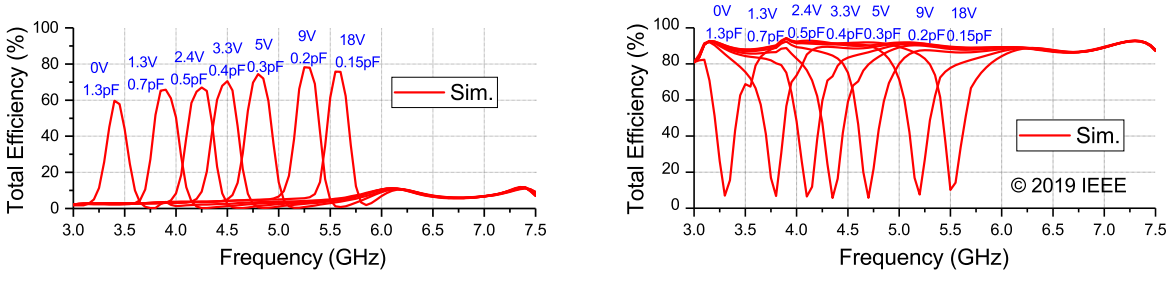

Figure 5.15. Simulated total efficiency for the bandpass and bandstop states of operation under different varactor capacitance. (a) Bandpass state. (b) Bandstop state.

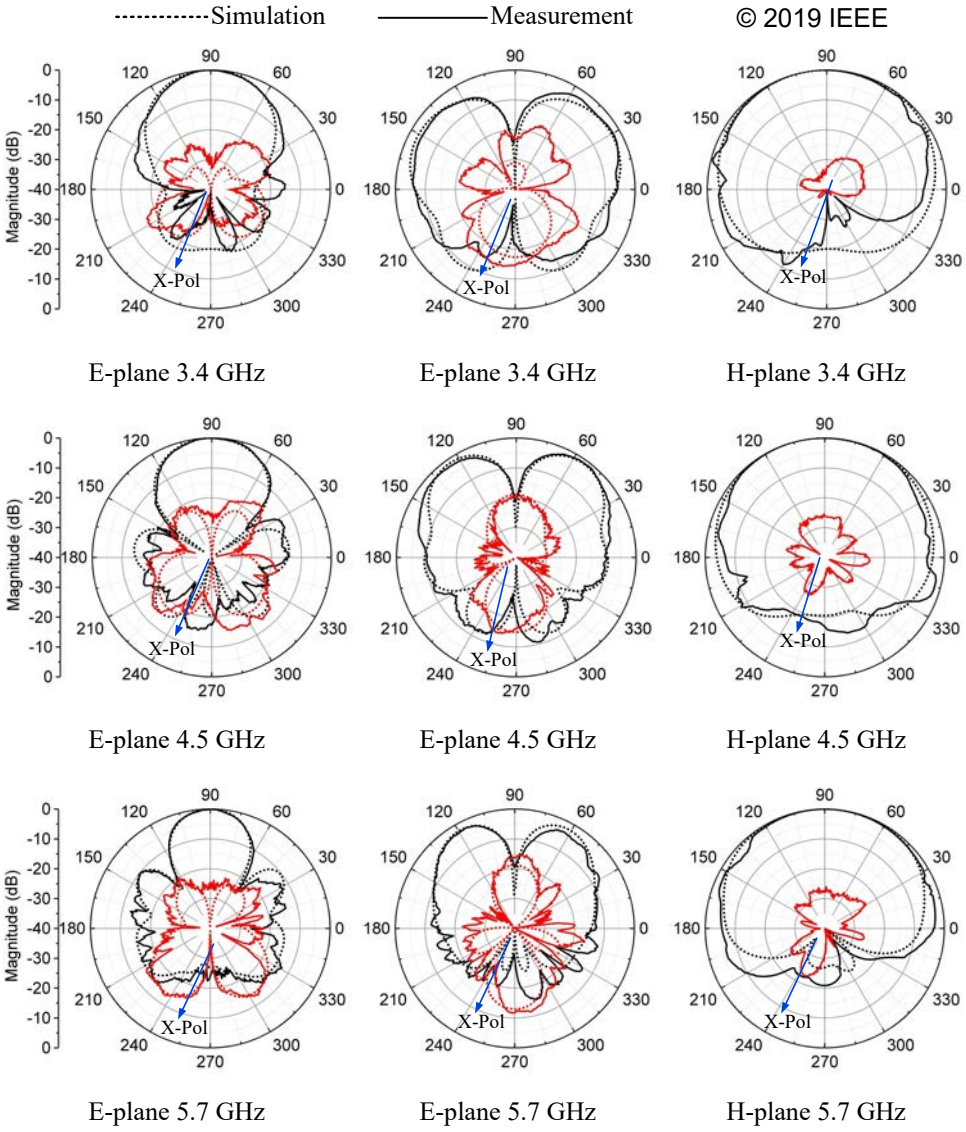

Figure 5.16. Measured versus simulated normalized realized gain patterns for the bandpass system at in-band frequencies. Left column: E-plane when difference (Δ) port of the coupler is excited. Middle column: E-plane when sum (Σ) port of the coupler is excited. Right column: H-plane when difference (Δ) port of the coupler is excited.

above 80%. The measured and simulated normalized radiation patterns under out-of-phase and in-phase input excitations are shown in Fig. 5.16 for the bandpass system operation and in Fig. 5.17 for the bandstop operation. Three sets of normalized radiation patterns when the capacitance of varactors are 1.3 pF (0 V), 0.4 pF (3.3 V), and 0.15 pF (18 V) are shown in Fig. 5.16 for the corresponding bandpass frequencies of 3.4 GHz, 4.5 GHz, and 5.7 GHz, respectively. For the bandstop state, three representative out-of-band frequencies of 3 GHz, 6 GHz, and 7.5 GHz are selected and compared with the simulated results in Fig. 5.17. As observed, the radiation patterns for

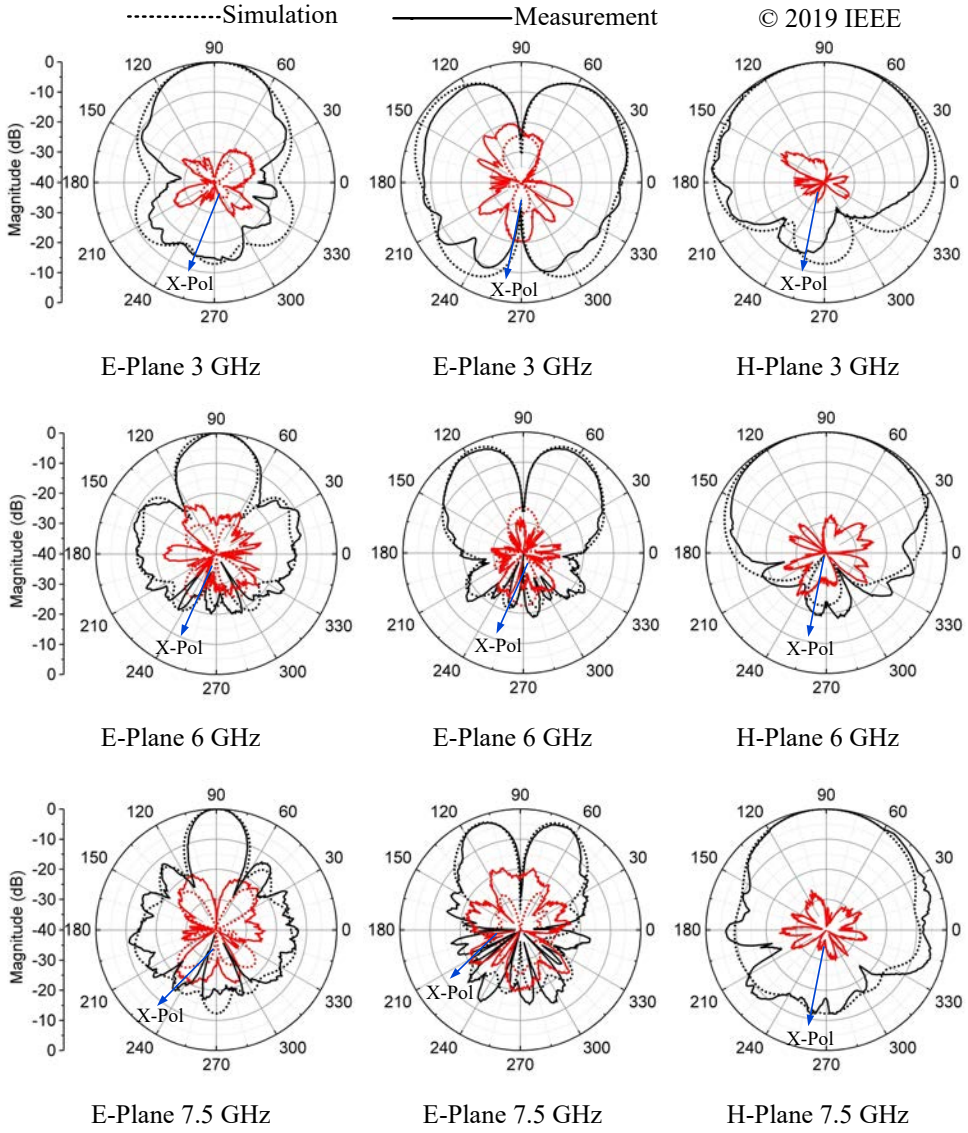

Figure 5.17. Measured versus simulated normalized realized gain patterns for the bandstop system at out-of-band frequencies. Left column: E-plane when difference (Δ) port of the coupler is excited. Middle column: E-plane when sum (Σ) port of the coupler is excited. Right column: H-plane when difference (Δ) port of the coupler is excited.

both bandpass and bandstop operation states are the same as the radiation patterns for the wideband double-element antenna. This indicates that the introduction of the filters has no adverse effects on the radiation patterns, except that the cross-polarization value is slightly increased. For the simulated H-plane patterns in both bandpass and bandstop cases, the cross-polarization is not visible within the defined dynamic range. The measured and simulated maximum realized gain versus frequency plots for the bandpass and bandstop states are shown in Fig. 5.18 for the case when the system is

excited by out-of-phase signals. In the bandpass state, shown in Fig. 5.18a, the simulated (measured) results indicate that the two strong transmission zeros of the input filter that are adjacent to the passband frequencies provide high selectivity and reduce the out-of-band gain. The in-band maximum realized gain varies from 4.1 dBi (3.3 dBi) when the capacitance of the varactors is 1.3 pF (0 V) to 7.5 dBi (6.9 dBi) when the capacitance of the varactors is 0.15 pF (18 V). The difference between the maximum gain of the double-element antenna and the bandpass antenna system is attributed to the insertion loss of the filter that is mainly due to the varactors series resistances. In the bandstop case, illustrated in Fig. 5.18b, the whole system is working on its wideband state and the gain is reduced at the selected notch frequencies. Based on the simulated (measured) results, the difference between the realized gain of the wideband double-element antenna and the realized gain of the stopband system at the notch frequencies is roughly 12 dBi (10 dBi), justifying the sound functionality of the stopband case. The simulated (measured) out-of-band maximum realized gain of the bandstop case varies from 5.2 dBi (5.5 dBi) to 10.0 dBi (9.1 dBi). The out-of-band realized gain for the bandstop state is slightly lower than the realized gain for the isolated double-element antenna without the filters. The gain drop can be attributed to the internal series resistance of the PIN diodes when they are forward biased. A comprehensive comparison with recently published papers is difficult since the various proposed systems have different functionalities. Nevertheless, Table 5.3 summarizes the most important features of selected published work in the same area for comparison with this work. For better consistency, the available simulated results of the filters for all references are included in the last four columns. It is noted that the relatively large area of the proposed structure is inherently due to the fact that two antenna elements are required for producing sum and difference radiation patterns. Overall, the presented design has the highest value of roll-off rate meaning that the bandpass response is far more selective than achieved in all other references. The main reason for the high selectivity is the presence of two transmission zeros adjacent to the passband. The performance stability is due to the fact that these zeros are being tuned when varying varactors capacitance. This is contrary to [124] where the two transmission zeros are in fixed position deteriorating the selectivity for some frequencies. In comparison with the only reference generating reconfigurable sum and difference radiation patterns [133], the proposed system has much smaller substrate area. In terms of the mode of operation, besides the proposed design, the design in [94] can generate bandpass-to-bandstop mode of

operation with 57.0% tunability in each case, albeit with a fixed omnidirectional radiation pattern, a low selectivity, and low out-of-band suppression in the bandpass case. Hence, the proposed design can successfully implement a sharply defined bandpass-to-bandstop tunable system with continuous tuning range of 50.0% in bandpass and 50.4% in bandstop states, while at the same time it can generate sum and difference radiation patterns by out-of-phase and in-phase input excitation, respectively.

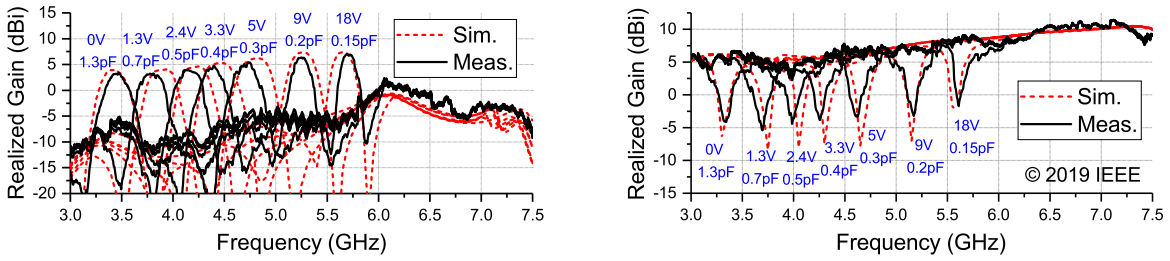

(a) (b)

Figure 5.18. Measured versus simulated realized gain for different values of varactor capacitance values. (a) Bandpass state. (b) Bandstop state.

5.6 Conclusion

A design of a frequency-tunable switchable bandpass-to-bandstop quasi Yagi-Uda antenna system with the ability of producing sum and difference radiation patterns at different states of operation has been proposed and experimentally validated in this work. The system comprises three fundamental parts including:

1. A double-element E-plane quasi Yagi-Uda antenna with the ability to produce sum and difference radiation patterns with high beam symmetry.

2. An integrated tunable bandpass-to-bandstop filter with selective response having minimum roll-off rate of 57 dB/GHz and <-12 dB of out-of-band $|S_{21}|$ for the bandpass state and strong notch <-13 dB with out-of-band poles >-1 dB for bandstop state, with consistent performance extending over the whole tuning range.

3. A commercially available wideband rat-race coupler to excite the input ports and generate the sum and difference radiation patterns.

Table 5.3. Comparison of the proposed bandpass-to-bandstop system with some recently published antennas featuring tunable filtering response.

Refs.	ε_r	Size $(\lambda_0)^2$	Mode of Operation	D/C	Patterns	Tuning Range	RO (dB/GHz)	Out-of-Band BP $\lvert S_{21}\rvert$	In-Band BS $\lvert S_{21}\rvert$	No. of BP TZs
[93]	2.2	0.72×0.30	wideband-to-bandpass	C	omnidirectional	21.0%	17.0	-20 dB	--	0
[122]	4.4	0.3×0.27	wideband-to-bandpass	D	omnidirectional	--	N/A	-2 dB	--	1
[123]	4.4	0.27×0.25	wideband-to-bandpass	D	omnidirectional	--	N/A	-2 dB	--	1
[124]	3.48	0.4×0.23	wideband-to-bandpass	C	omnidirectional	36.0%	11.33	-12 dB	--	2
[127]	2.33	0.5×0.3	wideband-to-narrowband	D	unidirectional	--	no filtering	no filtering	no filtering	--
[128]	3.48	0.4×0.36	wideband-to-narrowband	C	omnidirectional	18.0%	no filtering	no filtering	no filtering	--
[132]	2.22	0.68×0.45	bandpass	C	monopole pattern diversity	5.0%	40.0	-20 dB	--	1
[133]	2.2	2.0×2.0	narrowband	--	reconfigurable sum and difference	--	no filtering	no filtering	no filtering	--
[94]*	2.2	0.42×0.30	bandpass*-to-bandstop	C	omnidirectional	BP*: 57.0% BS: 57.0%	N/A	-5 dB	-13 dB	1
This work	3.38	0.75×0.7	bandpass-to-bandstop	C	sum and difference	BP: 50.0% BS: 50.4%	57.0	-12 dB	-13 dB	2

D/C: Discrete/Continuous

BP: Bandpass

BS: Bandstop

RO: Roll-Off Rate $= \left|\frac{(-20dB)-(-3dB)}{f_{(-20dB)}-f_{(-3dB)}}\right|$

N/A: Not Applicable ($|S_{21}|$ does not reach -20 dB and thus roll-off rate cannot be measured based on -20 dB points)

TZ: Transmission Zero

* No experimental validation for bandpass case is provided in this reference.

The experimental validation of this design for bandpass and bandstop states of operation shows a unique combination of features over the existing references. Hence, the proposed design can be a favorable candidate for bandpass-to-bandstop cognitive radio systems with pattern diversity requirements.

Chapter 6

Sum and Difference Pattern-Reconfigurable Antennas

PATTERN-reconfigurable antennas use switches or tunable lumped components in their resonance structures to change their radiation patterns, thereby reducing the overall size and complexity compared to other types of pattern diversity antennas. In Chapter 5, an antenna system with two operation states of tunable bandpass and tunable bandstop was realized and tested. However, there were two drawbacks which were, firstly the lack of a wideband state of operation used to scan a frequency spectrum and detect unused bands in cognitive radio systems, and secondly the requirement for an external coupler for input excitation.

In the first part of this chapter, the mentioned drawbacks are addressed by realizing all the three different frequency states of cognitive radio systems in a single structure. This is achieved through combining and integrating a wideband antenna structure with a filter featuring multiple-state frequency agility. Importantly, an allpass state of operation is added to the filter structure formerly presented in Chapter 5. Furthermore, sum and difference patterns are obtained by using a triple-element antenna array with in-built phase inversion method fed by a PIN diode switchable power divider. In the second part of this chapter, a concept of patch antenna with sum and difference pattern diversity in its E- and H-plane is proposed. Extension of sum and difference pattern diversity to both E- and H-plane conventionally requires three input couplers which increases cost and complexity of the antenna system. However, the use of PIN switches in a patch antenna structure enables the simplification of the overall structure and reduces the requirement to a single input coupler to achieve four beam switching functions.

6.1 Introduction

SPECTRUM scarcity due to the exhaustive utilization of available frequency bands by licensed users motivates the development of reconfigurable antennas for cognitive radio systems. Various antennas with frequency agility [56, 145–148], pattern reconfigurability [87, 149–151], polarization reconfigurability [152–155] and combinations of these modalities [40, 43, 86, 156–158] have been proposed recently to accommodate this need. According to [47], three states of operation are required to observe and react to the spectrum utilization in cognitive radio systems. First, a wideband state, which is used to scan the frequency spectrum for finding unoccupied frequencies. Second, a tunable narrowband state to allocate an idle frequency to a primary user. Third, a tunable notch-band state to allocate a wideband spectrum to a secondary user without any interference with the already occupied frequency band. For hardware implementation, a number of wideband to discretely tunable narrowband [123, 125, 126, 159], as well as wideband to continuously tunable narrowband antenna structures [93, 124, 127, 128, 160] have been presented. More recently, some tunable bandpass-to-bandstop antennas have been proposed in [53, 94]. However, an essential functionality of cognitive radio systems, namely the wideband operation state was missing in these realizations. To the best of the authors' knowledge, no system implementing all these three operation states in a single reconfigurable structure has hitherto been reported.

Pattern diversity is also a useful feature for cognitive radio systems for wider space signal coverage and multipath fading mitigation. To meet this requirement, dual-input antennas with sum and difference pattern diversity have widely been explored in [10, 11,48,53,130]. In these studies, the use of a microwave comparator generating in-phase and out-of-phase input signals was inevitable, leading to a relatively high complexity of the overall system. As an alternative, aiming at lowering the complexity, the design presented in [133] employed a planar structure with electrically switchable sum and difference patterns for narrowband operation and circular polarization. A wider band design was presented in [85], where sum and difference patterns were switched using a phase-inversion feeding network in a three dimensional structure.

In the first part of this chapter, we are aiming at realizing three different frequency states of cognitive radio systems combined with a low complexity pattern diversity function in a single antenna system. To this end, a switchable and tunable filter is

integrated with a switchable three-output power divider and a triple-element quasi-Yagi-Uda antenna with in-built phase inverter, as shown in Fig. 6.1. The filter generates three different states of switchable allpass to tunable bandpass and tunable bandstop functionalities. The switchable power divider excites two antenna elements at a time and keeps the third element inactive. When the input signal is split into the leftmost output branches of the power divider, a sum directive radiation pattern is generated. In contrast, a difference beam radiation pattern with a null in its boresight direction is generated when the input signal is split into the two rightmost output ports of the power divider. The 3D models of the two different beams are illustrated in Fig. 6.2a and Fig. 6.2b. Contrary to the reported designs in the open literature, there is no need for a microwave comparator and external phase inverter to generate the sum and difference radiation patterns. The only drawback of that simpler arrangement is that the two radiation pattern functionalities are achieved sequentially. There are four distinct novel aspects to this design which improve the response over the design presented in Chapter 5 [53]. They include:

1. The allpass state of operation has been added to our previously published filter in Chapter 5. This means that the enhanced filter features an allpass state which can be switched to a bandpass state and to a bandstop state, both with tunable operating frequencies.

2. Switchable sum and difference radiation patterns are realized by exploiting in-built phase inversion function in the mirror arrangement of the rightmost antenna feeding structure. This sequential pattern switching is in contrast to our presented design in Chapter 5 where a double-input antenna and an external coupler were used to generate simultaneous sum and difference pattern diversity.

3. A unique combination of functionalities in a single antenna system is demonstrated, including the switchable generation of sum and difference patterns over 79.8% bandwidth, 51.3% bandpass tuning range, and 50.3% bandstop tuning range.

4. Compared to the design in Chapter 5, this structure eliminates the requirement for a prohibitive external coupler and facilitates the integration of a single filter structure as opposed to two filters necessary in Chapter 5, thereby reducing

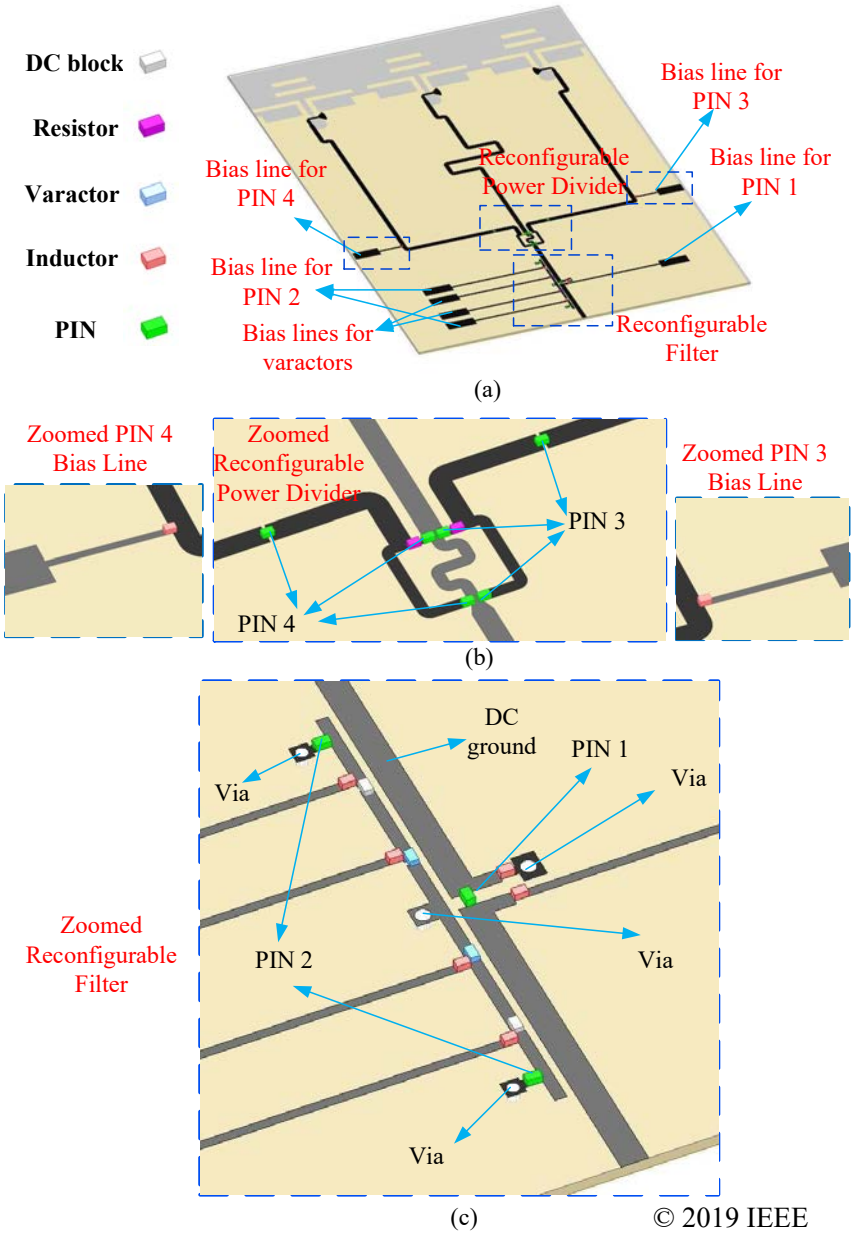

Figure 6.1. (a) Proposed antenna system structure. (b) Magnified reconfigurable power divider section in conjunctions with bias lines for its PIN diodes. (c) Magnified reconfigurable filter.

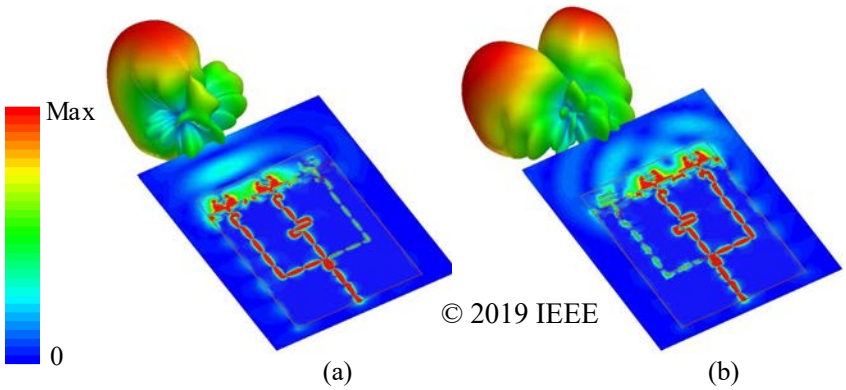

Figure 6.2. Instantaneous E-field distribution and generated radiation pattern for (a) the sum beam configuration, and (b) the difference beam configuration.

the cost and complexity of the overall system while offering additional states of reconfigurability.

In the second section of this chapter, an arrangement of patch antennas with switchable beams in E- and H-plane is proposed. Using PIN switches, the two fundamental TM01 and TM02 modes of a patch antenna are exploited in a single reconfigurable radiating element to selectively generate sum and difference radiation patterns along the E-plane of the antenna. Based on this single element, a double-element antenna along the H-plane is developed to extend the functionality in a second dimension. To this end, the two elements are fed by in-phase and out-of-phase inputs to enhance the pattern diversity functions so that the sum and difference beams can be generated along both E- and H-plane. Similar performance has been developed in the past using four hybrid couplers feeding a 4×4 antenna elements [161]. Therefore, the proposed design can reduce the complexity and cost of manufacturing in applications where sequential use of the modes is acceptable.

6.2 Pattern-reconfigurable antenna with multi-state filtering function design

A three-dimensional view of the antenna system is illustrated in Fig. 6.1a, comprising a triple-element antenna, a reconfigurable power divider (magnified in Fig. 6.1b) and a reconfigurable filter (magnified in Fig. 6.1c). The antenna elements excited by the power divider will enable pattern diversity over a wideband frequency, while feeding

this structure by the switchable and tunable filter helps generate three states of wideband, tunable bandpass and tunable bandstop operation. Hence, the combination of these three circuits brings about a unique functionality that has not been reported in the open literature thus far. All the required lumped components and bias lines are included in these representations. The PIN diodes are all MACOM MA4FCP300 diodes with an equivalent OFF state simulation model of 20 KΩ resistance and 0.04 pF shunt capacitance, while the ON state simulation model is purely resistive with 4 Ω resistance. The varactor diodes in this design are MACOM MA46H120 with a simulation equivalent model of a varying capacitance from 0.15 pF to 1.30 pF connected to a series resistance of 1.6 Ω and a series inductance of 0.05 nH. The resistors are 0402 surface mount resistors with 100 Ω resistance. The used RF choke inductors are Murata LQW15AN15NG00 with 15 nH inductance, and the utilized DC block capacitor models are GRM0332C1H100JA01 with 10 pF capacitance. All the constituents of the antenna system described in this section are integrated and printed on a Rogers RO4003C substrate with a relative permittivity of 3.38, loss tangent of 0.0027, and thickness of 0.8128 mm. The next three subsections elaborate on the building blocks of this antenna system and their simulated functionalities. All the simulations are conducted using HFSS in Ansys Electronics Desktop software.

6.2.1 Triple-element antenna

The quasi-Yagi-Uda antenna structure in [34] is adopted as individual antenna element with some modifications in the feeding lines and the operating frequency. The structure presented in [34] is an ultrawideband and compact quasi-Yagi-Uda antenna element which is an ideal choice for developing arrays of several elements. This is because the compact size of the antenna in terms of wavelength allow a sufficiently close packing of the elements, which prevents the appearance of grating lobes at higher frequencies, while the remaining separation between the antenna elements keeps the mutual coupling to an acceptable level. The triple-element quasi-Yagi-Uda antenna configuration (without the reconfigurable power divider and the reconfigurable filter) is shown in Fig. 6.3a with the annotated dimensions tabulated in Table 6.1. The middle transmission line feed for the central element is meandered to have the same electrical length as the lateral feeding transmission lines. Importantly, for the pattern reconfiguration, the rightmost feeding line is mirrored with respect to the other two feeding lines to generate an intrinsic and frequency independent 180° phase difference between

the middle and rightmost antenna elements. Although the fundamental antenna elements are the same as in the design presented in Chapter 5, three antenna elements are required to enable additional functionality in this chapter, as opposed to the two antenna elements excited by an external coupler in Chapter 5. The third antenna element is used to facilitate pattern switchability and obviate the need for lossy and expensive external coupler by providing inherent and frequency-independent phase inversion. The working principle of this antenna system is illustrated in Fig. 6.3b where it can be

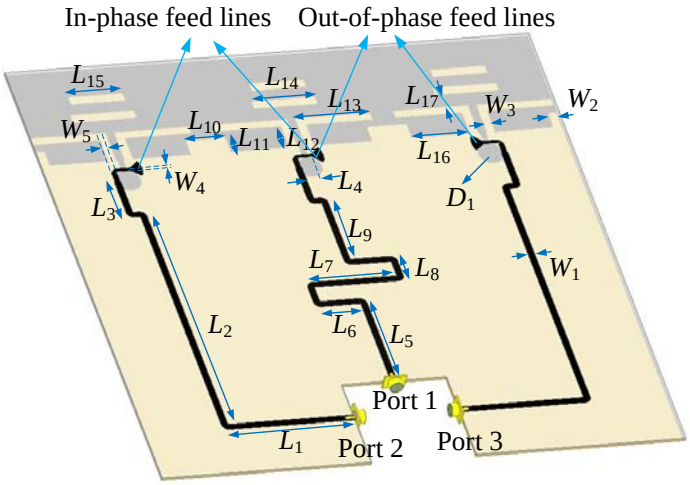

(a)

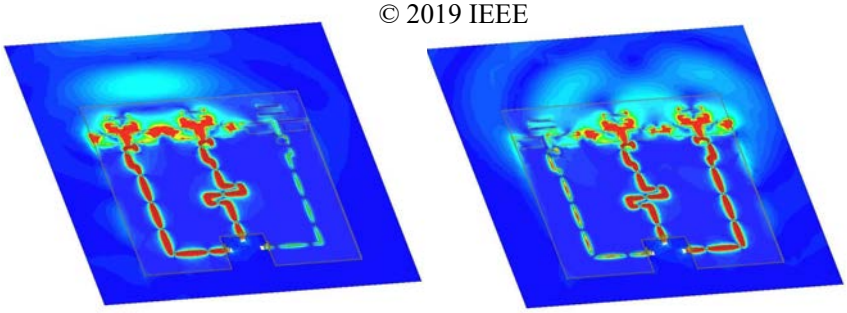

(b)

Figure 6.3. Proposed three-element antenna structure. (a) 3D view with in-built in-phase and out-of-phase feed lines and related dimensions. (b) Instantaneous E-field distribution when two ports are excited and one port is inactive.

observed that only two elements are contributing to the radiation at a particular time, with the third element remaining inactive. As shown on the left-hand side of Fig. 6.3b, when Port 1 and Port 2 are excited by an in-phase signal and Port 3 is inactive, the

electric fields of the two leftmost antennas are combined constructively in endfire direction, thereby generating a sum radiation pattern. By contrast, when Port 1 and Port 3 are excited by an in-phase signal and Port 2 is inactive, the electric fields of the two rightmost antennas are combined destructively in the endfire direction due to their mirrored input transmission lines, thereby generating a difference radiation pattern.

The simulated scattering parameters of these antennas are illustrated in Fig. 6.4. The reflection coefficients for all the input ports are the same and remain below -10 dB in the range of 2.52 GHz to 6.24 GHz. This wide bandwidth of the antenna elements will be exploited for the three-state filtering functions of the overall antenna system. Within this band, the isolation between Port 1 and Port 2 is below -16 dB and the isolation between Port 2 and Port 3 is below -22 dB. It is noteworthy that the simulated efficiency of this triple-element antenna by itself is around 94%. This further confirms that this antenna is an appropriate element choice for our antenna system design in which the reconfigurable feeding network is the main source of inevitable loss.

The active reflection coefficient for the case where the two leftmost ports are excited is defined as follows

$$\text{Active } S_{22} = \frac{S_{22} + S_{21}}{2}, \tag{6.1}$$

whereas the corresponding active reflection coefficient for the case where the two rightmost ports are excited can be written as

$$\text{Active } S_{33} = \frac{S_{33} - S_{31}}{2}. \tag{6.2}$$

The negative sign between S_{33} and S_{31} in (6.2) is due to the intrinsic phase inversion of the mirrored input transmission line connected to Port 3. Due to reciprocity, the Active S_{11} will be the same as Active S_{22} when the two leftmost elements are excited. Likewise, when the two rightmost elements are excited, the Active S_{11} will be the same as Active S_{33}.

6.2.2 Switchable power divider

To selectively excite the presented triple-element antenna by two in-phase inputs and one inactive input, a switchable power divider is proposed as illustrated in Fig. 6.5a. It is composed of two side-by-side Wilkinson power dividers [162] which are isolated from each other by sets of PIN diodes clustered into PIN 3 and PIN 4 diodes. The related dimensions of this power divider are summarized in Table 6.1. Port 2, Port 3

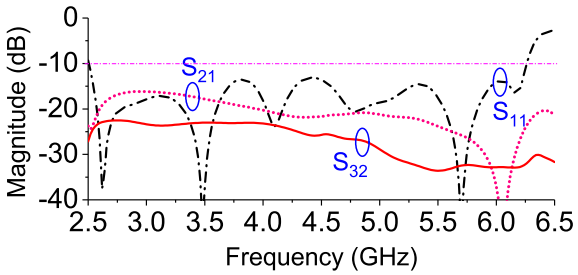

(a)

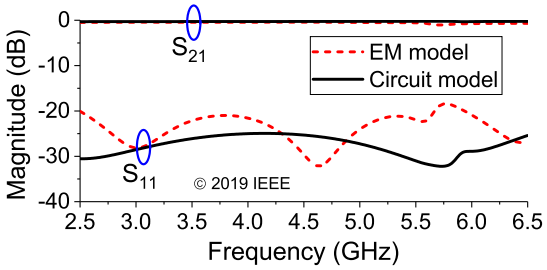

(b)

Figure 6.4. (a) Scattering parameters of the antenna array. (b) Active S_{22} when the two leftmost elements are excited and Active S_{33} when the two rightmost elements are excited.

and Port 4 of this power divider are respectively connected to Port 2, Port 3, and Port 1 of the the antenna structure shown in Fig. 6.3a. The six PIN diodes in this structure are clustered into two groups denoted as PIN 3 and PIN 4. Each group is biased by one biasing voltage and the DC ground is the middle line of the power divider. The bias lines for these PIN diodes, each of which is connected to a 15 nH RF choke, are shown in Fig. 6.1b. The proposed PIN diode arrangement is used to enhance the isolation between the excited and inactive antenna elements. Two 100 Ω resistors are employed for the output isolation of the power divider.

The instantaneous electric field densities for the cases when each group of PIN diodes is switched ON are represented in Fig. 6.5b. The common middle output branch is always excited while either of the two lateral output branches can be selected. When PIN 3 diodes are switched ON and PIN 4 diodes are switched OFF simultaneously, the input signal splits between the middle and the right output branches. When PIN 4 diodes are switched ON and PIN 3 diodes are switched OFF simultaneously, the input signal splits between the middle and the left output branches.

To analyze the power divider performance, the transmission line model of the triple-output power divider is illustrated in Fig. 6.6. Equivalent models of the PIN diodes are used for this analysis. The 70.7 Ω transmission line lengths are set to be equal to a

quarter wavelength at 4.2 GHz, i.e. near the middle of the wide operating bandwidth of the antenna.

The scattering parameters and the output phase difference of the Electromagnetic (EM) and circuit model of this power divider when the diodes PIN 4 are ON and the diodes PIN 3 are OFF are shown in Fig. 6.7. Due to the introduction of the PIN diodes in the circuit model of the triple-output Wilkinson power divider, the scattering performance is not ideal at the center frequency. In the EM model, bending and inevitable coupling of the transmission lines affect the scattering performances. This is the main reason behind the difference between the EM and circuit simulation results. Based on the EM and circuit simulation results, it is seen that the reflection coefficients are below -12 dB for the range of 2.5 GHz to 6.5 GHz. The transmission coefficient from Port 1 to Port 2 (S_{21}) and from Port 1 to Port 4 (S_{41}) are around -4 dB and -3 dB, respectively. The 1 dB transmission loss from Port 1 to Port 2 stems from the parasitic resistance of the PIN 4 diodes. This transmission loss is not present from Port 1 to Port 4 since there is no PIN diode between these two ports. The value of S_{31} is lower than -20 dB for the whole band demonstrating that only negligible power is transmitted to Port 3. The output phase difference in the EM simulation is varying from -2 degrees to 0 degrees, while the circuit simulation results exhibit constantly 0 degrees phase difference across this range. The isolation between the activated output ports (S_{42}) is below -12 dB from 2.5 GHz to 6.5 GHz. It will be demonstrated in subsection 6.2.4 that this value does not adversely affect the whole antenna system performance. The scattering parameters for the state when PIN 3 diodes are ON and PIN 4 diodes are OFF are identical to the state described above, with the only difference being that the input signal is equally split between Port 3 and Port 4 with no signal going to Port 2.

6.2.3 Switchable allpass to tunable bandpass and tunable bandstop filter

Based on the integration of the switchable power divider and the triple-element antenna, the sum and difference pattern diversity function is generated with wideband frequency response. To add the frequency selectivity function, a reconfigurable filter with switchable allpass to tunable bandpass/bandstop performance is required to feed the pattern reconfigurable antenna. While switchable and frequency-agile filters have widely been studied in the literature [92, 138–141, 163], a design which enables

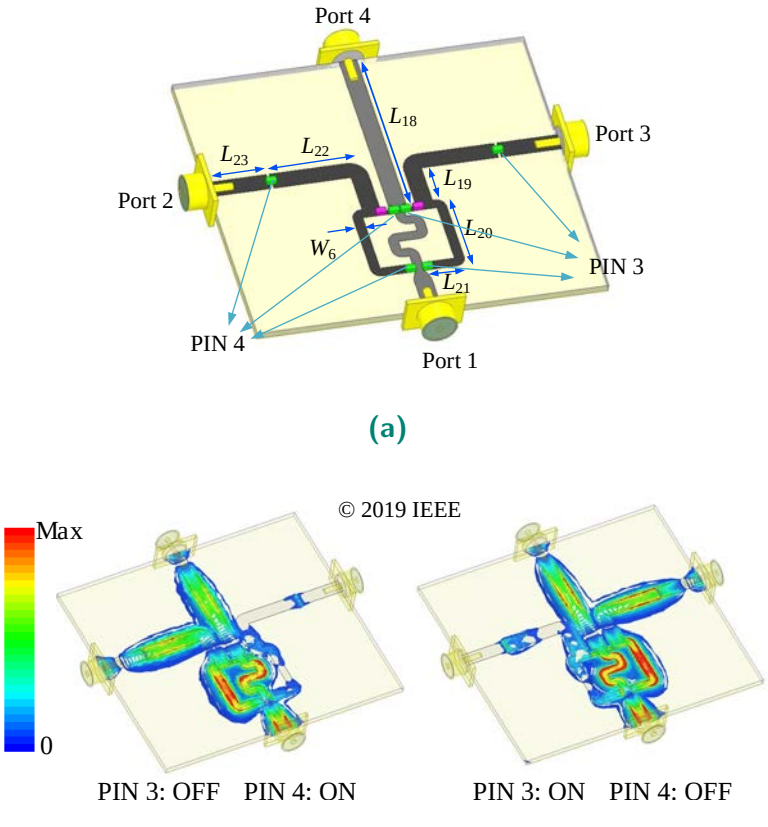

Figure 6.5. Three-way switchable power divider. (a) 3D view of the geometry with parameters defining the dimensions. (b) Instantaneous E-field distribution for the two states of the PIN diode switches.

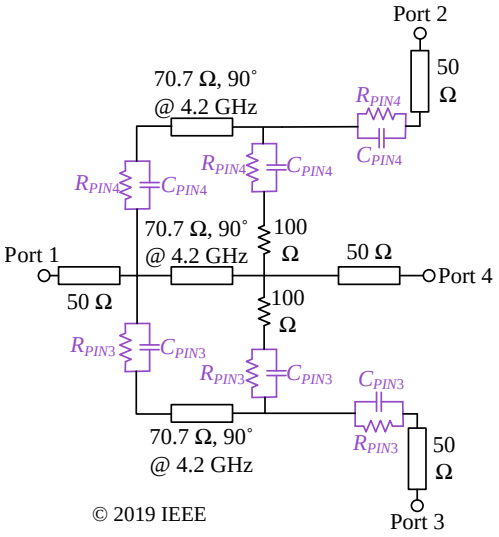

Figure 6.6. Circuit model of the presented power divider including the equivalent model of the PIN diodes.

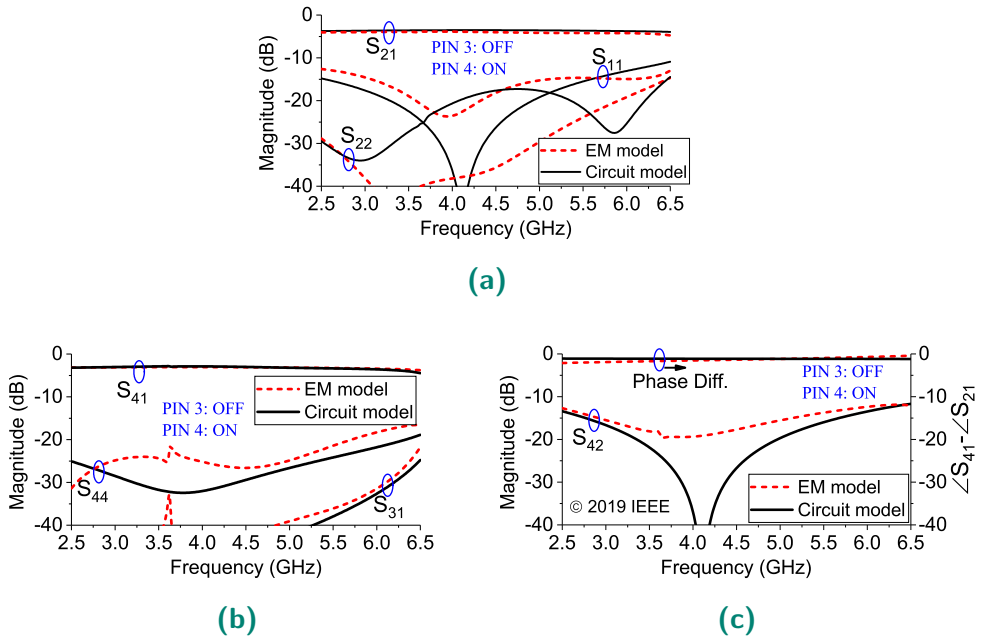

Figure 6.7. Scattering parameters calculated with the circuit model versus EM model of the power divider when PIN 3 diodes are OFF and PIN 4 diodes are ON. (a) S_{11}, S_{22}, and S_{21}. (b) S_{31}, S_{41}, and S_{44}. (c) S_{42} and the phase difference between the activated output ports.

to switch between all three states of cognitive radio namely allpass, tunable bandpass, and tunable bandstop is lacking. Herein, allpass functionality is added to the tunable bandpass-to-bandstop filter formerly presented in Chapter 5. The filter structure is depicted in Fig. 6.8a including two sets of PIN diodes namely PIN 1 and PIN 2 and two varactor diodes. PIN 2 diodes are switched ON or OFF together and the two varactors are biased with the same voltage. The dimensions of this filter are summarized in Table 6.1. For simplicity and clarity, the bias lines, choke inductors and DC block capacitors are not shown in Fig. 6.8a. However, they are displayed in the reconfigurable filter structure depicted in Fig. 6.1c. To bias the PIN and varactor diodes in the filter design, five inductors are connected to the DC bias lines, while one inductor is connected to the bottom layer of the filter which is RF and DC ground. This short-ended inductor provides a DC ground path for PIN 1 diode. Two DC block capacitors (visible in Fig. 6.1a) are used in the narrow coupled line of the reconfigurable filter to avoid the DC current of the PIN 2 diode to mix with the DC current of the varactors.

The instantaneous electric field density at the lowest passband and the frequency response of the reconfigurable filter in bandpass state are shown in Fig. 6.8b. In this state, all the PIN diodes are OFF and by changing the varactor capacitance, the operating frequency changes. The working principle in this case is that when PIN 1 diode is OFF,

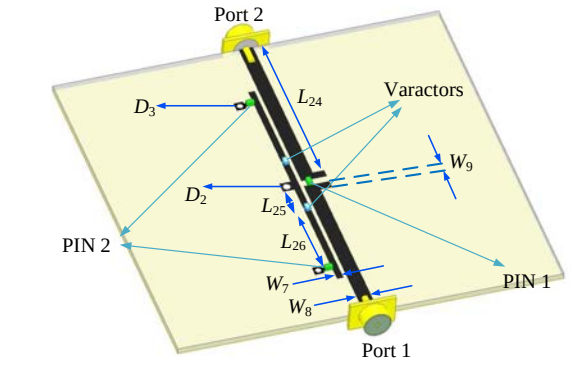

(a)

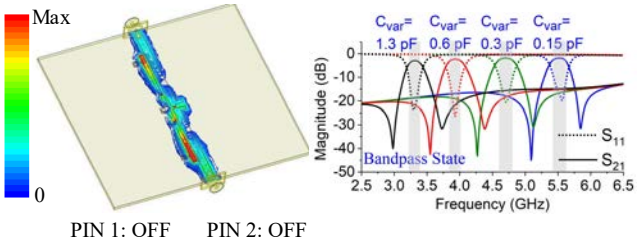

(b)

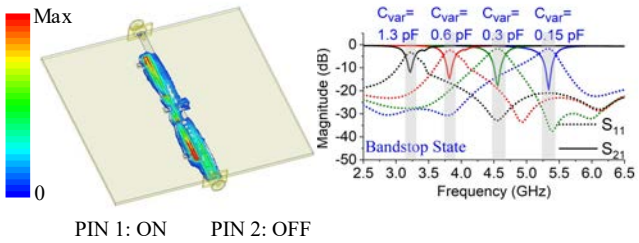

(c)

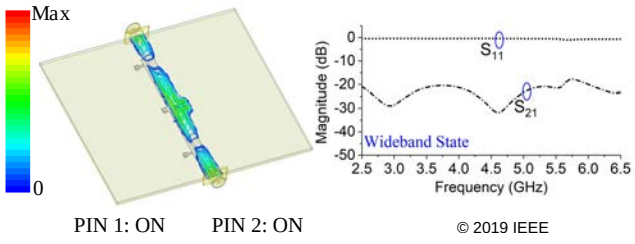

(d)

Figure 6.8. Proposed reconfigurable three-state filter. (a) 3D view and the related dimensions. (b) Passband E-field distribution at 3.3 GHz and simulated scattering parameters for bandpass state. (c) Notch-band E-field distribution at 3.2 GHz and simulated scattering parameters for the bandstop state. (d) E-field distribution at 3.5 GHz and simulated scattering parameters for allpass filtering state.

there is no direct path from input port to the output port. The input signal will pass through the narrow coupled line at a specific resonance frequency, which depends on the varactors capacitance thus generating a bandpass filtering response with tunable frequency. The PIN 2 diodes are OFF in this tunable bandpass state to allow the signal to pass through the narrow coupled line.

The instantaneous electric field density at the lowest notch band and the frequency response for the reconfigurable bandstop filtering state are shown in Fig. 6.8c. In this state, PIN 1 is switched ON providing a direct path for the input signal to reach the output. Nevertheless, the narrow coupled line will block this path at a specific resonance frequency which is tuned by varying the varactors capacitance. The PIN 2 diodes are switched OFF in this tunable bandstop filtering state. This, in turn, allows the narrow coupled line to create a notch frequency.

Given that the narrow coupled transmission line plays a key role in transmitting and blocking the input signal to the output port for the bandpass and bandstop states, respectively, neutralizing its effect can provide another operation state of allpass filtering response. This state is illustrated in Fig. 6.8d, where the PIN 1 diode is switched ON to provide a path from input to the output, while the short-ended PIN 2 diodes are switched ON to connect the narrow coupled line to the ground plane, thus neutralizing its effect. To minimize the power dissipation, no bias voltage is applied to the varactors in this state. The whole filter structure will be simplified to a 50 Ω transmission line in this state. Feeding inherently wideband antennas by this 50 Ω transmission line will result in a wideband response for the whole system. This wideband response is useful for the spectrum sensing case in cognitive radio systems, i.e. as an important state of operation missing in Chapter 5. Therefore, the newly proposed change in the structure will bring about a substantial improvement in the response of the overall system.

To analyze the filter performance, the behavior of its equivalent circuit model depicted in Fig. 6.9 is studied in the following. The distributed coupling capacitors are in red, the varactor equivalent elements are in blue and the PIN diode equivalent elements are in purple. When PIN 2 diodes are OFF, the equivalent model will behave the same way as the bandpass/bandstop filter presented in Chapter 5 with the same values of the lumped elements. The EM and circuit simulation results of the bandpass state are illustrated in Fig. 6.10a and Fig. 6.10b. In this state, because PIN 1 is OFF, the coupling capacitors provide a path between input and output at the resonance frequency which

Table 6.1. Dimension values of the proposed antenna system

par.	value (mm)	par.	value (mm)	par.	value (mm)	par.	value (mm)
W_1	1.8	L_2	73.2	L_{12}	7.4	L_{22}	7.9
W_2	2.2	L_3	10.8	L_{13}	20.5	L_{23}	6.2
W_3	2.2	L_4	4.3	L_{14}	17.4	L_{24}	22.0
W_4	0.9	L_5	27.2	L_{15}	14.9	L_{25}	3.3
W_5	1.4	L_6	10.7	L_{16}	16.0	L_{26}	10.3
W_6	1.0	L_7	23.2	L_{17}	4.5	D_1	7.0
W_7	0.8	L_8	5.0	L_{18}	18.5	D_2	1.0
W_8	1.8	L_9	20.0	L_{19}	4.1	D_3	0.8
W_9	1.0	L_{10}	10.8	L_{20}	6.5		
L_1	34.5	L_{11}	5.1	L_{21}	3.0		

is controlled by tuning the varactors. The EM versus circuit simulation results for the bandstop state are illustrated in Fig. 6.10c and Fig. 6.10d. In this state, PIN 1 is ON and the coupling capacitors take the opposite role, namely blocking the input signal to the output port at the resonance frequency which can be controlled by tuning the varactors. The last state of filter operation which distinguishes this filter from the one presented in Chapter 5 occurs when PIN 2 diode is ON. In this state, the effect of the distributed coupling capacitors is mitigated and the filter will turn into an allpass design when PIN 1 is ON. The EM and circuit simulation results for the allpass state are illustrated in Fig. 6.10e.

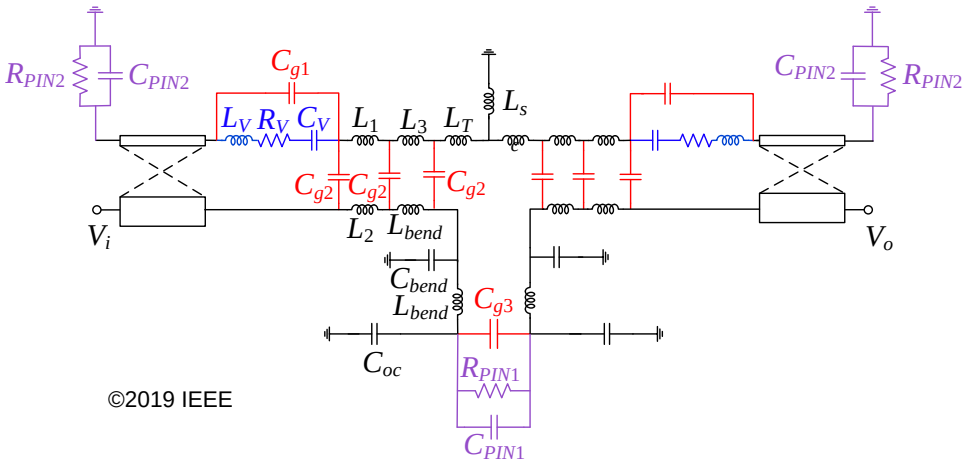

Figure 6.9. Equivalent circuit model of the filter.

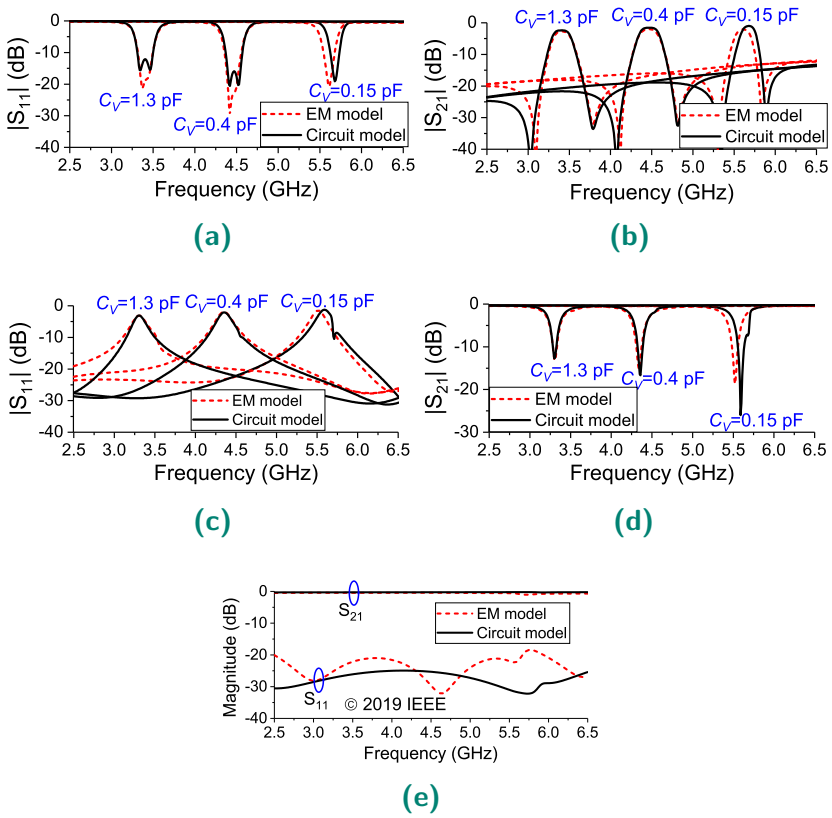

Figure 6.10. Scattering parameters of EM model versus circuit model of the filter. (a) S_{11} of the tunable bandpass state. (b) S_{21} of the tunable bandpass state. (c) S_{11} of the tunable bandstop state. (d) S_{21} of the tunable bandstop state. (e) S_{11} and S_{21} of the wideband state.

6.2.4 Measurement results

After integration of all the antenna components, the states of PIN and varactor diodes determine the overall system states as summarized in Table 6.2. Based on the proposed design refined through EM simulations, the antenna system has been fabricated and a photograph of the prototype is shown in Fig. 6.11. The total substrate volume is $W \times L \times H = 144 \times 190 \times 0.8182$ mm^3 corresponding to $1.24\lambda_0 \times 1.65\lambda_0 \times 0.007\lambda_0$ where λ_0 is the wavelength at the lowest operating frequency. There are seven biasing lines in the fabricated prototype which are AC-isolated from the antenna structure by seven RF chokes at the end of each line. The DC grounds are the antenna bottom layer as well as the antenna middle feeding line. It is noteworthy that the gaps used for mounting lumped elements are all 0.3 mm wide.

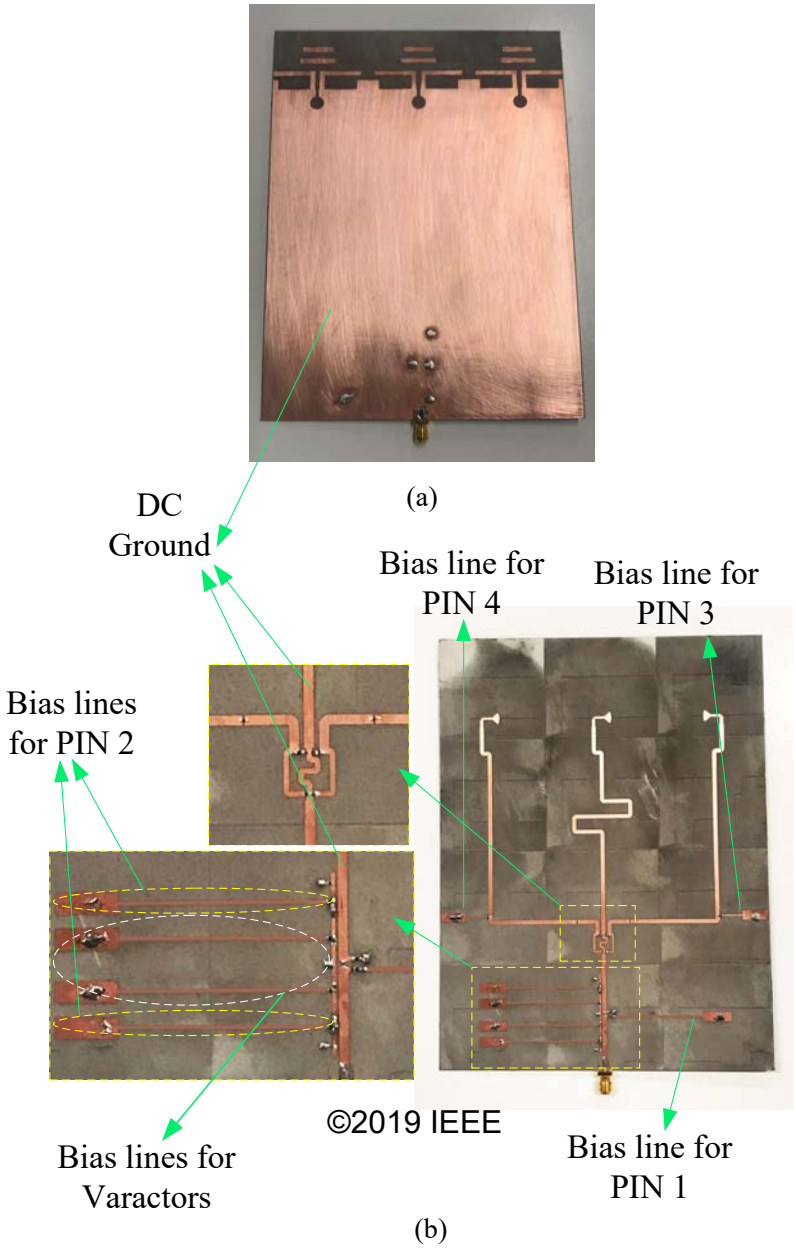

Figure 6.11. Photograph of the fabricated antenna. (a) Bottom layer. (b) Top layer with magnified feeding network.

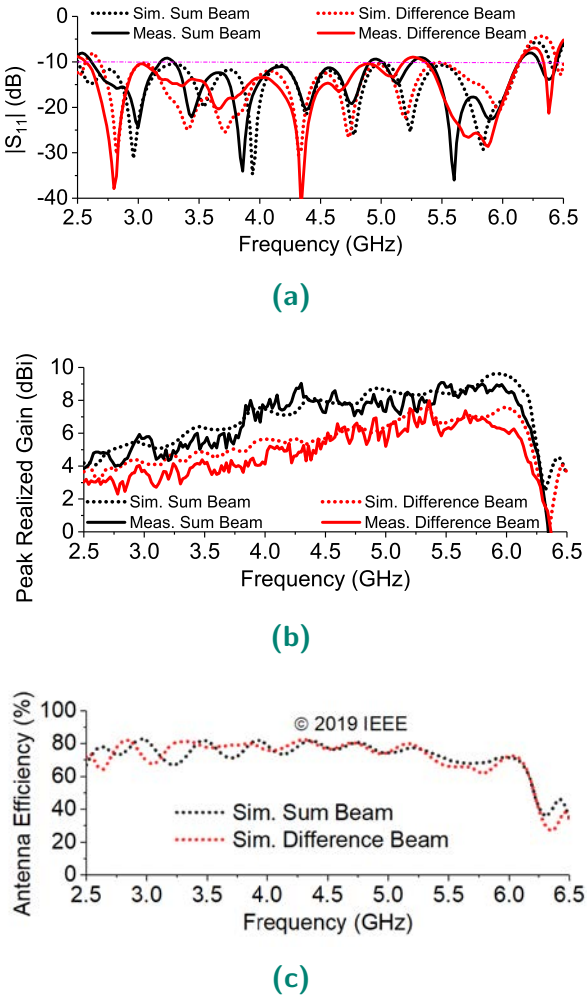

Figure 6.12. Frequency responses of the proposed antenna in the wideband state with sum and difference radiation patterns. (a) Reflection coefficient. (b) Maximum realized gain. (c) Total antenna efficiency.

Wideband operation state

According to Table 6.2, when PIN 1 and PIN 2 diodes are both switched ON and no voltage is applied to the varactors, the filter is in allpass state. This case is analogous to exciting the wideband pattern switchable antenna array by a 50 Ω transmission line. Hence, the wideband operation state for the whole system is activated. The reflection coefficients are illustrated in Fig. 6.12a with the simulated (measured) overlapping bandwidth for the sum and difference beams extending from 2.68 GHz (2.62 GHz) to 6.10 GHz (6.10 GHz). This corresponds to 77.9% (79.8%) fractional bandwidth with minor breaches of the −10 dB specification in the measured data. The simulated (measured) maximum realized gain of the antenna illustrated in Fig. 6.12b is varying from 4.8 dBi (4.8 dBi) to 8.7 dBi (7.7 dBi) for the sum beam pattern, while it is varying from

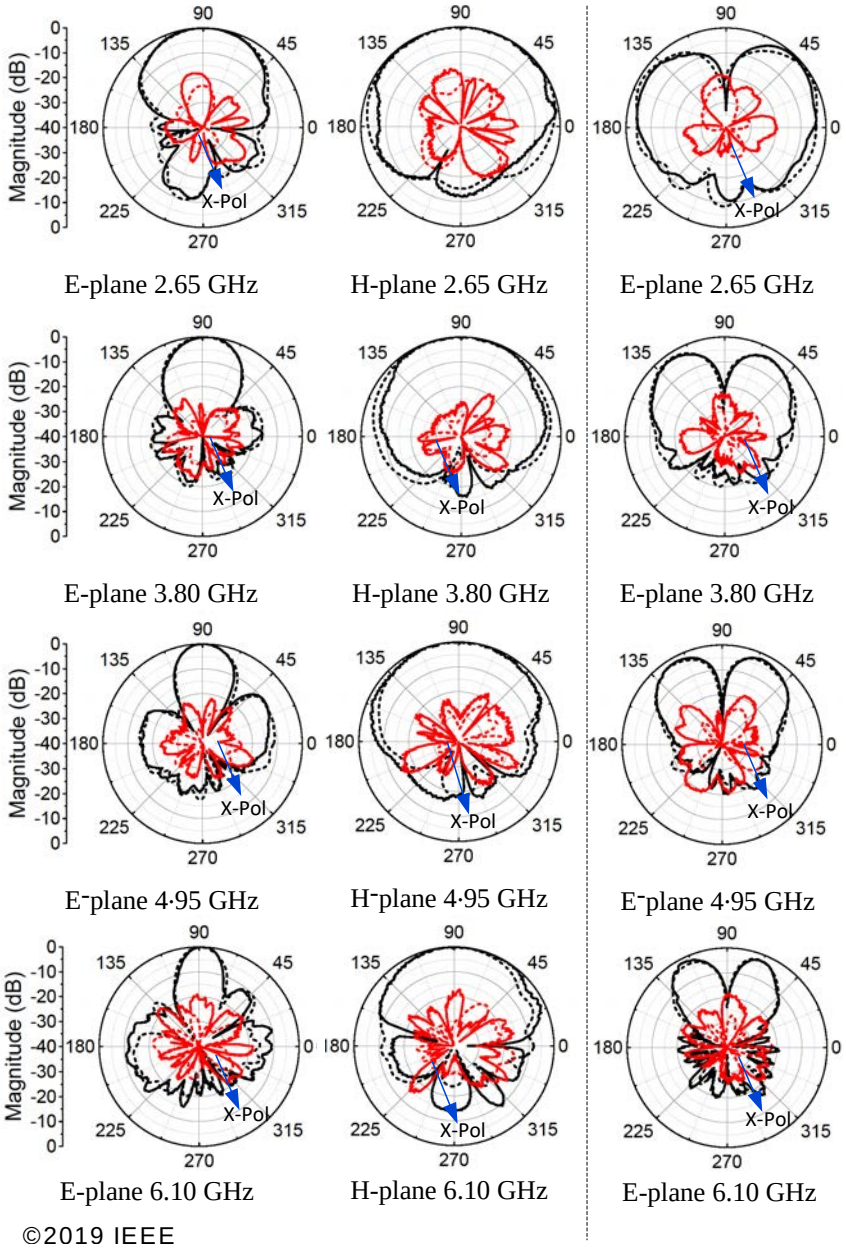

Figure 6.13. Measured and simulated radiation patterns at different frequencies for the wideband state of operation.

Left column: E-plane radiation pattern for the sum beam operation.

Middle column: H-plane radiation pattern for the sum beam operation.

Right column: E-plane radiation pattern for the difference beam operation.

Table 6.2. Switching patterns and the different frequency operation states

PIN 1	PIN 2	PIN 3	PIN 4	Varactors	Behavior
ON	ON	ON	OFF	1.3 pF	WB / Difference
ON	ON	OFF	ON	1.3 pF	WB / Sum
OFF	OFF	ON	OFF	0.15 pF to 1.3 pF	Tunable BP / Difference
OFF	OFF	OFF	ON	0.15 pF to 1.3 pF	Tunable BP / Sum
ON	OFF	ON	OFF	0.15 pF to 1.3 pF	Tunable BS / Difference
ON	OFF	OFF	ON	0.15 pF to 1.3 pF	Tunable BS / Sum

WB: Wideband, BP: Bandpass, BS: Bandstop

3.8 dBi (3.0 dBi) to 6.8 dBi (5.7 dBi) for the difference beam pattern. The simulated antenna efficiency is more than 62.0% within the whole bandwidth as represented in Fig. 6.12c. The simulated and measured sum and difference radiation patterns at four sample frequencies are plotted in Fig. 6.13.

Bandpass operation state

The tunable bandpass state of operation occurs when both PIN 1 and PIN 2 diodes are switched OFF and the varactor capacitances are controlled by the tuning bias voltage. In this state, the whole system takes on the frequency characteristic of the tunable bandpass filter. Based on the simulated (measured) reflection coefficient plots in Fig. 6.14a, the operating frequency can be tuned from 3.30 GHz (3.28 GHz) to 5.58 GHz (5.55 GHz) corresponding to a tuning range of 51.3% (51.3%). This value is roughly the same for both cases of sum and difference radiation patterns. Within this tuning range, the simulated (measured) maximum realized gain illustrated in Fig. 6.14b is varying from 2.9 dBi (2.4 dBi) to 7.0 dBi (6.0 dBi) for the sum beam case, while it is varying from 2.2 dBi (1.9 dBi) to 5.4 dBi (4.4 dBi) for the difference beam case. The simulated antenna efficiencies for both sum and difference radiation patterns are shown in Fig. 6.14c with the minimum value of 46.0% observed at the lowest operating frequencies, which is typical for varactor controlled frequency-tunable antennas. This value increases with raising tuning frequencies and this effect is attributed to the parasitic resistance of the varactor diode. The simulated and measured radiation patterns within the passbands of the tunable bandpass antenna are shown in Fig. 6.15.

Bandstop operation state

Referring to Table 6.2, when PIN 1 is switched ON and PIN 2 is switched OFF, the bandstop operation state is activated and the notched frequency is tuned by varying the bias voltage controlling the varactor capacitances. In this state, the frequency response of the whole systems takes on the characteristics of the tunable bandstop filter. It is seen in Fig. 6.16a that the simulated (measured) notched frequency can be tuned from 3.20 GHz (3.20 GHz) to 5.40 GHz (5.35 GHz) corresponding to a tuning range of 51.1% (50.3%) for the sum pattern and it is nearly the same for the difference beam pattern. Moreover, the simulated (measured) maximum realized gain attenuation within the notch-bands is higher than 13.0 dBi (10.4 dBi) for both the sum and difference radiation patterns based on Fig. 6.16b. As the varactor capacitance decreases, the attenuation level increases. The simulated antenna efficiencies for the sum and difference beams are illustrated in Fig. 6.16c. For both the sum and difference beams, the total antenna efficiency at the notch frequencies becomes well below 10.0% for the whole tuning range, thus lowering the realized gain. The simulated and measured out-of-band radiation patterns for the tunable bandstop state are very similar to the wideband counterparts.

6.2.5 Comparison with recently published designs

The performance of the proposed design is compared in Table 6.3 with some recently published designs featuring switchable and continuously tunable frequency performances. For better comparison, the selected references are all exhibiting continuous tunability in their narrowband states. It is observed that the proposed design is the only design generating all three states of wideband, tunable bandpass, and tunable bandstop performance. In contrast to the designs presented in [53] and [85] where sum and difference patterns were realized by an external coupler and a switchable ultrawideband phase inverter, respectively, the proposed design yields the sum and difference radiation patterns using an in-built phase inverter in the antenna structure, thus reducing the complexity of the feeding network. The large dimensions of the proposed design compared to the other references and sequential pattern switching compared to double-input pattern diversity antennas are the only sacrificed features to obtain this unique functionality. It is noteworthy that for some applications such as Global Positioning System (GPS) antennas, the shift in phase center due to the use of the proposed triple-element antenna configuration is a very critical issue affecting the

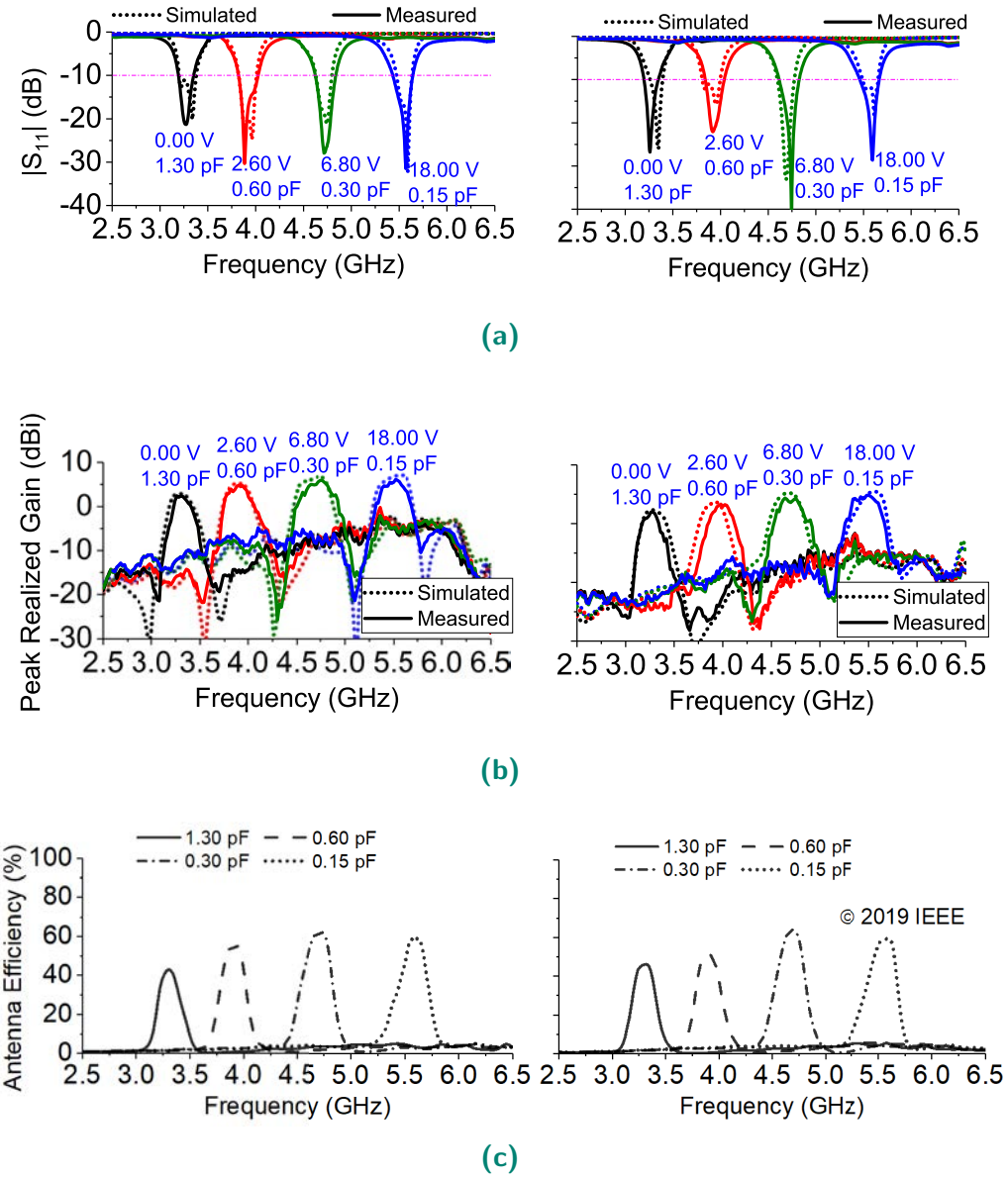

Figure 6.14. Frequency responses of the proposed antenna in the bandpass state. Left column: sum beam operation. Right column: difference beam operation. (a) Reflection coefficient. (b) Maximum realized gain. (c) Total antenna efficiency.

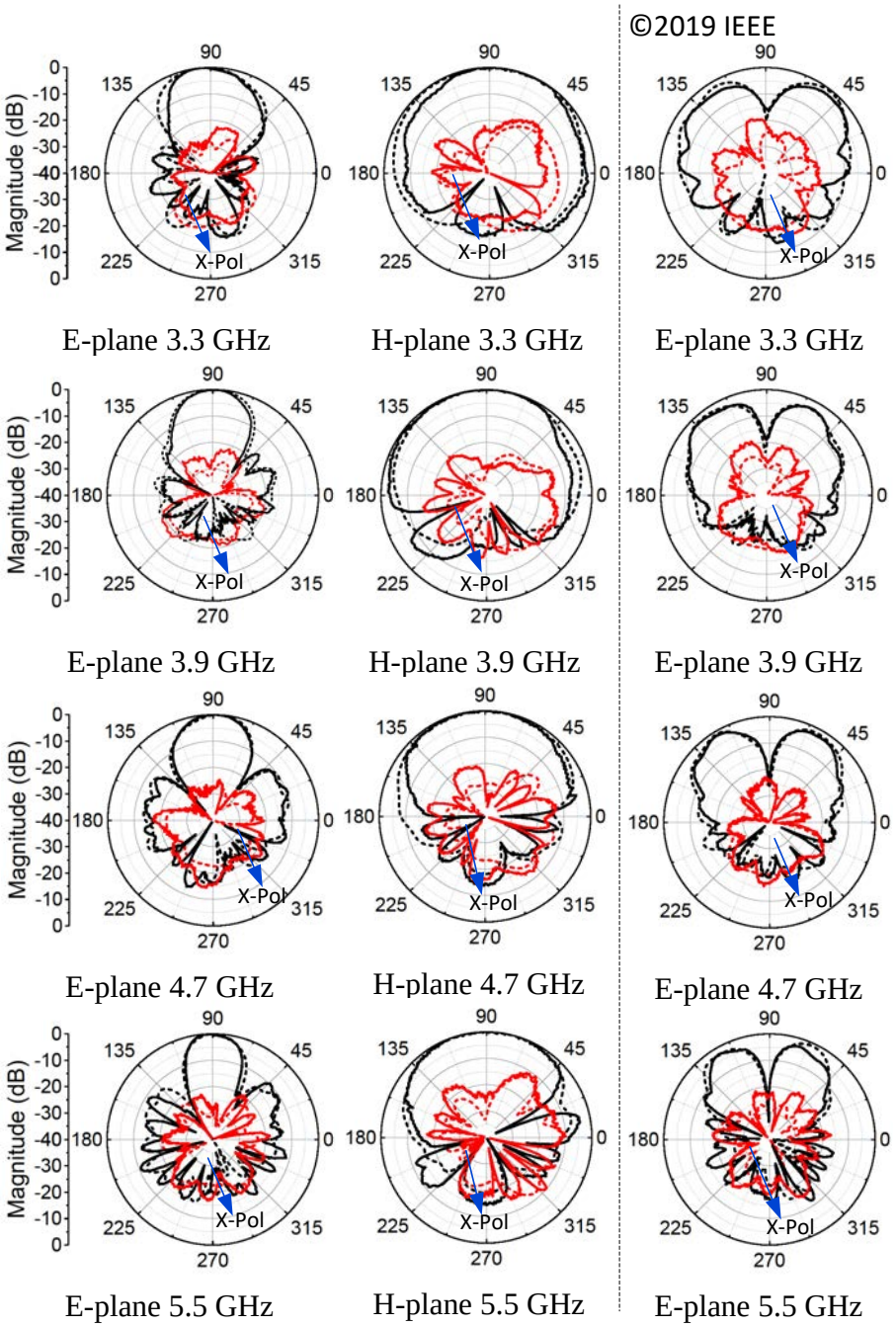

Figure 6.15. Measured and simulated radiation patterns at different frequencies for the bandpass state of operation.

Left column: E-plane radiation pattern for the sum beam operation.

Middle column: H-plane radiation pattern for the sum beam operation.

Right column: E-plane radiation pattern for the difference beam operation.

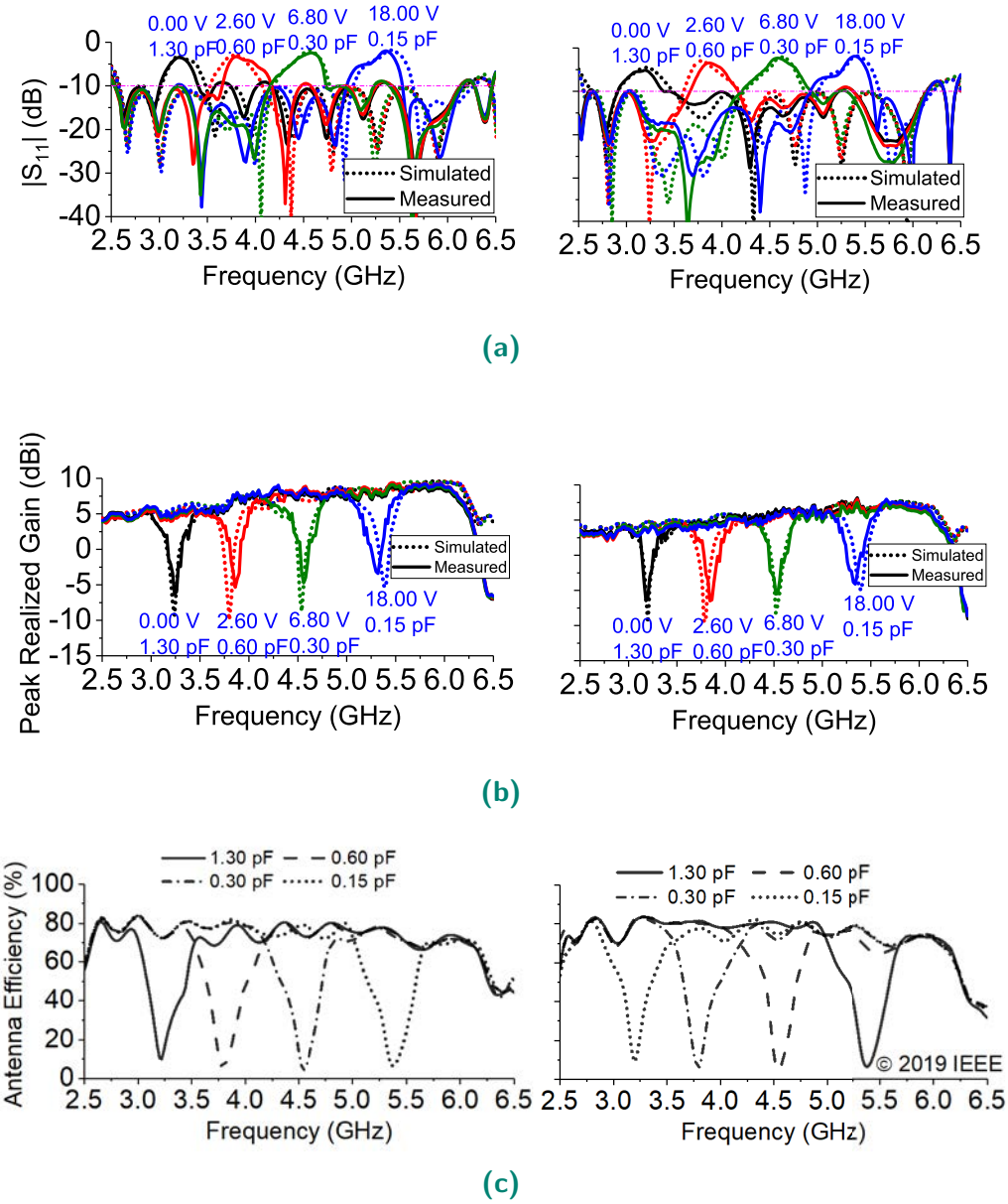

Figure 6.16. Frequency responses of the proposed antenna in the bandstop state. Left column: sum beam operation. Right column: difference beam operation. (a) Reflection coefficient. (b) Maximum realized gain. (c) Total antenna efficiency.

Table 6.3. Comparison of the proposed antenna system with some recently published antennas featuring tunable filtering response.

Refs.	ε_r	Size $(\lambda_0)^3$	Mode of Operation			Reconfig. Patterns	Pattern Type	In-built Phase Inverter
			Wideband (BW)	Tunable BP (TR)	Tunable BS (TR)			
[93]	2.2	0.72×0.30×0.01	✓ (44.9%)	✓ (21.0%)	✗	✗	omnidirectional	✗
[124]	3.48	0.39×0.23×0.011	✓ (71.7%)	✓ (36.0%)	✗	✗	omnidirectional	✗
[94]	2.2	0.42×0.3×0.002	✗	✓* (57.0%)	✓ (57.0%)	✗	omnidirectional	✗
[53]	3.38	0.75×0.7×0.008	✗	✓ (50.0%)	✓ (50.4%)	✗	sum and difference (two-port)	✗
[85]	3.0	1.21×1.21×0.17	✓ (60.2%)	✗	✗	✓	broadside to conical	✗
This Work	3.38	1.24×1.65×0.007	✓ (79.8%)	✓ (51.3%)	✓ (50.3%)	✓	sum and difference	✓

BW: Bandwidth, BP: Bandpass, BS: Bandstop, TR: Tuning Range

* No experimental validation for bandpass case is provided in this reference.

performance. However, for many other applications such as point-to-point base station communications, the amplitude of the far-field radiation is of critical importance which is at a satisfactory level in this design.

6.3 Dual-input patch antenna with sum and difference patterns in E- and H-plane

In this section, a single-element patch antenna with sum and difference pattern reconfigurability in its E-plane is evolved to a double-element antenna arranged along the H-plane of the patch antenna. This arrangement fed by a single rat-race coupler enables sum and difference pattern generation in both E- and H-plane.

6.3.1 Single-element pattern-reconfigurable patch antenna design and simulation

The fundamental single-element patch antenna structure is illustrated in Fig. 6.17a. It includes ten MA4FCP300 PIN diodes, a biasing network with a 15 nH inductor as a RF choke, and a decoupling via. The equivalent model of the PIN diodes in ON state is a 4 Ω resistor and in OFF state, it is the parallel arrangement of a 20 kΩ resistor and a 0.04 pF capacitor. When the PIN diodes are switched OFF, the patch antenna

works on its TM01 mode with broadside sum radiation pattern and the effective radiating element is the directly fed patch working at 5.97 GHz. When the PIN diodes are switched ON, the effective radiating element will include both patches operating in the TM02 mode. The odd symmetry of this mode results in the radiation of a difference beam with a null in the broadside direction. The reason for using ten PIN diodes in five columns is to minimize the capacitive effect of the PIN diodes in OFF state, thereby providing a high isolation between the two operating modes. Moreover, the surface current will flow to the other element with low parasitic resistance of the PIN diodes arrangement in ON state. The shorting via is also utilized to provide both a DC ground and an isolation between the TM01 and TM02 modes when the diodes are switched OFF. The electric field distribution for TM01 and TM02 modes is illustrated in Fig. 6.17b. The simulated scattering parameters are shown in Fig. 6.18, demonstrating that two antenna modes are working at 5.97 GHz with overlapping bandwidth of 1.2%. The fractional bandwidth can be increased by increasing the substrate height. The normalized sum and difference radiation patterns in elevation plane are shown in Fig. 6.19 with a maximum realized gain of 7.7 dBi for the sum beam and 5.6 dBi for the difference beam.

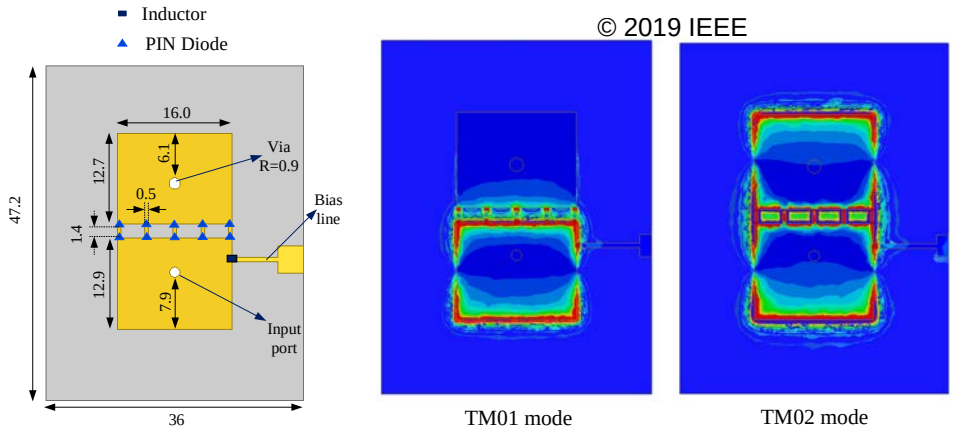

Figure 6.17. (a) Antenna schematic with the dimensions in mm. (b) Electric field distribution for two operation modes.

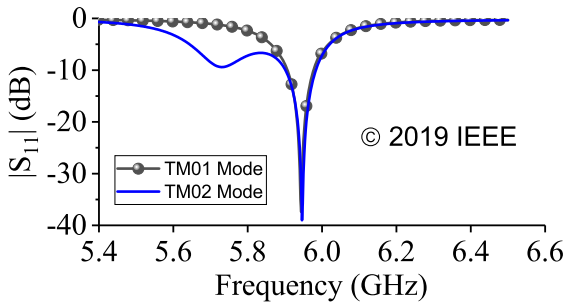

Figure 6.18. Reflection coefficient for the TM01 and TM02 modes.

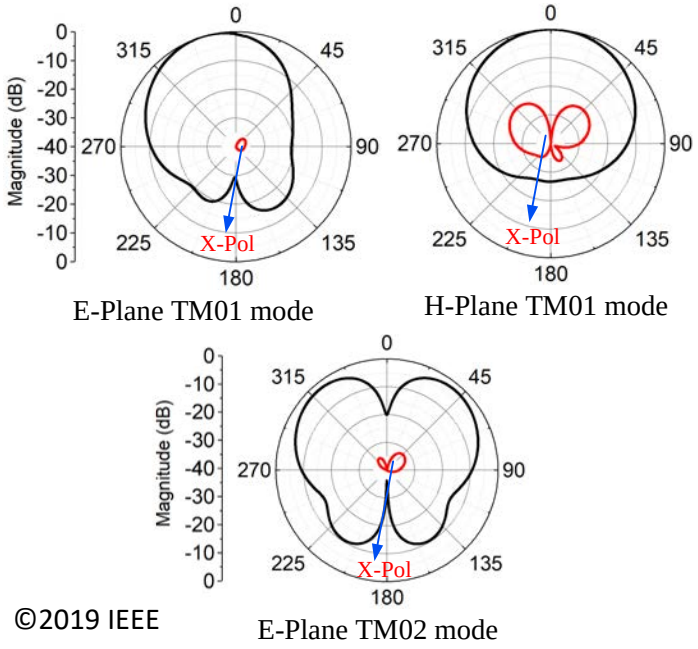

Figure 6.19. Radiation patterns for TM01 and TM02 modes.

6.3.2 Double-element pattern-reconfigurable patch antenna evolution

The single-element antenna provides the sum and difference radiation patterns in its E-plane based on PIN switches. To extend the pattern diversity to the H-plane of the antenna, another element is added along the H-plane direction. The optimal distance between the antenna elements is found to be 15 mm based on parametric analysis. The double-element antenna can be fed by in-phase and out-of-phase inputs to generate four total radiation patterns. The operation modes are shown in Fig. 6.20 with 3D radiation patterns. When the PIN diodes are switched OFF and the inputs are in-phase, a directive radiation pattern towards broadside is generated. When the PIN diodes

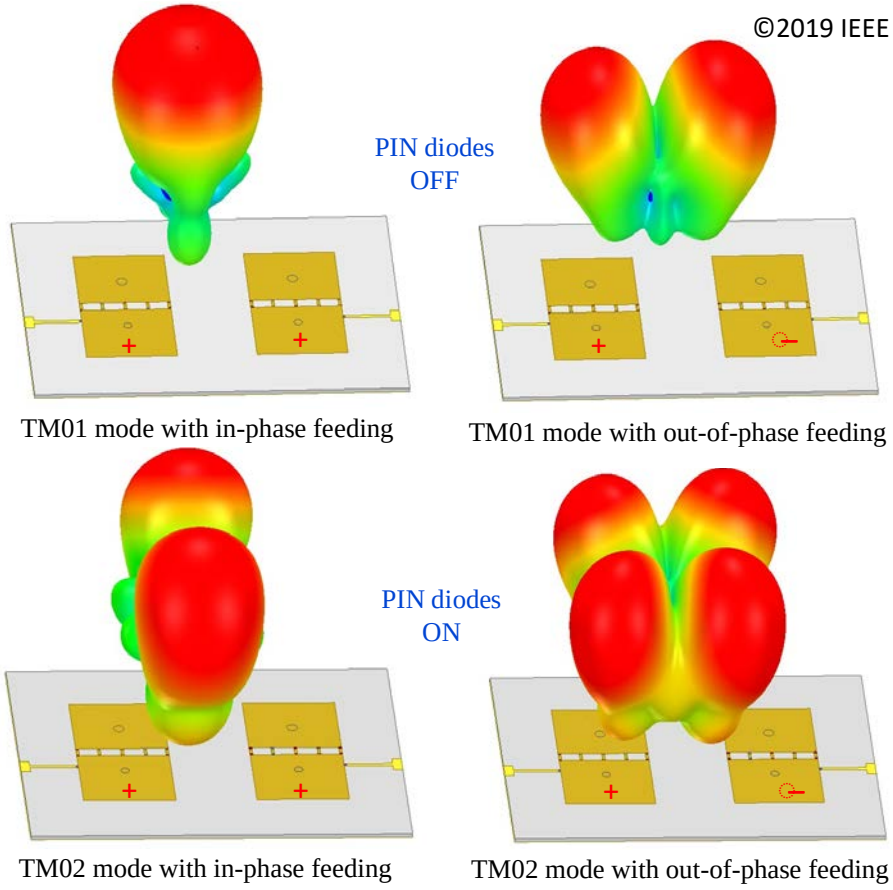

Figure 6.20. Four different patterns generated by in-phase and out-of-phase feedings and changing the states of the PIN diodes for the double-element antenna.

are switched OFF and the antennas are fed by out-of-phase inputs, a difference pattern along H-plane of the antenna is produced. When the PIN diodes are switched ON and the inputs are in-phase, the difference radiation pattern along the E-plane is generated. When the PIN diodes are switched ON and inputs ports are out-of-phase, a quad-lobe radiation pattern will be generated since there are two nulls along E- and H-plane of the antenna. The simulated reflection coefficient and the isolation between the antenna elements for TM01 and TM02 modes are shown in Fig. 6.21. The reflection coefficient of the antenna remains the same as the single-element antenna and the isolation between the elements is less than -15 dB for TM01 and TM02 modes. The simulated 2D radiation patterns are illustrated in Fig. 6.22. The maximum realized gain for the sum radiation pattern case is 10.2 dBi. It reaches 5.8 dBi for the H-plane difference radiation pattern, 7.7 dBi for the E-plane difference radiation pattern, and 2.5 dBi for the quad-lobe radiation pattern.

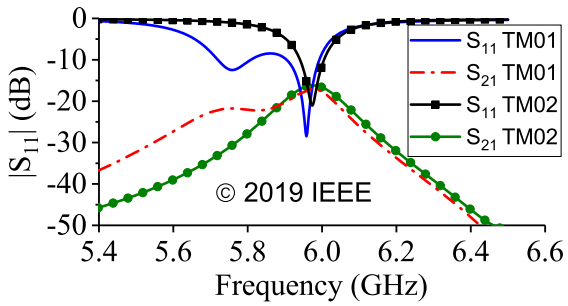

Figure 6.21. Reflection coefficient and isolation between the antenna elements for TM01 and TM02 modes of the double-element antenna.

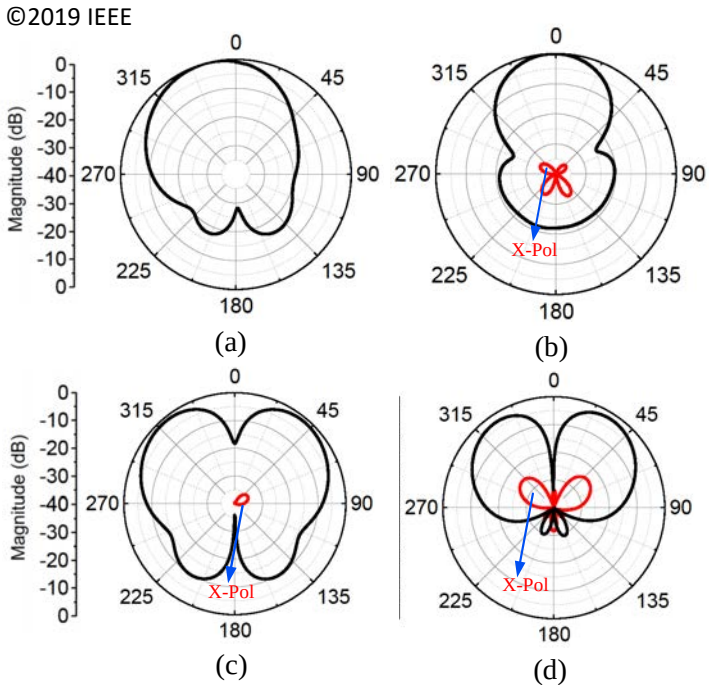

Figure 6.22. Double-element antenna radiation patterns. (a) E-plane sum patterns with x-pol lower than −40 dB. (b) H-plane directive pattern. (c) E-plane difference radiation pattern. (d) H-plane difference radiation pattern.

6.4 Conclusion

In the first part of this chapter, the design of a sum and difference pattern-reconfigurable antenna with three switchable states of wideband, tunable bandstop, and tunable bandpass operation has been presented. This antenna system has been developed by integration of a switchable and tunable filter, a modified switchable power divider, and a triple-element quasi Yagi-Uda antenna array with an in-built phase inverter. The simulation and measurement results have shown that this design can successfully achieve

wideband operation with a bandwidth of 79.8%, which can be switched to a tunable bandpass and tunable bandstop with 51.3% and 50.3% tuning range, respectively. The results also demonstrated that the system can switch between the sum and difference beam radiation patterns by exploiting its in-built phase inverter while working in each of the switchable filtering states.

In the second part of this chapter, A double-element planar microstrip patch antenna producing four different radiation patterns has been developed on the basis of a pattern-reconfigurable single-element patch antenna and a 180° hybrid coupler. This design structure could facilitate the generation of sum and difference radiation patterns along E- and H-plane without adding complexity to the design structure. This is in contrast to the conventional method of using four antenna elements and four couplers to generate sum and difference beams along both planes.

Chapter 7

Tunable Dual-Band Bandpass and Bandstop Antennas

ANTENNAS with independently tunable frequencies offer more flexibility while reducing the complexity of the overall wireless system. One consideration towards designing a multi-band antenna with independently tunable frequencies is the frequency selectivity. The frequency selectivity is usually weak for frequency-tunable antennas with embedded tunable elements in the antenna design. This metric can be enhanced by integration of a tunable selective filter with a wideband antenna.

In the first part of this chapter, the bandpass filter structure in Chapter 6 is evolved to a dual-band structure with independently tunable frequencies. This is achieved by adding a second resonator which functions independently from the first resonator. This filter is then used as a feeding network for a wideband monopole antenna to generate a dual-band independently tunable response. In the second section of this chapter, the single-band bandpass filter proposed in Chapter 6 is converted to a single-band bandstop filter by a slight (but important) modification. Through cascading two evolved single-band bandstop filters, a dual-band bandstop filter with independently tunable frequencies is then achieved. This filter is integrated with a wideband quasi-Yagi-Uda antenna. The resulted antenna filter integration has a wideband response with two notch frequencies which are independently tunable.

7.1 Introduction

Dual-band frequency agile antennas have been the subject of extensive research over the past few years. They can find applications in cognitive radio and carrier aggregation systems where separate tunable bands are required. They can also reduce the overall size and cost of a system by working on arbitrary frequencies with only one radiating element. There are two methods of realizing dual-band frequency tunable antenna. First, embedding tunable elements within an antenna resonant structure [164–167]. Second, integrating a tunable bandpass filter with a wideband antenna [53, 94].

Tunable dual-notchband antennas are also useful building blocks for interference rejection and cognitive radio applications. The implementation of filtering functions with independently tunable notch frequencies can increase the degree of freedom for ultrawideband antenna systems with multiple interference sources. Similar to dual-band frequency-tunable antennas, there are two methods for tunable dual-notchband antenna realization, which are embedding tunable elements in the antenna structure [168,169] and integration of tunable bandstop filters with a wideband antenna [94,170].

Several tunable bandpass [89, 171, 172] and tunable bandstop filters [90, 173–175] have been reported based on different technologies. They can be potentially useful for filter antenna integration. However, the considerations on compatibility with planar structures and integratability were not investigated in those publications.

In the first part of this chapter, an independently tunable dual-band filter using a dual-band source-to-load coupling scheme is designed based on the evolution of designs in [53, 142, 176] and Chapter 5. The filter is then integrated with a planar oval-shaped monopole antenna to select the two passbands from the intrinsic wideband spectrum of the monopole. In the second part of this chapter, the fundamental design of the bandpass filter has been slightly modified to work on completely different state of bandstop filtering with a tunable single-band response. On that basis, a tunable second-order bandstop filter which can operate as an independently tunable dual-band first-order filter is designed and integrated with a quasi-Yagi-Uda antenna.

7.2 Dual-band tunable bandpass monopole antenna

The antenna structure along with the fabricated prototype are shown in Fig. 7.1. The antenna is implemented on a Rogers RO4003C substrate with relative permittivity of

Table 7.1. Parameters of the proposed tunable dual-band bandpass monopole antenna

TL_1:	$W_1 = 1.8$ mm	$L_1 = 16.5$ mm	
TL_2:	$W_2 = 0.8$ mm	$L_2 = 12.6$ mm	
TL_3:	$W_3 = 0.8$ mm	$L_3 = 3.3$ mm	
TL_4:	$W_4 = 1.5$ mm	$L_4 = 1.4$ mm	
Via:	$D = 1.0$ mm		
Gaps:	$G_1 = 0.5$ mm	$G_2 = 1.0$ mm	$G_3 = 0.5$ mm
Monopole:	$a_1 = 24.0$ mm	$a_2 = 21.5$ mm	
Ground:	$a_3 = 63.5$ mm	$a_4 = 48.7$ mm	

3.38, loss tangent of 0.0027, and thickness of 0.8128 mm. The antenna system design dimensions, including widths and lengths of transmission lines TL_1 to TL_4, are provided in Table 7.1. The magnified section of Fig. 7.1a illustrates the bandpass filter structure with two coupled lines each of which containing two embedded varactor diodes. The input filtering structure is an evolution of the filter designs presented in [53, 142, 176] and Chapter 5. The gap shown as G_1 is providing a cross coupling between the input and output ports of the filter, i.e. blocking the input signal to reach the output port from the main transmission line. The input signal will reach the output port of the filter through the coupled-line resonators with embedded varactors. The embedded varactors in each coupled-line are biased with the same voltage. Because each coupled transmission line with two embedded varactors can create a source-to-load coupling path, it is possible to separate the passband frequencies generated by each coupled line. This is done by assigning different bias voltages to the coupled lines on either side of the main transmission line. However, close proximity of the two operating frequencies can cause distortion in the scattering parameter. This, in turn, defines the maximum tuning range of each passband. This filter excites a wideband monopole antenna with planar structure to filter out independently tunable frequencies from the wideband spectrum of the antenna. The simulation results have been obtained using Ansys Electronics Desktop where the equivalent circuit of the MA46H120 varactor diode (R = 1.6 Ω, L = 0.05 nH and 0.15 pF $< C_{var} <$ 1.30 pF) is used. To choke the RF signal for DC biasing 15 nH inductors with Self Resonance Frequency (SRF) of 3.5 GHz are used. The results from the simulation and measurement are illustrated in Figs. 7.2 and 7.3. As seen in Figs. 7.2a and 7.2b, by assigning a bias voltage of 0.00 V (1.30 pF) to Varactor 1, the first band is fixed at 3.3 GHz. In this case, by changing the bias voltage for Varactor 2 from 3.80 V (0.40 pF) to 18.00 V (0.15 pF), the second band is tuned from 4.30 GHz to 5.60 GHz, corresponding to 26.0% tuning range. Likewise, Figs. 7.3a and

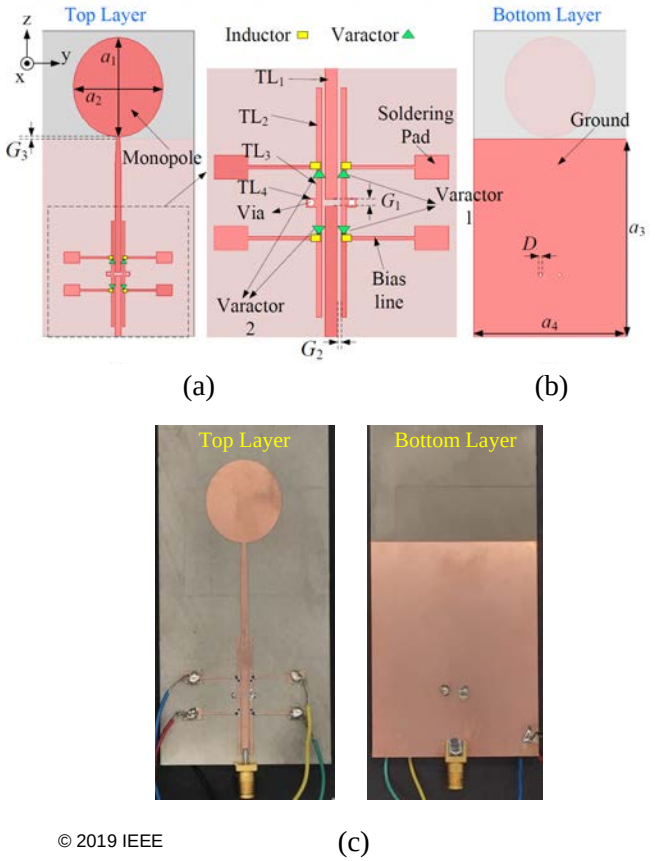

Figure 7.1. The proposed design of dual-band tunable bandpass monopole antenna. (a) Top layer. (b) Bottom Layer. (c) Top and bottom photograph of the fabricated design.

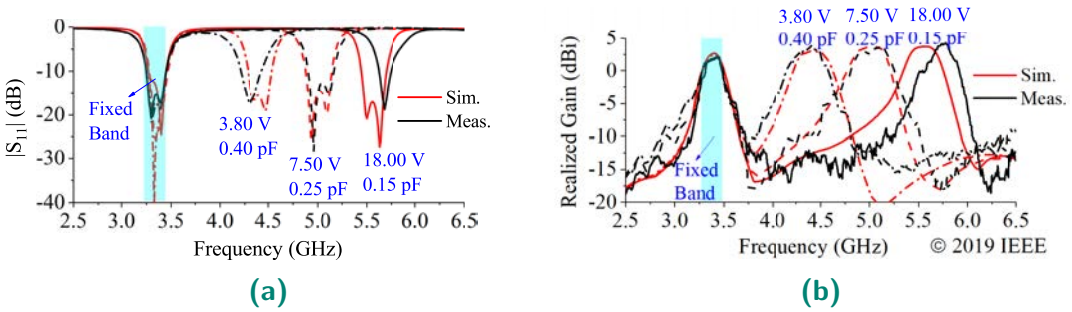

Figure 7.2. Measured and simulated antenna parameters versus frequency when the bias voltage of Varactor 1 is 0.00 V ($C_{var1} = 1.30$ pF) and the bias voltage of Varactor 2 is varying from 3.80 V to 18.00 V (0.15 pF $< C_{var2} <$ 0.40 pF). (a) Reflection coefficient (b) Realized gain.

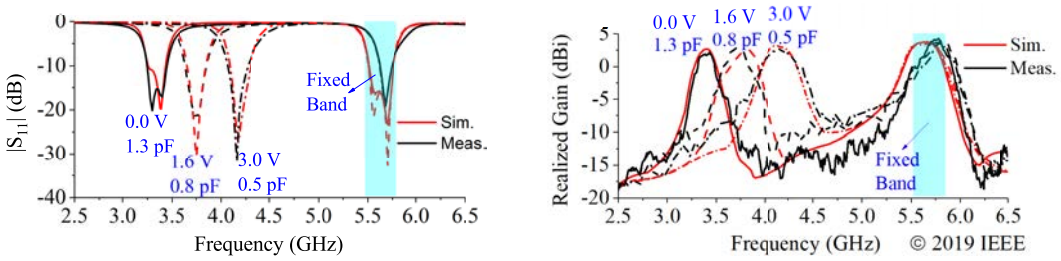

Figure 7.3. Measured and simulated antenna parameters versus frequency when the bias voltage of Varactor 2 is 18.00 V ($C_{var2} = 0.15$ pF) and the bias voltage of Varactor 1 is varying from 0.00 V to 3.00 V (0.50 pF $< C_{var1} <$ 1.30 pF). (a) Reflection coefficient (b) Realized gain.

7.3b show that the bias voltage of 18.00 V (0.15 pF) to Varactor 2 yields a fixed passband frequency at 5.60 GHz. By changing the bias voltage for Varactor 1 from 0.00 V (1.30 pF) to 3.00 V (0.50 pF), the other passband is tuned from 3.3 GHz to 4.2 GHz, corresponding to a 24.0% tuning range. The radiation patterns for YOZ and XOY planes are plotted in Fig. 7.4 for three different frequencies. It is seen that the lightly conical radiation pattern of the monopole remains unaffected by the integration of the filter to the input port.

7.3 Dual-band tunable bandstop quasi-Yagi-Uda antenna

The antenna structure along with the fabricated prototype are shown in Fig. 7.5. The substrate used to fabricate the antenna is a Rogers RO4003C substrate with relative permittivity of 3.38, loss tangent of 0.0027, and thickness of 0.8128 mm. The zoomed section of Fig. 7.5b illustrates that the gap G_1 in Fig. 7.1 is bridged to provide a direct path from input port of the filter to its output port. This path creates a wideband response for the filter with a notch frequency which is created by the coupled-line resonator. There are two shunt stubs adjacent to the bridged gap to improve the bandstop response. These shunt stubs create a barrier towards adding another bandstop resonator in parallel to the main transmission line. Hence, two bandstop filters with tunable frequencies are cascaded to generate dual-band response with independently tunable frequencies. There are four MA46H120 varactor diodes used in this structure with the equivalent model of R = 1.6 Ω, L = 0.05 nH and 0.15 pF $< C_{var} <$ 1.30 pF in the simulation results. Also, to choke the RF signal for DC biasing, 15 nH inductors are used [177]. In the present dual-filter configuration, the cascaded filter stages are not

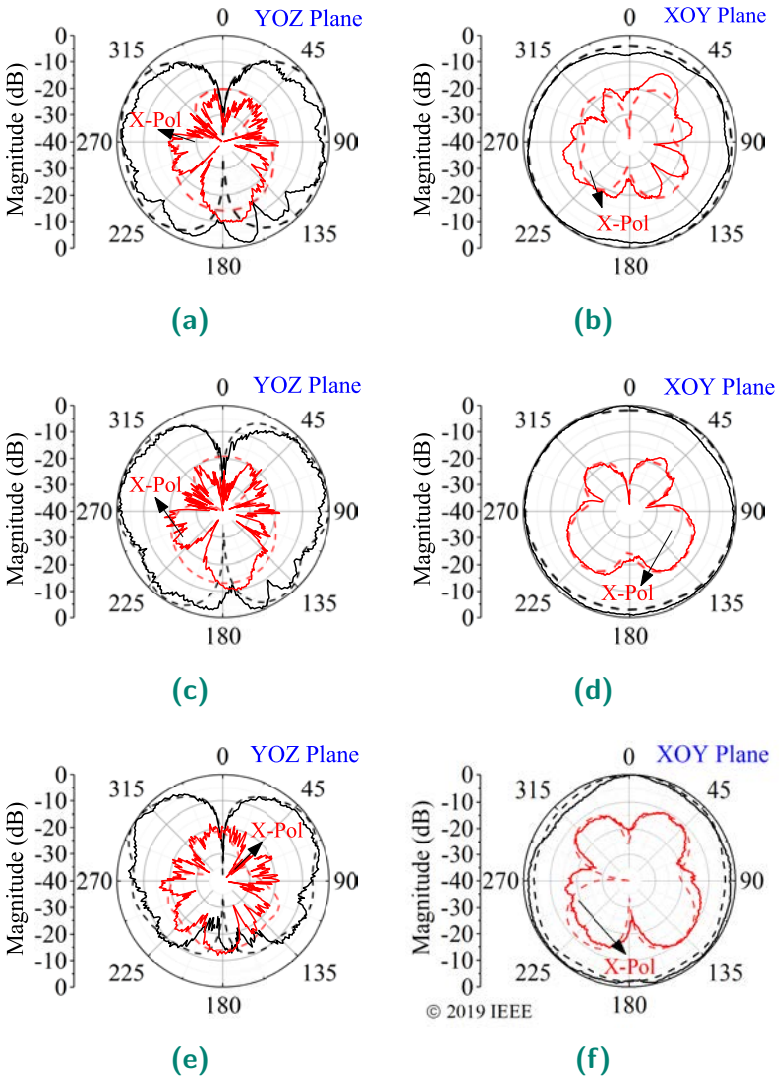

Figure 7.4. Solid lines: measured radiation patterns. Dashed lines: simulated radiation pattern for passband frequencies. (a) YOZ plane at 3.35 GHz. (b) XOY plane at 3.35 GHz. (c) YOZ plane at 4.4 GHz. (d) XOY plane at 4.4 GHz. (e) YOZ plane at 5.6 GHz. (f) XOY plane at 5.6 GHz.

exactly the same and the coupled-line for the second stage is longer than that of the first stage. This arrangement can help generate two adjacent transmission zeros in the stopband of the filter when all varactors are biased by the same voltage and the system is operating on a single-band state.

This filter excites a quasi-Yagi-Uda antenna structure which provides a wideband response covering the tuning range of the single/dual-band bandstop filter. The antenna system design dimensions, including widths and lengths of transmission lines are provided in Table 7.2. The simulation and measurement results for the single-band case are illustrated in Fig. 7.6. The notch-band frequency is tuned from 3.3 GHz to 5.40 GHz

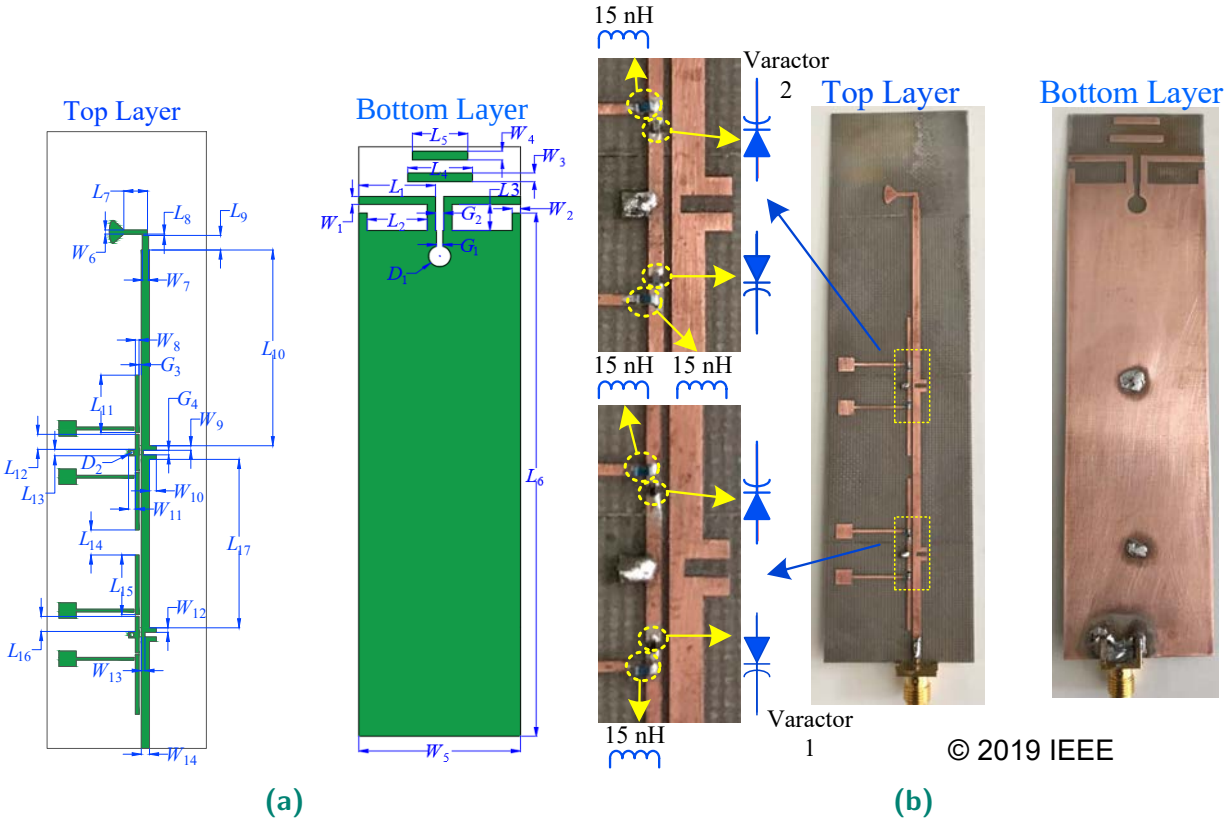

Figure 7.5. The proposed dual-band tunable bandstop antenna structure (a) Top layer and bottom layer of the simulated antennas. (b) Top layer and bottom layer of the fabricated prototype with zoomed section showing the position of varactors and inductors.

Table 7.2. Parameters of the tunable dual-band bandstop quasi-Yagi-Uda antenna

param.	value (mm)	param.	value (mm)	param.	value (mm)
W_1	1.8	W_{14}	1.8	L_{13}	1.4
W_2	1.8	L_1	16.6	L_{14}	5.5
W_3	2.0	L_2	13.0	L_{15}	13.1
W_4	2.0	L_3	6.0	L_{16}	3.3
W_5	35.0	L_4	14.0	L_{17}	37.0
W_6	0.9	L_5	12.0	D_1	4.8
W_7	1.4	L_6	120.1	D_2	1.0
W_8	0.8	L_7	5.2	G_1	1.4
W_9	1.0	L_8	0.3	G_2	1.9
W_{10}	1.5	L_9	3.2	G_3	0.5
W_{11}	1.5	L_{10}	43.0	G_4	1.0
W_{12}	1.0	L_{11}	12.6		
W_{13}	0.8	L_{12}	3.3		

with two adjacent transmission zeros in the stopband. For the dual-notch operation, as seen in Fig. 7.7, when the bias voltage of Varactor 1 is equal to 1.0 V (1.30 pF), the first band is fixed at 3.3 GHz. In this case, by changing the bias voltage for Varactor 2 from 4.80 V (0.40 pF) to 19.0 V (0.15 pF), the second notch-band is tuned from 4.40 GHz to 5.45 GHz. Likewise, based on Fig. 7.8, when the bias voltage of 19.0 V (0.15 pF) is applied to Varactor 2, a fixed notch-band at 5.45 GHz is generated and by changing the bias voltage for Varactor 1 from 1.0 V (1.30 pF) to 4.2 V (0.50 pF), the other stopband is tuned from 3.25 GHz to 4.2 GHz. Out-of-band radiation patterns at 6.5 GHz for E- and H-plane are plotted in Fig. 7.9. As seen, the radiation pattern of the quasi-Yagi-Uda antenna remains unaffected by the bandstop filter function.

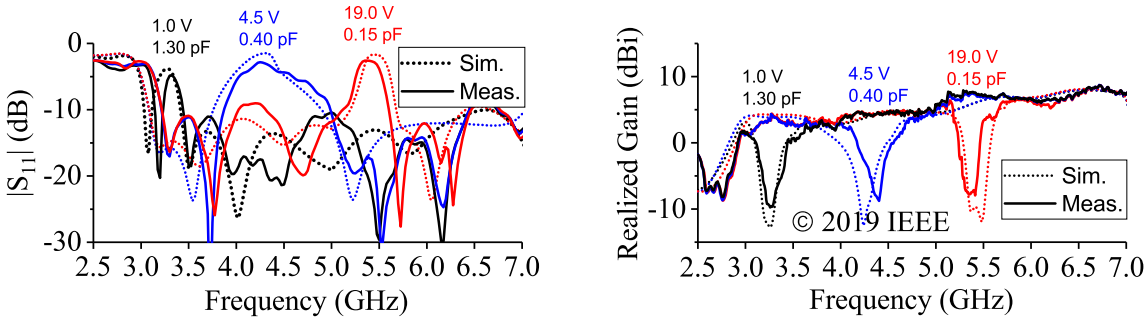

Figure 7.6. Measured and simulated frequency response of the antenna when the bias voltage of all varactors is varying from 19.0 V to 1.0 V (0.15 pF $< C_{var2} <$ 1.30 pF). (a) Reflection coefficient (b) Realized gain.

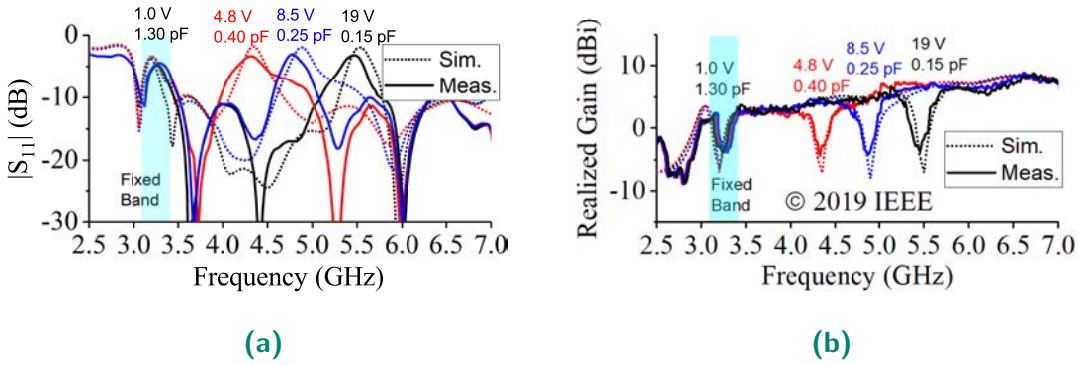

Figure 7.7. Measured and simulated frequency response of the antenna when the bias voltage of Varactor 1 is 1.0 V ($C_{var1} =$ 1.30 pF) and the bias voltage of Varactor 2 is varying from 19.0 V to 4.8 V (0.15 pF $< C_{var2} <$ 0.40 pF). (a) Reflection coefficient (b) Realized gain.

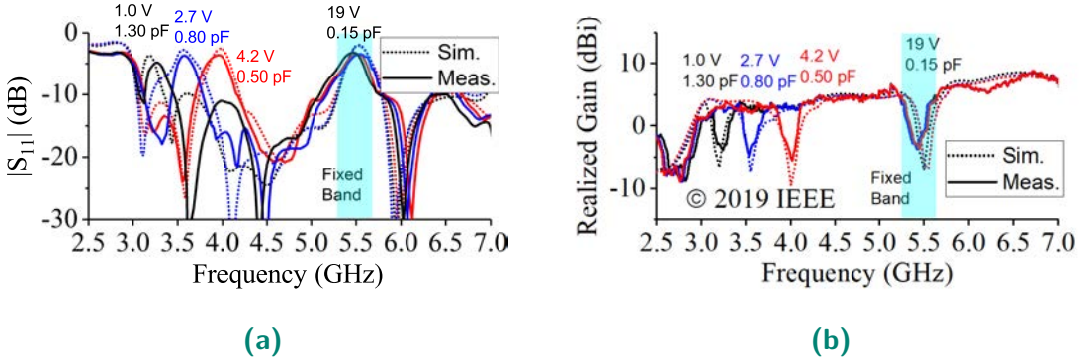

(a) (b)

Figure 7.8. Measured and simulated frequency response of the antenna when the bias voltage of Varactor 2 is 19 V (C_{var2} = 0.15 pF) and the bias voltage of Varactor 1 is varying from 4.2 V to 1.0 V (0.50 pF < C_{var1} < 1.30 pF). (a) Reflection coefficient (b) Realized gain.

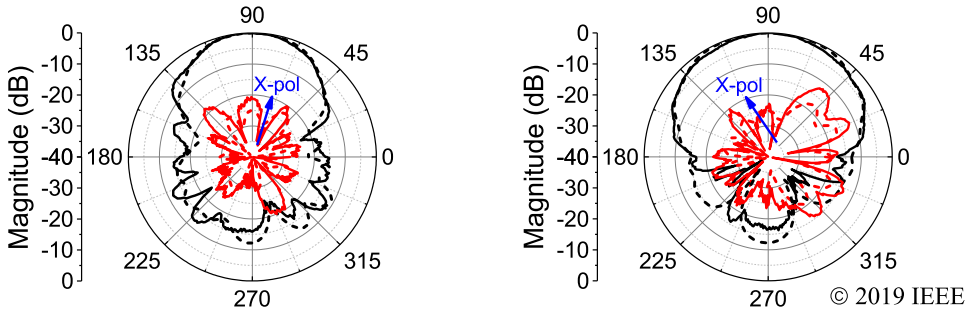

(a) (b)

Figure 7.9. Measured (solid line) versus simulated (dashed line) radiation pattern 6.5 GHz. (a) E-plane. (b) H-plane.

7.4 Conclusion

In the first part of this chapter, a design of an independently tunable dual-band bandpass antenna has been presented and experimentally verified. The antenna integrates a tunable filter and a printed oval-shaped monopole antenna. The two operating frequencies are controlled by four varactor diodes biased by two independent biasing voltages. Based on the measurement results, the relative tuning ranges for the lower band and the higher band are 24.0% and 26.0%, respectively. In the second part of the chapter, the single-band bandpass filter design has been evolved to a design of a second-order single-band or independently tunable first-order dual-band bandstop filter using cascaded filtering structures. The antenna integrates a tunable filter and a printed quasi-Yagi-Uda antenna. When the antenna is operating on its single-band

mode, all four varactors are biased by the same voltage. On the other hand, when the independently tunable dual-band state is activated, the operating frequencies are adjusted by two independent biasing voltages. The selection of antenna types for the tunable bandpass and tunable bandstop cases was only for demonstration and other combinations of planar wideband antennas could be in principle integrated with the presented filters.

Chapter 8

Conclusion and Outlook

THE research presented in this thesis has been clustered into two main parts which are pattern diversity antennas with wideband and ultrawideband responses on the one hand and pattern diversity and reconfigurable filtering antennas based on planar microstrip technology on the other hand. The first section has focused on different methods to enhance the bandwidth of sum and difference pattern diversity Vivaldi antennas. The general principle was based on a mitigation of mutual coupling between the antenna elements at lower frequencies while delaying the appearance of grating lobes at higher frequencies. This section has been followed by a description of a wideband microwave feeding network which is potentially applicable in pattern diversity antennas. The second part of the thesis has placed emphasis on different strategies for developing pattern diversity antennas with reconfigurable frequencies as well as different filtering functions. Multi-state reconfigurable filters have been integrated with multi-element wideband antennas to achieve the desired functionalities. This has been followed by a design of a pattern diversity patch antenna with sum and difference radiation patterns in both E- and H-plane. This chapter concludes these two major sections of this thesis and suggests prospective future investigation on related topics.

8.1 Summary preamble

This chapter provides a summary of the thesis original contributions, which is clustered into two major sections. The fundamental theme is the design of planar pattern diversity antennas. For future investigations, different research pathways are also suggested based on the research results obtained in this thesis.

8.2 Part I: Multi-element Vivaldi antennas with sum and difference radiation patterns

This part of the thesis consisting of Chapter 3 and 4 has focused on increasing the bandwidth and gain of multi-element Vivaldi antennas with sum and difference pattern diversity. To this end, a method to improve the trade-off between the two mutually exclusive problems of grating lobes at higher frequencies and high mutual coupling at low frequencies has been proposed.

8.2.1 Summary of original contributions

- As the first contribution presented in Chapter 3, an ultrawideband antipodal Vivaldi antenna with sum and difference pattern diversity has been proposed. The achieved operating bandwidth ranges from 2.3 GHz to 15 GHz, which corresponds to a ratio of 6.5:1. This bandwidth has been obtained through the reduction of the highest grating lobe level of -10 dB at 15 GHz by shortening the distance between each antenna element so that it meets the one wavelength distance criterion at 15 GHz. The mutual coupling has been reduced effectively by elongating the middle flare of the double-element antenna. This middle flare extends into a semicircle dielectric lens, which has been used for gain enhancement at higher frequencies. To further enhance the antenna performance, a combination of well-known methods, such as elliptical corrugations on the outer edges and optimal shaping of inner edges of the antenna has been adopted. An ultrawideband commercially available rat-race coupler has been used as a feeding network for this design. A near ideal beam symmetry has been attained for the proposed structure based on mirror symmetry of the antenna elements and using out-of-phase input signal for directive radiation pattern generation [48].

- The next contribution presented in Chapter 3 has helped enhance the gain of Vivaldi antennas with sum and difference radiation patterns by extending the idea of bandwidth enhancement to multi-element Vivaldi antennas. A quad-element antenna with increased proximity between its elements has been proposed in this chapter to tackle the problem of grating lobes while obtaining a higher gain. The three middle antenna flares have been elongated into the antenna dielectric lens to reduce the mutual coupling at lower operating frequencies. These four elements have been fed by two T-junction power dividers creating a dual-port structure. This structure has been externally fed by a commercially available wideband rat-race coupler. The antenna can generate sum and difference radiation patterns within the band of 3.9 GHz to 18 GHz, with a sum pattern gain increasing from 10 dBi at 3.9 GHz up to 16.5 dBi at 18 GHz [49].

- In Chapter 3, another method has been proposed to further enhance the bandwidth of double-element Vivaldi antennas with sum and difference pattern diversity to the range of 2.6 GHz to 18 GHz. This further bandwidth improvement has been facilitated by reduction of the mutual coupling level at lower frequencies of operation. It has been demonstrated that besides elongating the internal flare for double-element antennas, putting two vertical metal slabs between the elements can be an effective method for further isolation improvement. Through this isolation improvement method, the antenna elements can be arranged closer to one another, thereby delaying the grating lobe appearance at higher frequencies. Hence, the bandwidth can be extended [50].

- As a potential replacement for the external and expensive wideband coupler used to excite the multi-element Vivaldi antennas with sum and difference radiation patterns, a power divider structure has been presented in Chapter 4 which provides unequal power division at its output ports while covering a wideband response. This structure has been proposed based on the double-sided parallel-strip lines technology with an inserted conductor as a virtual ground. The wideband performance has been achieved based on optimizing an analytical design of a power divider with perfect matching at its port and ideal isolation between the output ports. The optimization has enhanced the overall band of operation by sacrificing the perfect isolation and return loss at the main frequency, which was achieved by modifying the impedance of only two transmission lines. The need for such optimization for each design iteration of the power divider has

been obviated using a third-order approximation based on the least squares fitting method. This design has been experimentally validated by developing a circuit with 25:1 power division ratio and 80% operational bandwidth referring to 15 dB return loss and isolation. Also, the other performance metrics, such as 0.8 dB amplitude deviation from the specified power division ratio and the phase difference between the output ports of $180\pm5^\circ$ based on experimental results have demonstrated that this design can potentially be a good candidate as pattern diversity antenna feeding network [51].

- The concept of active scattering parameters for multi-port antennas has been explained in the Appendix A with the emphasis on how using scattering parameters in lieu of active scattering parameters can lead to incorrect result interpretation for a multi-port antenna [52].

8.2.2 Future work

The pattern diversity antennas with ultrawideband responses presented in the first part of this thesis could be further improved to enhance their applicability in specific situations.

The first shortcoming is a linear polarization of these antennas. As circularly polarized pattern diversity antennas [6, 178] mitigate the effect of polarization mismatch in transceivers, development of pattern diversity antennas with ultrawideband and circular polarization or dual linear polarization is of vital importance that can be deemed as a possible future path of investigation for this topic.

The second shortcoming deals with the ability to generate sum and difference radiation patterns over the ultrawideband frequency range only on the E-plane of the antenna while for broader angular coverage, E- and H-plane pattern diversity is required. This can be acheived through perpendicular arrangement of two ultrawideband pattern diversity Vivaldi antennas. However, feeding network for this antenna arrangement will be quite bulky and expensive. Hence, a future investigation about the possible inexpensive and compact solutions is needed.

The third shortcoming is the bulky structure of the pattern diversity Vivaldi antennas we have proposed thus far. This necessitates further investigation about miniaturization of the feeding network while maintaining an ultrawideband response, as well as

development of more compact radiating elements featuring ultrawideband response and directive radiation patterns.

Last but not least, with the emergence of millimeter wave and terahertz applications in modern wireless communications, the need for ultrawideband pattern diversity antennas working in these regimes becomes highly desirable. Hence, designing pattern diversity antennas working at millimeter wave or terahertz frequencies, with high-performance fundamental building blocks for pattern diversity antennas at higher frequencies [179,180] can be another possible future investigation.

8.3 Part II: Reconfigurable antennas filter integration

This part of the thesis has focused on extracting unique responses for antennas based on the integration of several modules with different functionalities as presented in Chapters 5 to 7.

8.3.1 Summary of original contributions

- While the designs in Chapters 3 and 4 have emphasized on the bandwidth improvement of pattern diversity antennas, Chapter 5 has paid a particular attention to different states of reconfigurability for pattern diversity antennas. To this end, several modules have been integrated in an antenna system including a double-element E-plane quasi Yagi-Uda antenna, two tunable bandpass-to-bandstop filters, and a commercially available rat-race coupler. The double-element antenna has been designed to cover a wideband frequency range which is exploited for the overall tunable bandpass-to-bandstop filtering response. Tunable bandpass-to-bandstop filters have been developed using embedded PIN and varactor diodes in their structures. The PIN diodes have fulfilled the switching function between bandpass and bandstop states. The varactors have enabled the continuous frequency tuning function with tuning ranges reaching 50% for the bandpass state and 50.4% for the bandstop state. As the feeding module, an external coupler with wideband response has been utilized for sum and difference pattern diversity [53].

- Even though the tunable bandpass-to-bandstop filtering function in Chapter 5 is an attractive module for cognitive radio systems, a wideband operation state

for spectrum sensing has been missing in this particular design. Furthermore, the use of an external input coupler as a feeding network for sum and difference pattern generation was an inevitable requirement. These problems have sparked the motivation behind the antenna design presented in Chapter 6, where all three states of wideband, tunable bandpass, and tunable bandstop have been realized with sum and difference pattern switching in lieu of coupler-fed pattern diversity function. Hence, three different modules have been proposed and integrated for this purpose. The first module has been a triple-element quasi-Yagi-Uda antenna with a feeding arrangement which provides an in-built frequency independent phase inversion mechanism obviating the need for any external coupler. The second module which enables sum and difference pattern reconfigurability has been a triple-output and switchable power divider. The last module has been a filter which switches between three different states of allpass, tunable bandpass, and tunable bandstop with PIN diodes and varactors embedded in its structure. Based on the integration and experimental validation of these three modules, it has been demonstrated that this design can successfully implement sum and difference patterns over a 79.8% fractional bandwidth for the wideband state of operation, 51.3% tuning range for the bandpass state and 50.3% tuning range for the bandstop state [53].

- Another design presented in Chapter 6 has extended the idea of pattern diversity to two antenna planes, namely E- and H-plane. The requirement for broader angular space coverage and mitigation of multipath fading problem in modern communication systems has prompted the design of such pattern diversity antenna structure. To this end, a planar microstrip patch antenna with switchable E-plane sum and difference patterns has been proposed. The integration of ten PIN diodes in the patch antenna structure has facilitated this operation by selectively exciting two fundamental modes of TM01 and TM02 of the patch antenna. This design has then been extended to a double-element configuration along the H-plane with a rat-race coupler as a feeding network. As a result, a pattern diversity function along both E- and H-plane has been obtained [55], a performance which conventionally requires at least four antenna elements with three rat-race couplers as feeding networks.

- In Chapter 7, a dual-band independently tunable antenna has been designed which is potentially useful in applications such as carrier aggregation where one

primary fixed and one secondary tunable frequency response are required for higher throughput. The presented design has been proposed based on the integration of two different modules. The first module has been a wideband planar disc monopole antenna which has solely been used for demonstration and can be replaced by any other types of wideband and planar antennas. The second module has been a filter design with two independently tunable frequencies. The filter structure has been proposed based on the premise of the the tunable bandpass filter presented in Chapter 5. The two operating frequencies of the proposed dual-band filter have been shown to be continuously and independently tunable using four varactor diodes biased by two different and independent biasing voltages. Based on the integration of the filter and antenna, it has been observed and experimentally validated that the monopolar pattern of the whole antenna system remains intact at two independently tunable operating frequencies [56].

- Another design presented in Chapter 7 has investigated dual-band independently tunable and second-order single-band bandstop antennas based on antenna and filter integration. Such antennas are potentially applicable in cognitive radio and interference rejection systems. A quasi-Yagi-Uda antenna with a wideband performance has been adopted as the antenna module which covers the tunable dual-band bandstop tuning range. The independently tunable bandstop filter structure has been proposed based on cascading two tunable bandstop filter structures, similar as introduced in Chapter 5. Through this arrangement of the bandstop filters, the system can be used as a single-band tunable bandstop filter with second order response. The filter and antenna have been integrated to generate a bandstop antenna with a single second-order tuning notch frequency or a dual-band bandstop response with independently tunable frequencies. The design principle has been verified through measurement on a prototype, demonstrating the expected directive radiation pattern at the passband frequencies [57].

8.3.2 Future work

Several aspects of the reconfigurable antenna systems based on different design modules can be further investigated in future studies.

Firstly, the reconfigurable antenna systems proposed in this thesis suffered from a relatively high loss level at their lower operating frequencies mainly due to the quality

factors of the varactors and PIN diodes embedded in the structure. Hence, an emphasis can be put on using tuning elements with less loss or on developing structures with less susceptibility to the loss generated by these tuning elements.

Secondly, for the structure proposed in Chapter 6, the bandpass and bandstop tuning ranges are not covering the whole wideband spectrum of the antenna. This may limit the application of such antennas when the cognitive radio system, in its sensing state, detects an unused frequency band which is beyond the tuning range of bandpass or bandstop state. Hence, increasing the tuning range of the bandpass and bandstop filters can be explored in the future.

Thirdly, in Chapter 6 the beam symmetry of the sum and difference pattern-reconfigurable antenna systems has been sacrificed for other appealing functionalities. This is due to the use of three antenna elements as the radiating module. A possible future investigation can be a design of a pattern-reconfigurable antenna system with more beam symmetry in its radiation pattern.

Last but not least, the filters presented in Chapter 5 and Chapter 6 could benefit from increased selectivity in their bandstop states, since they have only weak poles in their passband. This will prompt the necessity for a future investigation of a filter design with multi-state reconfigurability and higher selectivity in its bandstop state.

8.4 Concluding statement

The research presented in this thesis has put an emphasis on the design, fabrication, and integration of several modules for ultrawideband and reconfigurable pattern diversity antennas. Different modules have been proposed including multi-element ultrawideband or wideband antennas, multi-state reconfigurable filters, switchable power dividers, switchable antennas, and wideband feeding networks. The main objective of this thesis has been to develop antenna systems with unique functionalities based on the integration of several modules each of which has a specific and novel characteristic. The successful and efficient realization of such antenna systems paves the way for development of future antenna systems with unique performance.

Appendix A

On the Importance of Active S-parameters for Multi-Port Antennas

THIS appendix investigates a misconception about antenna mutual coupling and its negative consequences on the interpretation of antenna results. This appendix also delves into the definition of Active S-parameters as utilized in several chapters through this thesis. To demonstrate the misconception and its adverse consequences on the result interpretation, the appendix specifically comments on an article recently published in the literature. To support the discussion and illustrate the misconception, an antenna prototype is fabricated and measured.

A.1 Introduction

As demonstrated in Chapter 3, the isolation between two antenna elements is of vital importance as it defines the amount of power loss and the operating bandwidth of multi-element antennas. When the level of mutual coupling between the antenna elements is high, the power will be coupled to the other ports rather then being radiated, and the functionality may be changed to a filtering function [181, 182].

In this appendix, a double-port microstrip patch antenna claimed to posses a broadband response with sum and difference radiation patterns is critically evaluated. It is demonstrated that the performance measures are misinterpreted, and that this misconception stems from neglecting the high level of mutual coupling between the antennas and considering the antenna gain instead of the antenna realized gain. These considerations are also to be published as comment on [183] in the Transactions on Antennas and Propagation [52].

A.2 Results and Discussions

In this appendix, some missing fundamental simulation and measurement results affecting the practical performance of the antenna presented in [183] are studied, as illustration of the importance of the concept of active S-parameters. In order to properly demonstrate the practical consequences of these omissions, we provide simulation results as well as experimental validation using a prototype with the exact dimensions as in [183], fed with an ultra-wideband coupler [109] as shown in Fig. A.1. The authors of [183] have claimed 68% fractional bandwidth for a multi-port antenna based only on a single-port input reflection coefficient (S_{11}). Unfortunately, the mutual coupling between the antenna ports (S_{21}) is not shown in their article. We have performed corresponding simulations using Ansys HFSS and found that the missing coupling coefficient between the elements within the band of interest has a magnitude close to 0 dB which is validated by the experimental results, as illustrated in Fig. A.2a. This suggests that the proposed design is operating as a wideband bandpass filter in lieu of a radiating element. The clear misunderstanding in the scattering performance arises from the fact that for dual-port antennas fed by in-phase and out-of-phase inputs, the *active scattering parameters* are of fundamental importance. Active scattering parameters for dual-port devices are defined as the combinations of S_{11} and S_{21} (some references such as [184, 185] use differential and common mode scattering parameters or S_{dd} and S_{cc}).

They determine the overall scattering performance when a feeding network is connected to a multi-port antenna. For instance, [186] ([[183], Ref. 20]) and also [184,185] aimed at reducing S_{dd11} to below -10 dB for the differential S-parameter. They use the correct definition of S_{dd11} as given below (equation (8) in [186]).

$$S_{dd11} = \frac{S_{11} - S_{12} - S_{21} + S_{22}}{2}. \tag{A.1}$$

Also, in [11] S_{cc11} and S_{dd11} are used to evaluate the S-parameters of a dual-port system with sum and difference radiation patterns. The definition of S_{cc11} is given as below according to [187,188]

$$S_{cc11} = \frac{S_{11} + S_{12} + S_{21} + S_{22}}{2}. \tag{A.2}$$

Moreover, [10,48] have used the Active S_{11} as the fundamental scattering parameters. In these cases, the formula used for Active S_{11} correspond to (A.1) when the input excitations are equal in amplitude and out-of-phase. Similarly, they correspond to (A.2) when the inputs are equal in amplitude and in-phase. On that basis, Fig. A.2b illustrates the missing active scattering parameters for the antenna in [183] under in-phase and out-of-phase excitations. The measured results at the Σ and Δ input ports of the coupler validate the high level of reflection for this structure when fed by a 180° hybrid coupler [109].

(a) (b)

Figure A.1. Photograph of the fabricated antenna with all the specified dimensions equal to those in [183]. (a) Top layer. (b) Antenna connected to the commercial hybrid coupler.

On the premise of the partial interpretation of scattering parameters, the authors of [183] have calculated and featured plots of the *gain* of the antenna versus frequency, as opposed to the *realized gain* of the antenna versus frequency. By definition, the gain of the antenna does not take the mismatch loss into account, whereas the realized gain

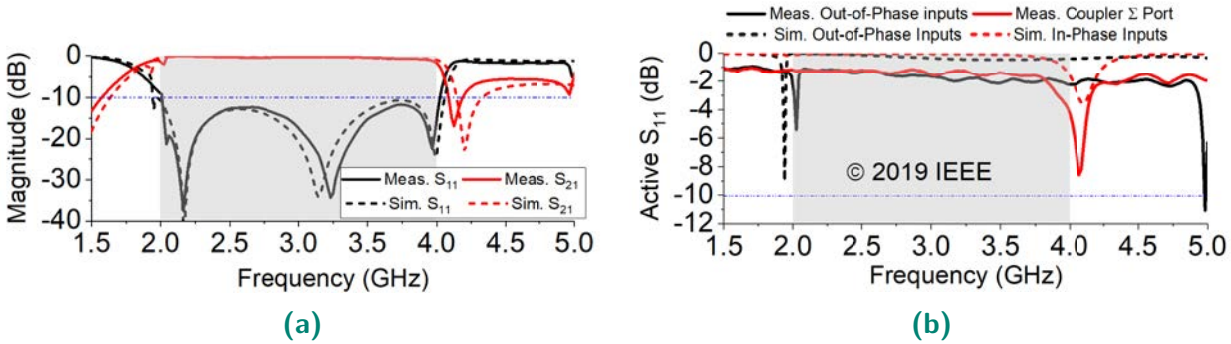

(a) (b)

Figure A.2. Scattering parameters of the antenna. (a) S_{11} which is shown in [183] and missing S_{21}. (b) Missing Active S_{11} for both in-phase and out-of-phase inputs. (The claimed bandwidth is indicated as the gray region)

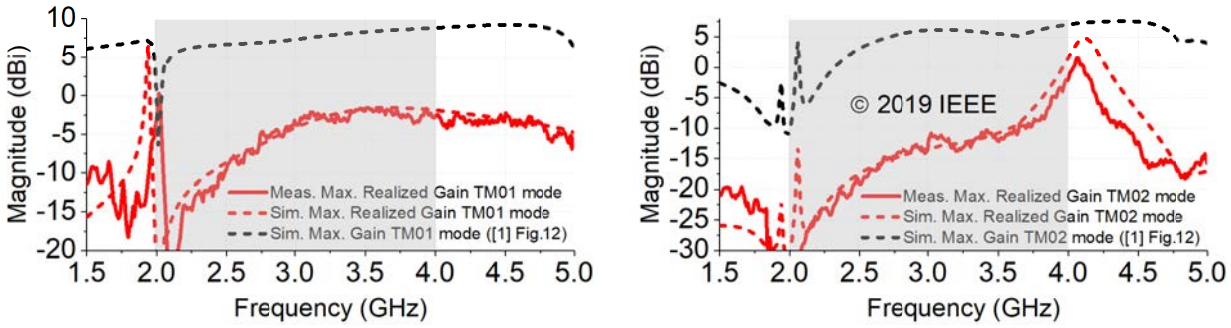

(a) (b)

Figure A.3. Variation of the maximum gain and maximum realized gain versus the frequency. (a) TM01 mode. (b) TM02 mode. (The claimed bandwidth is indicated as the gray region)

considers all mismatch losses. In fact, the realized gain corresponds to the gain directly measured in practice. This is why all aforementioned references apart from [183] are using realized gain as their radiation performance metrics. The difference between the maximum realized gain and maximum gain versus frequency is shown in Fig. A.3. It is also seen in Fig. A.3 that the measured values correlate well with the simulated realized gain. Evidently, the peak realized gain value is below 0 dB for both TM01 and TM02 modes of operation.

Figure A.4 further illustrates the issue by representing the gain pattern for the antenna in [183] compared to the realized gain, for both sum and difference patterns. There is a remarkable difference between the gain obtained without the mismatch loss and the realized gain taking into account the mismatch loss for the sum and difference excitation modes. This is also demonstrated by the measured results of the antenna. The measurement results agree well with the simulated realized gain patterns.

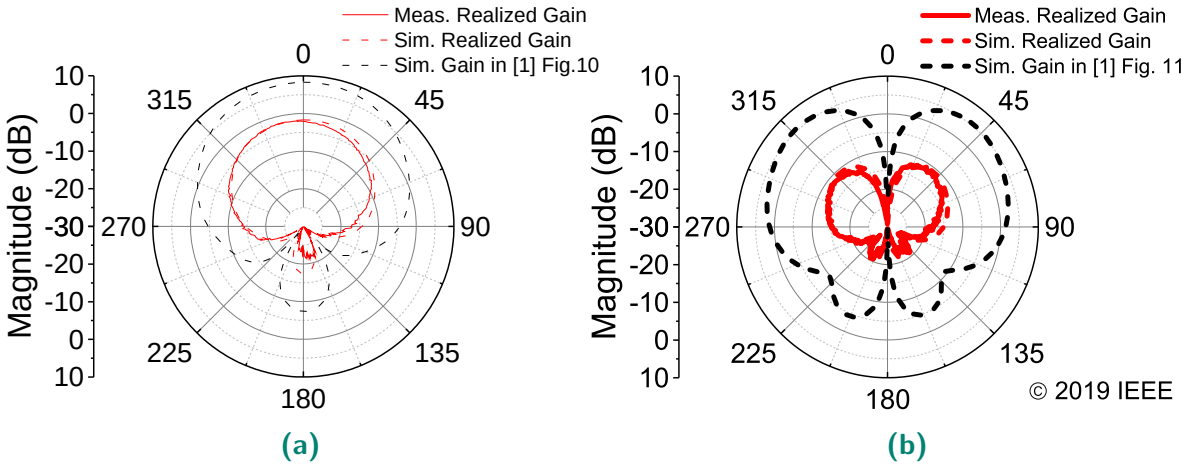

Figure A.4. Difference between the realized gain not shown in [183] and the gain shown in Fig. 11 of [183] at 3.5 GHz. (a) Sum radiation pattern $\phi = 0°$. (b) Difference radiation pattern $\phi = 0°$.

A.3 Conclusion

It has been demonstrated in this appendix that ignoring active scattering parameters and mutual coupling between the antennas can lead to an incorrect interpretation of the obtained results for dual-input antennas with pattern diversity. Based on the considerations, we have concluded that most of the input power for the antenna in [183] is transmitted to the second port, rather than being radiated. As such, the proposed structure performs like a wideband bandpass filter. Similarly, if the device is fed in common or differential mode, most of the input power is reflected.

Bibliography

[1] R. Vaughan and J. Andersen, "Antenna diversity in mobile communications," *IEEE Trans. Veh. Technol.*, vol. 36, no. 4, pp. 149–172, Nov. 1987.

[2] W. K. Toh, Z. N. Chen, X. Qing, and T. S. P. See, "A planar UWB diversity antenna," *IEEE Trans. Antennas Propag.*, vol. 57, no. 11, pp. 3467–3473, Nov. 2009.

[3] K. Wei, Z. Zhang, W. Chen, and Z. Feng, "A novel hybrid-fed patch antenna with pattern diversity," *IEEE Antennas Wireless Propag. Lett.*, vol. 9, pp. 562–565, 2010.

[4] X. Wang, Z. Feng, and K. Luk, "Pattern and polarization diversity antenna with high isolation for portable wireless devices," *IEEE Antennas Wireless Propag. Lett.*, vol. 8, pp. 209–211, 2009.

[5] S. Ko and R. Murch, "Compact integrated diversity antenna for wireless communications," *IEEE Trans. Antennas Propag.*, vol. 49, no. 6, pp. 954–960, Jun. 2001.

[6] C. Deng, Y. Li, Z. Zhang, and Z. Feng, "A circularly polarized pattern diversity antenna for hemispherical coverage," *IEEE Trans. Antennas Propag.*, vol. 62, no. 10, pp. 5365–5369, Oct. 2014.

[7] W. Lin, H. Wong, and R. W. Ziolkowski, "Circularly polarized antenna with reconfigurable broadside and conical beams facilitated by a mode switchable feed network," *IEEE Trans. Antennas Propag.*, vol. 66, no. 2, pp. 996–1001, Feb. 2018.

[8] L. Sun, G.-x. Zhang, B.-h. Sun, W.-d. Tang, and J.-p. Yuan, "A single patch antenna with broadside and conical radiation patterns for 3G/4G pattern diversity," *IEEE Antennas Wireless Propag. Lett.*, vol. 15, no. 1, pp. 433–436, 2016.

[9] L. Cui, W. Wu, and D.-G. Fang, "Wideband circular patch antenna for pattern diversity application," *IEEE Antennas Wireless Propag. Lett.*, vol. 14, pp. 1298–1301, 2015.

[10] Y.-W. Wang, G.-M. Wang, Z.-W. Yu, J.-G. Liang, and X.-J. Gao, "Ultra-wideband E-plane monopulse antenna using Vivaldi antenna," *IEEE Trans. Antennas Propag.*, vol. 62, no. 10, pp. 4961–4969, Oct. 2014.

[11] Y. Dong, J. Choi, and T. Itoh, "Vivaldi antenna with pattern diversity for 0.7 to 2.7 GHz cellular band applications," *IEEE Antennas Wireless Propag. Lett.*, vol. 17, no. 2, pp. 247–250, Feb. 2018.

[12] H. L. Peng, W.-Y. Yin, J.-F. Mao, and Y.-T. Xie, "A compact single/dual-polarized broadband antenna with sum and difference beam capabilities," *IEEE Antennas Wireless Propag. Lett.*, vol. 9, pp. 990–993, 2010.

[13] K. Saurav, N. K. Mallat, and Y. M. M. Antar, "A three-port polarization and pattern diversity ring antenna," *IEEE Antennas Wireless Propag. Lett.*, vol. 17, no. 7, pp. 1324–1328, Jul. 2018.

[14] R. Bhattacharya, R. Garg, and T. K. Bhattacharyya, "Design of a PIFA-driven compact Yagi-type pattern diversity antenna for handheld devices," *IEEE Antennas Wireless Propag. Lett.*, vol. 15, pp. 255–258, 2016.

[15] G. Kang, Z. Du, and K. Gong, "Novel compact quasi-dipole diversity antenna for mobile terminals," *IEEE Antennas Wireless Propag. Lett.*, vol. 10, pp. 1166–1169, 2011.

[16] N. P. Lawrence, C. Fumeaux, and D. Abbott, "Planar triorthogonal diversity slot antenna," *IEEE Trans. Antennas Propag.*, vol. 65, no. 3, pp. 1416–1421, Mar. 2017.

[17] N. Nguyen-Trong, S. X. Ta, M. Ikram, K. Bertling, and A. M. Abbosh, "A low-profile wideband tripolarized antenna," *IEEE Trans. Antennas Propag.*, vol. 67, no. 3, pp. 1946–1951, Mar. 2019.

[18] X. Li and Z.-P. Nie, "Mutual coupling effects on the performance of mimo wireless channels," *IEEE Antennas Wireless Propag. Lett.*, vol. 3, pp. 344–347, 2004.

[19] S. K. Dhar, M. S. Sharawi, O. Hammi, and F. M. Ghannouchi, "An active integrated ultra-wideband MIMO antenna," *IEEE Trans. Antennas Propag.*, vol. 64, no. 4, pp. 1573–1578, Apr. 2016.

[20] G.-S. Lin, C.-H. Sung, J.-L. Chen, L.-S. Chen, and M.-P. Houng, "Isolation improvement in UWB MIMO antenna system using carbon black film," *IEEE Antennas Wireless Propag. Lett.*, vol. 16, pp. 222–225, 2017.

[21] A. Toktas, "G-shaped band-notched ultra-wideband MIMO antenna system for mobile terminals," *IET Microwaves, Antennas Propag.*, vol. 11, no. 5, pp. 718–725, Apr. 2017.

[22] X. Zhao, S. P. Yeo, and L. C. Ong, "Planar UWB MIMO antenna with pattern diversity and isolation improvement for mobile platform based on the theory of characteristic modes," *IEEE Trans. Antennas Propag.*, vol. 66, no. 1, pp. 420–425, Jan. 2018.

[23] J. Tao and Q. Feng, "Compact ultrawideband MIMO antenna with half-slot structure," *IEEE Antennas Wireless Propag. Lett.*, vol. 16, pp. 792–795, 2017.

[24] M. Gallo, E. Antonino-Daviu, M. Ferrando-Bataller, M. Bozzetti, J. M. Molina-Garcia-Pardo, and L. Juan-Llacer, "A broadband pattern diversity annular slot antenna," *IEEE Trans. Antennas Propag.*, vol. 60, no. 3, pp. 1596–1600, Mar. 2012.

[25] M. G. N. Alsath and M. Kanagasabai, "Compact UWB monopole antenna for automotive communications," *IEEE Trans. Antennas Propag.*, vol. 63, no. 9, pp. 4204–4208, Sep. 2015.

[26] G. S. Reddy, A. Kamma, S. Kharche, J. Mukherjee, and S. K. Mishra, "Cross-configured directional UWB antennas for multidirectional pattern diversity characteristics," *IEEE Trans. Antennas Propag.*, vol. 63, no. 2, pp. 853–858, Feb. 2015.

[27] P. J. Gibson, "The vivaldi aerial," in *1979 9th European Microwave Conference*, Sep. 1979, pp. 101–105.

[28] R. Janaswamy and D. Schaubert, "Analysis of the tapered slot antenna," *IEEE Trans. Antennas Propag.*, vol. 35, no. 9, pp. 1058–1065, Sep. 1987.

[29] I. T. Nassar and T. M. Weller, "A novel method for improving antipodal Vivaldi antenna performance," *IEEE Trans. Antennas Propag.*, vol. 63, no. 7, pp. 3321–3324, Jul. 2015.

[30] L. Chang, S. He, J. Q. Zhang, and D. Li, "A Compact Dielectric-Loaded Log-Periodic Dipole Array (LPDA) Antenna," *IEEE Antennas Wireless Propag. Lett.*, vol. 16, pp. 2759–2762, 2017.

[31] X. Wei, J. Liu, and Y. Long, "Printed log-periodic monopole array antenna with a simple feeding structure," *IEEE Antennas Wireless Propag. Lett.*, vol. 17, no. 1, pp. 58–61, Jan. 2018.

[32] G. Zhai, Y. Cheng, Q. Yin, S. Zhu, and J. Gao, "Gain enhancement of printed log-periodic dipole array antenna using director cell," *IEEE Trans. Antennas Propag.*, vol. 62, no. 11, pp. 5915–5919, Nov. 2014.

[33] A. Gorbachev and V. Egorov, "A modified planar quasi-Yagi antenna for wireless communication applications," *IEEE Antennas Wireless Propag. Lett.*, vol. 8, pp. 1091–1093, 2009.

[34] J. Wu, Z. Zhao, Z. Nie, and Q.-H. Liu, "Bandwidth enhancement of a planar printed quasi-Yagi antenna with size reduction," *IEEE Trans. Antennas Propag.*, vol. 62, no. 1, pp. 463–467, Jan. 2014.

[35] J. Yeo and J.-I. Lee, "Bandwidth enhancement of double-dipole quasi-Yagi antenna using stepped slotline structure," *IEEE Antennas Wireless Propag. Lett.*, vol. 15, pp. 694–697, 2016.

[36] L. Lu, K. Ma, F. Meng, and K. S. Yeo, "Design of a 60-GHz quasi-Yagi antenna with novel ladder-like directors for gain and bandwidth enhancements," *IEEE Antennas Wireless Propag. Lett.*, vol. 15, pp. 682–685, 2016.

[37] G. S. Shiroma and W. A. Shiroma, "A two-element L-band quasi-Yagi antenna array with omnidirectional coverage," *IEEE Trans. Antennas Propag.*, vol. 55, no. 12, pp. 3713–3716, Dec. 2007.

[38] T. Li, H. Zhai, X. Wang, L. Li, and C. Liang, "Frequency-reconfigurable bow-tie antenna for bluetooth, WiMAX, and WLAN applications," *IEEE Antennas Wireless Propag. Lett.*, vol. 14, pp. 171–174, 2015.

[39] Y.-L. Ban, S.-C. Sun, P.-P. Li, J. L.-W. Li, and K. Kang, "Compact eight-band frequency reconfigurable antenna for LTE/WWAN tablet computer applications," *IEEE Trans. Antennas Propag.*, vol. 62, no. 1, pp. 471–475, Jan. 2014.

[40] L.-R. Tan, R.-X. Wu, and Y. Poo, "Magnetically reconfigurable SIW antenna with tunable frequencies and polarizations," *IEEE Trans. Antennas Propag.*, vol. 63, no. 6, pp. 2772–2776, Jun. 2015.

[41] C. Ni, M. S. Chen, Z. X. Zhang, and X. L. Wu, "Design of frequency-and polarization-reconfigurable antenna based on the polarization conversion metasurface," *IEEE Antennas Wireless Propag. Lett.*, vol. 17, no. 1, pp. 78–81, Jan. 2018.

[42] H. A. Majid, M. K. A. Rahim, M. R. Hamid, and M. F. Ismail, "Frequency and pattern reconfigurable slot antenna," *IEEE Trans. Antennas Propag.*, vol. 62, no. 10, pp. 5339–5343, Oct. 2014.

[43] N. Nguyen-Trong, L. Hall, and C. Fumeaux, "A frequency- and pattern-reconfigurable center-shorted microstrip antenna," *IEEE Antennas Wireless Propag. Lett.*, vol. 15, pp. 1955–1958, 2016.

[44] S. Raman, P. Mohanan, N. Timmons, and J. Morrison, "Microstrip-fed pattern- and polarization-reconfigurable compact truncated monopole antenna," *IEEE Antennas Wireless Propag. Lett.*, vol. 12, pp. 710–713, 2013.

[45] W. Cao, B. Zhang, A. Liu, T. Yu, D. Guo, and K. Pan, "A reconfigurable microstrip antenna with radiation pattern selectivity and polarization diversity," *IEEE Antennas Wireless Propag. Lett.*, vol. 11, pp. 453–456, Apr. 2012.

[46] N. Nguyen-Trong, A. T. Mobashsher, and A. M. Abbosh, "Reconfigurable shorted patch antenna with polarization and pattern diversity," in *2018 Australian Microwave Symposium (AMS)*, Feb. 2018, pp. 27–28.

[47] Y. Tawk, J. Costantine, and C. G. Christodoulou, "Cognitive-radio and antenna functionalities: A tutorial [wireless corner]," *IEEE Antennas and Propagation Magazine*, vol. 56, no. 1, pp. 231–243, Feb. 2014.

[48] S.-A. Malakooti, M. Moosazadeh, D. C. Ranasinghe, and C. Fumeaux, "Antipodal Vivaldi antenna for sum and difference radiation patterns with reduced grating lobes," *IEEE Antennas Wireless Propag. Lett.*, vol. 16, pp. 3139–3142, 2017.

[49] S. -A. Malakooti and C. Fumeaux, "Multi-element vivaldi antenna with sum and difference radiation patterns," in *2018 IEEE Asia-Pacific Conference on Antennas and Propagation (APCAP)*, Aug. 2018, pp. 1–2.

[50] S. A. Malakooti and C. Fumeaux, "Bandwidth enhancement of a double-element vivaldi antenna with sum and difference radiation patterns," in *2018 Asia-Pacific Microwave Conference (APMC)*, Nov. 2018, pp. 1166–1168.

[51] S. -A. Malakooti, M. Salarrahimi, and C. Fumeaux, "Wideband out-of-phase power divider with large power division ratios," in *2019 12th German Microwave Conference (GeMiC)*, Mar. 2019, pp. 174–177.

[52] S. -A. Malakooti and C. Fumeaux, "Comments on wideband radiation reconfigurable microstrip patch antenna loaded with two inverted U-slots," *IEEE Trans. Antennas Propag.*, vol. pp, no. 1, pp. 1–2, 2019.

[53] S. -A. Malakooti, S. M. H. Mousavi, and C. Fumeaux, "Tunable bandpass-to-bandstop quasi-Yagi-Uda antenna with sum and difference radiation patterns," *IEEE Trans. Antennas Propag.*, vol. 67, no. 4, pp. 2260–2271, Apr. 2019.

[54] S. -A. Malakooti and C. Fumeaux, "Pattern-reconfigurable antenna with switchable wideband to frequency-agile bandpass/bandstop filtering operation," *IEEE Access*, vol. 7, pp. 167 065–167 075, 2019.

[55] S. A. Malakooti and C. Fumeaux, "A pattern diversity microstrip antenna with switchable sum and difference beams in *e* - and *h*-plane," in *2019 International Conference on Electromagnetics in Advanced Applications (ICEAA), Granada, Spain*, Sep. 2019, pp. 0623–0625.

[56] S. -A. Malakooti and C. Fumeaux, "Dual-band bandpass filtering monopole antenna with independently tunable frequencies," in *IEEE Asia-Pacific Conference on Antennas and Propagation (APCAP), Incheon, Korea*, Aug. 2019, pp. 1–2.

[57] ——, "Independently tunable dual-band bandstop filtering antenna," in *IEEE Radio and Antenna Days of the Indian Ocean, Reunion Island, France*, Sep. 2019, pp. 1–2.

[58] H. Schantz, "A brief history of UWB antennas," in *IEEE Conf. Ultra Wideband Syst. Technol. 2003*, no. Apr. IEEE, 2003, pp. 209–213.

[59] T. Morgan, "Reduced size spiral antenna," in *1979 9th Eur. Microw. Conf.* IEEE, Sep. 1979, pp. 181–185.

[60] E. Soliman, S. Brebels, P. Delmotte, G. Vandenbosch, and E. Beyne, "Bow-tie slot antenna fed by CPW," *Electron. Lett.*, vol. 35, no. 7, p. 514, 1999.

[61] N. Agrawall, G. Kumar, and K. Ray, "Wide-band planar monopole antennas," *IEEE Trans. Antennas Propag.*, vol. 46, no. 2, pp. 294–295, 1998.

[62] C. Campbell, I. Traboulay, M. Suthers, and H. Kneve, "Design of a stripline log-periodic dipole antenna," *IEEE Trans. Antennas Propag.*, vol. 25, no. 5, pp. 718–721, Sep. 1977.

[63] A. Amini, H. Oraizi, and M. A. Chaychi zadeh, "Miniaturized uwb log-periodic square fractal antenna," *IEEE Antennas Wireless Propag. Lett.*, vol. 14, pp. 1322–1325, 2015.

[64] T. Ma, J. Ai, M. Shen, and W. T. Joines, "Design of novel broadband endfire dipole array antennas," *IEEE Antennas Wireless Propag. Lett.*, vol. 16, pp. 2935–2938, 2017.

[65] C. Yu, W. Hong, L. Chiu, G. Zhai, C. Yu, W. Qin, and Z. Kuai, "Ultrawideband printed log-periodic dipole antenna with multiple notched bands," *IEEE Trans. Antennas Propag.*, vol. 59, no. 3, pp. 725–732, Mar. 2011.

[66] J. George, M. Deepukumar, C. Aanandan, P. Mohanan, and K. Nair, "New compact microstrip antenna," *Electron. Lett.*, vol. 32, no. 6, p. 508, Jan. 1996.

[67] J. Bai, S. Shi, and D. W. Prather, "Modified compact antipodal vivaldi antenna for 4-50 GHz UWB application," *IEEE Trans. Microw. Theory Techn.*, vol. 59, no. 4, pp. 1051–1057, Apr. 2011.

[68] N. Rajesh, K. Malathi, S. Raju, V. Abhai KuMar., S. Deepak Ram Prasath, and M. G. N. Alsath, "Design of vivaldi antenna with wideband radar cross section reduction," *IEEE Trans. Antennas Propag.*, vol. 65, no. 4, pp. 2102–2105, Apr. 2017.

[69] Y. Qian, W. Deal, N. Kaneda, and T. Itoh, "Microstrip-fed quasi-Yagi antenna with broadband characteristics," *Electron. Lett.*, vol. 34, no. 23, p. 2194, 1998.

[70] D. Yang, J. Qu, Z. Zhao, S. Liu, and Z. Nie, "Planar quasi-Yagi antenna with band rejection based on dual dipole structure for UWB," *IET Microwaves, Antennas Propagation*, vol. 10, no. 15, pp. 1708–1714, Dec. 2016.

[71] J. G. Estrada, C. I. Pez, and A. Fajardo, "A new broadband quasi Yagi-Uda antenna with an EBG-truncated ground plane," *IEEE Antennas Wireless Propag. Lett.*, vol. 12, pp. 1392–1395, 2013.

[72] J. Wu, Z. Zhao, Z. Nie, and Q. Liu, "Design of a wideband planar printed quasi-Yagi antenna using stepped connection structure," *IEEE Trans. Antennas Propag.*, vol. 62, no. 6, pp. 3431–3435, Jun. 2014.

[73] A. Abbosh, "Ultra-wideband quasi-Yagi antenna using dual-resonant driver and integrated balun of stepped impedance coupled structure," *IEEE Trans. Antennas Propag.*, vol. 61, no. 7, pp. 3885–3888, Jul. 2013.

[74] J. Shi, X. Wu, Z. N. Chen, X. Qing, L. Lin, J. Chen, and Z. Bao, "A compact differential filtering quasi-Yagi antenna with high frequency selectivity and low cross-polarization levels," *IEEE Antennas Wireless Propag. Lett.*, vol. 14, pp. 1573–1576, 2015.

[75] K. Ebnabbasi, S. Sczyslo, and M. Mohebbi, "UWB performance of coplanar tapered slot antennas," *IEEE Antennas Wireless Propag. Lett.*, vol. 12, pp. 749–752, 2013.

[76] M. Abbak, M. N. Akinci, M. Cayoren, and I. Akduman, "Experimental microwave imaging with a novel corrugated Vivaldi antenna," *IEEE Trans. Antennas Propag.*, vol. 65, no. 6, pp. 3302–3307, Jun. 2017.

[77] Peng Fei, Yong-Chang Jiao, Wei Hu, and Fu-Shun Zhang, "A miniaturized antipodal Vivaldi antenna with improved radiation characteristics," *IEEE Antennas Wireless Propag. Lett.*, vol. 10, pp. 127–130, 2011.

[78] M. Moosazadeh, S. Kharkovsky, J. T. Case, and B. Samali, "Miniaturized UWB antipodal Vivaldi antenna and its application for detection of void inside concrete specimens," *IEEE Antennas Wireless Propag. Lett.*, vol. 16, pp. 1317–1320, 2017.

[79] M. Moosazadeh and S. Kharkovsky, "A compact high-gain and front-to-back ratio elliptically tapered antipodal Vivaldi antenna with trapezoid-shaped dielectric lens," *IEEE Antennas Wireless Propag. Lett.*, vol. 15, pp. 552–555, 2016.

[80] J. Huang and A. C. Densmore, "Microstrip Yagi array antenna for mobile satellite vehicle application," *IEEE Trans. Antennas Propag.*, vol. 39, no. 7, pp. 1024–1030, Jul. 1991.

[81] N. Kaneda, W. R. Deal, Yongxi Qian, R. Waterhouse, and T. Itoh, "A broadband planar quasi-Yagi antenna," *IEEE Trans. Antennas Propag.*, vol. 50, no. 8, pp. 1158–1160, Aug. 2002.

[82] P. T. Nguyen, A. Abbosh, and S. Crozier, "Wideband and compact quasi-Yagi antenna integrated with balun of microstrip to slotline transitions," *Electron. Lett.*, vol. 49, no. 2, pp. 88 –89, Jan. 2013.

[83] F. Yu, Y. Xie, and L. Zhang, "Single patch antenna with monopulse patterns," *IEEE Microw. Wireless Compon. Lett.*, vol. 26, no. 10, pp. 762–764, Oct. 2016.

[84] D. M. Pozar, *Microwave Engineering*, ser. Electrical science series. Hoboken, NJ, USA: John Wiley & Sons, 2014.

[85] X. Yang, H. Lin, H. Gu, L. Ge, and X. Zeng, "Broadband pattern diversity patch antenna with switchable feeding network," *IEEE Access*, vol. 6, pp. 69 612–69 619, 2018.

[86] N. Nguyen-Trong, L. Hall, and C. Fumeaux, "A frequency- and polarization-reconfigurable stub-loaded microstrip patch antenna," *IEEE Trans. Antennas Propag.*, vol. 63, no. 11, pp. 5235–5240, Nov. 2015.

[87] G. Jin, M. Li, D. Liu, and G. Zeng, "A simple planar pattern-reconfigurable antenna based on arc dipoles," *IEEE Antennas Wireless Propag. Lett.*, vol. 17, no. 9, pp. 1664–1668, Sep. 2018.

[88] W. Qin, J. Cai, Y. Li, and J. Chen, "Wideband tunable bandpass filter using optimized varactor-loaded SIRs," *IEEE Microw. Wireless Compon. Lett.*, vol. 27, no. 9, pp. 812–814, Sep. 2017.

[89] B. You, L. Chen, Y. Liang, and X. Wen, "A high-selectivity tunable dual-band bandpass filter using stub-loaded stepped-impedance resonators," *IEEE Microw. Wireless Compon. Lett.*, vol. 24, no. 11, pp. 736–738, Nov. 2014.

[90] A. Ebrahimi, T. Baum, J. Scott, and K. Ghorbani, "Continuously tunable dual-mode bandstop filter," *IEEE Microw. Wireless Compon. Lett.*, vol. 28, no. 5, pp. 419–421, May. 2018.

[91] Y. Wang, J. Chen, and K. Xu, "A system of tunable bandstop filters with wide tuning range of 1-6-GHz," in *2019 International Workshop on Electromagnetics: Applications and Student Innovation Competition (iWEM)*, Sep. 2019, pp. 1–2.

[92] Y. Cho and G.Rebeiz, "Two- and four-pole tunable 0.7-1.1-GHz bandpass-to-bandstop filters with bandwidth control," *IEEE Trans. Microw. Theory Techn.*, vol. 62, no. 3, pp. 457–463, Mar. 2014.

[93] P. Qin, F. Wei, and Y. J. Guo, "A wideband-to-narrowband tunable antenna using a reconfigurable filter," *IEEE Trans. Antennas Propag.*, vol. 63, no. 5, pp. 2282–2285, May. 2015.

[94] A. K. Horestani, Z. Shaterian, J. Naqui, F. Martn, and C. Fumeaux, "Reconfigurable and tunable S-shaped split-ring resonators and application in band-notched UWB antennas," *IEEE Trans. Antennas Propag.*, vol. 64, no. 9, pp. 3766–3776, Sep. 2016.

[95] B. J. Mohammed, A. M. Abbosh, S. Mustafa, and D. Ireland, "Microwave system for head imaging," *IEEE Trans. Instrum. Meas.*, vol. 63, no. 1, pp. 117–123, Jan. 2014.

[96] E. W. Reid, L. Ortiz-Balbuena, A. Ghadiri, and K. Moez, "A 324-element Vivaldi antenna array for radio astronomy instrumentation," *IEEE Trans. Instrum. Meas.*, vol. 61, no. 1, pp. 241–250, Jan. 2012.

[97] A. M. De Oliveira, M. B. Perotoni, S. T. Kofuji, and J. F. Justo, "A palm tree antipodal Vivaldi antenna with exponential slot edge for improved radiation pattern," *IEEE Antennas Wireless Propag. Lett.*, vol. 14, pp. 1334–1337, 2015.

[98] G. Teni, N. Zhang, J. Qiu, and P. Zhang, "Research on a novel miniaturized antipodal Vivaldi antenna with improved radiation," *IEEE Antennas Wireless Propag. Lett.*, vol. 12, pp. 417–420, 2013.

[99] Y.-W. Wang, G.-M. Wang, and B.-F. Zong, "Directivity improvement of Vivaldi antenna using double-slot structure," *IEEE Antennas Wireless Propag. Lett.*, vol. 12, pp. 1380–1383, 2013.

[100] C. Zhou, X. Gao, G. Wang, and Y. Wang, "Double-slot Vivaldi antenna with improved gain," *Electron. Lett.*, vol. 49, no. 18, pp. 1119–1121, Aug. 2013.

[101] Y. Q. Liu, J. G. Liang, and Y. W. Wang, "Gain-improved double-slot TSA with Y-shaped corrugated edges," *Electron. Lett.*, vol. 53, no. 12, pp. 759–760, Jun. 2017.

[102] Y. Zhang, E. Li, C. Wang, and G. Guo, "Radiation enhanced Vivaldi antenna with double-antipodal structure," *IEEE Antennas Wireless Propag. Lett.*, vol. 16, pp. 561–564, 2017.

[103] C. Chiu, F. Xu, S. Shen, and R. D. Murch, "Mutual coupling reduction of rotationally symmetric multiport antennas," *IEEE Trans. Antennas Propag.*, vol. 66, no. 10, pp. 5013–5021, Oct. 2018.

[104] M. Li, B. G. Zhong, and S. W. Cheung, "Isolation enhancement for mimo patch antennas using near-field resonators as coupling-mode transducers," *IEEE Trans. Antennas Propag.*, vol. 67, no. 2, pp. 755–764, Feb. 2019.

[105] J. Ghosh, D. Mitra, and S. Das, "Mutual coupling reduction of slot antenna array by controlling surface wave propagation," *IEEE Trans. Antennas Propag.*, vol. 67, no. 2, pp. 1352–1357, Feb. 2019.

[106] A. Jafargholi, A. Jafargholi, and J. H. Choi, "Mutual coupling reduction in an array of patch antennas using cll metamaterial superstrate for mimo applications," *IEEE Trans. Antennas Propag.*, vol. 67, no. 1, pp. 179–189, Jan. 2019.

[107] M. Moosazadeh, S. Kharkovsky, J. T. Case, and B. Samali, "Improved radiation characteristics of small antipodal Vivaldi antenna for microwave and millimeter-wave imaging applications," *IEEE Antennas Wireless Propag. Lett.*, vol. 16, no. 6, pp. 1961–1964, May. 2017.

[108] Y.-W. Wang, "Antipodal Vivaldi antenna with novel differentially fed structure for lowering cross-polarisation level," *Electron. Lett.*, vol. 53, no. 20, pp. 1341–1342, Sep. 2017.

[109] T. J. Russell, "High directivity TEM mode strip line coupler and method of making same," Granted Patent US 4 139 827 A, 1979.

[110] Y. So, W. Kim, J. Kim, Y. J. Yoon, and J. Park, "Double-slot antipodal vivaldi antenna for improved directivity and radiation patterns," in *2016 International Symposium on Antennas and Propagation (ISAP)*, Oct. 2016, pp. 382–383.

[111] C. Jian-Xin, C. H. K. Chin, and Q. Xue, "Double-sided parallel-strip line with an inserted conductor plane and its applications," *IEEE Trans. Microw. Theory Techn.*, vol. 55, no. 9, pp. 1899–1904, Sep. 2007.

[112] J.-X. Chen and Q. Xue, "Novel 5:1 unequal wilkinson power divider using offset double-sided parallel-strip lines," *IEEE Microw. Wireless Compon. Lett.*, vol. 17, no. 3, pp. 175–177, Mar. 2007.

[113] J.-X. Chen, C. H. K. Chin, K. W. Lau, and Q. Xue, "180° out-of-phase power divider based on double-sided parallel striplines," *Electron. Lett.*, vol. 42, no. 21, pp. 1229–1230, Oct. 2006.

[114] L. Chiu and Q. Xue, "A parallel-strip ring power divider with high isolation and arbitrary power-dividing ratio," *IEEE Trans. Microw. Theory Techn.*, vol. 55, no. 11, pp. 2419–2426, Nov. 2007.

[115] G. Dai, X. Wei, E. Li, and M. Xia, "Novel dual-band out-of-phase power divider with high power-handling capability," *IEEE Trans. Microw. Theory Techn.*, vol. 60, no. 8, pp. 2403–2409, Aug. 2012.

[116] Y. L. Lu, G.-L. Dai, X. Wei, and E. Li, "A broadband out-of-phase power divider for high power applications using through ground via (tgv)," *IEEE Trans. Microw. Theory Techn.*, vol. 137, pp. 653–667, 2013.

[117] Y. L. Lu, G. Da, and K. Li, "A novel unequal broadband out-of-phase power divider using dspsls," *ETRI Journal*, vol. 36, no. 1, pp. 116–123, 2014.

[118] S. M. H. Mousavi, M. Salar Rahimi, B. Afzali, and B. S. Virdee, "A broadband out-of-phase gysel power divider based on a dual-band circuit with a single fixed isolation resistor," *International Journal of RF and Microwave Computer-Aided Engineering*, vol. 26, no. 9, pp. 796–802, 2016.

[119] A. M. Abbosh, "Planar out-of-phase power divider/combiner for wideband high power microwave applications," *IEEE Trans. Compon. Packag. Manuf. Technol.*, vol. 4, no. 3, pp. 465–471, Mar. 2014.

[120] U. H. Gysel, "A new N-way power divider/combiner suitable for high-power applications," in *1975 IEEE-MTT-S International Microwave Symposium*, May. 1975, pp. 116–118.

[121] K. M. Cheng and P. Li, "A novel power-divider design with unequal power-dividing ratio and simple layout," *IEEE Trans. Microw. Theory Techn.*, vol. 57, no. 6, pp. 1589–1594, Jun. 2009.

[122] J. Deng, S. Hou, L. Zhao, and L. Guo, "Wideband-to-narrowband tunable monopole antenna with integrated bandpass filters for UWB/WLAN applications," *IEEE Antennas Wireless Propag. Lett.*, vol. 16, pp. 2734–2737, 2017.

[123] J. Deng, S. Hou, L. Zhao, and L. Guo, "A reconfigurable filtering antenna with integrated bandpass filters for UWB/WLAN applications," *IEEE Trans. Antennas Propag.*, vol. 66, no. 1, pp. 401–404, Jan. 2018.

[124] M. Tang, Z. Wen, H. Wang, M. Li, and R. W. Ziolkowski, "Compact, frequency-reconfigurable filtenna with sharply defined wideband and continuously tunable narrowband states," *IEEE Trans. Antennas Propag.*, vol. 65, no. 10, pp. 5026–5034, Oct. 2017.

[125] M. R. Hamid, P. Gardner, P. S. Hall, and F. Ghanem, "Switched-band vivaldi antenna," *IEEE Trans. Antennas Propag.*, vol. 59, no. 5, pp. 1472–1480, May. 2011.

[126] M. R. Hamid, P. Gardner, P. S. Hall, and F. Ghanem, "Vivaldi antenna with integrated switchable band pass resonator," *IEEE Trans. Antennas Propag.*, vol. 59, no. 11, pp. 4008–4015, Nov. 2011.

[127] L. Ge and K. M. Luk, "Band-reconfigurable unidirectional antenna: a simple, efficient magneto-electric antenna for cognitive radio applications." *IEEE Antennas and Propagation Magazine*, vol. 58, no. 2, pp. 18–27, Apr. 2016.

[128] E. Erfani, J. Nourinia, C. Ghobadi, M. Niroo-Jazi, and T. A. Denidni, "Design and implementation of an integrated UWB/reconfigurable-slot antenna for cognitive radio applications," *IEEE Antennas Wireless Propag. Lett.*, vol. 11, pp. 77–80, 2012.

[129] Y. Tawk, J. Costantine, and C. G. Christodoulou, "A varactor-based reconfigurable filtenna," *IEEE Antennas Wireless Propag. Lett.*, vol. 11, pp. 716–719, 2012.

[130] Y. Dong and T. Itoh, "Planar ultra-wideband antennas in ku- and k-band for pattern or polarization diversity applications," *IEEE Trans. Antennas Propag.*, vol. 60, no. 6, pp. 2886–2895, Jun. 2012.

[131] Y. Yao, X. Wang, X. Chen, J. Yu, and S. Liu, "Novel diversity/MIMO PIFA antenna with broadband circular polarization for multimode satellite navigation," *IEEE Antennas Wireless Propag. Lett.*, vol. 11, pp. 65–68, 2012.

[132] A. Ramadan, J. Costantine, Y. Tawk, C. Christodoulou, and K. Kabalan, "Frequency tunable and pattern diversity antennas for cognitive radio applications," *International Journal of Antennas and Propagation*, vol. 2014, pp. 1–7, Mar. 2014.

[133] Z. Hao, H. Wang, and W. Hong, "A novel planar reconfigurable monopulse antenna for indoor smart wireless access points application," *IEEE Trans. Antennas Propag.*, vol. 64, no. 4, pp. 1250–1261, Apr. 2016.

[134] T. H. Lim, J. Park, and H. Choo, "Design of a vivaldi-fed hybrid horn antenna for low-frequency gain enhancement," *IEEE Trans. Antennas Propag.*, vol. 66, no. 1, pp. 438–443, Jan. 2018.

[135] H. Jin, Y. M. Huang, H. Jin, and K. Wu, "E-band substrate integrated waveguide orthomode transducer integrated with dual-polarized horn antenna," *IEEE Trans. Antennas Propag.*, vol. 66, no. 5, pp. 2291–2298, May. 2018.

[136] R. Hashmi and K. Esselle, "A class of extremely wideband resonant cavity antennas with large directivity-bandwidth products," *IEEE Trans. Antennas Propag.*, vol. 64, no. 2, pp. 830–835, Feb. 2016.

[137] R. Hashmi and K.Esselle, "Single-feed low-profile resonant cavity antenna covering entire ku-band," *Electron. Lett.*, vol. 52, no. 9, pp. 683–684, Apr. 2016.

[138] E. J. Naglich, J. Lee, D. Peroulis, and W. J. Chappell, "A tunable bandpass-to-bandstop reconfigurable filter with independent bandwidths and tunable response shape," *IEEE Trans. Microw. Theory Techn.*, vol. 58, no. 12, pp. 3770–3779, Dec. 2010.

[139] J. Lee, E. J. Naglich, H. H. Sigmarsson, D. Peroulis, and W. J. Chappell, "New bandstop filter circuit topology and its application to design of a bandstop-to-bandpass switchable filter," *IEEE Trans. Microw. Theory Techn.*, vol. 61, no. 3, pp. 1114–1123, Mar. 2013.

[140] T. Yang and G. M. Rebeiz, "Bandpass-to-bandstop reconfigurable tunable filters with frequency and bandwidth controls," *IEEE Trans. Microw. Theory Techn.*, vol. 65, no. 7, pp. 2288–2297, Jul. 2017.

[141] Y. Cho and G. Rebeiz, "0.7-1.0-GHz reconfigurable bandpass-to-bandstop filter with selectable 2- and 4-pole responses," *IEEE Trans. Microw. Theory Techn.*, vol. 62, no. 11, pp. 2626–2632, Nov. 2014.

[142] D. Lu, N. S. Barker, and X. Tang, "A simple frequency-agile bandpass filter with predefined bandwidth and stopband using synchronously tuned dual-mode resonator," *IEEE Microw. Wireless Compon. Lett.*, vol. 27, no. 11, pp. 983–985, Nov. 2017.

[143] J. S. Hong and M. J. Lancaster, *Microstrip filters for RF/microwave applications*, ser. Electrical science series. New York: Wiley, 2011.

[144] R. Garg, I. Bahl, and M. Bozzi, *Microstrip Lines and Slotlines*, ser. Electrical science series. Boston: Artech House, 2013.

[145] Y. Tawk, A. El-Amine, S. Saab, J. Costantine, F. Ayoub, and C. G. Christodoulou, "A software-defined frequency-reconfigurable meandered printed monopole," *IEEE Antennas Wireless Propag. Lett.*, vol. 17, no. 2, pp. 327–330, Feb. 2018.

[146] M. Shirazi, J. Huang, T. Li, and X. Gong, "A switchable-frequency slot-ring antenna element for designing a reconfigurable array," *IEEE Antennas Wireless Propag. Lett.*, vol. 17, no. 2, pp. 229–233, Feb. 2018.

[147] Y. Cai, K. Li, Y. Yin, S. Gao, W. Hu, and L. Zhao, "A low-profile frequency reconfigurable grid-slotted patch antenna," *IEEE Access*, vol. 6, pp. 36 305–36 312, 2018.

[148] F. Sun, F. Zhang, H. Zhang, H. Zhang, C. Li, and C. Feng, "A frequency diversity printed-yagi antenna element for apertures selectivity wideband array application," *IEEE Trans. Antennas Propag.*, vol. 66, no. 10, pp. 5634–5638, Oct. 2018.

[149] M. S. Alam and A. M. Abbosh, "Wideband pattern-reconfigurable antenna using pair of radial radiators on truncated ground with switchable director and reflector," *IEEE Antennas Wireless Propag. Lett.*, vol. 16, pp. 24–28, 2017.

[150] Y. Tawk, J. Costantine, and C. G. Christodoulou, "An eight-element reconfigurable diversity dipole system," *IEEE Trans. Antennas Propag.*, vol. 66, no. 2, pp. 572–581, Feb. 2018.

[151] S.-L. Chen, P.-Y. Qin, W. Lin, and Y. J. Guo, "Pattern-reconfigurable antenna with five switchable beams in elevation plane," *IEEE Antennas Wireless Propag. Lett.*, vol. 17, no. 3, pp. 454–457, Mar. 2018.

[152] A. Panahi, X. L. Bao, K. Yang, O. OConchubhair, and M. J. Ammann, "A simple polarization reconfigurable printed monopole antenna," *IEEE Trans. Antennas Propag.*, vol. 63, no. 11, pp. 5129–5134, Nov. 2015.

[153] H. Sun and S. Sun, "A novel reconfigurable feeding network for quad-polarization-agile antenna design," *IEEE Trans. Antennas Propag.*, vol. 64, no. 1, pp. 311–316, Jan. 2016.

[154] J. Row and Y. Wei, "Wideband reconfigurable crossed-dipole antenna with quad-polarization diversity," *IEEE Trans. Antennas Propag.*, vol. 66, no. 4, pp. 2090–2094, Apr. 2018.

[155] F. Farzami, S. Khaledian, B. Smida, and D. Erricolo, "Reconfigurable linear/circular polarization rectangular waveguide filtenna," *IEEE Trans. Antennas Propag.*, vol. 66, no. 1, pp. 9–15, Jan. 2018.

[156] P. K. Li, Z. H. Shao, Q. Wang, and Y. J. Cheng, "Frequency- and pattern-reconfigurable antenna for multistandard wireless applications," *IEEE Antennas Wireless Propag. Lett.*, vol. 14, pp. 333–336, 2015.

[157] S. Chen, P. Qin, C. Ding, and Y. J. Guo, "Cavity-backed proximity-coupled reconfigurable microstrip antenna with agile polarizations and steerable beams," *IEEE Trans. Antennas Propag.*, vol. 65, no. 10, pp. 5553–5558, Oct. 2017.

[158] J. Hu and Z. Hao, "A compact polarization-reconfigurable and 2-D beam-switchable antenna using the spatial phase shift technique," *IEEE Trans. Antennas Propag.*, vol. 66, no. 10, pp. 4986–4995, Oct. 2018.

[159] E. Ebrahimi, J. R. Kelly, and P. S. Hall, "Integrated wide-narrowband antenna for multi-standard radio," *IEEE Trans. Antennas Propag.*, vol. 59, no. 7, pp. 2628–2635, Jul. 2011.

[160] A. Mansoul, F. Ghanem, M. R. Hamid, and M. Trabelsi, "A selective frequency-reconfigurable antenna for cognitive radio applications," *IEEE Antennas Wireless Propag. Lett.*, vol. 13, pp. 515–518, 2014.

[161] Z. Yu, G. Wang, and C. Zhang, "A broadband planar monopulse antenna array of C-band," *IEEE Antennas Wireless Propag. Lett.*, vol. 8, pp. 1325–1328, 2009.

[162] E. J. Wilkinson, "An N-way hybrid power divider," *IRE Transactions on Microwave Theory and Techniques*, vol. 8, no. 1, pp. 116–118, Jan. 1960.

[163] F. Chen, R. Li, and J. Chen, "A tunable dual-band bandpass-to-bandstop filter using p-i-n diodes and varactors," *IEEE Access*, vol. 6, pp. 46 058–46 065, 2018.

[164] Q. Bai, R. Singh, K. L. Ford, T. OFarrell, and R. J. Langley, "An independently tunable tri-band antenna design for concurrent multiband single chain radio receivers," *IEEE Trans. Antennas Propag.*, vol. 65, no. 12, pp. 6290–6297, Dec. 2017.

[165] B. Avser and G. M. Rebeiz, "Tunable dual-band antennas for 0.7-1.1-GHz and 1.7-2.3-GHz carrier aggregation systems," *IEEE Trans. Antennas Propag.*, vol. 63, no. 4, pp. 1498–1504, Apr. 2015.

[166] N. Nguyen-Trong, A. Piotrowski, and C. Fumeaux, "A frequency-reconfigurable dual-band low-profile monopolar antenna," *IEEE Trans. Antennas Propag.*, vol. 65, no. 7, pp. 3336–3343, Jul. 2017.

[167] H. Lee, K. L. Ford, and R. J. Langley, "Independently tunable low-profile dual-band high-impedance surface antenna system for applications in UHF band," *IEEE Trans. Antennas Propag.*, vol. 60, no. 9, pp. 4092–4101, Sep. 2012.

[168] M. Tang, H. Wang, T. Deng, and R. W. Ziolkowski, "Compact planar ultrawideband antennas with continuously tunable, independent band-notched filters," *IEEE Trans. Antennas Propag.*, vol. 64, no. 8, pp. 3292–3301, Aug. 2016.

[169] B. Rahmati and H. R. Hassani, "Wideband planar plate monopole antenna with dual tunable notch," *Electron. Lett.*, vol. 46, no. 7, pp. 480–481, Apr. 2010.

[170] T. Li, H. Zhai, L. Li, C. Liang, and Y. Han, "Compact UWB antenna with tunable band-notched characteristic based on microstrip open-loop resonator," *IEEE Antennas Wireless Propag. Lett.*, vol. 11, pp. 1584–1587, 2012.

[171] R. Gmez-Garca and A. C. Guyette, "Reconfigurable multi-band microwave filters," *IEEE Trans. Microw. Theory Techn.*, vol. 63, no. 4, pp. 1294–1307, Apr. 2015.

[172] D. Psychogiou, B. Vaughn, R. Gmez-Garca, and D. Peroulis, "Reconfigurable multiband band-pass filters in evanescent-mode-cavity-resonator technology," *IEEE Microw. Wireless Compon. Lett.*, vol. 27, no. 3, pp. 248–250, Mar. 2017.

[173] Y.-H. Cho and G. M. Rebeiz, "Tunable 4-pole dual-notch filters for cognitive radios and carrier aggregation systems," *IEEE Trans. Microw. Theory Techn.*, vol. 63, no. 4, pp. 1308–1314, Apr. 2015.

[174] M. Esmaeili and J. Bornemann, "Novel tunable bandstop resonators in SIW technology and their application to a dual-bandstop filter with one tunable stopband," *IEEE Microw. Wireless Compon. Lett.*, vol. 27, no. 1, pp. 40–42, Jan. 2017.

[175] C.-H. Ko, A. Tran, and G. M. Rebeiz, "Tunable 500-1200-MHz dual-band and wide bandwidth notch filters using rf transformers," *IEEE Trans. Microw. Theory Techn.*, vol. 63, no. 6, pp. 1854–1862, Jun. 2015.

[176] D. Lu, X. Tang, N. S. Barker, and Y. Feng, "Single-band and switchable dual-/single-band tunable BPFs with predefined tuning range, bandwidth, and selectivity," *IEEE Trans. Microw. Theory Techn.*, vol. 66, no. 3, pp. 1215–1227, Mar. 2018.

[177] N. Nguyen-Trong, T. Kaufmann, L. Hall, and C. Fumeaux, "Analysis and design of a reconfigurable antenna based on half-mode substrate-integrated cavity," *IEEE Trans. Antennas Propag.*, vol. 63, no. 8, pp. 3345–3353, Aug. 2015.

[178] S. Maddio, "A circularly polarized switched beam antenna with pattern diversity for WiFi applications," *IEEE Antennas Wireless Propag. Lett.*, vol. 16, pp. 125–128, 2017.

[179] M.-Y. Huang and H. Wang, "An ultra-compact folded inductor based mm-wave rat-race coupler in CMOS," in *2016 IEEE MTT-S International Microwave Symposium (IMS)*, May. 2016, pp. 1–4.

[180] S. M. Moghaddam, J. Yang, and A. A. Glazunov, "Ultra-wideband millimeter-wave bowtie antenna," in *2017 International Symposium on Antennas and Propagation (ISAP)*, Oct. 2017, pp. 1–2.

[181] H. Zhang and K. J. Chen, "A tri-section stepped-impedance resonator for cross-coupled bandpass filters," *IEEE Microw. Wireless Compon. Lett.*, vol. 15, no. 6, pp. 401–403, Jun. 2005.

[182] C. Tang and M. Chen, "A microstrip ultra-wideband bandpass filter with cascaded broadband bandpass and bandstop filters," *IEEE Trans. Microw. Theory Techn.*, vol. 55, no. 11, pp. 2412–2418, Nov. 2007.

[183] S. Radavaram and M. Pour, "Wideband radiation reconfigurable microstrip patch antenna loaded with two inverted U-slots," *IEEE Trans. Antennas Propag.*, vol. 67, no. 3, pp. 1501–1508, Mar. 2019.

[184] Q. Xue, S. W. Liao, and J. H. Xu, "A differentially-driven dual-polarized magneto-electric dipole antenna," *IEEE Trans. Antennas Propag.*, vol. 61, no. 1, pp. 425–430, Jan. 2013.

[185] N. Liu, L. Zhu, W. Choi, and J. Zhang, "A low-profile differentially fed microstrip patch antenna with broad impedance bandwidth under triple-mode resonance," *IEEE Antennas Wireless Propag. Lett.*, vol. 17, no. 8, pp. 1478–1482, Aug. 2018.

[186] N. Liu, L. Zhu, X. Zhang, and W. Choi, "A wideband differential-fed dual-polarized microstrip antenna under radiation of dual improved odd-order resonant modes," *IEEE Access*, vol. 5, pp. 23 672–23 680, 2017.

[187] W. Li, Z. Tu, Q. Chu, and X. Wu, "Differential stepped-slot uwb antenna with common-mode suppression and dual sharp-selectivity notched bands," *IEEE Antennas Wireless Propag. Lett.*, vol. 15, pp. 1120–1123, 2016.

[188] D. E. Bockelman and W. R. Eisenstadt, "Combined differential and common-mode scattering parameters: theory and simulation," *IEEE Trans. Microw. Theory Techn.*, vol. 43, no. 7, pp. 1530–1539, Jul. 1995.

Biography

Seyedali Malakooti was born in Tehran, Iran. He received his B.S. and M.S. degrees from the Faculty of Electrical & Electronic Engineering, Razi University, Kermanshah, Iran in 2010, and 2013, respectively. He was awarded the Adelaide Scholarship International (ASI) in August 2016 to pursue his PhD degree in the School of Electrical & Electronic Engineering, the University of Adelaide, under the supervision of Prof. Christophe Fumeaux and Assoc. Prof. Damith Ranasinghe. His research interests include ultrawideband and multi-state reconfigurable antennas, pattern diversity antennas, and reconfigurable microwave passive circuits.

During his candidature, he received a number of scholarships from the university of Adelaide including the Adelaide Scholarship International (2016), Applied Electromagnetics Industrial Supplementary Scholarship (2018), and Research Travel Scholarship (2019). He also received a GeMiC 2019 Travel Scholarship from the University of Stuttgart, Germany, covering his travel expenses to attend the German Microwave Conference 2019. He was the recipient of two awards for his international conference presentations, including the second prize in student paper contest of 7th Asia-Pacific Conference on Antennas and Propagation (APCAP 2018) in Auckland, New Zealand and the top (platinum) student paper award in 8th Asia-Pacific Conference on Antennas and Propagation (APCAP 2019) in Incheon, Korea.

Seyedali Malakooti has served as a reviewer for a number of recognized journals including *IEEE Transactions on Microwave Theory and Techniques*, *IEEE Microwave and Wireless Component Letters*, *IEEE Antennas and Wireless Propagation Letters*, *IEEE Access*, *IET Electronics Letters*, and *IET Microwave and Antennas Propagation Letters*. He is a student member of the Institute of Electrical and Electronics Engineers (IEEE), IEEE Young Professionals, and IEEE Antennas and Propagation Society.

Seyedali Malakooti
seyedali.malakooti@adelaide.edu.au